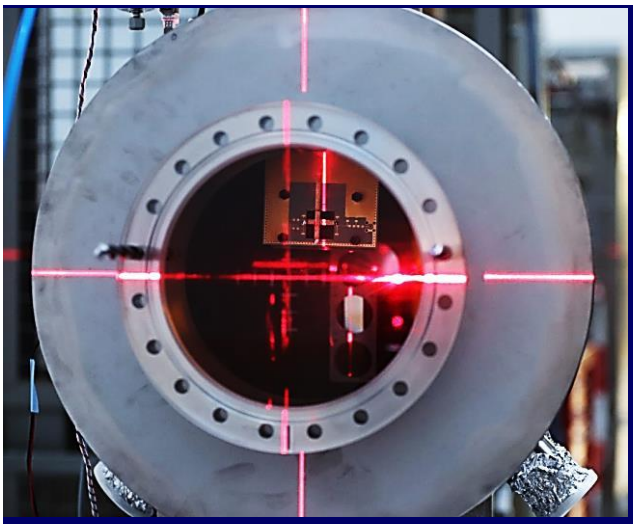

Compressed Baryonic Matter experiment at FAIR

CBM

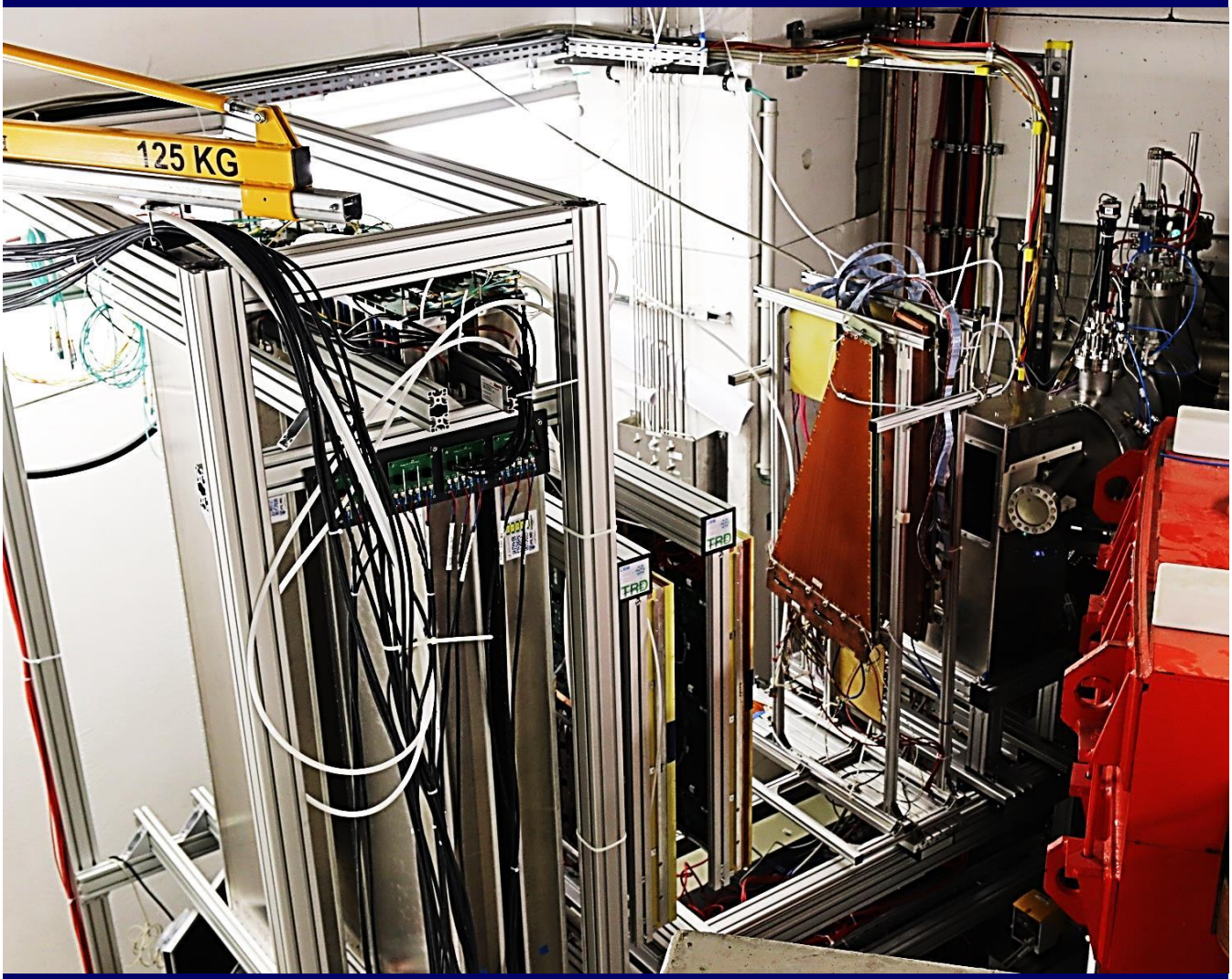

PROGRESS REPORT 2018

CBM Progress Report 2018

Imprint

Publishers

CBM Collaboration (https://fair-center.eu/for-users/experiments/cbm-and-hades/cbm.html)
GSI Helmholtzzentrum für Schwerionenforschung GmbH, Darmstadt, Germany (http://www.gsi.de)
GSI is member of the Helmholtz association of national research centers (http://www.helmholtz.de)

Editors

Ilya Selyuzhenkov (ilya.selyuzhenkov@gmail.com)
Volker Friese (v.friese@gsi.de)

Reviewers

P.P. Bhaduri, C. Blume, S. Chattopadhyay, J. de Cuveland, I. Deppner,
D. Emschermann, V. Friese, M. Golubeva, F. Guber, N. Herrmann, J. Heuser,
C. Höhne, W. Müller, C. Müntz, I. Selyuzhenkov, P. Senger, C. Sturm, A. Toia

Cover page: The mCBM full-system test setup at GSI

ISBN 978-3-9815227-6-1

DOI:10.15120/GSI-2019-01018

Printed in Darmstadt by GSI, October 2019

This work was supported by
Bundesministerium für Bildung und Forschung, Germany, through grants 05P15RGFCA, 05P15PXFCA, 05P15RFFC1, 05P15VHFC1, 05P16PMFC1, 05P16VTFC1, 05P19RGFCA,
FAIR Facility for Antiproton and Ion Research through cooperation contracts FAIR-INR,
GSI Helmholtzzentrum für Schwerionenforschung GmbH through F&E cooperations contracts with Goethe-Universität Frankfurt and Justus-Liebig-Universität Giessen,
HGS-HIRe for FAIR,
HIC for FAIR Helmholtz International Center,
EU/FP7-HadronPhysics3/WP19,
National Program on Key Basic Research Project of China-973 Program under grants 2015CB856902 and 2016YFA0400100,
the Ministry of Science and Technology of China under grant 2015CB856905,
the National Natural Science Foundation of China for International cooperation and Exchanges under grants 11420101004, 11461141011, and 11275108,
Czech MEYS - LM2015049 , OP VVV - CZ.02.1.01/0.0/0.0/16_013/0001677,
Department of Atomic Energy (DAE), Government of India,
National Institute of Science Education and Research (NISER), India, using the computing resources of the HPC cluster GARUDA,
Ministry of Science and Higher Education, Poland,
Romanian Ministry of Research and Innovation RO-FAIR F04/16.09.2016 and NUCLEU Project Contract PN 19060103,
Russian Science Foundation grant 17-72-20234, and the
FAIR-Russia Research Center.

Preface

An experimental project like CBM necessarily comprises a vast number of activities in many different areas: research on detector technology, development of readout electronics and components for data acquisition, computing and software tools for data processing and physics analysis, and many more. The series of annual CBM Progress Reports, started back in 2006, was intended to collect and document these manifold activities. Browsing through the past volumes unfolds a large spectrum of scientific work in the process of the realization of the project: from conceptual studies over thorough R&D to the implementation and testing of prototypes.

This CBM Progress Report 2018 continues along these lines. Its contents, however, reflect that some six years before the planned start of data taking, the CBM project is undergoing a gradual transition. The long period of planning and R&D is giving way to the large-scale production and integration of detector hardware, a process to be finished by 2024, when the CBM apparatus is expected to be commissioned in its experimental area. An important step towards this realisation of the experiment is the full-system test setup mCBM, allowing to study the joint in-beam operation of several detector systems and the read-out and data processing, following the ambitious CBM concept of free-running data acquisition. Further important technological experience is gained by the deployment of CBM detector systems at running experiments: TOF in STAR, RICH in HADES, PSD in BM@N. These detector operations will contribute important technological expertise for the preparation of the full CBM experiment.

We hope this reports conveys some of the enthusiasm of the CBM collaboration in the realization of a technologically very challenging experimental project which promises a rich physics output once taking data. Our thanks go to all who have contributed to this report: the reviewers, who helped getting it into shape, and all authors having delivered the actual content.

Darmstadt, October 2019

Volker Friese and Ilya Selyuzhenkov, editors

Contents

Several of the contributions to this volume also appear in the GSI Scientific Report 2018.

Status of the Compressed Baryonic Matter (CBM) experiment at FAIR

N. Herrmann and the CBM Collaboration
Physikalisches Institut, Univ. Heidelberg, Heidelberg, Germany

The exploration of the QCD phase diagram in the region of high baryon densities is the primary goal of the physics program of the Compressed Baryonic Matter (CBM) experiment at FAIR. During 2018 the collaboration faced a detailed evaluation in the context of the FAIR project review that was successfully passed with the arguments presented below.

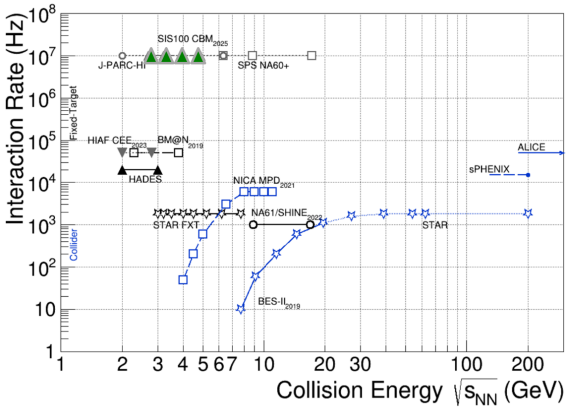

Figure 1: Rate capabilities as function of collision energy of existing and planned experiments (Figure adapted from [1]).

In order to make substantial progress beyond existing data and currently running experiments the CBM experiment is designed to be operated at extremely high reaction rates of up to peak rates of 10 MHz. This unprecedented rate capability allows to perform unique systematic measurements of multi-differential observables and at the same time the measurement of rare diagnostic probes. Fig. 1 depicts a comparison of the interaction rates of existing and future heavy-ion experiments as function of collision energy [1].

In order to address the different physics observables CBM pursues a modular detector setup concept with radiation hard detector components that all implement a triggerless digitization scheme and interface to a common data driven readout system. Event selection is done in a high performance compute farm by efficient software algorithms.

The various experiment configurations are depicted in Fig. 2. The first configurations (dubbed "Day-1") that will be realized are shown in the center and right side and include all subsystems. The anticipated average rates and

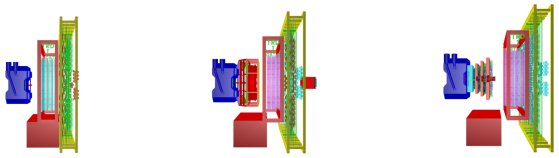

Figure 2: CBM setups for different physics topics: Hadron (left), Electron/Hadron(center) and Muon(right). For details see text.

event sizes are summarized in the following table.

Setup	Included subsystems	Average rate (max.)		Event size
		MSV	Day-1	
Hadron	STS, TRD, TOF	5 MHz	0.5 MHz	50 kB
Electron /Hadron	MVD, STS, RICH, TRD, TOF, PSD	0.1 MHz	0.1 MHz	75 kB
Muon	STS, MUCH, TRD, TOF	5 MHz	0.5 MHz	30 kB

With these setups several unique measurements become feasible with the first SIS100 beams arriving at the CBM target:

- Excitation function of Di-electron distribution
  Di-leptons have not been measured in the SIS100 energy range up to now and promise direct access to the properties of the QCD matter forming the fireball of the reaction. The initial temperature, lifetime and partial chiral symmetry restoration of the constituents imprint on the final spectra. For instance the slope parameter of the invariant mass distribution in the mass range from 1.2 GeV to 3 GeV is sensitive to the fireball temperature. The measurement of the excitation function might indicate phase changes of the constituent matter. A measurement with a statistical precision of 10% is estimated to require 10^{11} events and needs about 20 days of beam time. Note that the maximum rate of such a measurement with the Electron/Hadron setup is limited by the readout speed of the MVD subsystem.

- Excitation function of Di-muon distribution
  Due to lepton universality the di-muon spectrum is sensitive to the same constituent matter properties addressed within the di-electron channel. However, the systematic errors are completely different since the relevant backgrounds are of very different origins. Since in both cases the signal - to - background ratio is comparable and in the order of 10^{-2} utmost

care must be taken when quantitatively subtracting the background. Comparing both methods will give an additional level of confidence when reaching consistent results. As shown in the table the muon setup has an advantage in terms of rate capability eventually allowing for more systematic coverage of different reaction systems.

- Excitation function of multi-strange baryon production
  The production rate of multiply strange baryons and anti-baryons like Ξ and Ω in the SIS100 energy range is strongly influenced by the surrounding matter since the production reactions occur in the vicinity or below the free Nucleon-Nucleon production thresholds. Typical production rates are predicted to be in the order of $10^{-3}(10^{-5})$ for $\Omega^{-}(\bar{\Omega}^{+})$ at an incident energy of 10A GeV and quickly dropping towards lower beam energies. The superb quality of the CBM STS system allows to reconstruct those particles with an efficiency in the order of 5% and allows to gather sufficient statistics to map out the differences that are predicted when different assumptions on the properties of the surrounding matter are made. Sensitivities to the equation-of-state, chiral symmetry restoration in the hadronic phase and deconfinement are reported in the literature, e.g. in [2].

The data samples gathered for these key observables will also be used to explore other interesting observables that will benefit from large statistics like collective flow of identified particles or event-by-event fluctuations of conserved quantities. Some details concerning those additional observables are given in the physics performance chapter of this report.

While the statistical significance of the "Day-1" - measurements after a year of operation will be better than any other of the experiments listed in Fig. 1 in the SIS100 energy range, CBM's rate capability reachable in its final version (dubbed "Modular Start Version (MSV)" in the table above) adds a significant discovery potential. This includes the possibility to measure exotic quasi-bound hadronic states and sizeable amounts of light double strange hypernuclei. For example, ${}^{6}_{\Lambda\Lambda}$He - nuclei should be reconstructed at a rate of 60 events per week when running at full luminosity with the Hadron setup provided their production rate is described properly by the Statistical Hadronisation Model [3]. With the Muon setup the full rate capability allows to address charm production in cold nuclear matter.

The interaction rates demanded for the anticipated CBM measurements require a robust detector system and a stable data acquisition and selection concept. Since the latter is solely done in software prototype concepts and implementations need to be evaluated as soon as possible. CBM is currently in a state of verifying the detector and data acquisition systems and exercising the data transport stability within the framework of its demonstrator setup, mCBM. Data were successfully transferred at high speed into the Green Cube housing GSI's high performance compute farm and currently CBMs entry node cluster. The event selection software, however, is still in its infancy and needs substantial extensions.

Details on the detector and computing subsystems and on the first commissioning run of mCBM are given in this report and show that CBM is on the right track. However, it is also apparent that still a substantial effort is necessary to start series production of the detector components and to develop the necessary software for operating and controlling the experiment as a whole.

References

[1] T. Galatyuk, Nucl. Phys. A982 (2019) 163

[2] W. Cassing at al., Phys. Rev. C93 (2016) 014902

[3] A. Andronic at al., Phys. Lett. B697 (2011) 203

Micro-Vertex Detector

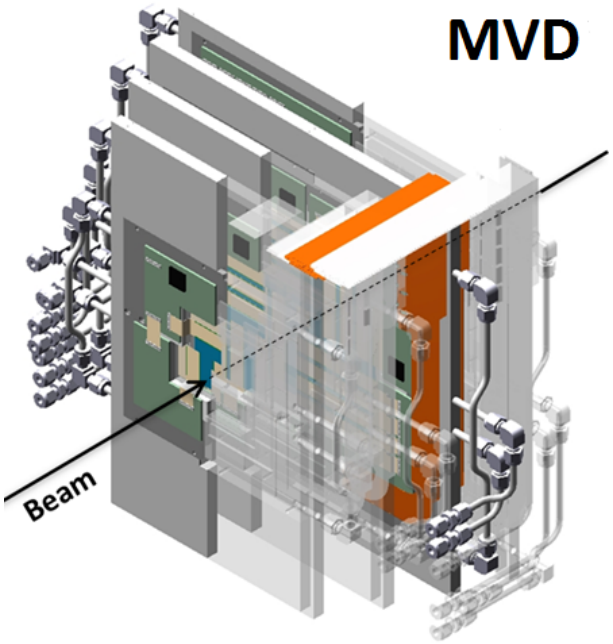

Micro Vertex Detector - Summary

C. Müntz[1], *J. Stroth*[1,2], *and the CBM MVD team*[1,2,3]

[1]Goethe University Frankfurt, Germany; [2]GSI, Darmstadt, Germany; [3]PICSEL group, IPHC Strasbourg, France

The R&D carried out by the MVD team in 2018 focused on qualifying and validating the first dedicated CBM pixel sensor precursor MIMOSIS-0, both at IPHC Strasbourg and Goethe-University. The results, especially on aspects of radiation-hardness, will impact the design of the first full-size sensor MIMOSIS-1, expected in 2019. Its completion represents the crucial milestone towards the final pixel sensor for the MVD. A number of optimization studies are ongoing, e.g. concluding the final dimension of the full-size sensor, optimize the configuration of the sensors on the quarter stations, efficient integration to the readout system, estimating the expected local fluences for different running scenarios, etc. Lastly, the PRESTO project on prototyping a large station module was successfully followed up by running and controlling PRESTO 24/7 in vacuum.

Sensor:

The future CBM pixel sensor MIMOSIS represents a derivative of the ALICE ITS sensor ALPIDE, considering in addition local occupancy and hit rate hot spots due to CBM's fixed target geometry and challenging interaction rates. The first prototype MIMOSIS-0, together with further test structures, was produced and is still being extensively tested. A focus was put on the on-pixel signal processing circuits. Besides systematic lab test series on the pixel response, sensors have been exposed to both ionizing (20 Mrad) and non-ionizing (10^{14} n_{eq}/cm^2) radiation with promising results so far. These studies are continuing while preparing the submission of MIMOSIS-1.

Sensor read out and hit rates:

The readout concept of the MIMOSIS day-1 sensor has been concluded. Occupancy and hit rate hot spots, together with beam fluctuations, are coped with concepts of load balancing, elastic buffers, and an adjustable number of 320 Mbps links per sensor. Based on the on-sensor readout architecture, CBM's physics cases and planned interaction rates it is possible to define the read-out topology, and to deduce the number of GBTx links MVD will consume, i.e. below 100 in worst case for both detector geometries VX (VerteXing) and TR (TRacking). By doing so, options to even increase the interaction rate beyond the nominal ones have been identified. These studies also helped scrutinizing the concept of controlling and reading out the MVD mounted in the vacuum, i.e lay-outing the electrical feed-throughs at the target chamber.

Detector geometries and keep-out volumes:

Starting from the MIMOSIS geometrical dimensions the station layout was revisited and tuned. Two detector geometries have been optimized, featuring different station-to-station distances, z-position of the first and the following stations, as well as the station layout. These detector geometries meet the requirements w.r.t. secondary vertex finding (VX) and tracking (TR), built out of three different station geometries only, to simplify e.g. manufacturing. Both detector geometries were made available for Monte Carlo simulations. As a follow-up respective CAD geometries have been set up to engineer the MVD detector inside the target chamber, including readout and services, and to define unique mechanical interfaces to CBM. Most prominently, the target chamber flange layout, housing both the target station and the feed-throughs for connecting to the MVD, was proposed. In order to ease the installation concept and minimize conflicts with other systems, we have defined so-called keep-out volumes, which are housing exclusively MVD components, and voids to reserve space for target and beam pipe installations. Both serves as a starting point to arrive at a mature layout of the installations inside the magnet gap.

Status of the station module PRESTO:

Our prototype of a larger MVD station module, called PRESTO, was finally commissioned and moved in the vacuum vessel to study long-term stability of mechanical and electrical components under moderate vacuum and different temperature settings. Hence, a dedicated vacuum feed-through for steering and controlling the sensors was designed and manufactured. The sensors are read-out by customized front-end and TRBv3 hardware and can be actively temperature-controlled. An EPICS-based control system was setup and guarantees 24/7 safe operation. So far, we did not notice malfunctioning or degradation of the sensor performance even when running pressure cycles. These tests will continue and further consolidated.

MIMOSIS, a sensor for the CBM-MVD

M. Deveaux[1], *M. Winter*[2], *and the CBM-MVD team*[1,2]
[1]Goethe-Universität Frankfurt am Main, Germany; [2]PICSEL group, IPHC Strasbourg, France

Introduction

The Micro Vertex Detector (MVD) of CBM will be located 5 to 20 cm downstream the target of CBM in the target vacuum. Being designed to register 10^5 Hz Au+Au collisions or 10^7 Hz p+Au collisions, the detector has to provide an outstanding rate capability. To scope with this challenge, the MVD will be equipped with a next generation CMOS Monolithic Active Pixel Sensor named MIMOSIS, which is currently being developed.

Requirements and technical design

MIMOSIS will host 1024 columns of 504 pixels each. The pixel dimensions will be 26.88×30.24 μm^2. The pixel, which was inspired by the ALPIDE sensor [1] used for the ALICE ITS upgrade, will perform signal discrimination as required for an accelerated, non-sequential readout providing a time resolution of 5 μs. Unlike ALPIDE, MIMOSIS may optionally be equipped with AC-coupled pixels, which allow to extend the radiation tolerance of the device by depleting the pixel. This might allow to reach a radiation tolerance well beyond the 3×10^{13} $\mathrm{n_{eq}/cm^2}$ plus 3 Mrad expected for one year of CBM operation.

The readout concept of MIMOSIS aims at handling the high, above mentioned, collision rates and to moreover tolerate beam fluctuations (peak to average) of a factor three. This turns into the need to scope with a peak hit rate of ~ 70 MHz/cm^2. Thanks to the fixed target geometry of the MVD and the beam fluctuations, this rate is reached only for short times and at dedicated hot spots. Spatial load balancing and an elastic output buffer are applied to reduce the initial peak data rate from a theoretical maximum of 102 Gbps to 2.6 Gbps, which is transmitted to the outside by up to 8 parallel 320 Mbps data links. Optionally, some of those links may be switched off in order to save power and data traces.

Observations from the first prototype sensor

A first prototype, MIMOSIS-0, was produced and is being tested. The sensor hosts a full set of on-pixel signal processing circuits and the circuits for the non-synchronous pixel readout. Moreover, they are equipped with a full slow control, still relying in a JTAG interface. The buffer structure and the data sparsification circuits providing a partial on-chip clustering were not yet implemented. The sensor submission was complemented by so-called CE18 test structures, which host uniquely pixels with the aim to study specific questions of their analogue circuit design. The pixels of MIMOSIS-0 are equipped with an analogue pulse generator, which allows for quantitative studies of the properties of the on-pixel amplification circuits.

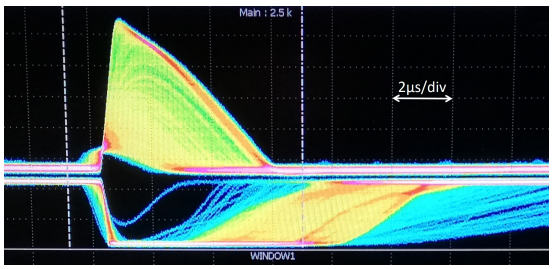

Figure 1: Accumulated hits from an ^{55}Fe radioactive source as recorded with the analogue output of MIMOSIS-0. The signal of the on-pixel pre-amplifier (upper signal) and of the on-pixel discriminator (inverted lower line) are shown.

First results confirm the sensitivity of the pixels to 5.9 keV photons as emitted from a ^{55}Fe radioactive source (see Fig. 1). An analysis of the pulse shapes showed a maximum time walk of 0.6 μs and a jitter of slightly below 0.3 μs for a signal of 200 e. Signals below 150 e may be recorded as well but the time walk and jitter increase to 1.2 μs and 0.8 μs respectively. The maximum pulse length, which determines the dead time of the pixels, amounts < 10 μs. The response of the amplifier is linear from a signal of ~ 150 e up to ~ 600 e and saturates hereafter. This intended saturation is to limit the pulse length.

Next steps

First MIMOSIS-0 and CE18 sensors were irradiated with up to 20 Mrad and up to 10^{14} $\mathrm{n_{eq}/cm^2}$ and they are currently being studied. First tests suggest that the sensors survived those high radiation doses without major damage but their sensitivity to minimum ionizing particles remains to be confirmed. In 2019, a submission of a first full size sensor prototype (MIMOSIS-1) hosting the remaining building blocks is scheduled.

References

[1] M. Suljic, JINST 11.11 (2016): C11025.

Expected CBM-MVD hit rates for p+A and Au+Au reactions

Q. Li[1], *M. Deveaux*[1], *J. Michel*[1], *C. Müntz*[1], *J. Stroth*[1,2], *and the CBM MVD team*[1,2,3]
[1]Goethe University Frankfurt, Germany; [2]GSI, Darmstadt, Germany; [3]PICSEL group, IPHC Strasbourg, France

Simulation setup

We report on MC simulation results based on the envisaged sensor response and data conversion of the CBM pixel sensors MIMOSIS. The most recent sensor architecture has been used to derive the data output format and hits per frame for a given number of active 320 MBits/s links. Each link can transport 100 words for one frame of 5 μs. Both detector geometries VX and TR have been employed, optimized for vertex-finding and tracking, respectively. Each version comprises four detector stations of three different station types, equipped with MIMOSIS sensors. Both benchmark reactions have been studied, Au+Au (4 and 10 AGeV, 100 kHz nominal interaction rate, also with 50% mgn. field) and p+Au (25 GeV, 10 MHz), assuming a fake hit rate of 10^{-5} and relying on the average no. min. bias reactions in the 1% interaction probability target. Setup and results are detailed in [1]. The fixed-target setup imposes very inhomogeneous hit occupancies[1] even on single sensors, counteracted by the possibility to individually set the no. of links per sensor. 55 (190, 460) hits/frame can be transported with 2 (4, 8) links. Finally, estimating the no. of GBTx links was driving this study.

Results

Interaction rates: For all three station types, the reaction Au+Au, 10 AGeV at 50% mgn. field yields the largest hit occupancies dominated by delta electrons, led by the VX geometry with 250 hits/frame of the hottest sensor of the first station. Figure 1 shows, as example, the average hit number per frame vs. the sensor ID for two reactions. However, the study suggests to run with even higher interaction rates (factors 2 to 3) than the nominal ones, if data losses between 20 and 40% can be accepted for these hot sensors (VX), or the inner sensors run with additional links (TR). As an example for the reaction Au+Au, 10 AGeV and full mgn. field, the interaction rate can increase to 250 kHz if accepting a data loss of 30% in the two innermost sensors only[2].

Data links and GBTx count: Exploring the matrix of reaction systems and detector geometries realized with different station types the total no. of links and GBTx chips employed can be deduced. Each GBTx chip can serve 10 sensor links. We arrive at 76 and 84 GBTx chips for the VX and TR detector geometry, respectively. These numbers can be reduced to 70 (VX) and 76 (TR) by treating outermost sensors special w.r.t. number of links connected. This scenario would help to reduce the total power consumption, which is most pressing for the large-area detector stations. On the other hand, trying to further push the maximum interaction rate beyond the nominal ones, the total no. of GBTx chips increases to 88 (VX) and 96 (TR).
The overall no. of link could eventually further decreased by (i) considering one mgn. field polarity only, (ii) revise the sensor design to allow for running with one link only, and (iii) disabling those sensors in specific stations positioned outside of the CBM geometrical acceptance.
In conclusion, the results presented and detailed in [1] provide firm estimates for planning the number of GBTx chips employed by MVD, as well as e.g. designing the layout of the electrical feed-throughs of the target chamber front plate. They are based on the projected MIMOSIS r/o architecure and geometrical dimension, considering the nominal interaction rates for AA and pA reactions and conceivably reduced mgn. field.

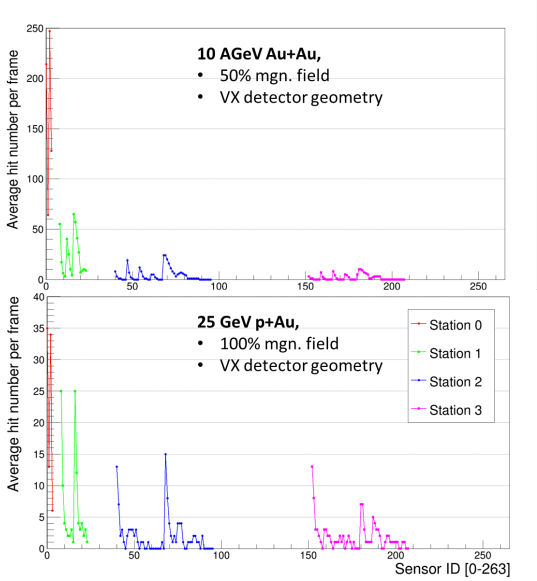

Figure 1: Average hit number per frame vs. sensor ID for an Au+Au (upper) in comparison to a p+Au reaction, shown for all four station half sides, assuming left-right stations geometry.

References

[1] Q. Li et al., *CBM Technical Note TN-19002, 2019*

[1]Note, we assume left-right symmetry for the individual stations to allow for reversing the mgn. field.
[2]Assuming minimum bias interaction rate averaged over 100 μs.

MVD keep-out volumes

P. Klaus[1], *M. Koziel*[1], *J. Michel*[1], *C. Müntz*[1], *J. Stroth*[1,2], *and the CBM MVD team*[1,2,3]
[1]Goethe University Frankfurt, Germany; [2]GSI, Darmstadt, Germany; [3]PICSEL group, IPHC Strasbourg, France

The MVD [1] is the vertex silicon pixel detector of the CBM experiment, placed closest to the target and in front of the STS. Based on our current knowledge, we have been working on a realistic MVD CAD model that could help in joining forces resulting in a common understanding of the MVD environment, see Figure 1, the target volume and the installation process.

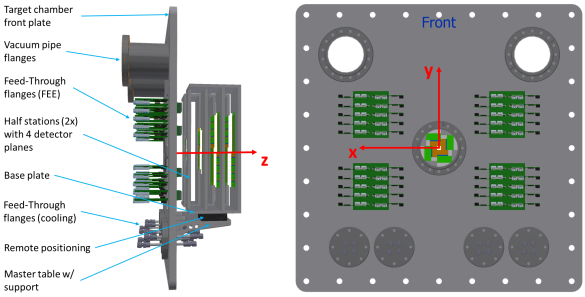

Figure 1: Schematic side (left) and front (right) view of the MVD setup, including support structures and functional unites referred to in the text; (0,0,0): target position.

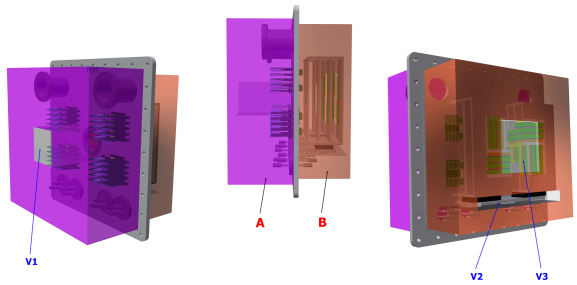

Figure 2: CAD illustrative view on the keep-out volumes located outside (A) and inside (B) the target chamber, with void areas (V1 - target volume, V2 - detector support volume, V3 - vacuum window between MVD and STS).

The design as depicted in Figure 1 was the guideline for the recently submitted CBM Technical Note [2], comprising a proposal of key responsibilities of the MVD team (see Table 1), interfaces to the CBM experiment, as well as geometrical volumes exclusively reserved for the MVD setup, so-called MVD keep-out volumes, shown in Figure 2.

We have identified the two physically touching interfaces between the MVD and the CBM environment: (a) Mounting of the two MVD half station base plates to the remote positioning units and (b) Mounting of MVD feed-through flanges to the target chamber front plate. Figure 1 depicts the (at present) realistic estimate of the number and the layout of the required feed-through flanges for MVD electrical signals, biasing and cooling medium. We concluded that, for the MVD, most pressing is the detailed design of the target chamber front plate including the volume taken by the target and upstream beam pipe.

MVD team	Detector stations, base plates, MVD cabling (data, DCS, power), MVD cooling, feed-through flanges (mounted to target chamber front plate), FEE outside the vacuum
To be assigned	Target chamber (with front plate and services) with beam pipes connected, target setup, remote positioning units, master table (mounted to the front plate)

Table 1: Proposed allocation of responsibilities of the MVD team in and close to the target chamber.

Volume	x_1	x_2	y_1	y_2	z_1	z_2
A	-350	350	-350	350	-280	-20
B	-330	330	-330	330	0	225
V1	-80	80	-80	80	-280	-20
V2	-240	240	-198	-248	0	225
V3	-110	110	-110	110	210	225

Table 2: Coordinates of MVD keep-out volumes (A and B) and voids (V1, V2, V3) inside the CBM magnet's gap given in [mm]. No safety margins are included. Coordinates axes: see Figure 1.

The MVD keep-out volumes as defined in Table 2 have been implemented with Autodesk Inventor 2019. A link is to be found in our corresponding Technical Note [2].

References

[1] M. Koziel et al., *https://doi.org/10.1016/j.nima.2016.05.093* and references therein.

[2] P. Klaus et al., CBM Technical Note TN-19004, 2019

MVD: Status of detector integration and operation

P. Klaus[1], *M. Koziel*[1], *C. Müntz*[1], *J. Stroth*[1,2], *and the CBM MVD team*[1,2,3]
[1]Goethe University Frankfurt, Germany; [2]GSI, Darmstadt, Germany; [3]PICSEL group, IPHC Strasbourg, France

This report summarizes the activities at the Institut für Kernphysik Frankfurt (IKF) related to the precursor of the CBM-MVD station called PRESTO [1]. Figure 1 depicts PRESTO module just before closing the large vessel hosting the prototype. The PRESTO sensors from both sides of the TPG carrier were tested before and after moving the module from its assembly jigs into its position as seen in figure 1.The performance of all sensors remained unchanged after this operation.

The module is currently connected to three different systems: the readout, the liquid cooling, and temperature surveillance with Pt-100 sensors. Concerning the read-out, the sensors are connected to FEE boards inside the vacuum chamber with custom low-mass single-layer flexible printed circuit (FPC) cables and from there commercial FPCs go to through the vacuum flange on top of the assembly. The liquid cooling is connected with flexible plastic tubes to our Huber CC-405 cooling system via a 6 mm Swagelok feed-through flange on the left side of the image (not visible). Two Pt-100 sensors serve as temperature surveillance and thermal runaway protection. They are attached to the heat sink inside the vacuum chamber and connected to a customized 8-ch PT100 board. Processed and calibrated values are then sent to the outside world via a multi-pin D-SUB feed-through on the left side of the chamber. The customized feed-through flange (DN 160 CF) was processed at a local workshop (IKF) to create the slits for readout cables insertion. The inserted cables were then preliminary fixed and sealed with a dense TorrSeal product. In a second step we used a EPO-TEC 301-2 low-viscosity, low-out-gassing adhesive listed in NASA's outgassing database to fill all the remaining gaps and make the flange vacuum tight.

In an effort to evaluate the reliability and performance of the prototype under regular working conditions, we operated it inside the chamber under vacuum, cooled to a constant temperature with automated 24/7 detector controls in place. Figure 2 depicts trend plots taken within 3 months of running PRESTO continuously in the vacuum vessel. Aiming to reduce complexity, the controls system is implemented fully in EPICS with some further systems required for other purposes such as data acquisition. This work is offloaded to battle-proven web tools provided by the TRB3 collaboration.

To go beyond, in 2018 about 50% of sensors needed to accomplish a follow-up module "PRESTO-II" were probe-tested (addressing the yield problem reported in [2]), however these tests were interrupted by a probe station failure (fixed) and focus on MIMOSIS-0 evaluation. PRESTO tests and efforts will continue in 2019.

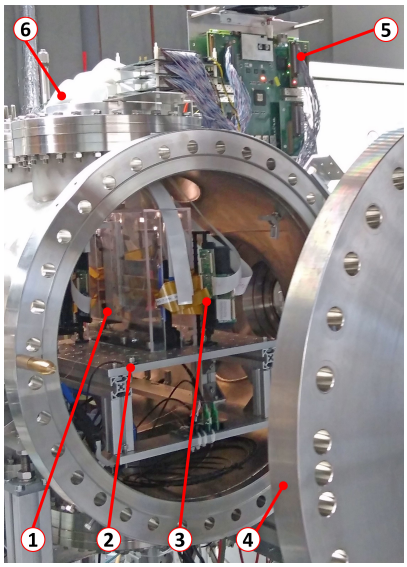

Figure 1: PRESTO (1) mounted on movable table (2); FEE board (3) interconnecting low-mass flex (orange) with standard flex (white) cables; front flange (4), TRBv3 r/o (5), customized feed-through flange (6) for r/o cables.

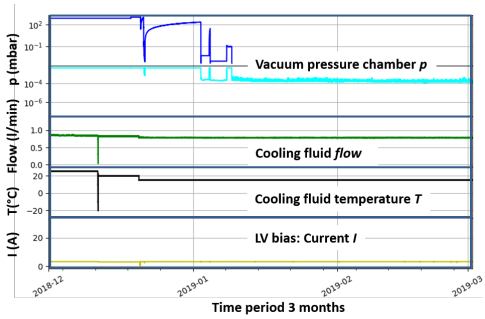

Figure 2: Trend plots of environmental parameters recorded 24/7 within a time period of 3 months with PRESTO inside the vacuum vessel.

References

[1] M. Koziel et al., CBM Progress Report 2014, p.9.
[2] C. Müntz et al., CBM Progress Report 2017, p.10.

Silicon Tracking System

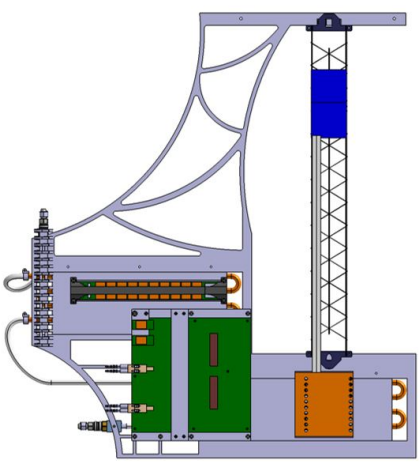

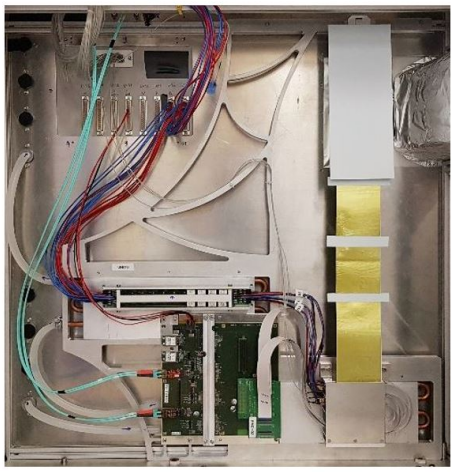

Silicon Tracking System – Summary

H. R. Schmidt[1,2], J. M. Heuser[2], and the CBM STS working group
[1]Universität Tübingen, Germany; [2]GSI, Darmstadt, Germany

The Silicon Tracking System (STS) is the exclusive detector in the CBM experiment to provide unambiguous trajectory identification and momentum measurement of the charged particles produced in beam-target interactions up to the highest collision rates, i.e. 10^7 Hz. The detector, installed in a 1 Tm dipole magnet, will consist of 8 logical tracking stations populated with double-sided silicon microstrip sensors of strip lengths matched to the varying particle densities across its aperture. The silicon sensors are read out with custom-designed self-triggering front-end electronics. Digitized and time-stamped channel data is streamed to a computing farm for on-line event reconstruction. The detector will be housed in a thermal enclosure that will allow operating the sensors at lower-than-ambient temperatures to limit radiation induced leakage currents. Additional substantial cooling will be provided to remove the power disspated by the front-end and read-out electronics, the local power supply boards and losses in cables. The detector is conceived as a low-mass system in the common CBM aperture, as to minimize multiple scattering of the particles and thus to provide best momentum resolution. Therefore the basic operational structure, the STS module, spatially separates sensors from the front-end electronics with thin multi-line microcables, so that the electronics with its powering and cooling infrastructure can be placed outside of the physics aperture.

Thanks to the efforts of the members of the STS project teams we made progress in many of the activity fields towards the finalization of the detector components, the system design, and demonstrator systems. The progress reports in this chapter inform on sensor readiness and advancement with read-out electronics, front-end electronics boards, module assembly at GSI, KIT and JINR, power supply, cooling and further system integration topics. The situation was assessed in two CBM-STS reviews; detailed technical notes on the various topics were supplied to the discussion [1]:

(1) The *Sensor Production Readiness Review* [2] was organized at GSI in April 2018. It covered all essential issues from the design of the CBM final prototype sensors, over performance w.r.t. signal-to-noise and detection efficiency in modules, performance of irradiated sensors w.r.t. charge collection, sensor thickness, acceptance criteria and quality assurance, to vendor capabilities and tendering. The review yielded the recommendation to start the administrative tendering procedure for the sensor procurement in industry.

(2) The *Core Preliminary Design Review* [3], held at GSI in November 2018, was an important milestone on the way to preparing for start of STS construction in 2019. The main STS building blocks, modules and ladders, require fabrication to be launched first. The review asked for the readiness of their construction, object definitions, assembly procedures, tools, sites and teams, and where open issues or even show stoppers might be in the system concept. The conclusion of the reviewers stated good progress with the module and ladder assembly, powering and read-out, while for detailed system design completion there is still work ahead but also time left. Cooling was identified as a critical topic where in particular the gas cooling for the sensors requires experimental proof.

Next to investigations in laboratory test stands, two important system test activities were carried out supporting the discussions made at the reviews:

(1) An in-beam test of prototype STS modules, demonstrating realistic electrical configuration but not yet full sensor read-out, has been carried out at COSY, Research Center Jülich, Germany, to verify the track point measurement efficiency in a reference tracking telescope. This gave important feedback into the Sensor Production Readiness Review.

(2) The first two fully assembled STS modules were integrated onto the first STS ladder, constructed for the mSTS demonstrator detector. It was installed into the mCBM experiment at the end of November 2018, yielding one half of the first mSTS tracking station for mCBM start-up in December 2018. The preceding integration of the mSTS detector gave important insight into combining different services, power supplies, regulating and distributing boards and data aggregation boards, with the detector ladder on the mechanical frame, cooling and cabling.

In February 2019, the STS project timeline as derived from the 2018 progress was included into the updated FAIR baseline planning. It requires sensor production starting in 2019, module and ladder construction from 2020 - 2023, and the STS system commissioned for installation into the CBM cave in 2024.

References

[1] Technical Notes accompanying the reviews are archived at https://indico.gsi.de/event/7450/

[2] CBM-STS Sensor Production Readiness Review, 23 April 2018, https://indico.gsi.de/event/7128/

[3] STS Core Preliminary Design Review, 30 November 2018, https://indico.gsi.de/event/7929/

Production readiness of STS microstrip sensors

J. M. Heuser[1], *O. Bertini*[1], *D. Emschermann*[1], *J. Eschke*[1,2], *E. Friske*[3], *U. Frankenfeld*[1], *R. M. Kapell*[1], *E. Lavrik*[3], *J. Lehnert*[1], *P. A. Loizeau*[1], *A. Lymanets*[1], *O. Maragoto-Rodriguez*[4], *Ie. Momot*[1], *I. Panasenko*[3], *P. Pfistner*[7], *V. Pugatch*[5], *A. Rodriguez-Rodriguez*[3], *H. R. Schmidt*[1,3], *C. J. Schmidt*[1], *C. Simons*[1], *M. Teklishyn*[2,5,6], *F. Uhlig*[1], *and R. Visinka*[1]

[1]GSI, Darmstadt, Germany; [2]FAIR, Darmstadt, Germany; [3]Universität Tübingen, Germany; [4]Goethe Universität, Frankfurt, Germany; [5]KINR, Kiev, Ukraine; [6]now Université catholique, Louvain, Belgium; [7]KIT, Karlsruhe, Germany

In 2018, the STS project reached an important milestone on the way towards starting its construction. Production readiness for its silicon microstrip sensors was declared following a review held in April at GSI [1]. This enabled the project team to start a tendering procedure through FAIR. It lead to final offers in January 2019. Conclusion of a contract with an industrial supplier is expected still in the first quarter of 2019.

The double-sided silicon microstrip sensors for the CBM Silicon Tracking System have been overviewed in [2]. About 1100 specimen (including 15% extra material to compensate limited integration yield) are required in four variants (6.2 cm width; 2.2, 4.2, 6.2 and 12.4 cm height). They feature on an around 300 μm thick substrate 1024 strips per side, arranged at 58 μm pitch under 7.5° between front- and back sides. The key requirements on the sensors are (a) design fitting to the module integration concept, (b) high homogeneity, minimal defects of its structures, (c) radiation tolerance fitting the CBM environment, (d) high track point efficiency, and (e) production in specifications, time and budget.

Three important experimental verifications had been made in the forefront of the review: (1) A detailed optical and electrical quality inspection instrumentation and procedure allowed assessing the sensor prototypes of two vendors independently of the factory accepatance tests [3]. (2) A detailed irradiation campaign studied the radiation tolerance of the silicon sensors beyond the expected lifetime dose [4]. (3) A test of sensors in a realistic prototype module structure (Figs. 1, 2) exposed to intense proton beam at COSY, Research Center Jülich, Germany, proved high track point efficiency [5].

A detailed technical note has been compiled [6] discussing all of the above points, answers to the reviewers' questions and a summary of the conclusion: the recommendation to proceed with the administrative tendering procedure through FAIR to enable STS construction start in 2019.

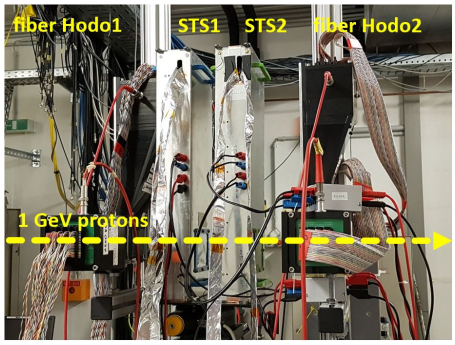

Figure 1: Test beam telescope of two scintillating fiber hodoscopes and two prototype STS modules under study.

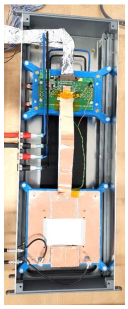

Figure 2: Prototype STS module demonstrating double-sided read-out of a microstrip sensor through 25 cm long microcables with two STS-XYTERv2.0 ASIC boards.

References

[1] CBM-STS Sensor Production Readiness Review, https://indico.gsi.de/event/7128/, 23 April 2018

[2] J. M. Heuser et al., *Status of micro-strip sensor development for the CBM Silicon Tracking System*, CBM Progress Report 2016, p. 22

[3] CBM-STS QA Workgroup, *Specifications for Quality Assurance of Microstrip Sensors in the CBM Silicon Tracking System*, CBM-STS Note 2016-1

[4] Ie. Momot, M. Teklishyn, A. Lymanets, O. Bertini, J. M. Heuser, *Evaluation of the STS sensor prototypes irradiated with 23 MeV proton beam using relativistic β-electrons*, CBM-STS Note 2018-1

[5] J. M. Heuser et al., *CBM Silicon Tracking System tested in 2018*, in: Application for testing CBM detectors in beam at COSY in Q2/2019, CBAC#9, 14 January 2019, http://www.ikp.fz-juelich.de/CBAC/documents/cbac09.html

[6] O. Bertini et al., *Production Readiness Review for the Silicon Sensors of the CBM Silicon Tracking System*, CBM-TN-18010

Electrical qualification of the microstrip sensors for mSTS

I. Panasenko[1,2], *H. R. Schmidt*[1,3], *and E. Lavrik*[1,3]
[1]University of Tübingen, Germany; [2]KINR, Kiev, Ukraine; [3]GSI, Darmstadt, Germany

Five out of thirteen double-sided CBM06 microstrip sensors 6×6 cm^2 large, selected for the mSTS setup [1] were received in the Tübingen Quality Test Center for quality assurance (QA) tests. The sensors are of the final design as foreseen for the STS and corresponding details can be found elsewhere [2]. Here we report only on the results of the QA tests. Guidelines and the description of the measurement procedures used at CBM are covered in details in [3].

Results of the IV-CV measurements are summarized in Table 1 where V_{FD} is the full depletion voltage, C_b the strip backplane capacitance and V_{BD} the breakdown voltage.

Table 1: Global parameters of the tested CBM sensors for mSTS. C=CiS, H=Hamamatsu.

Sensor ID	Vendor	V_{FD} [V]	C_b [pF/cm]	V_{BD} [V]
5552-301	H	52	0.19	550
5552-310	H	51	0.19	550
352151-04	C	87	0.21	220
352151-05	C	69	0.21	500
352151-13	C	72	0.22	150

The difference in C_b is due to different thickness of the silicon wafers used by CiS and Hamamatsu. One sensor exhibits a breakdown below 200 V of bias voltage while it is required for a sensor to operate without a breakdown up to 200 V. In order to investigate such behavior, IV-CV measurements with guard rings were performed. Figure 1 shows measured IV curves revealing the origin of the breakdown. It occurs through the sensor edge region where defects caused by blade dicing and handling appear. It is considered the most frequent cause of the breakdown of the CiS prototypes. The bulk of all tested sensors does not show any breakdown signs below 500 V of bias voltage. The total leakage current of the Hamamatsu and CiS sensors is around 7 nA/cm^2 and 170 nA/cm^2 at 150 V, respectively. Only sensor 352151-13 has higher current of 250 nA/cm^2 due to a cluster of leaky strips on the p side of the sensor. No visual damage was found for those strips suggesting a manufacturing defect during implantation or a crystal defect.

Strip integrity tests were performed on all sensors in order to find "bad" strips, i.e. those with one or more defects or parameters outside acceptance criteria [2]. "Pinholes", i.e short circuited AC decoupling layers between strip implant and aluminum read-out line, leaky strips, implant/metal breaks and short circuits, polysilicon resistor

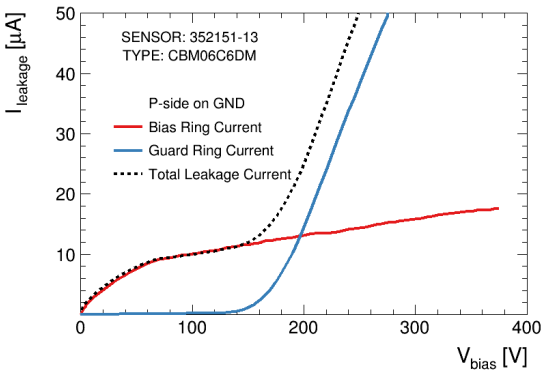

Figure 1: Bulk and edge currents of a 6×6 cm^2 CiS sensor as a function of reverse bias voltage.

break are identified here. Manufacturers provide only pinhole test results which also is a part of tests performed at CBM entrance control. Figure 2 shows the results of such measurements for one of the sensors with the largest fraction of the bad strips found. Here, we only look at deviations from common levels of capacitance and current. Most of the identified defects are breaks of the strip implantation. It was confirmed in visual inspection. An example of an unusual large implant break cluster is shown in Fig. 3.

Such types of defects are observed for Hamamatsu sensors while they are not common for CiS ones. Metal layers of few pairs of strips are electrically shorted on one of the CiS sensors. In addition, few leaky strips were found. The identified pinholes are in accordance with the data provided by the manufacturers. All defects are summarized in Table 2.

Table 2: Statistics on the identified defects of the tested CBM sensors for mSTS.

Sensor ID	Pinholes	Breaks	Shorts	Other	Total
5552-301	3	24	0	0	27
5552-310	1	3	0	2	6
352151-04	1	0	0	0	1
352151-05	0	0	4	0	4
352151-13	16	1	0	0	17

The total amount of bad strips per sensor per side is well below the required acceptance limit of 1.5% for the CBM-STS [2] except for the sensor with ID number 5552-301 where all 27 bad strips belong to the p side of the sensor. However, the sensor is fully operational and still can be used for module assembly in mSTS. Because implant

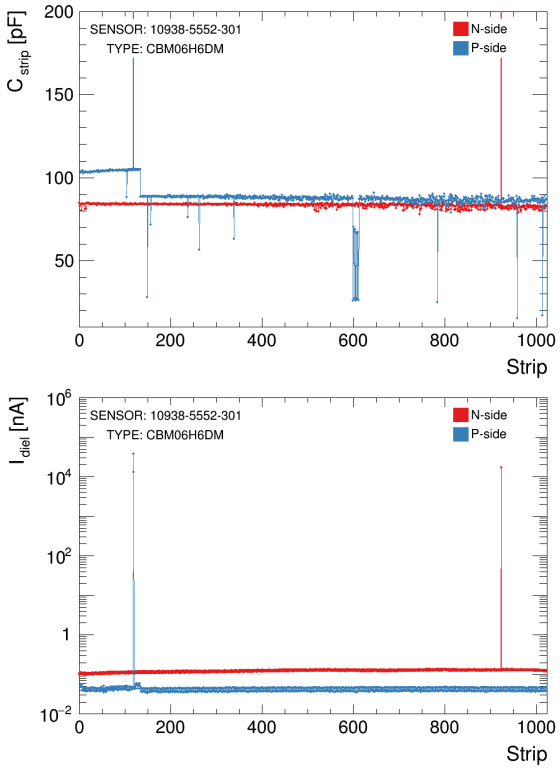

Figure 2: Example of the results of the strip integrity scan on one of the CBM06 sensors: Strip series capacitance (top) and dielectric current at 20 V across the coupling capacitors (bottom).

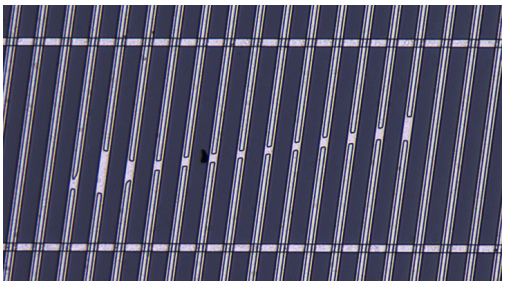

Figure 3: Cluster of strips with broken implants. Dark areas are interstrip gaps, horizontal lines correspond to second metal layer. Implant breaks can be seen through the thin metalization layers shown in white.

breaks can be identified visually, other Hamamatsu sensors are suggested to be checked as this was the most abundant defect type. No defects related to the second metal layer or polysilicon resistors were found.

In addition to the above described measurements, coupling and interstrip capacitances were measured for few strips on both sides of the sensors, as functions of test signal frequency and applied bias voltage. It is necessary to check that they are within the CBM design specification. Moreover, such extra measurements can reveal very complicated defects not seen in integrity tests but which are crucial for the microstrip sensor to be functional. The obtained capacitances are summarized in Table 3. The values satisfy our requirements and no further defects were found.

Table 3: Coupling and interstrip capacitances of the tested sensors for mSTS.

Sensor ID	C_c [pF/cm]		C_{is} [pF/cm]	
	p-side	n-side	p-side	n-side
5552-301	10	11	0.36	0.37
5552-310	10	11	0.36	0.37
352151-04	20	17	0.44	0.47
352151-05	20	17	0.52	0.49
352151-13	20	17	0.47	0.50

Summarizing, all CBM microstrip sensors accepted for QA tests did not show any critical issues. One exception is the early breakdown of the CiS sensor with ID number 352151-13 – it can not be operated at bias voltages higher than 150 V. The amount of strip defects as well as strip parameters are within the CBM acceptance limits. The tested sensors can be assembled into detector modules for mSTS.

References

[1] The CBM Collaboration, *mCBM@SIS18 – A CBM full system test-setup for high-rate nucleus-nucleus collisions at GSI/FAIR*, Letter of Intent, 19 June 2017

[2] O. Bertini et al., *Production Readiness Review for the Silicon Sensors of the CBM Silicon Tracking System*, CBM-TN-18010

[3] CBM-STS QA Workgroup, *Specifications for Quality Assurance of Microstrip Sensors in the CBM Silicon Tracking System*, CBM-STS Note 2016-1

STS-XYTER2.1, a revised prototype readout ASIC for the STS and MUCH detectors

W. Zubrzycka, K. Kasinski, and R. Szczygiel
AGH University of Science and Technology, Cracow, Poland

The readout chip for the STS and MUCH detectors is a 128 channels prototype integrated circuit for time (14-bit timestamp and 3.125 ns resolution) and energy (5-bit ADC) measurements. The previous prototype, STS/MUCH-XYTER2, designed at AGH UST and fabricated in 2016 with the UMC 180 nm CMOS MM/RF process was tested in 2017 [1,2,3]. As a result of detailed chip characterization a new revision of the IC, STS/MUCH-XYTER2.1 (SMX2.1) was fabricated in Q3 2018 based on a proposed list of modifications [4].

The main objective of the new design was to lower the output noise level and enhance functionality. To achieve proper operation of the fast Charge Sensitive Amplifier (CSA) reset circuitry, and the lower leakage current related noise component of the overall system noise [5] the ESD (Electrostatic Discharge) protection circuits were removed. The area was used for VDDM supply and GND distribution as well as additional guard rings. Instead of internal ESD protection, a separate ESD protection chip for MUCH detector purposes was designed implementing various ESD protection schemes (64 MOS-based circuits, 64 diode-based circuits, and 36 other test structures). Improvement of the global threshold resolution of the slow signal path was implemented to enable better control of the noise discrimination in the ADC (LSB 2000 e^- down to at least 200 e^-). The changes include implementation of range switching of the 6-bit ADC_VREFT biasing circuit output: from 600 mV (as it was in SMX2) down to 84 mV with two mid-range operation modes (243 mV and 101 mV). Other changes to improve the overall noise level include adding 3 pF MOS capacitor in each channel to filter the noisy reference in Polarity Selection Circuit (PSC) and some layout modifications. The CSA layout was amend-ed so that series resistance of input transistor gate poly silicon is reduced by half. The series resistance of input traces on even and odd channels was decreased from 17 and 36 Ohm to 7 and 9 Ohm respectively. Further reduction of even/odd channels discrepancies was achieved by adding pads for external decoupling on both sides of the chip for both DACs driving even/odd channel input biasing current source reference node. The calibration range switching to better match the STS and MUCH detectors operation modes was implemented by adding switchable capacitance value of the calibration pulse injecting capacitor. The timing comparator in SMX2.1 is provided with a differential threshold to enable evaluation of noise level without the signal and better control of the absolute threshold of the fast comparator. This was implemented by adding an identical 8-bit DAC as existing in SMX2 for discriminator threshold setting to control the other branch of the comparator input stage. The radiation related effects immunity was improved. Better Single Event Latchup (SEL) and Total Irradiation Dose (TID) effects tolerance is ensured by tightening the DRC rule regarding substrate/well contact density and spacing. Dual-Interlocked (DICE) memory cells and counter layout was enhanced in terms of area of guard rings and location of contacts to the rings to equalize the Single Event Upset (SEU) cross section. Diagnostic features in SMX 2.1 are extended with internal diagnostic circuit to monitor selected biasing and supply potentials inside the ASIC. The diagnostic circuit was designed to be immune to PVT variations and is provided with a pad for external calibration and monitoring any external potential [6].

The digital backend changes included the control frame rejection based on CRC error, duplicate-frame related malfunction fix, as well as enabling precise synchronization of timestamp counters.

Changes were introduced to the pad layout for better testability and wire bonding. Test pads and IN_CSA_front/back bias pads in the front area of the chip were relocated. Pogo-probe pads are available in the new revision to enable e-fuse control via pogo prober. The bond pads on the LVDS I/O, test pads and power pads are enlarged and the fiducial visibility is enhanced by opening the passivation. The HW-ADDR pads were changed from pulldown to pullup to simplify layout of the test PCB. A detailed description of all modifications and test scenario is provided in [7]. The chips are available for evaluation from January 2019.

References

[1] K. Kasinski et al., Proc. MIXDES 2017, DOI: 10.23919/MIXDES.2017.8005217.

[2] K. Kasinski et al., JINST 12, C03023, (2017).

[3] K. Kasinski, et al., NIM A, 2018 vol. 908, s. 225–235, DOI: 10.1016/j.nima.2018.08.076

[4] K. Kasinski, W. Zubrzycka, R. Szczygiel, CBM Report 2017 p.34.

[5] W. Zubrzycka, K. Kasinski, JINST 13, T04003, (2018).

[6] W. Zubrzycka, K. Kasinski, Proc. MIXDES 2017, DOI: 10.23919/MIXDES.2017.8005190

[7] K. Kasinski, W. Zabolotny, R. Szczygiel, W. Zubrzycka, SMX2.1 Manual v2.03.

FEB8 PCB test concept and tool

R. Kapell and C. Simons
GSI, Darmstadt, Germany

FEB8 PCB description

A single sensor of the Silicon Tracking System (STS) is connected via thin microcables to two FEB8 electronics boards (n-side and p-side). Each FEB8 PCB can be equipped with eight STS-XYTER readout ASICs.

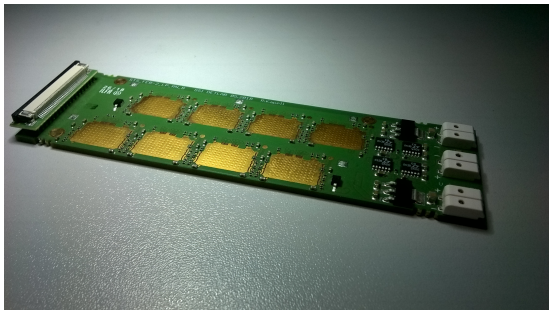

Figure 1: Previous version of the FEB8 board.

Before bonding the STS-XYTER ASICs, the PCB has to be tested in order to use only fully functional FEB8 boards. After bonding of the STS-XYTER it is almost impossible to repair any none working parts.

Main sources of error

The following circuit parts are the most sensitive ones on the FEB8 PCB:

- **Capacitor array below the ZIF-connector**
  Galvanical isolation of the data signals is realized with 36 vertically arranged HV ceramic SMD capacitors (3.3 nF / 500 V / type 0603). These parts are very sensitive to lateral forces and can break in case of improper handling.
- **LDO voltage regulators**
  With the new version of the FEB8 layout the LDOs from SCL, India, will be used. Bonding of these chips is difficult due to very small bond pads. Therefore it is necessary to test if the output voltage at nominal load is correct.

FEB8 PCB layout with test points

The third version of the FEB8 PCB is the first one with the LDOs from SCL and also the first one with 46 test points for accessing the capacitors and the LDOs. Also two drill holes for test adapter guide pins are foreseen.

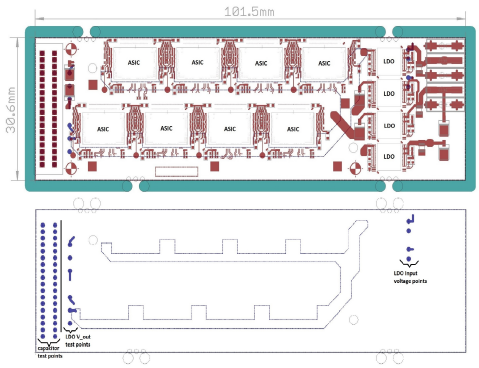

Figure 2: New FEB8 board layout with test points.

Test adapter concept

For testing the capacitors and the LDOs after assembly a suitable PCB test adapter is needed. One possible solution is the APS adapter for PCB from WinWay Technology [1].

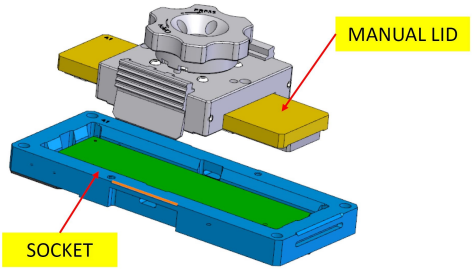

Figure 3: APS adapter for PCB from WinWay Technology.

The test points are electrically contacted by using small spring loaded pins. The opposite side of the HV capacitors is accessible via the ZIF connector. With an external electronic circuit the capacitance of the HV capacitors can be determined by measuring the charging time of a RC network. The LDOs can be tested by applying an input voltage and a switchable load resistor, measuring the corresponding output voltage.

References

[1] *APS adapter for PCB design concept*, WinWay Technology Co. Ltd., version v1.0, October 2018

Assembly of modules for mSTS applying complete quality assurance

C. Simons[1], *R. Visinka*[1], *M. Dogan*[1,2], *A. Rodriguez-Rodriguez*[1,3], *J. Lehnert*[1], *and R. Kapell*[1]
[1]GSI, Darmstadt, Germany; [2]Istanbul University, Turkey; [3]Goethe University, Frankfurt, Germany

For the first time, real STS modules have been assembled for the first tracking station of the mSTS detector. The station consists of two units, each with one ladder that is equipped with two sensor-modules (Fig. 1). Based on the experience with dummy modules the assembly was performed according to the detailed process workflow sheet that documents every step taken. Silicon sensors were chosen with regard to their characteristics, the STS-XYTER ASICs were tested and calibrated before use and also the quality of the TAB- and wirebonding steps was checked during the assembly.

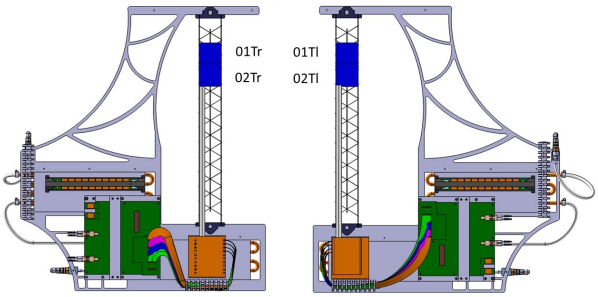

Figure 1: Tracking station 0 of the mSTS, made from Unit 0 (left) and Unit 1 (right) shown in an unfolded view. Every Unit has one ladder with two modules mounted. The sensors are shown in blue along side the module type code.

Test and quality of STS-XYTER ASICs and TAB bonds

Operational verification of the STS-XYTER ASICs was the main procedure during the Quality assurance (QA) of mSTS module assembly. Four modules were required for the initial mSTS configuration with its first tracking station. The module types are encoded as 01Tr, 01Tl, 02Tr and 02Tl. During their assembly, measurements were done in several stages that include test of the bare ASICs , test of ASICs after bonding to microcables, and ASIC test after full connection to the sensor. The QA measurements of the ASICs for mSTS modules were performed using a newly designed pogo pin socket, fitted with a lid that allows precise contacting of the ASIC. This new socket as well as the possibility of vacuum fixation of the ASIC provided practical and offered an efficient QA progress at each stage.

After the bare ASIC tests, basic functionality such as electrical connections and channel performance was checked in a second stage with the pogo-pin socket by measuring the noise level. Good ASICs were chosen for assembly and tests were implemented after the TAB-bonding process of microcables to ASICs as can be seen in Fig. 2. The biggest advantage during this stage is the possibility of rebonding any unconnected channel found.

Figure 2: Test of TAB bonds between STS-XYTER-ASIC and microcable.

As a third stage, ASICs were tested in order to check for the electrical connectivity between the ASIC, microcable and sensor with same procedure as in the second stage. Likewise, during this stage it is possible to rebond any unconnected channel at the sensor side. All test stages took 5 minutes per ASIC. The tests were performed on the bonding machine as shown in Fig. 3.

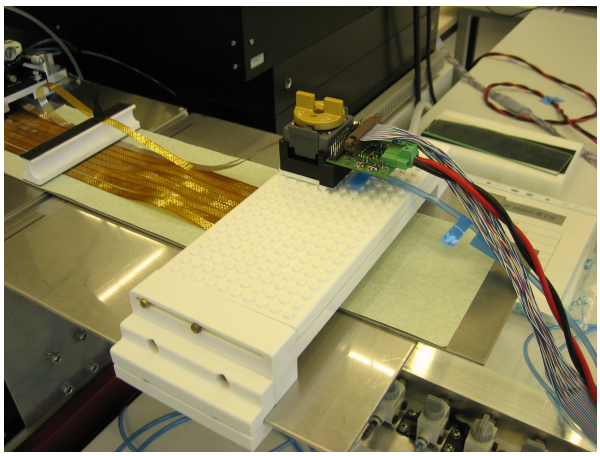

Figure 3: STS-XYTER test socket on the bonding machine.

Unconnected channels were identified by checking the hit distributions in the noise pattern. As an example, Fig. 4 shows the connection check result of an ASIC. The unconnected channel, seen as a continuous line at low channel number, becomes visible when evaluating the hit distribution in terms of ADC values.

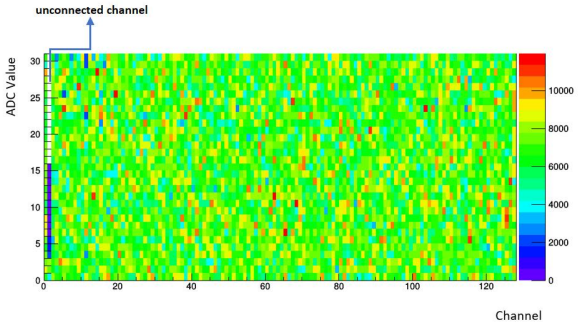

Figure 4: Noise hits read at the ASIC's ADC counters.

Table 1: Quality statistics of the ASIC bondings.

module	tested ASICs	bad bonds
01Tr	16	3
01Tl	8 (p-side)	0
02Tr	16 (only with microcable)	2
01Tr	16	0

Measurement results from the mSTS module assembly are shown in Table 1. For the module 02Tr untested ASICs were used due to unavailability of the pogopin socket at that time, and for module 01Tl only one side could be fully tested. Since some ASICs showed problems on Front End Boards during module operation after the bonding process, it is thought that testing ASICs for several times can lead to damage of the bonding area. Consequently, carrying out bare ASIC tests was decided to be sufficient during module assembly. Thus forthcoming module productions will be done with one ASIC test stage only.

Testing of FEB8-boards

After wirebonding each row of ASICs to the FEB8 (i.e. with 4 or 8 ASICs mounted on the FEB8), a basic test of the ASIC communication and functionality is done. The FEB8 is connected to the readout board and the low-voltage supply (Fig. 5). Power consumption with and without ASIC clock is measured and compared to the expected values. The synchronization procedure is executed for each ASIC, which establishes the communication between the ASIC and the FPGA backend. A subset of configuration registers is written and read back. These tests show that, after the bonding and related processing steps, the ASIC powering is working and proper functionality of the readout interface is available: the common clock and downlink signals and the individual uplinks are connected and operational, ASIC adressing is working properly and basic communication with the ASIC (configuration and status readback) is possible.

After having completed the FEB8 tests, the modules (Fig. 6) are completed with its shielding which is connected to the FEB8, and the power cable contacts are soldered to the FEB8. Finally the module can then be completely tested in a dedicated test stand before it is ready to be integrated on a ladder.

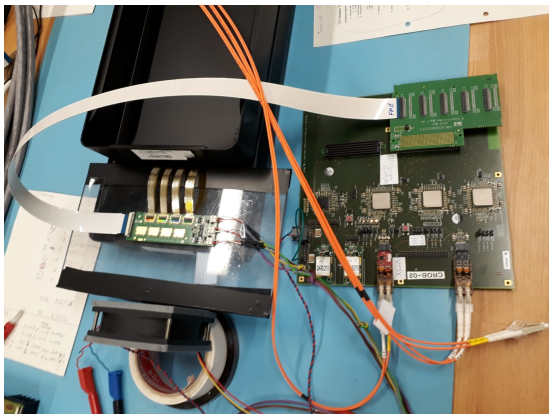

Figure 5: Testing of the FEB8 after the wire bonding of ASIC-rows.

Figure 6: Full STS module assembled, awaiting to be fitted with the external microcable shield layer.

Development of bonding quality control for assembly of the silicon microstrip sensor modules

N. Sukhov[1], *D. Dementev*[1], *M. Dogan*[2], *A. Kolozhvari*[1], *A. Rodriguez Rodriguez*[2], *C. J. Schmidt*[2], *M. Shitenkow*[1], *C. Simons*[2], *R. Visinka*[2], *and Yu. Murin*[1]

[1]JINR, Dubna, Russia; [2]GSI, Darmstadt, Germany

The Silicon Tracking System of the CBM experiment will include 896 silicon microstrip sensors; each one having 2048 analog readout channels connected to the front-end XYTER chips via microcables. Hence, it is necessary to perform around TAB 4096 bondings per sensor.

A system for testing of the bonding of every analog channel during the module assembly process is developed. It allows testing the connectivity among the ASICs, the microcables, and the sensor, before the chips are finally installed on the front-end board (FEB).

The tests are based on measurement of the magnitude of noise at inputs of the XYTER. There is an increment in the noise amplitude when an additional capacitance is connected to the amplifier's input. If the expected increase is not observed - the connection is absent.

The magnitude of noise is obtained from measurement of the S-curve using the internal pulse generator of the ASIC. A chip with a bonded microcable (or without it, for reference measurement) is placed in the pogo pin device, which provides connections to the readout electronics. After the measurement is completed, the chip may be easily extracted and further assembly operations may be performed.

Components of the sensor module together with the pogo pin device are being placed inside the shielding box during the measurement (Fig. 1) to avoid the influence of electromagnetic interference.

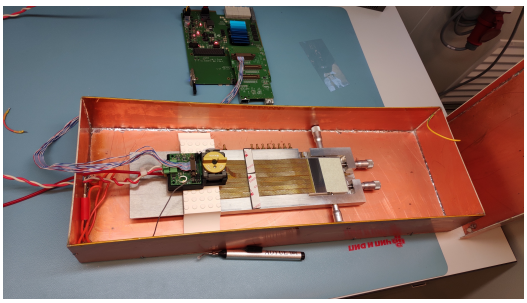

Figure 1: The bonding tool with a sensor, installed inside the shielding box. The tested microcable plus ASIC goes to the pogo pin device on the left.

There is an isolating pad on the bottom of the shielding box. For tests of bondings between XYTER and a microcable, the loose end part of the cable is placed on the pad. For cable to sensor bondings tests, the bonding tool together with bonded cables and chips is being extracted from the bonding machine and placed on the pad, the correcponding chip being installed in the pogo pin. The copper surface of the shielding box and the bonding tool are electrically connected to the grounding of the input circuit of the XYTER via the pogo pin connector.

The controlling software "BondingTest" runs on a Linux PC and communicates to the XYTER using the IPbus protocol via the chain : copper ethernet, ethernet to SATA D-LINK adapter, SATA link, AFCK, gDDB_FMC1 board, twistwed pair links to the pogo pin tool. It is a standalone application written in C++ using the CERN Root toolkit [1] and the CERN IPbus software suite [2]. At each technological step an operator may test a bonded component with this system. In a "standard" situation the operator inputs the chip code into the GUI and performs the measurement in 3 clicks.

The measurement takes a few minutes depending on the techonological step. The states of each electronics channel of the XYTER are shown on the GUI in colors indicating good and bad bonding, noisy and dead channels (Fig. 2). A histogram of measured noise versus the channel number is displayed together with similar histograms measured at the previous technological steps. The results of the measurements are stored in ROOT files.

Figure 2: GUI: bonding of a microcable to 6x2cm sensor.

References

[1] R. Brun and F. Rademakers, *ROOT - An Object Oriented Data Analysis Framework*, Proceedings AIHENP'96 Workshop, Lausanne, Sep. 1996, Nucl. Inst. & Meth. in Phys. Res. A 389 (1997) 81-86. See also http://root.cern.ch/

[2] C. Ghabrous Larrea, K. Harder, D. Newbold, D. Sankey, A. Rose, A. Thea and T. Williams, *IPbus: a flexible Ethernet-based control system for xTCA hardware*, JINST 10 (2015) no.02, C02019.

Advances in STS module assembly at KIT

P. Pfistner, T. Blank, M. Caselle, and M. Weber
KIT, Karlsruhe, Germany

Introduction

STS module assembly based on aluminum TAB bonding is an elaborate and time-consuming process. Therefore, KIT has developed a double-layered copper microcable with the aim of establishing a more automated assembly procedure [1]. Finite element simulations and actual measurements on the Cu microcables have shown a capacitance comparable to the aluminum microcables [2]. Disadvantages of smaller radiation length can be compensated through narrower signal lanes maintaining line resistivity. Therefore it is concluded that the Cu microcables are suitable alternatives for the STS. Based on the Cu microcables, a novel gold stud to solder paste bump bonding process has been developed [3]. As this new approach still needs further research and to be prepared for module production, also the Al TAB bonding process has been established at KIT.

Gold stud to solder paste bump bonding

A typical gold stud bump-bonding interconnection is not possible for STS, as the gold studs cannot be placed on the compressible microcable. Instead, the gold stud is replaced with fine-grained solder paste which is stencil-printed directly onto the Cu microcable. The individual process steps of the novel bump bonding assembly process based on the Cu microcable are depicted in Fig. 1.

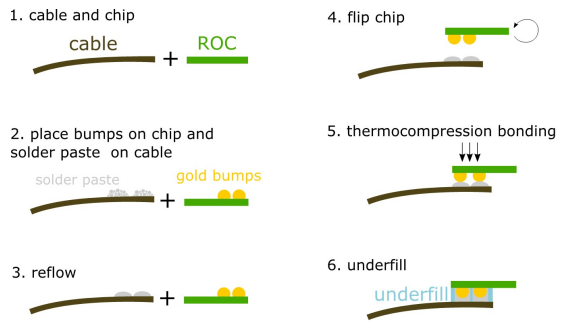

Figure 1: Individual process steps of gold stud to solder bump bonding connection.

In a first step, gold studs are placed on the ASIC and sensor, see Fig. 2. Gold stud bumping is a fast, flexible and reliable technology.

In parallel, solder paste type 7 is stencil-printed onto the microcables. Up to eight cables, i.e. a full set of cables for one sensor side, can be printed simultaneously. The

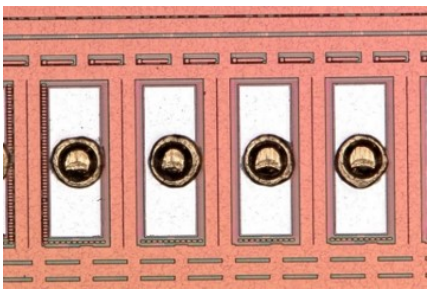

Figure 2: Gold stud bumps on STS-XYTER.

cables are then immediately reflown for ease of handling and storage (Fig. 3). Next, cable and die are connected in a flip chip thermocompression bonding process. A Finetech femto flip chip bonder guarantees an alignment accuracy of 0.5 μm. Finally, Polytec EP 601-LV underfill glue is applied to strengthen and protect the interconnection.

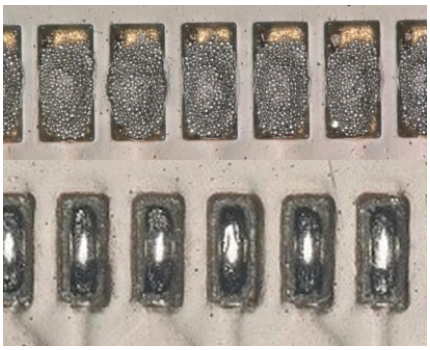

Figure 3: Top: Solder paste printed on Cu microcable. Bottom: Solder paste after reflow.

Status of Cu microcable interconnects

The gold stud to solder paste interconnection technology has been established and characterized. First ASIC-microcable structures have been assembled showing high mechanical strength and a reliable electrical connection (Fig. 4).

A cross-section of the gold stud to solder interconnection can be seen in Fig. 5. The pogo pin sockets which are used for quickly and conveniently testing the Al TAB bonding modules cannot be copied as is but have to be adapted to the slightly different geometry of the Cu microcable. As

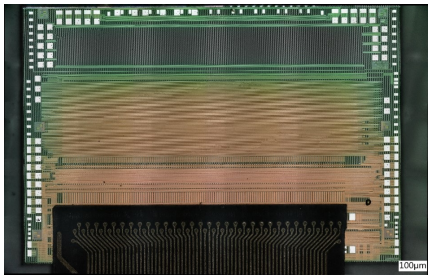

Figure 4: Cu microcable (at the lower edge of the photo) connected to STS-XYTER with gold stud to solder paste bump bonding technology.

the commercial flip chip machines are not suitable for handling the sensor-microcable interconnection, an in-house bonding machine has been developed which is close to finalization.

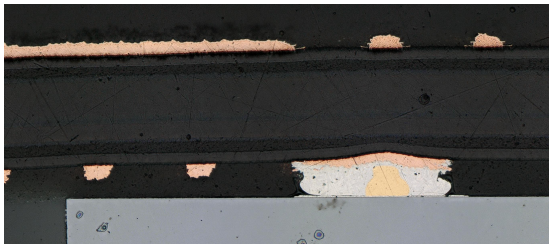

Figure 5: Cross-section of the gold stud to solder paste interconnection showing excellent wetting of the gold stud.

Advances on the Cu microcable

Several versions of test cables with a length of 200 mm and 186.5 mm have been produced. Special focus was put on the solder stop, as early versions have shown improper solder stop mask development resulting in an unwanted solder height of 20 μm. The latest microcable version is based on a liquid resist solder stop. The pad release is excellent as can be seen in Fig. 6.

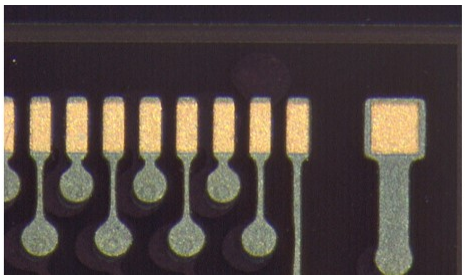

Figure 6: Cu microcable with liquid resist solder stop showing excellent release of the bond pads.

Al TAB bonding

Next to the Cu microcable assembly approach, the Al TAB bonding has also been pushed towards production. All relevant mechanical fixtures for bonding of the ASIC and the sensor have been adapted to the KIT bonder machine. Experience in the TAB bonding process has been gained during assembly of first dummy modules. Application of room temperature curing Polytec EP 601-LV underfill glue is investigated to protect the TAB bonding area and to provide tension relief of the microcables. It has the potential to reduce the amount of necessary gluing steps and to facilitate the assembly process.

Conclusion and outlook

Based on a double-layered Cu microcable a novel gold stud to solder paste bump bonding process has been developed. With this approach, a faster, more automated STS module assembly can be established. First ASIC-microcable structures have been assembled showing high mechanical strength and reliable electrical connection. The pogo pin sockets used for testing the Al TAB bonding modules have to be adapted to the slightly different geometry of the Cu microcable. For the sensor-microcable connection an in-house bonding machine has been developed and is close to finalization. First dummy modules are expected very soon with which a comparison in noise performance between the two assembly processes is to be conducted. In parallel, the Al TAB bonding process has been established at KIT and experience in the TAB bonding assembly has been gained with first dummy modules.

References

[1] T. Blank et al., *Investigation on low-mass copper flex cables for the STS detector*, CBM Progress Report 2015 p. 37

[2] T. Blank et al., *Investigation on low mass copper flex microcables for the STS detector*, CBM Progress Report 2016 p. 42

[3] P. Pfistner et al., *Novel production method for large double-sided microstrip detectors of the CBM Silicon Tracking System at FAIR*, Proceedings of Science, TWEPP 2018

Towards length specification of ultra-light microcables for the BM@N STS

V. Elsha, D. Dementev, A. Sheremetev, M. Shitenkow, N. Sukhov, and Yu. Murin
JINR VBLHEP, Dubna, Russia

The BM@N experiment has been approved by the CBM STS team as a "phase zero" experiment to be conducted in Dubna in 2021-2022. Joint activity in the design of the system has just started with the definition of technical specifications to the components of the system. The length specification for the BM@N STS microcables was estimated within the tentative design of the BM@N STS model v18f [1].

The stations of the STS comprise six types of ladders carrying the modules. Each module consists of the silicon sensor, two Front-End Electronics Boards (FEBs) and signal transmissing ultra-light microcables. The microcables are made fromtwo layers of 16 analog signal cables for the P and N sides of the sensor, meshed spacers and shield layers [2]. It is important to estimate the lengths of the microcables which depend on the type of the sensor, the type of the ladder and their positions within the station considered.

Within the model of the STS, the "Base Length" (L_B) of the microcables is introduced to systematize the estimations. L_B is defined as the distance from the sensor edge to the corresponding cooling fin which is planned for the housing of two FEBs of the module as demonstrated in Fig. 1. The P and N sides of the modules are read out with corresponding layers of the microcable of different lengths schematically depicted by Fig. 2.

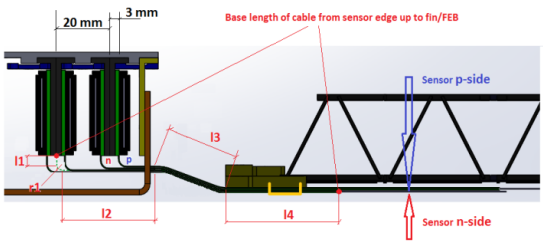

Figure 1: Schematic picture of module connectivity.

The Base Length of the microcable can be calculated with the following equation:

$L_B = l_1 + l_{r1} + l_2 + l_3 + l_4$

where:

l_1, l_2 - depend on the FEB position in the FEBs container,

l_{r1} – constant,

l_3 - depends on the relative position of the FEB container and the CF-truss,

l_4 - depends on the position of the sensor on the CF-truss.

The lengths of P and N- layers are calculated as:

$L_p = L_B - 3.65mm + L_S + L_F$

$L_n = L_B + 3.65mm + L_S + L_F$,

where:

L_p– cable length for the P-layer,

L_n - cable length for the N layer,

L_S, L_F – distances from the edges to contact pad, respectively for module sensor and FEB.

The distances from the edges of both sensors and FEB to the contacting pads follow specifications acquired from the vendors.

The base lengths for all BM@N STS modules were finally tabulated (Fig. 3) and distributed within the BMN@STS collaborating teams for final approval and subsequent production of first batches of cables.

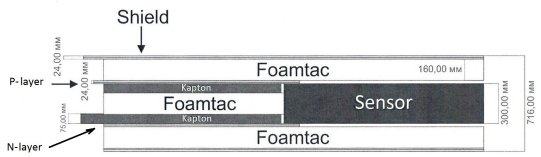

Figure 2: Difference in N and P- layers of the cable.

Station	Ladder	Number of Ladders	Module type	Number of modules in each ladder	Number of modules	l1 mm	Arc length r1=3 mm	l2 mm	l3 mm	l4 mm	Base lenth mm	Base lenth (rounded) mm
STS1	Ladder 294-66	6	Module 294-6-155	2	12	1,425	4,7	13,675	33,33	101,86	154,99	155
			Module 294-6-117	2	12	2,725	4,7	33,675	33,33	42,36	116,79	117
	Ladder 294-444	2	Module 294-4mt-175	2	4	1,425	4,7	13,675	33,33	121,86	174,99	175
			Module 294-4-157	2	4	2,725	4,7	33,675	33,33	82,36	156,79	157
			Module 294-4-139	2	4	4,025	4,7	53,675	33,33	42,86	138,59	139
STS2 & STS3	Ladder 414-666	18	Module 414-6-215	2	36	1,425	4,7	13,675	33,33	161,86	214,99	215
			Module 414-6-177	2	36	2,725	4,7	33,675	33,33	102,36	176,79	177
			Module 414-6-139	2	36	4,025	4,7	53,675	33,33	42,86	138,59	139
	Ladder 454-4466	4	Module 454-4mt-255	2	8	1,425	4,7	13,675	33,33	201,76	254,89	255
			Module 454-4-237	2	8	2,725	4,7	33,675	33,33	162,26	236,69	237
			Module 454-6-198	2	8	4,025	4,7	53,675	33,33	102,76	198,49	198
			Module 454-6-160	2	8	5,325	4,7	73,675	33,33	43,26	160,29	160
STS4	Ladder 538-6666	12	Module 538-6-277	2	24	1,425	4,7	13,675	33,33	223,46	276,59	277
			Module 538-6-238	2	24	2,725	4,7	33,675	33,33	163,96	238,39	238
			Module 538-6-200	2	24	4,025	4,7	53,675	33,33	104,46	200,19	200
			Module 538-6-162	2	24	5,325	4,7	73,675	33,33	44,96	161,99	162
	Ladder 538-44466	2	Module 538-4mt-298	2	4	1,425	4,7	13,675	33,33	243,26	296,39	296
			Module 538-4-278	2	4	2,725	4,7	33,675	33,33	203,76	278,19	278
			Module 538-4-260	2	4	4,025	4,7	53,675	33,33	164,26	259,99	260
			Module 538-6-222	2	4	5,325	4,7	73,675	33,33	104,76	221,79	222
			Module 538-6-184	2	4	6,625	4,7	93,675	33,33	45,26	183,59	184
	Total	44			292							

Figure 3: Base length and number of analog cables.

References

[1] V. Elsha, *Tentative Design of the BM@N STS Mainframe*,32nd CBM Collaboration Meeting

[2] V. M. Borshchov et al., CBM Progress Report 2016, p. 41

Test of the first fully assembled STS modules

A. Rodriguez Rodriguez[1], *J. Lehnert*[2], *A. Lymanets*[2], *M. Dogan*[3], *O. Maragoto Rodriguez*[1], *and S. Mehta*[1,4]

[1]Goethe University, Frankfurt, Germany; [2]GSI, Darmstadt, Germany; [3]Istanbul University, Istanbul, Turkey; [4]Tübingen University, Tübingen, Germany

The assembly of the first detector modules is a crucial step towards the realization of the STS. In the framework of the mCBM project, the STS will contribute with two tracking stations using a total of 13 detector modules. These are built with 6.2 $\times$ 6.2 cm^2 sensors and micro cables of approximately 45 cm length. Every sensor is readout by two prototype frontend boards witch 8 STS-XYTER ASICs each (FEB8). Further details on the assembly and quality assurance are given in [1].

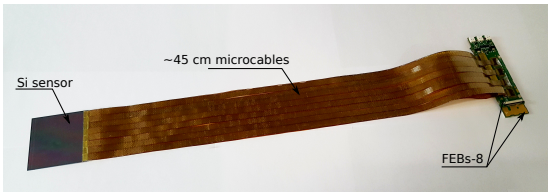

Figure 1: Fully assembled module before its installation in the mSTS setup.

Module test setup

The first mSTS station is constructed out of 4 modules. Before installation in the mSTS setup, a set of tests to evaluate the module performance was carried out. The FEB8 are connected with flexible flat cable to a common readout board (C-ROB) [2] where data are aggregated and transported via a high-speed optical link to the data processing board, implemented in an FPGA based (AFCK) board.
A dedicated setup has been assembled to carry out the module tests with a fully biased sensor. It consists of a light-tight aluminum box, which also provides shielding against electromagnetic interference. It is equipped with a water cooling system for the FEB8. This "module test box", also integrates a holder for accurately positioning a radioactive source for performing position sensitive signal studies.
The setup allows checking the response of every ASIC to synchronization and configuration commands. Besides, the overall system noise, the ADC gain, threshold uniformity and broken or unconnected channels can be investigated. Results of these studies are shown in Fig. 2 for the module 02Tr.

Test Experiences

Module assembly and testing provided invaluable practice in handling and operating the STS modules. Among those were the development of iterative QA procedures during the assembly, e.g. using the pogo-pin station, finding a suitable balance between finding problems in the assembly and potential damage to the ASIC during testing; Also experiences in proper cooling of the FEB8 during operation were gained to avoid thermal damage to the readout ASICs.

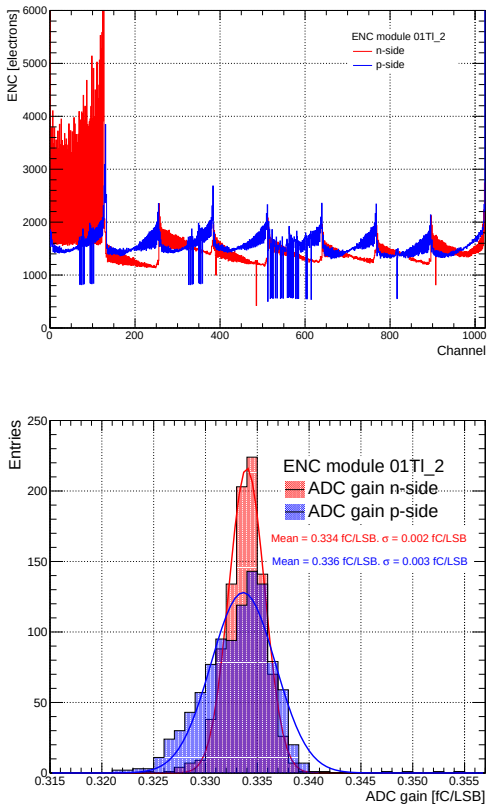

Figure 2: First tests of a fully assembled module before its installation in the mSTS setup. Top-panel shows the estimated noise level per channel. In the bottom panel is shown the distribution of the ADC gain for both polarities.

References

[1] C. Simons et. al, *The assembly of sensor-modules for the miniSTS with complete QA-measurements*, this report

[2] J. Lehnert and D. Gottschalk, *Development and test of the CBM Common Readout Board (CROB)*, CBM Report 2017, p. 45

Tests of CBM STS module prototypes with electron beam at Linac-200

D. Dementev, P. Kharlamov, Yu. Murin, M. Shitenkow, and A. Voronin
JINR VBLHEP, Dubna, Russia

Linac-200 is a linear accelerator at JINR LNR in Dubna which can provide beams of electrons with maximum energy of 200 MeV. This facility can be used for in-beam tests of prototype detector components and readout electronics for the Silicon Tracking Systems of the CBM and BM@N experiments during the shutdown of the Nuclotron. A first in-beam test was performed with a detector station built using miniature microstrip sensors produced along with CBM-STS prototype sensors. The aim of the beam time campaign was to test readout electronics and the TS system based on AFCK boards, to estimate Signal-to-Noise ratio and charge-collection efficiency for the module prototypes and to prepare the test bench for future tests of the CBM-STS modules. We report here preliminary results of the in-beam test performed in December 2018.

The test setup is shown in Fig. 1. It consists of two test stations with silicon sensors having 256 strips per side, produced by Hamamatsu. The sensors are installed on a printed circuit board with connectors for the front-end electronics boards (FEBs). For the readout of one sensor four FEBs with one STS-XYTER 2.0 ASIC per PCB were installed. For the data processing two AFCK boards with gDPB FMCs were used. Additional AFCK with tDPB FMC was used as a TS master. Data were collected on a server node via FLIB board. For the time reference we used the start pulse from the accelerator. It triggers a pulse generator which injects a trapezoidal pulse to the Amp Cal pads of two additional FEBs. These boards were connected to two different AFCKs which allows us also to control time synchronization. The setup was tested with electron beam at energies of 50 and 150 MeV. Beam profiles are shown in Fig. 2.

The mean noise level was estimated for each of the eight ASICs connected to two sensors. The noise ranges from 1500 to 2200 e for even channels and from 1800 to 3400 e for odd channels. The noise difference between even and odd channels of the ASICs originates due to the topology of STS-XYTER v.2.0, which is improved in a new generation of the ASIC [1]. High-energy electrons predominantly lose energy in matter by bremsstrahlung. That is why the signal amplitudes are sufficiently higher than typical MIP signals. It allows us to use higher thresholds to minimize noise contribution. Examples of signals from electrons of 50 and 150 MeV energy are shown in Fig. 3. In order to eliminate the effect of hit duplication [2] only 15 channels per ASIC were unmasked for this measurement. For the estimation of charge collection efficiency further analysis must be done.

Figure 1: Test bench (top). Test station with baby sensor (bottom).

The prototype CBM readout chain and the TS timing system based on AFCK boards was tested. Time synchronization between multiple ASICs connected to different AFCK boards was stable. Time differences between signals from P and N sides of sensors are shown in Fig. 4.

References

[1] K. Kasiński and W. Zubrzycka, in: *CBM STS-XYTER v2.1 and SPADIC v2.2 Submission Review*, 15 March 2018, https://indico.gsi.de/event/6883/

[2] P.-A. Loizeau and M. Barej, *Characterization of a logic error in the STS-MUCH-XYTER v2.0 ASIC*, 32nd CBM Collaboration Meeting, 1 October 2018

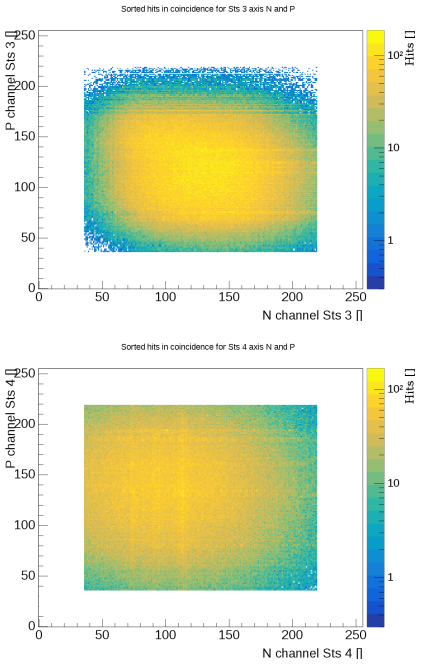

Figure 2: Beam profile, Station 1 (top); Station 2 (bottom).

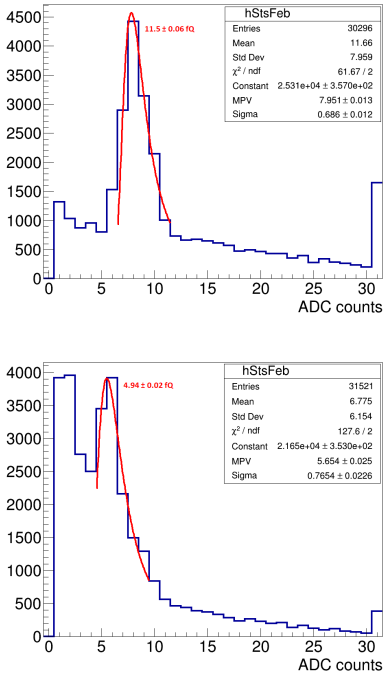

Figure 3: Energy deposition Station 1 N side, 150 MeV (top); 50 MeV (bottom).

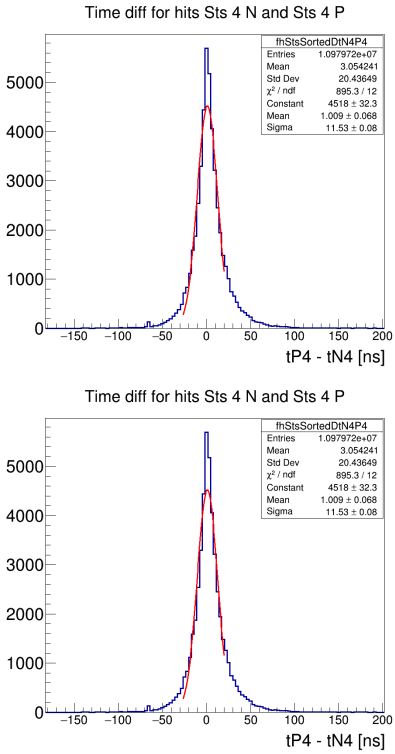

Figure 4: Time difference between signals from N and P side of Station 1 (top); Station 2 (bottom).

STS carbon fiber ladders – pre-series production in industry

J. M. Heuser, W. Niebur, and M. Faul
GSI, Darmstadt, Germany

Low-mass carbon fiber ladders of triangular cross section serve as mechanical carriers for the STS detector sensors. Being in the acceptance besides the sensors, ultra-thin read-out cables, the upstream beam window and the downstream STS wall, they constitute the only significant material in the pathway of the charged particles traversing the STS from the target to the other CBM detectors further downstream. The requirements to the ladders are mechanical position stability of better than the detector spatial resolution, i.e. of the order of 10 μm. The manufacturing itself requires achieving an accuracy of within $\pm$ 200 μm in particular for the base side width.

The ladder design and manufacturing procedure was originally conceived for the ALICE Inner Tracking System [1]. Initial prototypes have been manufactured along this procedure also in CBM-STS geometry [2]. As the manual assembly of many side pieces to the three side bars, made from angled prepreg, could not be sustained for the CBM-STS project, we turned to industry. We developed a winding-based process, laying high-modulus carbon fibers around three support tubes on a hub as temporary support [3]. After investigation for several improvements, now with [4], we finally started pre-series production using the same hub but now manufactured from stainless steel for improved geometrical straightness. Also additional precision pins were put in place so that accurately positioned crossing points of the fiber layers are obtained. The fibers have been twisted before application and are handled manually during the winding procedure. Table 1 lists a number of parameters related to the production. Figure 1 shows a ladder still on the hub, while several pre-series ladders produced are shown in Fig. 2.

The pre-series ladders are currently being surveyed on a 3D optial metrology station at GSI.

Table 1: Specifications of the pre-series ladders.

parameter	value
support	DPP Pultrusion carbon tube, 0.7/1.50 mm ∅, 120 cm long
roving	Tenax, HTA40 E13, 3K, 200tex, twist of 3 rovings at 45 revolutions/m
resin	EP resin, Hexion GmbH, resin L284, hardener H287
glue	between carbon tubes and roving, GP49 (Gößl & Paff GmbH)
winding	manually over precision pins
curing	on rotating hub, tempering 8 hours at 80 °C
weight	14.8 g/1.2 m

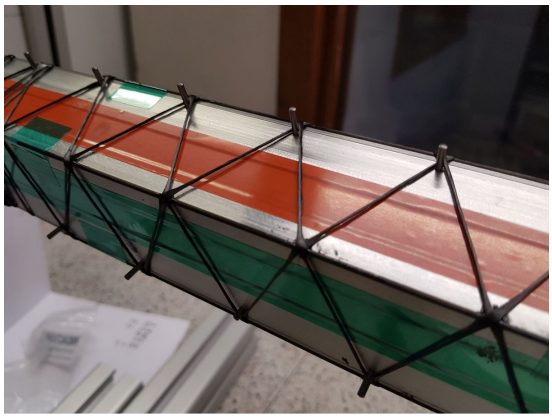

Figure 1: Carbon fiber ladder on a hub (photo: ICM).

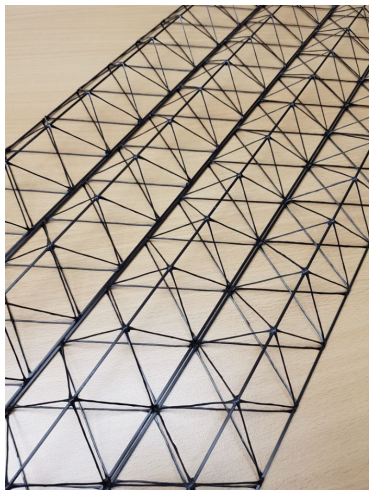

Figure 2: Pre-series carbon fiber ladders of 1.2 m length.

References

[1] ALICE Collaboration, *ALICE technical design report of the inner tracking system (ITS)*, CERN-LHCC-99-12 (1999)

[2] S. Igolkin et al., *Design and prototyping of a carbon fiber support frame for the central ladders of the CBM Silicon Tracking System*, CBM Progress Report 2014, p. 48

[3] W. Niebur, M. Faul, and J. M. Heuser, *Prototype carbon fiber ladders for the STS made in industry*, CBM Progress Report 2016, p. 52

[4] ICM-Composites, Weiterstadt, Germany; www.icm-composites.de

STS ladder assembly

S. Mehta[1,2], *U. Frankenfeld*[1], *H. R. Schmidt*[1,2], *P. Schweigert*[1], *C. Simons*[1], *O. Vasylyev*[1], *and R. Visinka*[1]

[1]GSI, Darmstadt, Germany; [2]Universität Tübingen, Tübingen, Germany

Ladder Assembly

The stations of the Silicon Tracking System (STS) are build of Carbon Fibre support structures (CF ladders) which hold the double-sided silicon microstrip sensors. Before mounting the sensors, they are assembled with read-out-cables and front-end electronics forming detector modules [1]. The positioning requirement for the sensors is within 100 µm. For the optical survey of the sensor positions on the ladder, a three axis measurement table is used [2].

Assembly of prototype ladder

A large scale prototype tool (Fig. 1 (a)) has been designed to assemble STS ladders. Initially, a half-ladder has been populated with 5 non-functional modules to prove the assembly procedure. The tool has further been used to assemble a ladder with functional modules for use in the mCBM demonstrator experiment. Using the tools, the mounting precision of sensors is limited by the mechanical tolerances of the tools and fittings.

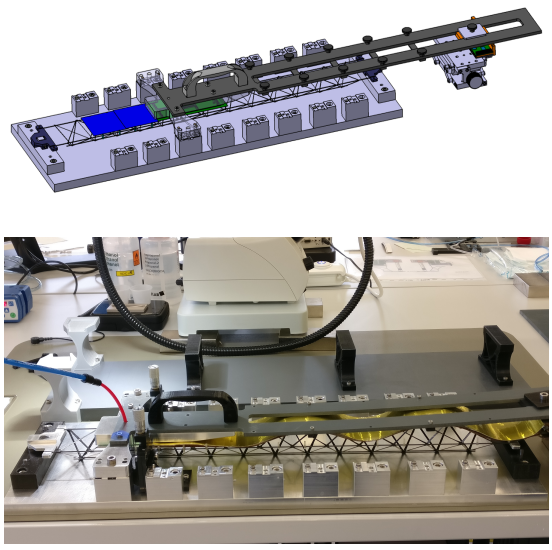

Figure 1: (a) Positioning tool on the base plate; (b) Module positioned onto the ladder.

The positioning of modules on the ladder is defined by the dowel pins that fit inside the positioning blocks on the base plate. The holding structure for the sensors (L-legs) are glued to the ladder. A precised tool which was designed to transfer the the modules to the ladder. One part of the module holder holds the sensor and other part holds the microcables and FEBs. When the sensor is positioned on the module holder, vacuum is applied so that it should not fall while transferring to the ladder. Before the module is shifted to the ladder, silicon glue CAF4 is applied on the surface of the L-legs and a pre-positioning vertical tool is fixed on the base plate of the tool (Fig. 1 (b)). The module is transferred to the ladder and inspected to make sure that it sits on the surface of the vertical tool. Then it is leveled down and this way the modules are glued onto a ladder one after the other (Fig. 2 (a)). It remains in the same position for 24 hours to make sure that module is firmly glued to the l-legs. The ladder holding the modules is shifted to the C-frame with the help of a further transfer tool(Fig. 2 (b)). As a last step the C-frame is installed in the STS mainframe.

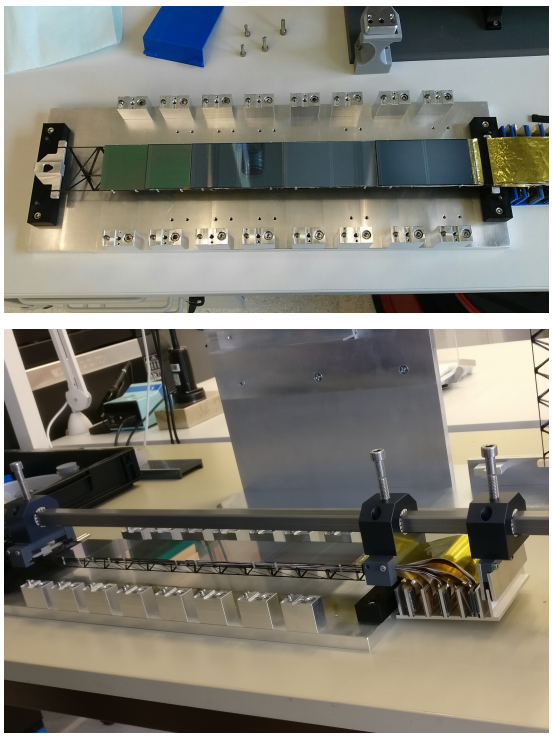

Figure 2: (a) Module positioned onto the ladder; (b) Prototype ladder assembled with five non-functional modules.

Metrology

In order to determine the position of silicon sensors in all three dimensions, a three-axis measurement instrument has been re-commissioned at GSI, having an X, Y and Z range of 1100, 800 and 170 mm. The setup is equipped with a movable camera and the procedures developed for the quality assurance of sensor are being adapted for the metrology of ladders [3]. The measurement resolution of the surface of the table was found to be $\pm 10\,\mu$m. The determination of the Z-dimension (height) is based on a Fast Fourier Transform (FFT) analysis of the microscopic images. The positions in the X-Y plane are calculated from the result of pattern recognition algorithms and the sensor position is measured by finding the markers on their surface. The deviation of the X-Y position and the rotation along the Z-axis are calculated for the individual sensors and are summarized in Table 1. The goal is to tune the assembly procedure such that the sensor positions do not deviate from the nominal position by more than $100\,\mu$m. As can be estimated from Table 1, the measured positions in X-Y, with three outliers, are within that range. With the help of this method, we can check the precision of the mounting and gluing procedure of the sensors. The accurate measurement of the 3D positions will be used to further improve the assembly procedure. Because of the non-flatness of the sensors the deviation from the nominal height is shown for the surface measurement of the sensors. Figures 3 (a) and (b) show the 3D view of the ladder. The Z-position of the sensors are shifted to a nominal height for a better visualization of deviations from the nominal positions.

Table 1: Lateral and rotational deviation of the sensors from the nominal position.

Sensor	ΔX [μm]	ΔY [μm]	$\Delta\Phi$ [mrad]
1	287	-45	-2.74
2	151	-68	0.12
3	40	-42	0.61
4	56	-107	-1.23
5	40	-44	0.96

Conclusion

A half ladder was assembled with non-functional modules using the prototype tool and studies have demonstrated that the procedure works as intended. The same technique was used further to build a ladder with two functional modules for the mSTS detector, shown in Fig. 4, used in the startup configuration of the mCBM experiment in December 2018.

References

[1] A. Sheremetev et al., CBM Progress report 2017, p. 34

[2] U. Frankenfeld et al., CBM Progress report 2017, p. 41

[3] E. Lavrik et al., arXiv:1807.00211

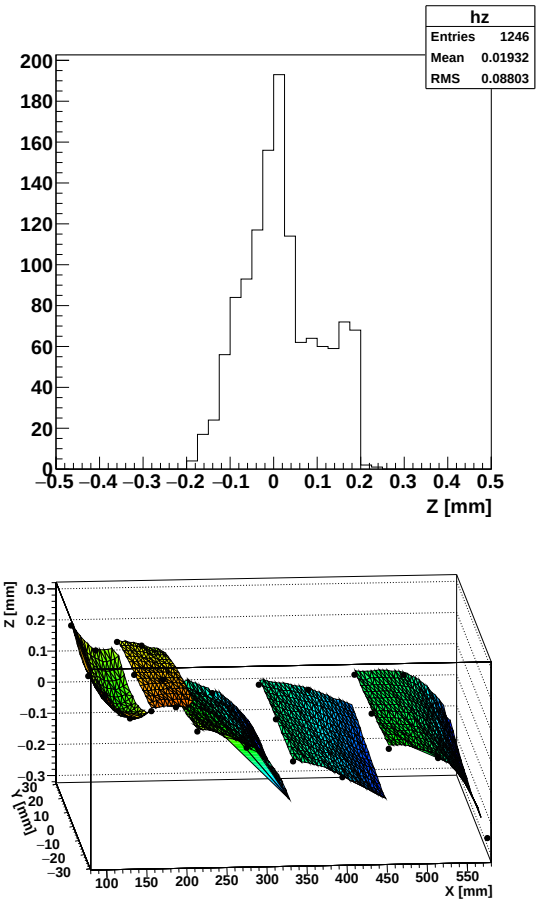

Figure 3: (a) Histogram showing the deviation of the measured Z-position from the nominal position; (b) Measurement of the sensor surface space points with a step size of 5 mm. The black dots refer to the alignment marks on the sensors.

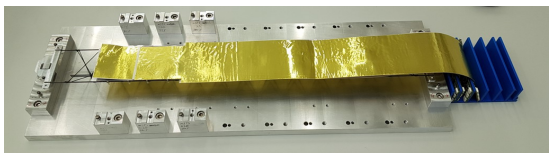

Figure 4: First functional ladder assembled for the mSTS detector in the assembly fixture. Two modules with one 6.2 by 6.2 cm sensor each are mounted. The sensors, located on the left hand side of the carbon frame, are covered by the microcable shielding layer that was not removed there yet.

Pull test of adhesives for ladder assembly

S. Mehta[1,2], *U. Frankenfeld*[1], *P. Schweigert*[1], *O. Vasylyev*[1], *and R. Visinka*[1]
[1]GSI, Darmstadt, Germany; [2]Universität Tübingen, Tübingen, Germany

For the integration of the STS detector, different kinds of adhesives are used. During the assembly of a ladder, adhesives are mainly used to glue the glass fibre structures "L-legs" [1] with their long legs to the carbon fiber ladders, and then in turn to mount the sensors to the short arm of the legs. There are a large number of adhesives, which requires different tests to characterize the properties of the glue. In addition, their use in high-radiation environment for several years of operation imposes requirements of radiation hardness and long-term stability [2].

During the assembly of a ladder, the crucial part is to glue the sensor on the L-legs. To approve a glue suitable, a pull test has been performed to determine the adhesive strength between the sensor and the L-leg, resulting in minimum pull-off force for different adhesives. We used an Instron 5944 instrument [3] to perform the pull test. This instrument allows sensitive tests for compression and tension in small specimens. It combines an ultra-high precision-drive system with high accuracy load measurement having a load force range between 2 mN up to 2 kN. This instrument is compatible with a software that controls the testing system, running tests and analyses the test data to produce test results and save them into a file.

To perform this test, 28 L-legs were taken and the short part of each L-leg was glued on a 6.2 x 6.2 cm^2 sensor (Fig. 1 (a)) using 5 different adhesives: Araldite 2011, silicon glue CAF4, Epolite FH5313, Epotek 302-3M, Epotek T7110. On the long part of each L-leg, holes of 1 mm diameter were drilled before gluing their shorter leg on the surface of the sensor. The sensor was kept for 24 hours under 23 degree Celsius temperature for the hardening of adhesives. After the adhesives had cured, the sensor was kept on the base adapter of the instrument having a scale attached to it. To perform the pull test, a long metal wire was clamped in the cross head of the instrument with a swivel screw at the bottom ($\approx$ 0.7 mm thick). Before every measurement, the fishing screw was put inside the hole of the L-leg and pull off force was noted. The same process was followed for all the L-legs and value of variation in tensile force was measured. It was noticed that the strength varies from one adhesive to the other. For most of the L-legs, they finally came out of sensor surface after sufficient pull off force was applied. For a few of them the hole structure failed and the leg remained attached to the surface, as is seen in Fig. 1 (b).

Figure 1: (a) L-legs glued on the surface of the sensor with 5 different adhesives; (b) L-legs remaining attached to the sensor's surface after the pull test.

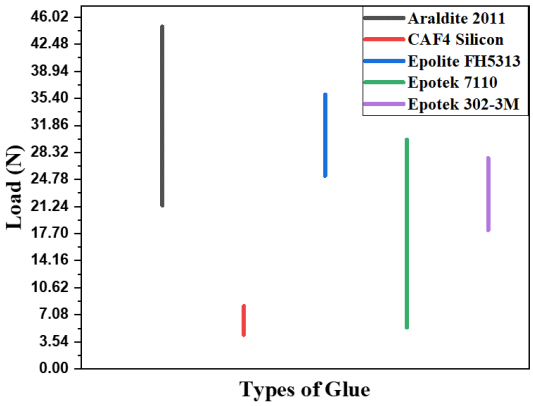

Figure 2: Pull-off forces for different adhesives.

Conclusion

The pull test has been performed to determine the pull-off force between a single L-leg and sensor using various adhesives. From the plot above (Fig. 2), it can be concluded that silicon glue CAF4 is suitable to glue the L-legs on sensor with a minimal pull of force of about 3.5-7 N.

References

[1] A. Voronin, A. Sheremetev, and O. Chikalovet, *Production and gluing of the L-legs for the silicon sensors*, CBM Progress Report 2016, p. 54

[2] A. Lymanets et al., *Radiation hardness of adhesives in the STS module*, CBM Progress Report 2017, p. 39

[3] Instron 5944 Manual, www.instron.de

Irradiation tests on the 1.8 V final prototype LDOs delivered by SCL Chandigarh/India

P. Koczoń[1], *C. J. Schmidt* [1], *S. Löchner* [1], *and J. Swakoń*[2]
[1]GSI, Darmstadt, Germany; [2]IFJ Kraków, Poland

LVR in the low voltage power supply chain for the STS FEB

In order to achieve the required noise power density level for low voltage powering of the STS-XYTER ASIC, a Low Voltage Regulator (LVR) will be applied as the last element of the supplying chain. Among other properties this chip has to stand high ionising radiation dose of 10 kGy. Its resilience for radiation has been tested and the results are reported beneath.

Experimental arrangement

Three PCBs with 4 LVRs each had been delivered from Semi-Conductor Laboratory Chandigarh/India [1] for measurements and irradiation tests. The LVRs on the boards were supplied pairwise with V_{in} and the load on the output side was chosen such that at V_{out} = 1.8 V the output current was set to around 1.4 A. The Enable pin was set to GND in all cases so that chips were active and could be observed continuously (in Fig. 1 for a pair of ASICs).

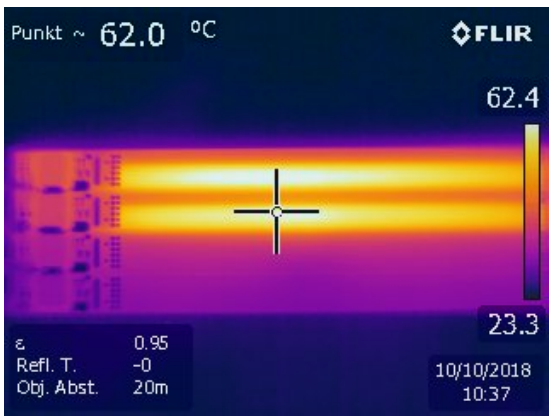

Figure 1: Thermal image of one of the three PCBs under test with only two LVR chips active. The resistor traces reached more than 60°C without cooling.

On one PCB one of the LVRs was not operational, so that together 11 samples could be tested and irradiated.

Treatment with 58 MeV protons at a cyclotron of the Institute of Nuclear Physics [2] of the Polish Academy of Science in Krakow, Poland, was conducted on October 22 and 23, 2018, in several runs. The proton beam was defocused to cover all 4 LVR ASICs at once and the dose of the beam was continuously measured with a calibrated, small Markus chamber placed in close vicinity of the DUTs and connected to a PTW UNIDOS [3] device, which was read out outside of the experimental hall. The LVR devices were all irradiated in an active state and their output monitored during all the irradiation. Beam homogeneity (depicted in Fig. 2) was proven by means of Gafchromic EBT QD+ film [4] (blue insert) which was scanned on a densitometer after irradiation. The proton dose varied not more than $\pm$5% within an area of 28 mm in diameter. The PCBs were connected to the power supply with a 1.5 mm^2 thick cable to reduce the voltage drop on the input channel. Additional sense wires were used to monitor the V_{in} (of chip pairs) and V_{out} of every chip continuously during the irradiation runs. Every parameter was registered also in a log file, what allows for an analysis of the chips' behavior before, during and after the exposure.

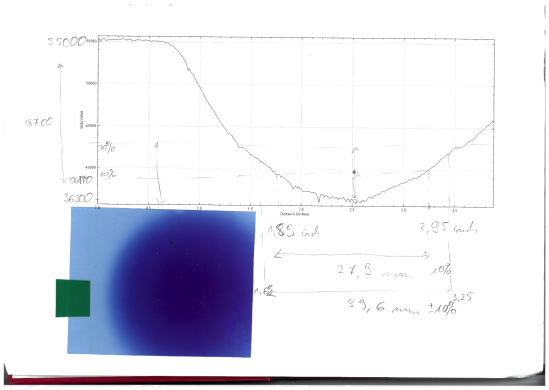

Figure 2: Proton beam homogeneity measured with GAFCHROMIC EBT QD+ film and scanned on a densitometer. Within the area of LVRs the deposited dose was homogeneous to within $\pm$ 5%.

Test results

The measured output voltage of the LVR, V_{out}, and the relative deviation of V_{out} from the starting value during the irradiation for 8 of the tested chips is shown in Fig.3.

All 11 LVR chips survived more than the required 10 kGy of ionising dose (20, 22 and 25 kGy). Sudden drop of all 4 output voltages in the last set of LVRs after ca. 25 kGy of proton dose was observed. The simultaneous breakdown of all four ASICs within few seconds cannot be easily explained but cannot be attributed to the irradiation.

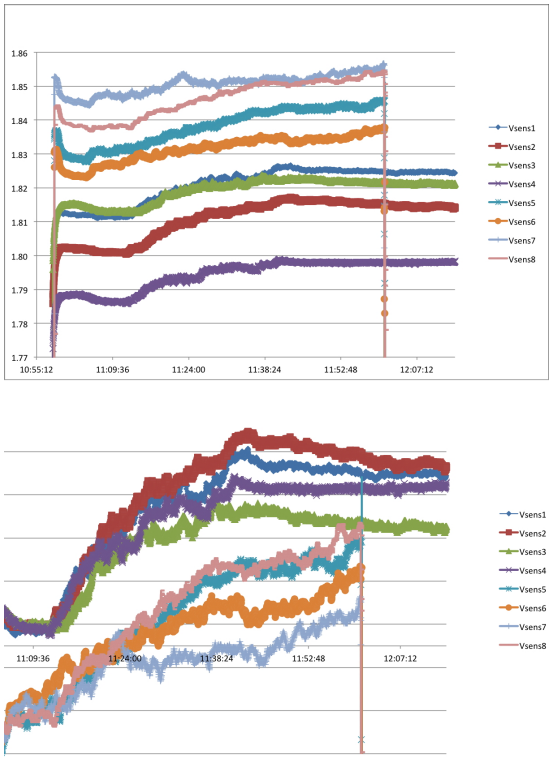

Figure 3: Changes in V_{out} in volt of 8 tested 1.8 V LVR chips with increasing dose (upper) and relative deviation of V_{out} (normalized to the starting value) in percent (lower part). Values in the upper part have been intentionally shifted by 0.01 V against each other for better readability. The vertical break-off at late times marks the situation after 25 kGy where some devices were shut down for yet unknown reasons. As four devices shut-down simultaneously, this event is not interpreted as irradiation induced.

Conclusions

All 11 LVR ASICs survived irradiation with 58 MeV protons for much more than required 10 kGy and showed remarkable stability of output voltage (+1% to -0.5%) at full load output current during the test. They even survived an irradiation dose of 25 kGy. Unlike earlier measurements the output voltage for these devices rather increased through the irradiation dose. This time a slight increase by about 15 mV or 0.9% was the observed effect of the irradiation to the output voltage. For the earlier, larger devices that had been tested, a much more severe drop was observed. The change in output voltage observed this time appears entirely uncritical. In order to make sure that the targeted output voltage will be met also taking connectivity into account, the 1.8 V devices should be designed for an output voltage of 1.85 V $\pm$ 0.05 V. For the 1.2 V device, that was not tested here, there is the specification for the absolute minimum supply voltage needed of 1.1 V on VDDM. In order to make sure that this voltage will always be supplied over the lifetime, the 1.2 V LDO should be designed for a nominal output voltage of 1.25 V $\pm$ 0.03 V at full load of 1.6 A.

References

[1] http://http://www.scl.gov.in/

[2] https://www.ifj.edu.pl/

[3] https://www.ptw.de/unidos webline dosemeter rt0.html

[4] https://iopscience.iop.org/article/10.1088/0031-9155/52/14/013/meta

Assembly and commissioning of the mSTS detector for mCBM startup

J. M. Heuser[1], M. Dogan[1,2], D. Emschermann[1], U. Frankenfeld[1], R. Kapell[1], P. Kocon[1], J. Lehnert[1], P. A. Loizeau[1], A. Lymanets[1], O. Maragoto-Rodriguez[3], S. Mehta[1,4], A. Rodriguez-Rodriguez[3], P. Schweigert[1], C. J. Schmidt[1], H. R. Schmidt[4,1], C. Simons[1], R. Visinka[1], and O. Vasylyev[1]

[1]GSI, Darmstadt, Germany; [2]Istanbul University, Turkey; [3]Goethe Universität, Frankfurt, Germany; [4]Universität Tübingen, Germany

The miniCBM (mCBM) experiment installation in Cave HTD at GSI's SIS-18 accelerator intends to prove the concept of free-streaming data generation, transport and reconstruction as to be applied in the main CBM experiment at FAIR [1]. At the same time, prototypes of CBM detector systems can be tested under realistic high-rate beam-target collisions and deliver the free-streaming data.

The mSTS detector has been conceived as a small two-station tracking system [2]. In comparison with the full STS detector, several simplifications have been made, giving room to focus on a few essential components and system design aspects. Due to the limited spatial conditions in the mCBM cave, the mSTS detector is located close to the target and can image the particle spray from the target in the angular range of about 2.5-25 ° with just 13 silicon microstrip sensors of 6.2 by 6.2 cm, arranged as 2 by 2 on the upstream station, and 3 by 3 on the downstream station. Every sensor is comprised in an individual detector module. Two or three detector modules are arranged on a carbon fiber support structure, forming a ladder, so that the upstream station is made from two, the downstream station from three ladders. The detector ladders are mounted onto C-frames, which are mechanical units that can be installed into the detector mainframe and hold cooling plates circulating chilled water for the modules' front-end electronics, powering electronics and read-out boards.

For the mCBM startup in December 2018, the first STS modules with full 2048 channel read-out have been constructed [3], proving the assembly concept and its quality assurance measures. The detector modules feature the longest, about 50 cm long microcables of the largest, most downstream tracking station of the later full STS detector. From two modules, the first STS ladder was assembled [4] demonstrating the assembly tooling and procedure functional. It was installed on a mechanical Aluminum C-frame. Power supply was realized with prototypes of the STS power boards and low/high-voltage supply systems. The read-out was channeled through C-ROB boards. The opened detector is shown in Fig. 1, the mSTS installed in Cave HTD in Fig. 2.

One of the two detector modules proved functional. In the data taking runs of mSTS alone and together with other prototype detectors, valuable data was obtained, demonstrating detailed insight into the detectors' operational performance, data rates, timing and correlation of hits. The mSTS will be further completet for the next mCBM beam times.

Figure 1: mSTS enclosure with downstream wall removed.

Figure 2: mSTS installed on the beam table in Cave HTD.

References

[1] The CBM Collaboration, *mCBM@SIS18 – A CBM full system test-setup for high-rate nucleus-nucleus collisions at GSI/FAIR*, Letter of Intent, 19 June 2017

[2] O. Vasylyev et al., *Progress with the integration of the mCBM Mini Silicon Tracking System*, CBM Progress Report 2017, p. 177

[3] C. Simons et al., this report

[4] S. Mehta et al., this report

A realistic thermal demonstrator for qualification of the STS sensor and front-end electronics cooling

K. Agarwal[1], M. Kis[2], P. Kuhl[2], H. R. Schmidt[1,2], and O. Vasylyev[2]
[1]Universität Tübingen, Tübingen, Germany; [2]GSI, Darmstadt, Germany

The major heat producing sources of the Silicon Tracking System (STS) and their respective cooling requirements are as follows [1]:

Silicon Sensors Due to the expected irradiation damage, sensors will dissipate $\sim$ 6 mW/cm^2 at -10°C. Thus they have to be kept at or below -10°C to avoid thermal runaway & reverse annealing.

Front-End Electronics FEE placed outside detector acceptance are connected to the sensors via up to 55 cm long microcables and emit $\sim$ 40 kW. So they have to be at $<$ -10°C to avoid any heat transfer to the sensors.

Power Cables Due to joule heating in the powering connections between the DC-DC converters and the FEE, an additional heat dissipation of $\sim$ 2 kW is expected (0.4 – 0.8 W/m)

Thermal Enclosure Walls An estimate of $\sim$ 40 W/m^2 of heat is expected to pass through the insulation walls of the enclosure and must be removed to maintain the STS thermal environment.

This contribution will describe the ongoing R&D to experimentally solve the aforementioned problems by building a thermal demonstrator comprising up to 3 STS half-stations (all from Unit 01) under realistic constraints.

Silicon Sensor Cooling

STS sensors will be cooled by forced N_2 cooling to ensure that no extra material budget is included inside the active detector volume. As a preliminary design, gas nozzles located on the top of individual ladders will be used to cool the respective sensors (see Fig. 1). Cold and dry gas (-30°C; 0.1% RH at 20°C) will be supplied by commercial gas chillers to every nozzle.

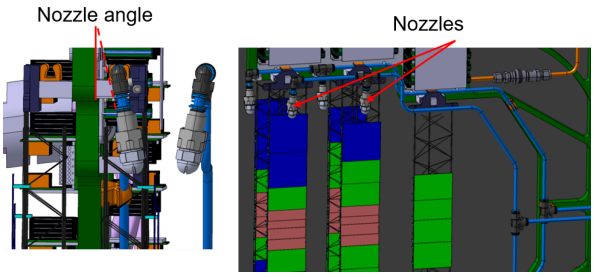

Figure 1: Placement of nozzles in the C-Frame.

Silicon power resistors will be used to mimic the heat produced by STS sensors. These resistors are comprised of an electrically conducting Inconel layer (Ni-Cr Alloy; 200 nm) deposited on 300 μm silicon bulk. This allows the resistors to produce joule heat by varying the voltage drop accross the conducting layer. This has been designed as per the R&D of the ATLAS Alpine Thermal Demonstrator [2].

FEE Cooling

Bi-phase CO_2 delivered by TRACI-XL will be used for FEE cooling in the demonstrator [3]. Simulations described in [1] are being performed to obtain the needed operational parameters (such as input pressure, temperature, mass flow) to maintain max. FEE temperature $<$ -10°C.

The simulation results for the FEE cooling plate to be used in the thermal demonstrator, i.e. for STS Unit 01, are summarized below and shown in Fig. 2.

Power Dissipated	594 W
Tube Geometry	4 mm (I.D.) / 2.36 m (L)
Fluid Inlet Temperature	-30°C
Fluid Inlet Pressure	14.41 bar
Total Pressure Drop	0.14 bar
Mass Flow	7 g/s
Dry-Out Margin	56% (x_{dryout} = 0.63)
Maximum ASIC Temperature	-14.5°C

Note that air convection, radiation, cable heating and thermal interface materials have not been taken into consideration for this analysis.

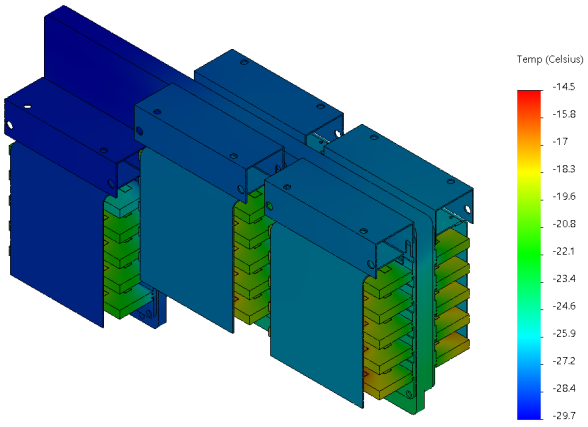

Figure 2: Thermal FEA results for FEE cooling.

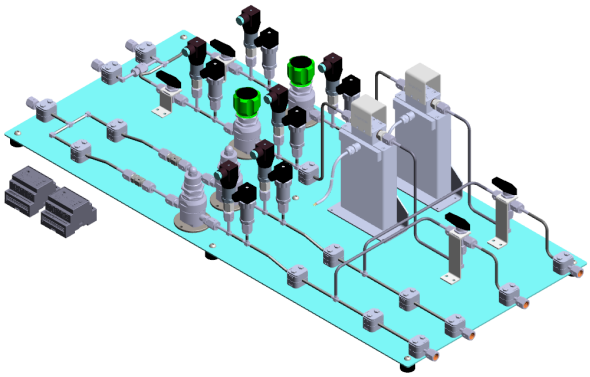

Figure 3: Distribution System Design.

The inlet and outlet parameters of the FEE cooling setup are controlled by a distribution and control system, which acts as an interface between TRACI-XL and the FEE setup. A sophisticated distribution system for controlling these parameters has been designed and ordered (Fig. 3).

Power Cables Cooling

In order to remove the ~ 2 kW additional heat in the FEE setup, its aimed to derive the needed cooling from existing sources without major geometry changes. So a modified FEE box will be used, where cable cooling is done by a metallic cable cover attached on the corner fin of the FEE box (Fig. 4).

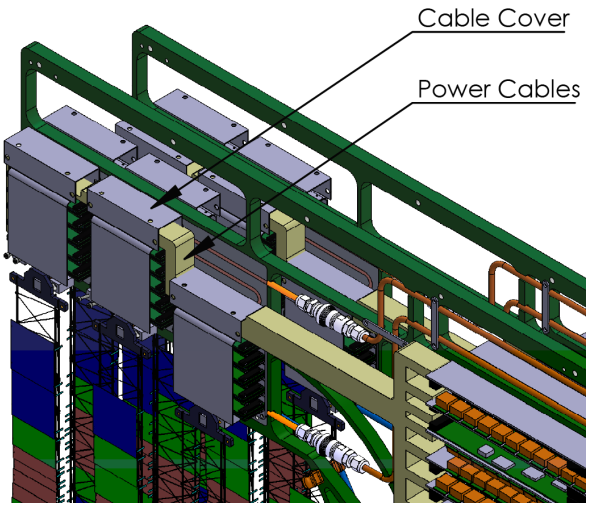

Figure 4: Power cables cooling by FEE box.

Thermal Enclosure Walls and Integration

The temperature inside the thermal enclosure will be $< -10°C$ which requires that all the thermal power produced inside is neutralized by the measures described above. The walls of the insulation box will be 20 mm thick, with two layers or carbon composite enclosing 16 mm of insulating foam, e.g., Airex. It has been calculated that this insulation thickness is enough to avoid condensation on the outside surface of the box [1]. For safety, it is well possible to cover the outer surface with additional heating foils (idea extensively used in ATLAS and CMS). The necessary structural support for these insulation panels is provided by an aluminium skeleton made from ITEM profiles.

Additionally, a feedthrough concept applicable for the many HV connections has been developed, which is both thermally insulating and diffusion tight.

Project Outlook and Timeline

Other integration topics, such as the dummy sensor-ladder assembly, thermal enclosure integration etc are still in progress. Ordering of most components is either already done or is ongoing. The timeline of different major tasks within the thermal demonstrator project covers the coming 12 months.

References

[1] K. Agarwal *et al.*, *Conceptual Design Report of the STS Cooling System*, CBM-TN-18004 (2018)

[2] E. Petit, *Alpine stave mechanical proposal for the ATLAS pixel upgrade project*, Forum on Tracking Detector Mechanics (2017)

[3] J. Sanchez *et al.*, *TRACI-XL, the test cooling system for the CBM Silicon Tracking System, CBM Progress Report*, 2012, p. 21

Feasibility analysis of monophase NOVEC cooling for STS-FEE

K. Agarwal[1] *and H. R. Schmidt*[1,2]
[1]Universität Tübingen, Tübingen, Germany; [2]GSI, Darmstadt, Germany

The Front-End Electronics (FEE) of the Silicon Tracking System (STS) is placed outside of the detector acceptance and is expected to dissipate $\sim$ 40 kW of power. As the silicon sensors have to be operated at -10°C to limit radiation induced leakage currents, the electronics has to be cooled to below this temperature at all times to avoid any heat transfer to the silicon sensors which are only 10 – 50 cm away [1].

For achieving the same, the following requirements are essential for choosing the coolant:

- High Volumentric Heat Transfer Coefficient,
- Low Global Warming Potential ($\sim$ 1),
- Radiation hard up to 10 kGy.

Given the aforementioned needs and proven performance, biphase CO_2 is the first choice coolant for STS-FEE [1]. But due to potential difficulties in finding a commercial pump-based CO_2 cooling system, 3M^{TM} NOVEC^{TM} 649 Engineered Fluid [2] is seen as a viable alternative. The following sections will summarise a short feasibility study for NOVEC cooling within STS boundary conditions.

Computation Fluid Dynamics (CFD) Analysis for a realistic FEE cooling setup (STS Unit 08) has been done for monophase NOVEC 649 with the following assumptions:

- Power Dissipated = 1080 W,
- Tube Geometry = 6 mm (I.D.) / 2.7 m (L),
- Coolant Inlet Cond. = -40 ... -45°C / 150 ... 200 g/s.

Corresponding results are summarized in Table 1 and shown in Fig. 1. It could be inferred that FEE temperatures $<$ -10°C could be obtained with managable pressure drops and fair amount of flexibility in inlet parameters (temperature and mass flow).

Table 1: CFD analysis results with NOVEC cooling

Input Temp. [°C]	-40	-40	-45	-45
Mass Flow Rate [g/s]	150	200	150	200
Max. FEE Temp. [°C]	-13.4	-16.8	-17.7	-21.2
Pressure Drop [bar]	1.25	2.09	1.27	2.13

The tube geometry figures are based on the fact that press-fitted tube channels will be used for cooling plate manufacturing. Note that air convection, radiation, cable heating and thermal interface materials have not been taken into consideration for this analysis.

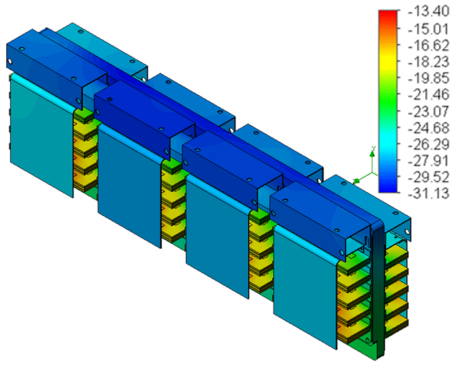

Figure 1: CFD result for 8 FEE boxes dissipating heat on both sides of a cooling plate. The simulation considers a coolant temperature T = -40°C and mass flow $\dot{m}$ = 150 g/s. The color scale shows temperatures in °C.

As the liquid viscosity of NOVEC 649 is ten times higher than liquid CO_2, thicker tubes are needed for reducing the pressure drops in the transfer lines. This could potentially lead to larger feedthroughs on the STS front wall.

The feasibility to use a LHCb-VELO like distribution system [3] for STS is under investigation, which would imply that a single inlet line through the STS box would serve multiple FEE cooling plates. This will allow saving space on the front wall, but leads to additional pressure drop across calibrated orifices needed for a balanced flow.

The most important technical parameters for initial inquiries on the NOVEC cooling plant are summarised as follows:

- Cooling Power at min. temp. 50 kW
- Temp. Range 20 ... -45°C
- Flow Rate up to 5.5 l/sec
- Pump output pressure up to 20 bar

A technical note explaining the details of the feasibility analysis is under preparation. The note is oriented towards manufacturing companies to prepare a comprehensive offer for the production of (parts of) the system.

References

[1] K. Agarwal *et al.*, CBM-TN-18004 (2018)
[2] CERN EDMS Doc. Id. 1751219
[3] CERN EDMS Doc. Id. 1892359

Ladder alignment of the CBM-STS detector using cosmic muons

S. Das[1] *and H. R. Schmidt*[1,2]
[1]Universität Tübingen, Tübingen, Germany; [2]GSI, Darmstadt, Germany

Abstract

The purpose of the detector alignment to determine the accurate positions of its components in space in order to deliver highest particle reconstruction quality. To achieve such a spatial precision in a complex hierarchically structured detector, a track based alignment algorithm is developed, starting off a mechanically surveyed detector after its construction.

The *unit* based STS geometry *version 16g* is used for the test of the algorithm, where 8 logical stations are realized with 9 mechanical units and each unit is divided into two half units. The geometry is categorized by 5 hierarchies; 3 active hierarchies to be used for the alignment: half mechanical units (highest level), ladders, sensors (lowest level) and 2 inactive hierarchies to be used for the global referencing: (1) global reference system, (2) half side of the detector. The alignment of the ladder hierarchy is addressed in this report with a toy misalignment scenario upfront.

Preparation of Cosmic Muon Tracks

To be able to align the detector components ("alignables") successfully using a track based alignment algorithm, the alignables should have a decent number of reconstructed tracks (at least 4 STS hits on a track) passing through them. For straight tracks, originating from the target, some ladders located at large angles have not enough overlap with other ladders for a meaningful track based alignment strategy (see Fig. 1).

To align these edge ladders as well, cosmic ray induced tracks having random incident angles are needed. For this purpose a simple cosmic ray generator has been set up. One million cosmic straight muon tracks with a fixed momentum of 5 GeV/c have been simulated without magnetic field. Approximately 110 thousand tracks (see Fig. 2) can be used for the alignment with the help of the reconstruction algorithm, employing the ideal track finder. In future, a more realistic zenith angle (θ) distribution will be implemented for the cosmic muon simulation along with the usage of broad momentum range based on the cosmic ray vertical flux.

Alignment Results

A toy misalignment scenario is proposed on the ladder hierarchy to test the newly built track based alignment algorithm. The first ladder in the first half unit and the last ladder in the last half unit are kept fixed (for global referencing). The other 104 ladders are randomly displaced using the virtual method (i.e. instead of modifying the geometry, just modifying the hit position accordingly, during the track reconstruction step) by taking $\sigma_x = 100$ μm, $\sigma_y = 100$ μm for the translations along the X and Y axes. The Z values are kept fixed throughout. Then, this misalignment scenario is treated by the standard alignment al-

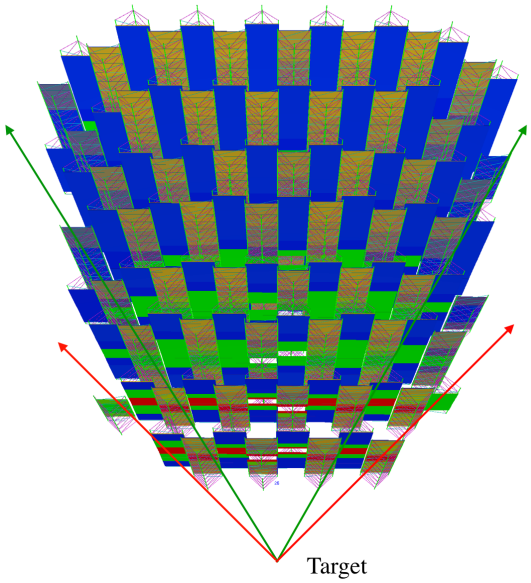

Figure 1: Green tracks are reconstructable (can be used for the alignment), where red tracks are not.

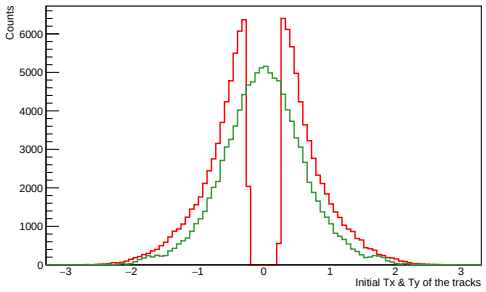

Figure 2: Cosmic muon track slope distribution in X direction (T_x, green) and in Y direction (T_y, red) with respect to the beam axis.

gorithm to produce the alignment corrections. The alignment results are discussed below.

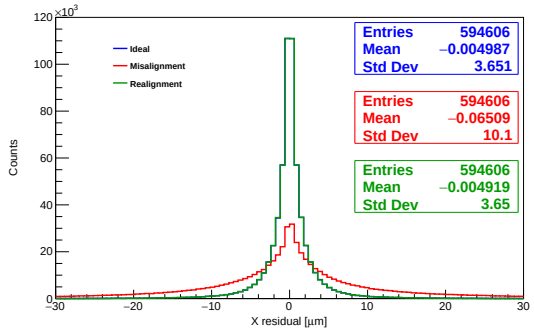

Figure 3: Residual distribution in X direction.

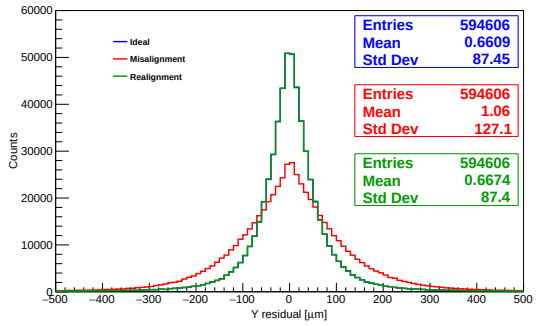

Figure 4: Residual distribution in Y direction.

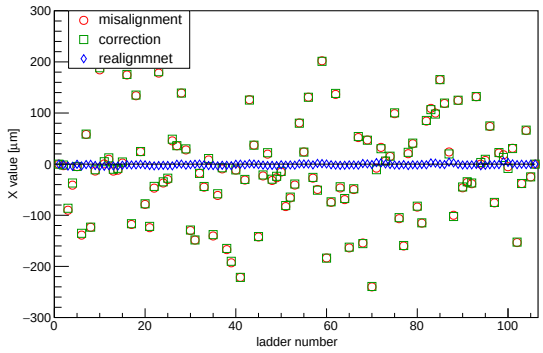

Figure 5: X directional misalignment correction.

From the Figures 3 and 4, the residual distributions (the indicator of the track fit quality) in both the X and Y directions can be seen resolved to the ideal scenario after the alignment corrections. The accuracy of the alignment corrections are of the order of 5 μm in X direction (see Fig. 5) and 20 μm in Y direction (see Fig. 6). The alignment corrections show systematic errors, inherent to the fitting procedure (as seen on the Y corrections). This might be due

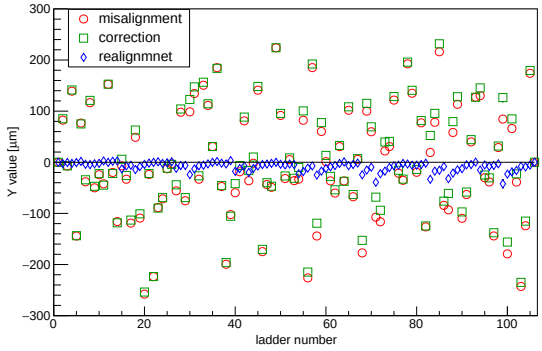

Figure 6: Y directional misalignment correction.

to the lack of suitable geometrical constraints. And such bias fits become predominant once the rotational degrees of freedom (DOF) are introduced which correlate translational DOF's. So, further investigations are needed to evaluate additional constraints, which should then be added to the alignment algorithm for the proper χ^2 fit, to avoid such biases of the alignment corrections.

Conclusion

The alignment method for the ladder hierarchy is working within the spatial precision limit for the translational DOF. But at present fit biases of the alignment corrections are not resolved for the rotational DOF (work in progress). Once, this problem is solved by the proper geometrical average constraints, the sensor level alignment will be implemented.

Acknowledgement

I am really grateful to Dr. Claus Kleinwort from DESY, Hamburg for his personal advice and constant support.

References

[1] Technical Design Report for the CBM Silicon Tracking System, GSI Report 2013-4

[2] V. Blobel, *Millepede II*, Institut für Experimentalpyhsik, Universität Hamburg, 2007, http://www.desy.de/ blobel/mptalks.html

[3] C. Kleinwort, *General Broken Lines as advanced track fitting method*, NIM A673 (2012), 107-110, doi:10.1016/j.nima.2012.01.024

[4] S. Das and H. R. Schmidt, *Introduction of General Broken Lines refit algorithm for CBM-STS*, CBM Progress Report, 2017

[5] S. Das and H. R. Schmidt, *Track Based Alignment Procedure for CBM-STS Using Millepede II*, CBM Progress Report, 2017

Ring-Imaging Cherenkov Detector

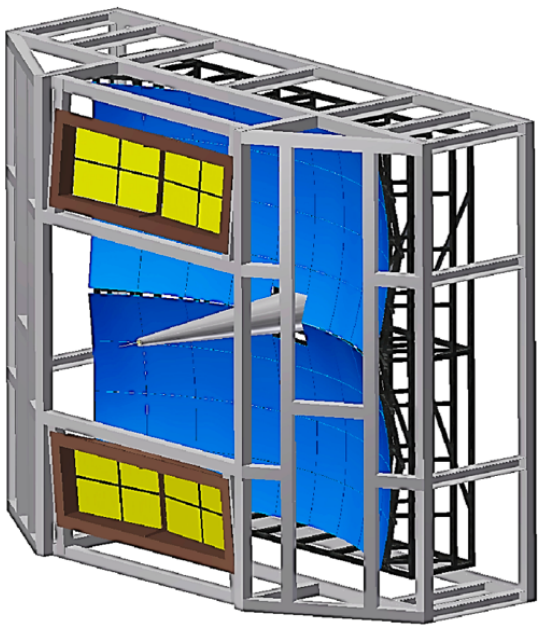

RICH - Summary

C. Höhne[1,2] and the CBM RICH working group
[1]Justus Liebig University Giessen, Germany; [2]GSI, Darmstadt, Germany

The CBM RICH project has made substantial progress in various fields in 2018 as will be presented in this CBM Progress Report. The reports on RICH developments and corresponding progress made are distributed in various sections of this Progress Report: Feasibility studies, Computing, DAQ, Fair phase 0 (HADES) and the RICH detector chapter itself. In this summary all those developments are considered together.

The largest success in 2018 which is presented in the FAIR phase 0 (HADES) chapter is certainly the successful upgrade of the HADES RICH detector with H12700 MAPMTs originally purchased for CBM. This upgrade included the development of a readout concept based on 12 DiRich boards (TDC-FPGAs), one combiner and one power board for each group of 6 MAPMTs. In total, 428 H12700 MAPMTs have been included in the RICH detector, 48 of those were additionally covered with a WLS film. Since beginning of March 2019 the upgraded HADES RICH detector is running successfully in the HADES beamtime delivering high quality data. Good electron rings are seen clearly by eye (fig. 1) and typically show approx. 16 hits per ring, depending on cuts. The noise can be suppressed to a very low level adding proper timing cuts in the analysis. The operation of the HADES RICH detector will teach and already did teach various lessons for the future CBM RICH detector, e.g. on the cooling concept but also on effects of the magnetic stray field on signal efficiencies.

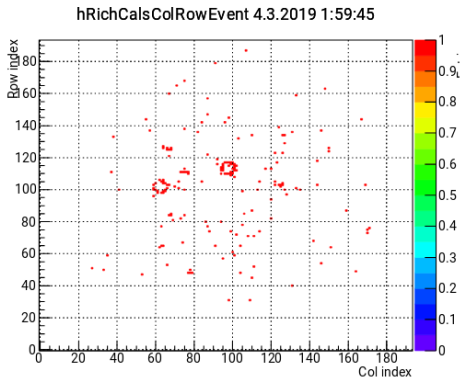

Figure 1: Online event display from the HADES RICH, no timing cuts applied yet.

In the RICH chapter of this report an important aspect that is covered in several reports is the mechanical construction of the RICH detector itself. A rather large scale prototype of the mirror holding scheme has been build including two real size pillars of the RICH detector. An important aspect to be studied is the mechanical stability of the system under load and also over time. For the photodetector plane a further prototype has been build including 4 segments of the cylindrical plane. With this prototype the cooling system can be developed and tested as well as integration issues such as gas- and light-tightness if the cylindrical frame is implemented into the larger shielding box. Large improvement has been made in the design of this shielding box as during an iterative progress various configurations of field clamps and shielding box designs have been studied. A new proposal with largely reduced weight has been prepared for further evaluation. In the process of preparing mirror alignment control the last missing step has been performed showing that a carefully calibrated CLAM method can provide quantitative evaluation of mirror misalignments. All 1100 H12700 MAPMTs have been finally delivered and tested showing overall high performance. Before the mass production of the HADES readout electronics a COSY testbeam has been performed end of 2017. Results are presented here qualifying the readout performance. In particular the time-over-threshold information proves to work well and can suppress pixels with signals from capacitive coupling in the padplane of the MAPMTs. Important for high timing precision is a timing calibration of each TDC channel which has been implemented directly in the FPGAs and will be performed online.

Further important developments not included in the RICH chapter are presented together with software and DAQ developments as well as feasibility studies: In order to proceed from the triggered readout and ring finding as now implemented in the HADES RICH to the self-triggered readout in CBM huge improvements have been made in software and the DAQ. A time-base RICH analysis has been implemented in CbmRoot and thoroughly tested, no efficiency losses up to interaction rates of 10 MHz are observed. A DAQ concept has been developed and implemented in firmware that can connect the triggered readout on the TRB3/TRB3sc platform to the free-running CBM DAQ system. The RICH DPB provides the interface between the two and will be tested in the mCBM beamtime campaign in March 2019 at GSI. The corresponding prototype using an aerogel as radiator is in preparation. Feasibility studies of di-electron observables such as π^0 or η production as well as low-mass di-electrons have been studied for SIS 100 energies. In addition, Ag+Ag collisions at 4.5 AGeV beam energy have been simulated as this might be a potential overlap system between HADES and CBM.

Development of an FPGA based online TDC calibration

A. Weber[1], *J. Michel*[2], *and C. Höhne*[1]
[1]Justus-Liebig Universität, Giessen, Germany; [2]Goethe-Universität Frankfurt, Germany

The CBM and HADES RICH detector readout electronics is based on the TRB electronics with FPGA based time-to-digital converters (TDCs). The FPGA based TDC technology is build on delay chains made up from subcomponents of the FPGA. An incoming data signal is propagating through the delay chain for a certain time up to 5 ns (finetime). In combination with a coarsetime (5 ns granularity) from a 200 MHz counter and an EPOCH time, an exact time information is calculated [1]. The propagation through the FPGA is dependant on the internal FPGA structure as well as the place and route of the FPGA design. This gives a dependence of the time information on the voltage and also on temperature changes. Therefore a calibration of the time information is necessary. Instead of the resource intensive bin-by-bin calibration (RMS $<$ 11 ps), a linear calibration was implemented on the FPGA [2]. The linear calibration uses the lowest and highest bin of the finetime distribution which is filled and projects the data on a range between 0 and 5000 ps - the time between two coarse times. As this method does not correct for different delay times in different delay chain elements, it is less precise compared to the bin-by-bin calibration.
The FPGA based calibration uses the output of the TDC entity. The incoming TDC data is used to derive the minimum and maximum values for the linear calibration of each TDC channel separately and the incomeing data are calibrated with an existing calibration set in parallel. If a certain amount of statistics is reached, a new calibration set is used to calibrate the following data in the corresponding channel. The output of the calibration is a value between 0 and 1000 (as well as two error values). This number has to be multiplied by a factor of 5 to get the finetime in picoseconds. The calibration is controllable via slow control registers. In addition to setting the amount of statistics it is possible to stop the calibration and/or the creation of new calibration sets as well as the creation of calibrations only on a certain trigger type.
The FPGA based calibration is available for the Trb3Sc board as well as for the DiRICH Combiner boards.
The precision of the FPGA based calibration was compared to the classic software based methods. As first step a set of measurement at different temperatures between 5°C and 50°C was taken with a Trb3Sc and a pulser add-on. Fig. 1 shows the influence of the calibration methods in software on the TDC precision. The exact and the linear calibration differ by 5 ps only. This value is rising with higher offsets in the pulser. The green line shows the effect of a calibration that is not renewed after temperature changes.

Fig. 2 shows the measured precision in 10 different channels of a Trb3Sc with the linear calibration in software (blue) and the calibration on the FPGA (red). The difference in precision between both methods is on a level of 1 ps only verifying the FPGA implementation. Within the errors of the measurements and the implementation, the software and FPGA calibration give comparable results with an outstanding precision.

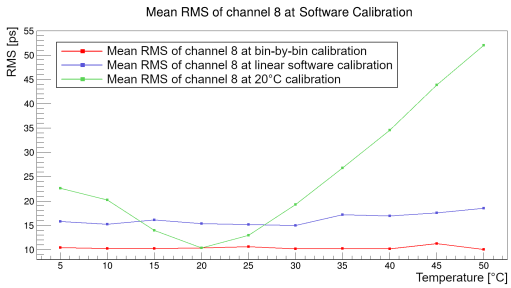

Figure 1: Mean value of the RMS for different measurements between 5°C and 50°C of channel 8. The measurements were done with a software based bin-by-bin (red), linear (blue) and constant bin-by-bin calibration from 20°C.

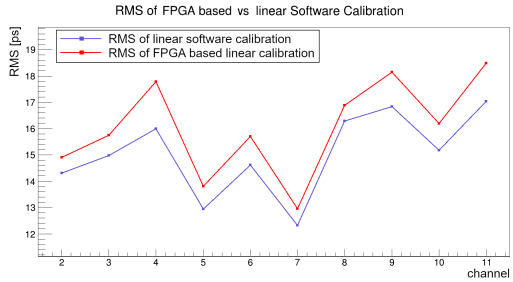

Figure 2: Measured RMS for different channels of a Trb3Sc with a software (blue) and FPGA (red) based linear calibration.

References

[1] Ugur, Cahit et al. (2012). *A 16 channel high resolution (<11 ps RMS) Time-to-Digital Converter in a Field Programmable Gate Array*. Journal of Instrumentation. 7. C02004. 10.1088/1748-0221/7/02/C02004.

[2] A. A. Weber, *Entwicklung von FPGA basierter Ausleseelektronik für den HADES RICH upgrade und CBM RICH Detektor*, Master Thesis, Justus-Liebig-Universität Giessen, September 2017

Production and testing of the RICH mirror supporting frame prototype

D. Ivanishchev[1], *C. Höhne*[2,3], *A. Khanzadeev*[1], *N. Mifstahov*[1], *C. Pauly*[4], *E. Rostchin*[1], *Yu. Ryabov*[1,5], *V. Samsonov*[1], *O. Tarasenkova*[1], *and D. Tyts*[1]

[1]PNPI, Gatchina, Russia; [2]Justus Liebig University, Giessen, Germany; [3]GSI, Darmstadt, Germany; [4]Bergische Universität Wuppertal, Germany; [5]St.Petersburg State Polytehnical University, St.Petersburg, Russia

A lightweight aluminum full-scale prototype of the mirror supporting frame for the CBM RICH detector [1] was produced and tested this year. As a first step, in order to further reduce the amount of materials in detector acceptance, lightweight small frames and six mounts were produced and tested with mirror tile imitators (Fig. 1).

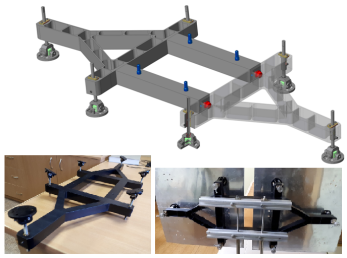

Figure 1: Small frame design model (above), photo of the produced frames with imitations of the mirror tiles (bottom).

Test shows that the design meets all requirements. But, as a result of the tests, additional design improvements were proposed. Major changes have been made to simplify the assembly and installation of the mirror tile in the correct position. All the changed components were produced separately, installed and successfully tested.

Next, all components for a full-scale prototype [2] of the mirror supporting frame were manufactured, tested [3] and assembled (Fig. 2). Tests were carried out on the deformation and stability of the structure.

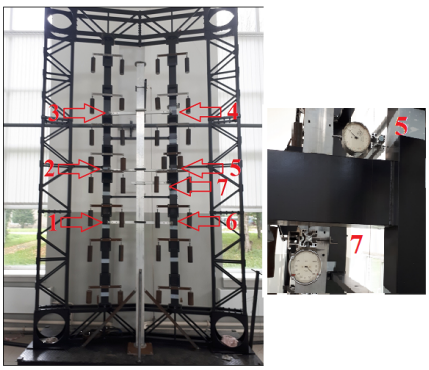

Figure 2: Loaded mirror supporting frame prototype with indication of the micrometers positions (left). Right: Micrometers for measuring horizontal (No. 5) and vertical displacements (No. 7).

To imitate the mirror system, the frame was loaded with a weight of about one and half times of the nominal parameters, i.e. with 9 kg. During the loading and unloading of the frame deformation measurements were performed at the points shown in Fig. 2. For both pillars of the prototype in total six micrometers measured deviations in the horizontal direction, the seventh micrometer measured the deviation of the largest console in the vertical direction.

The measurement results are shown in Fig. 3. The results of measurements coincide with calculations within 10-15%. As you can see, during the tests we did not observe any significant displacements of the pillars (maximum 30-40 μm). The test continues.

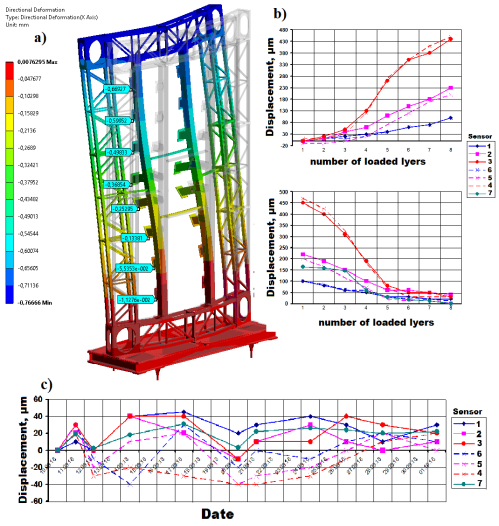

Figure 3: Example of ANSYS deformation calculations under load (a), measured displacements during loading (top) and unloading (bottom) of the frame (b), example of displacement measurements during three weeks (c).

Successful testing of mirror frame deformations and stability allows us to proceed to the next stage of testing with real mirror tiles.

References

[1] Ya.Berdnikov *et al.*, CBM Progress report 2015, Darmstadt 2016, p. 52

[2] Ya.Berdnikov *et al.*, CBM Progress report 2016, Darmstadt 2017, p. 63

[3] Ya.Berdnikov *et al.*, CBM Progress report 2017, Darmstadt 2018, p. 53

Time over Threshold (ToT) cuts for optimising the signal information of MAPMT signals

V. Patel, C.Pauly, I. Kres, J. Förtsch, and K-H. Kampert
University of Wuppertal

Introduction

In November of 2017, a full system test of the future HADES- and CBM- RICH electronic readout chain was carried out using a prototype detector carrying 2×6 H12700 Multi Anode Photomultiplier (MAPMT) and 24 DiRICH frontend modules. The prototype setup was installed at an external beam cave at the COSY accelerator at FZ Jülich. All the details of the experimental set-up are available at [1]. The main purpose of this beam test was to check the performance of the readout electronics under realistic conditions. The data generated during the beam test was analysed over the last year, first results were already presented in [2].

Time over Threshold (ToT) cuts

The focus in the analysis presented now is to use time over threshold information of the signal to suppress the capacitive crosstalk signals. These can be observed on H12700 MAPTs in cases where an individual pixel is not hit by a photon, but the number of coincident photons on other MAPMT pixels is large ($>5-10$). Initial lab measurements based on first DiRICH prototypes have been already presented in [3]. The next step is now to test this approach under real beam conditions. In order to make use of the ToT information it is necessary to compensate the time offset among the individual channels. Figure 1 is a plot of the time over threshold information of all 800 channels from the prototype readout operating at 30 mV threshold, before (left) and after (right) T0 calibration/alignment: A linear fine time calibration was implemented for a precise measurement of timing by the TDC [4]. Individual T0 offsets were derived in order to align the ToT signal peaks of all channels.

In the calibrated ToT spectrum one can observe two distinct peaks: the first, left peak with a small ToT is caused by capacitive crosstalk hits and the peak on the right side (larger ToT) is caused by the main signal. Quality and usability of the ToT information depends strongly on the discrimination threshold which becomes evident by comparing the observed ToT distribution from figure 1 (low threshold of 30 mV) and figure 2 (high threshold of 120 mV). The clear separation of crosstalk- and signal peak which can be observed at low threshold almost vanishes at high threshold because crosstalk hits are already suppressed due to high threshold and also at high threshold the ToT information itself deteriorates.

Once proper ToT calibration is achieved, a cut on a ToT value can be implemented in order to suppress crosstalk background even at low threshold values, and thus optimising detection efficiency. Figure 3 shows the plot of hit multiplicity per event for two different thresholds of 30 mV (left) and 120 mV (right). The blue line in the plot represents the hit multiplicity without ToT cut and the red dotted line shows the hit multiplicity after applying ToT cut. The mean value of multiplicity for both the threshold values with and without ToT cut is given in red and blue text boxes respectively. From this we can infer that even after applying ToT cut we do not compromise on signal quality. At low threshold (left plot of figure (3)) one can see that the peak is in-fact enhanced after ToT cut and the tail of the blue curve is reduced (sigma is improved) while the

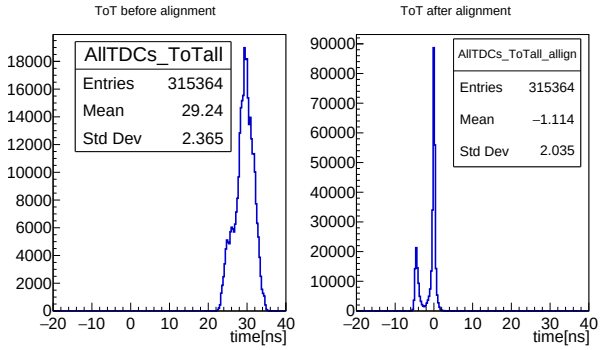

Figure 1: Time over threshold for all the channels (operating threshold: 30 mV) before (left) and after (right) ToT peak alignment

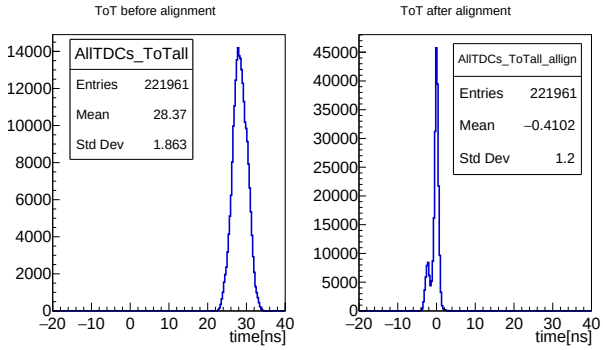

Figure 2: Time over threshold for all the channels (operating threshold: 120 mV before (left) and after (right) ToT peak alignment)

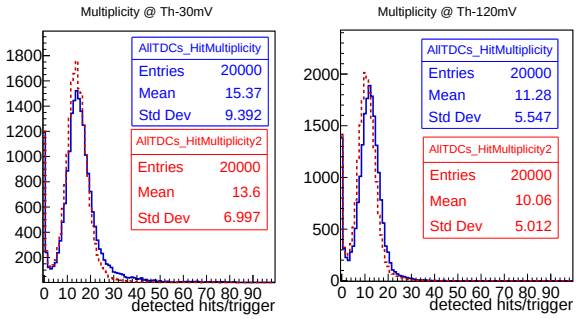

Figure 3: Multiplicity of detected hits without ToT cut (blue) and after applying ToT cut (dotted red) for discrimination threshold of 30 mV (left plot) and 120mV (right plot)

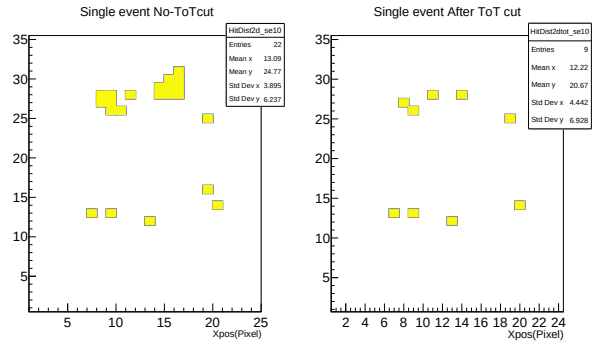

Figure 4: Single event plots of the same event without ToT cut (left) and after ToT cut (right) (operating threshold: 30 mV)

mean is not compromised significantly. This is also confirmed by single event plots shown in figure 4 and figure 5. In figure 4 we can see a single event plot for threshold of 30mV. Left and right side of Figure 4 show the same event with (right) and without (left) application of the ToT cut. One can easily see that the ring quality is improved by

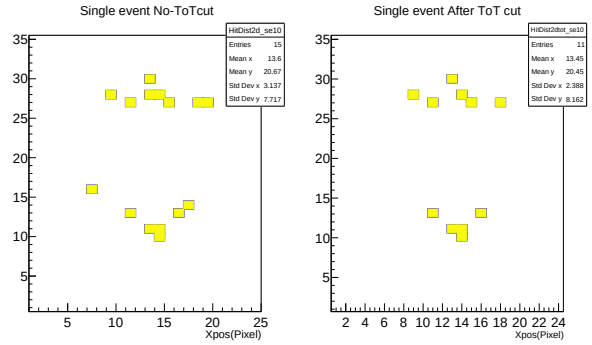

Figure 5: Single event plots without ToT cut (left) and after ToT cut (right)(operating threshold: 120 mV)

the ToT cut and many of the crosstalk hits are suppressed. However, the same is not valid at higher threshold. The ToT information deteriorates at a higher threshold [3] and using ToT cut at higher threshold, in turn, affects the signal quality and we start cutting into efficiency. This is evident by looking at figure 3 and comparing red dotted line (with ToT cut) and blue line (without ToT cut). Both curves have similar shape (no tails, indicating a lack of crosstalk in both cases) however the red curve is shifted towards lower values of multiplicity compared to the blue line indicating the loss of efficiency.

Thus, from the plots above, we can conclude that by applying a cut on a ToT value one can improve the suppression of capacitive crosstalk without loosing the signal information. However one needs to keep a caution that the ToT cuts are effective only when the detector is operated at a low discrimination threshold where one can get maximum signal efficiency without compromising on the leading- and trailing edge timing information.

References

[1] C. Pauly, *COSY testbeam for DiRICH qualification*, GSI Scientific Report 2017. (2017) 60.

[2] V. Patel, *First results testbeam analysis*, GSI Scientific Report 2017. (2017) 64.

[3] V. Patel and M. Traxler, *The HADES-RICH upgrade using Hamamatsu H12700 MAPMTs with DiRICH FEE + Readout*, JINST vol 13, March 2018, p. 3038.

[4] A. A. Weber, *Entwicklung von FPGA basierter Ausleseelektronik für den HADES RICH upgrade und CBM RICH Detektor*, Master Thesis, Justus-Liebig-Universität Giessen, September 2017.

Construction of the CBM RICH cameras

D. Pfeifer[1], *C. Pauly*[1], *V. Patel*[1], *I. Kres*[1], *C. Höhne*[3], *and K.-H. Kampert*[1]
[1]Bergische Universität Wuppertal, Germany; [2]GSI Darmstadt, Germany; [3]Justus-Liebig Unversität Giessen, Germany

The photon detection system of the CBM RICH detector consists of two separate camera boxes, carrying the H12700 Multianode Photomultipliers from Hamamatsu, as well as all frontend readout modules. The MAPMTs are organized on backplanes, each backplane consisting of 3x2 MAPMTs on one side, and 12 DiRICH frontend modules plus power- and combiner module on the backside. Each camera box is surrounded by an iron shielding box in order to shield the MAPMTs from the magnetic stray field of the CBM dipole magnet, guiding the magnetic field lines around the MAPMT array.

The design of these camera boxes has evolved over the past years, starting from an initial, purely simulation driven design towards a construction design which is also mechanically feasible. An important step in this design process was the change from the initial wing shaped design towards a cylindrical geometry of the photon detection plane, which allows for easier mechanical integration of the readout electronics directly behind the MAPMTs, avoiding mechanical overlap of the individual electronic modules. Details on the geometrical optimization procedure can be found in [1].

In the latest design, each camera is made of 14 individual aluminum frame elements (columns), forming a cylindrical carrier frame of radius R=1650mm. The backplanes with MAPMTs will then be mounted onto this frame structure using proper sealing in order to achieve gas tightness. Taking into account the additional height of the MAPMTs, this results in a cylindrical photo cathode area of radius R=1699mm, in good agreement with the optimal geometry obtained from simulation. A sketch of the photon detector including the iron shielding box is shown in Fig. 1.

A first small scale prototype consisting of 5 columns and 10 backplanes has been built in order to check the mechanical feasibility of this design. The prototype is shown in Figure 2. Tests for stability and gas tightness using this prototype are still in progress.

Cooling of the camera electronics is another important issue. The total heat dissipation for one camera module is about 100 Watt from the 500 MAPMT active voltage dividers, and about 2.5 kW from the readout electronics. Care has to be taken to asure that the MAPMTs stay cool, below 30 °C, since the dark rate of PMTs increases exponentially with temperature, as has been confirmed for these particular MAPMTs in [2]. A sophisticated cooling system has been designed, providing cool air blown directly onto the backplanes, see [3]. This provides indirect cooling also for the MAPMTs due to the good thermal contact between MAPMT and backplane via their multipin connectors. Using the prototype frame we plan to test this cooling concept under realistic conditions.

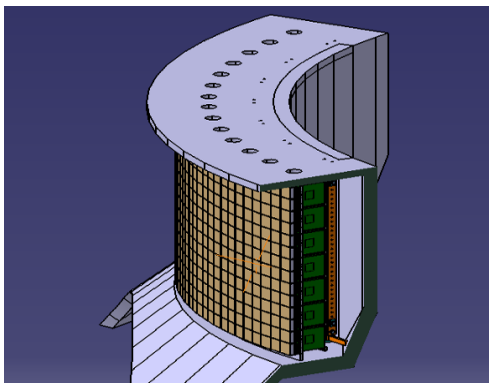

Figure 1: Sketch of the latest CBM RICH camera design.

Figure 2: The first small scaled prototype of the CBM RICH camera with readout electronics. All electronic readout modules are fixed by using special clamps. On the left side you can see solid copper rails, these are going to be used for the low voltage / high current distribution.

References

[1] I. Kres et al., RICH geometry optimization, CBM Progress Report 2016, Darmstadt 2017, p.64

[2] V. Patel et al., Temperature dependence of dark noise for H12700 MAPMTs, CBM Progress Report 2016, 7, p.74

[3] D. Pfeifer et al., Readout electronics cooling: concept and first measurements, https://indico.gsi.de/event/4759/session/14/contribution/137/material/slides/0.pdf

Status of RICH magnetic shield simulations

E. Ovcharenko[1,2] *and C. Höhne*[1,3]

[1]II. Physikalisches Institut, Justus-Liebig-Universität Gießen, Gießen, Germany; [2]LIT JINR, Dubna, Russia; [3]GSI, Darmstadt, Germany

Magnetic field simulations are being performed with the major aim being a reduction of the stray field in the area of the RICH photosensitive camera down to below 1 mT. This value is given by the operating conditions of the photomultipliers and it has been obtained using dedicated studies in the lab [1].

Two approaches aiming at a stray field suppression exist which, according to our current considerations, will be used simultaneously. First, the field clamp of the magnet reduces the field and its structure and shape can be optimized. Second, an additional RICH magnetic shielding box has to be positioned around the camera to further suppress the field.

Results of stray field simulations are known to be realistic within approx. 30% margin. An additional safety factor has to be considered, the final value still being under discussion. As results might differ depending on simulation software and exact material definitions, all results were evaluated with respect to the reference from the magnet TDR.

Field clamp The effect of the magnetic field clamp on the stray field in the RICH photosensitive camera area has been studied.

The reference model features a solid steel 190mm-thick field clamp proposed in the magnet TDR. For this model the vertical component B_y of the stray field in the lateral vertical ZY plane in the lowest point of the camera is approx. 6 mT.

Different geometries and material compositions have been simulated using ANSYS Maxwell 19.2. All three spacial symmetries of the magnet were used, thus leaving 1/8 of the magnet in the simulation model.

Several different field clamp configurations have been simulated. In the "layered" configuration the field clamp is composed of three layers: 90 mm steel, 40 mm air, 60 mm steel. Configurations connecting upper and lower field clamps were studied as well. Typical variations of the resulting field in the region of the lower border of the PMT plane are about $\pm$ 1 mT only.

RICH shielding box The possibility to suppress the stray field in the area of the RICH camera using a shielding box has been studied conceptually in the past ([2, 3]), resulting in a design providing safe suppression. However that design was not realistic from the manufacturing point of view, not acceptable due to its large weight (approx. 1700 kg each), posing tough constrains in the RICH box mechanical design. It also spoiled the RICH performance by introducing a lot of material in the geometrical acceptance.

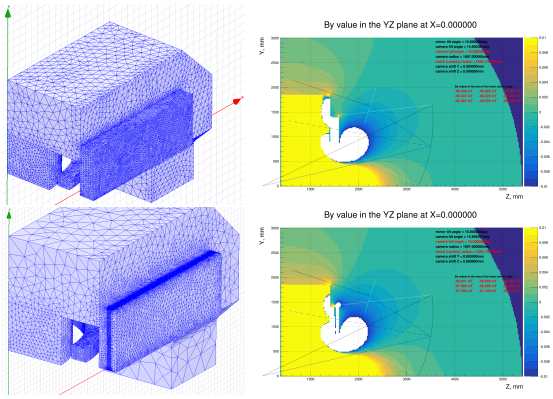

Figure 1: "Original" and "layered" field clamp designs and their simulation results.

The most recent shielding box design (fig. 2) is made from simple plates and weights about 1000 kg. It provides stray field suppression down to below 1 mT which is already close to the design value. Further shape optimization will be performed.

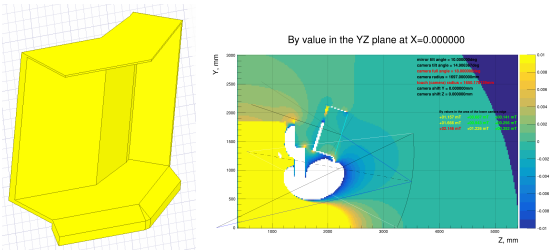

Figure 2: Current shielding box design and simulation results. The B_y component of the stray field in the lateral plane is suppressed below 1 mT.

References

[1] C. Pauly et al., "Single-photon and magnetic field measurements on H8500 MAPMTs", CBM Progress Report 2010, p.26.

[2] E. Ovcharenko et al., "Development of the magnetic shielding box for the CBM RICH camera", CBM Progress Report 2015, p.53

[3] P. Akishin et al., "Design of a shielding box for the CBM RICH Camera", CBM Progress Report 2017, p.54

Event reconstruction of free-streaming data for the RICH detector

S. Lebedev[1,2] *and C. Höhne*[1,3]

[1]Justus Liebig University Giessen, Giessen, Germany; [2]LIT JINR, Dubna, Russia; [3]GSI, Darmstadt, Germany

The CBM experiment will work in a triggerless mode: data received from the detectors are not associated with events. All raw data within a given time period are collected continuously in containers, so-called time-slices. The reconstruction algorithms take time-slices as input.

In the simulation the start time of an individual event is generated using the Poisson process. A time stamp of a RICH hit is the sum of the event time, the time of flight from the collision point to the detector, and a measurement error of the detector. For the Cherenkov photons originating from signal $e^{\pm}$ the time of flight until the photon detector plane equals to around 19 ns and is almost the same for all photons. The time resolution of the photon detector was obtained after several lab and in-beam tests and is expected to be less then 1 ns. In the simulation each RICH hit time is smeared according to a Gaussian distribution with $\sigma = 1$ ns. The dark noise of individual pixels is set to 1 kHz. One can see these noise hits (light blue color) in Figure 1. The event correlated noise depends on the event multiplicity (5 noise hits / MC RICH point / pixel / second). The pixel dead time is set to 50 ns.

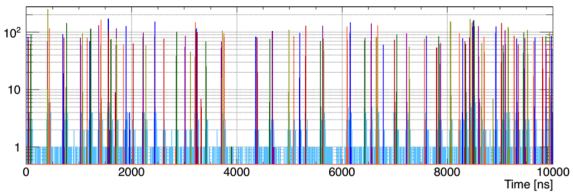

Figure 1: Distribution of the number of RICH hits in time (UrQMD Au-Au minimum bias, 8 AGeV, 10 MHz). Each color corresponds to an individual event. Light blue color corresponds to the noise hits.

The developed ring recognition algorithm is an updated version of the algorithm which works in the event-by-event mode. The ring reconstruction begins with the ring-candidate search which is based on the Hough Transform where hit triplets are combined. Instead of combining all possible hit triplets in the whole photon detector plane, only hits within a predefined local area around the initial hit are selected and additionally only hits within 3σ (detector time resolution: 1 ns) time window are selected. Thus the triplets are build only for a small fraction of selected hits which makes the whole procedure very fast. For each triplet the corresponding ring parameters (X, Y, R) are calculated and Hough histograms are filled. Analyzing the peaks in the histograms one either accepts the ring-candidates or rejects them. In the next step the ring-candidate array is filtered using an artificial neural network in order to reject all fake ring-candidates which are formed by random combinations of hits. For all found rings the time measurement is calculated as the average time of all hits belonging to the ring.

The implemented algorithm was tested in simulation studies performed for UrQMD Au-Au minimum bias collisions at 8 AGeV beam energy assuming 10 MHz interaction rate (IR). In addition 5 e^+ and 5 e^- were embedded into each UrQMD event at the primary vertex. The initial distribution of RICH hits and reconstructed rings in time is shown in Figure 2. The reconstructed rings clearly represent groups, corresponding to events. The ring reconstruction efficiency integrated over the momentum range from 0 – 12 GeV/c is 96.5% for primary $e^{\pm}$ and 97.7% for the reference set, i.e. for rings with at least 15 hits (see Figure 3 left). The performance of the ring reconstruction algorithm does not depend on the IR and is the same as the event-by-event reconstruction performance (see Figure 3 right). To summarize, a time-based reconstruction for the RICH detector was developed and shows good performance in the simulation studies.

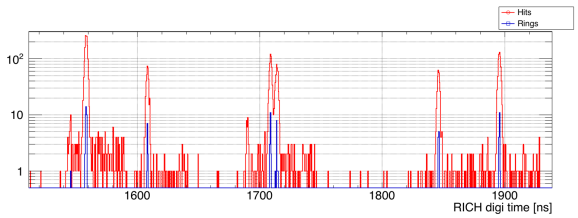

Figure 2: Distribution of the number of RICH hits (red) in time and the number of reconstructed rings (blue) in time.

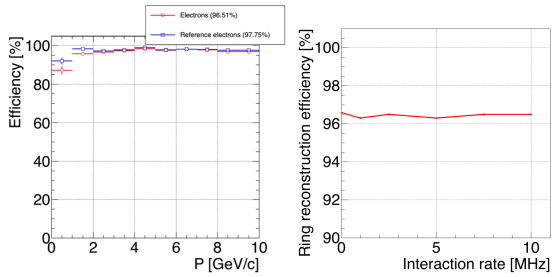

Figure 3: Ring reconstruction efficiency. Left: in dependence on momentum. Right: in dependence on IR. "Zero" IR corresponds to the event-by-event mode.

Final report on MAPMT delivery and series testing

J. Förtsch, D. Pfeifer, C. Pauly, V. Patel, and K.-H. Kampert
Bergische Universität Wuppertal, Germany

To cover the photo-detection plane of the CBM-RICH detector, 1100 HAMAMATSU H12700 MAPMTs were ordered by GSI in Summer 2015. The delivery starting in November 2015 did consist of 50 delivered MAPMTs each month. In 2018 all MAPMTs were delivered and tested with a test bench specifically built to characterize each 64 ch MAPMT (see [1]). Characterizing each MAPMT gives the unique opportunity to not only check for selection criteria (see [2]) but rather group all MAPMTs into gain categories. These gain categories serve the purpose to ensure a homogeneous distribution of groups of six MAPMTs, with common HV-supply, over the detection plane. The necessity to sort by gain is shown in figure 1. Here one sees the large spread in gain for all measured MAPMTs varying by a factor of ~ 4.5. To average out the gain differences also a gain over HV scan is made, where the gain is measured for different HV settings. Knowing the dependence of the gain on the high voltage and the gain for each individual pixel allows to optimize the grouping of MAPMTs and their respective HV setting. The procedure to average out the different gains was used already for the HADES experiment at GSI which uses the same H12700 MAPMTs and is described in [3].

Other very descriptive stats of the MAPMT are the Efficiency-Index,the Dark rate and the Skewness. The Efficiency-Index is the average efficiency of each MAPMT divided by the average Efficiency of the reference MAPMT being of same type. The Dark rate is the rate measured without illumination after at least 9 h of storage in darkness. The Skewness is the average efficiency of each MAPMTs left side divided by the average efficiency on its right side. This measure is describing the H12700 MAPMTs main reason for inhomogeneity. The average measurement results of all these measures are compiled in table 1. The average values and coefficient variations shown there clearly tell, that the Gain and Dark rate have a large variation, whereas Efficiency-Index and Skeweness do not vary strongly for the measured MAPMTs. Over the whole time of production the produced MAPMTs did show some trends regarding their characteristics which are compiled in [4].

From all measured MAPMTs, 19 MAPMTs were successfully reclaimed, failing the selection criteria. This follows the trend described in [4], that the number of reclaimable MAPMTs did decrease over time, although apart of Dark rate no overall improvement of the MAPMT's key characteristics could be observed.

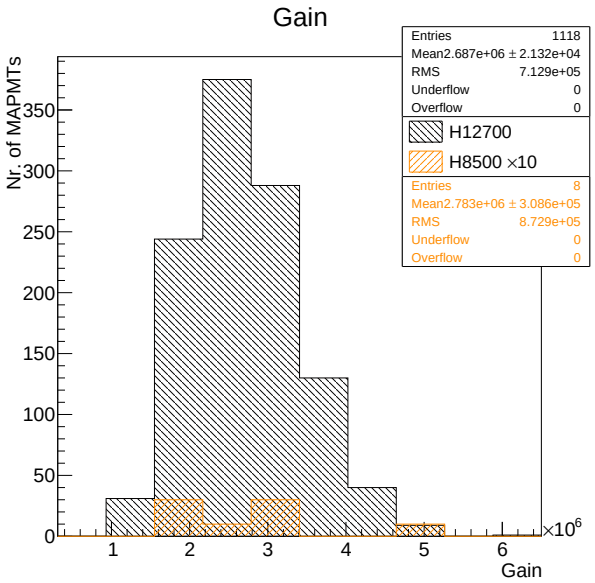

Figure 1: Average gain over all pixels of all measured 1119 MAPMTs excluding the reference MAPMT for a high voltage of -1000 V. Orange histogram shows the HAMAMATSU H8500 64 ch MAPMT for comparison.

Table 1: Characteristics of all measured 1119 MAPMTs (excluding the reference MAPMT)

Measure with systematic errors	avg. value	range of measured values
Efficiency-Index (± 0.027)	0.9711	$0.81 - -1.17$
Gain $\times 10^6$ ($\pm 0.025 \times 10^6$)	2.687	$1.3 - -6.2$
Dark rate (± 0.376) in kHz	1.056	$0.056 - -6.08$
Skewness (± 0.013)	0.9591	$0.76 - -1.23$

References

[1] J. Förtsch et al., Development of a MAPMT test stand and first results, CBM Progress Report 2015, Darmstadt 2016, p.58

[2] J. Eschke et al., Ordering of 1100 MAPMTs H12700 for the CBM-RICH photon detector, CBM Progress Report 2015, Darmstadt 2016, p.57

[3] C. Pauly et al., HADES, this report

[4] J. Förtsch et al., Status of MAPMT delivery and series testing, CBM Progress Report 2017, Darmstadt 2017, p.58

Quantification of mirror rotations with the CLAM method for the CBM RICH detector

J. Bendarouach and C. Höhne
Justus Liebig University, Gießen

A crucial aspect to guarantee optimal performance of the CBM RICH detector is the alignment of the 80 trapezoidal mirror tiles the reflecting mirror wall is made of.

A correction cycle was specifically developed for the CBM RICH to allow a proper operation of the detector under mirror misalignments [1, 2]. It employs two methods. The first one, inspired from the CLAM method of the COMPASS experiment, uses a dedicated hardware system to quickly detect mirror misalignments [3, 4]. The other technique comes from the HERA-B experiment and was implemented on the CbmRoot software. It uses collected data to quantify misalignments of each individual mirror tile [5, 6, 7].

In addition to its quick mirror alignment check, the CLAM method can also be employed to quantify mirror rotations. This allows a cross check with the information obtained from the software technique. To do so a prior laboratory calibration is required and needs to be conducted on each mirror tile.

Mirrors are previously aligned and a reference picture of the mirror wall is taken. On this picture an unbroken grid of retroreflective stripes is observed (Figure 1a). A rotation is then applied on one mirror tile and another picture of the mirror wall is taken (Figure 1b). On this picture, stripes now appear broken at the edges of the rotated tile. This picture is subsequently subtracted from the reference one. A threshold is applied on the resulting picture to facilitate the measurement of the visible bands of pixels (Figure 2a).

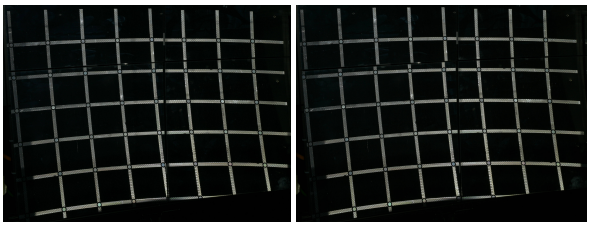

(a) (b)

Figure 1: Left: 4 mirror test set-up after initial alignment and used as reference picture. Right: Lower left mirror rotated by 3 mrad around its horizontal axis. The grid appears broken at the edges of the rotated mirror.

The laboratory calibration consists in establishing a relation between a given mirror rotation and the induced width of the pixel bands obtained on the threshold picture. It needs to be carried out on all mirrors, for both rotation axes and in both rotation directions. For a rotation around the vertical axis, the 4 chosen measurement rows are illustrated on Figure 2a. A linear relation between mirror rotation and band width was found for all mirror tiles of the 4 mirror test set-up. Figure 2b shows the band widths obtained on the second measurement row for several vertical mirror rotations.

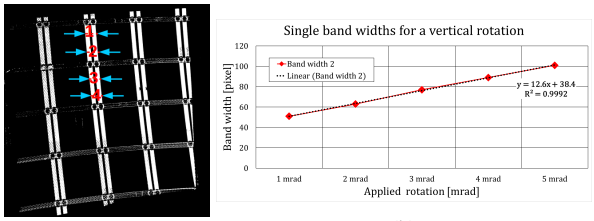

(a) (b)

Figure 2: Left: Picture obtained after subtracting the reference and rotated pictures and after applying a threshold. Right: Width of the band number 2 for vertical rotations ranging from 0 to 5 mrad (red line) and linear fit (dashed black). Similar results are obtained for all 4 bands.

The set-up employed during the laboratory calibration reproduced the one used during a previous test beam at CERN, although not being exactly the same because of the transport back to Giessen [3]. From the pictures taken at CERN, mirror rotations were computed using the described calibration. For a vertical rotation by 1, 2 and 4 mrad, rotations of 1.02, 2.36 and 4.11 mrad were calculated. The method was also tested for a mirror rotated by 4 mrad around its horizontal and vertical axes simultaneously. In this case, rotations of 4.57 mrad around the horizontal axis and 4.07 mrad around the vertical axis were obtained.

References

[1] J. Bendarouach et al., CBM Progress Report 2017, p.59

[2] J. Adamczewski-Musch et al., NIMA (2019) https://doi.org/10.1016/j.nima.2019.01.026

[3] J. Bendarouach et al., CBM Progress Report 2014, p.56

[4] J. Bendarouach (CBM Collab.) J. Phys.: Conf. Ser. 742 2016 012007 http://dx.doi.org/10.1088/1742-6596/742/1/012007

[5] J. Bendarouach et al., CBM Progress Report 2015, p.62

[6] J. Bendarouach et al., CBM Progress Report 2016, p.68

[7] J. Adamczewski-Musch et al., NIMA 876 (2017) 119

Muon Detection System

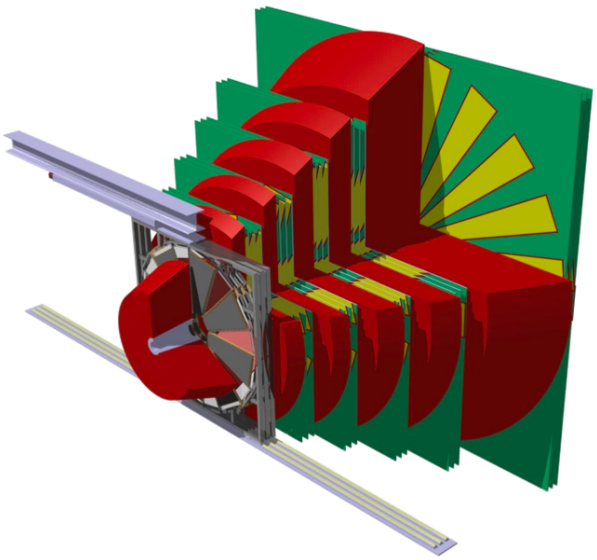

Myon System – Summary

S. Chattopadhyay, A. Dubey, and the CBM MUCH working group
Variable Energy Cyclotron Centre, Kolkata, India

In 2018, significant progress has been made on various areas of MUCH, a few of which are described in somedetail as contributions to the present CBM report.

1. GEM chamber development: Two GEM chambers of dimensions suitable for 1^{st} MUCH station have been installed in the mCBM setup. The chambers were operated using MUCH-XYTER based readout and full DAQ in the mCBM setup in December 2018. As a startup, only one FEB was used to take data. The quality of data have been demonstrated by the clearly observed spill structure and time correlations between MUCH and other detector in the setup. The setup used Low Voltage Distribution Board (LVDB) developed at VECC and opto-coupler-based High Voltage distribution for the first time.

2. RPC development: R&D on high rate RPC is a part of our effort to find a detector technology suitable for 3rd and 4th stations of MUCH. The peak particle rate on these two stations are 15 KHz/cm^2 and 4 KHz/cm^2 respectively. After detailed discussions at the Falta CBM-India meeting, it was decided to explore the possibility of low gain operation of RPC and use of MUCH-XYTER as readout. This will help to have a uniform readout system for the entire MUCH. In this direction, R&D have been reported from VECC, BI and NISER. VECC has reported operation of ALICE muon-trigger RPC with MUCH-XYTER readout. As a first step, the chamber (30cm x 30cm) was coupled with charge-sensitive preamplifier giving $> 95\%$ efficiency with cosmic muons. The chamber was then tested at the GIF++ facility using MUCHXYTER board. The results show that the chamber can be operated with $> 90\%$ efficiency at 9.2 kV and incident muon rate $> 1Kz/cm^2$. Even though efficiency has been found to reduce with photon flux, however, the hit rate at which efficiency is 90% is about 300 kHz/strip. The test shows that the chamber can comfortably be used for the 4th station and the possibility of using it in the 3rd station is reasonably high. In NISER, a single-gap RPC has been built and tested and compared with detailed simulation. At BI, a new low resistivity material has been used to build RPC, however, the efficiency does not rise above 60% before the start of discharge.

3. Simulation: Dedicated simulations are being done for estimating the response after implementation of most realistic MUCH geometry. It has been reported to have Al cooling plate implemented and the signal to background ratio was found to remain unaffected. Digitization for RPC has been implemented in 3rd and 4th stations but a significant lowering of efficiency is observed. The results are being looked into in further details. On analysis front, a method has been developed to subtract the combinatorial background that has been used to extract omega signals.

4. On the hardware front, significant efforts are made on control systems for LV, HV, pressure, humidity. These FPGA-based system is built in such a way that the system is fault-tolerant and radiation resistant. At VECC, detailed investigations have been done on MUCH-XYTER eg., automatic calibration system and reading of a GEM chamber to obtain Fe55 spectra.

5. R&D efforts have been reported on straw tube eg, fabrication of rectangular straw tube (50cm x 50cm), its long term stability and development of a new readout system for straw.

Installation, commissioning and testing of mMUCH modules in the mCBM experiment

A. Kumar[1,2], *A. K. Dubey*[1], *J. Saini*[1], *C. Ghosh*[1], *V. Negi*[1], *S. Chattopadhyay*[1], *and S. K. Prasad*[3]
[1]Variable Energy Cyclotron Centre, Kolkata, India; [2]HBNI, Mumbai, India; [3]Bose Institute, Kolkata, India

The mCBM (mini-CBM) experiment is designed to facilitate a long run test of all the detector subsystems of CBM namely, the STS, MUCH, TRD, TOF, etc. It would also be a continuous testing ground for the DAQ system, long distance data transport and for online and offline software. In this contribution, we report the installation, commissioning and testing of mMUCH modules with Ag+Au collision at SIS18 facility. The schematic of the test setup including all the detector subsystem (mSTS, mMUCH and mTOF) is shown in the Fig.1. Detectors were placed ∼25° from the beam axis. The mMUCH subsystem consisted of two real-size triple GEM modules, that were fabricated with final design parameters. These were locally tested with radioactive sources before installation. Several components of the mMUCH GEM modules were being implemented and tested for the first time which included the use of first version of MUCH-XYTER for readout, use of a novel opto-coupler based HV biasing of GEM foil-segments, use of Common Readout Board (CROB) based DAQ and an elaborate Low Voltage Distribution Board (LVDB) for powering of FEBs, opto-couplers, etc. The first GEM module (GEM1) was positioned at ∼ 128 cm from the target and the other at ∼ 150 cm on the beam-table. Consisting of ∼1900 pads, these have progressively increasing dimensions starting from ∼3 mm in the inner (narrow portion of the trapezoid) region to about ∼17 mm in the outermost region.

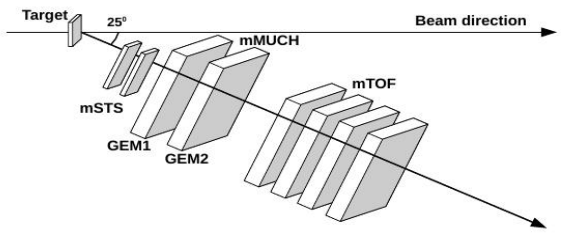

Figure 1: Schematic of the detector setup inside mCBM cave

The picture of the modules installed in the HTD cave of SIS18 beamline is shown in the Fig.2. Each module consisted of 18 Front End Boards (FEBs), and these were powered via LVDB boards developed at VECC. CROB boards (Common Readout Board) were positioned close to the modules. The active area of each module was ∼1900 cm^2. A gap configuration 3-2-2-2 was used for the three GEM layers inside the detector. The top surface of each GEM foil has 24 segments. A ceramic resistive chain providing asymmetric voltages to each GEM layers was used for each half of the detector, thus powering 12 segments. Each

Figure 2: Picture of the detector installed inside mCBM cave. Viewing downstream(left) and upstream(right)

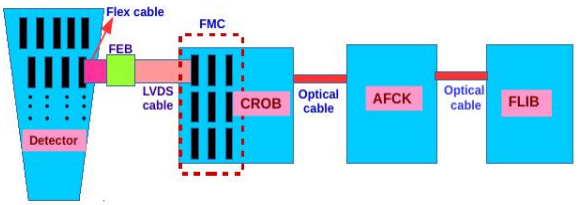

Figure 3: Block diagram of data acquisition system

of these foil segments was connected to the respective resistive chain via optocouplers[1,2]. Thin Alumina sheets were glued on the ceramic resistors to enhance air-cooling. A premixed gas cylinder with Ar/CO(70/30) provided the operating gas-mixture. The schematic of the DAQ for mMUCH is shown in the Fig. 3. The detector was mounted on Al-cooling plate having cut-out slots for every readout connector. Water cooling through 6-mm diameter Al-pipe spiralling inside 6 mm of the two half-plates of Aluminium joined together was used for the FEE boards. The boards were screw-fixed on the other side of the plate. A 3 mm Cu-square provided the cooling contact. Flexible Kapton cables of 10 cm length (ref. Fig. 2) was used to connect the FEBs to the detector. A flat LVDS (Low Voltage Distribution Signal) cable was connected from FEBs to the FMC connector of CROB. An optical cable of ∼63 m (multi-mode) length was used from CROB to AFCK (Data Processing Board) board, placed inside DAQ room. Combined data from all the subsystem was transported to the Green Cube (Computing Node) of GSI via optical cables of length ∼310 m (single mode).

The mMUCH detector was commissioned with data collected from GEM1 module and using one FEB only. The 128 channels spanned an area of ∼ 42 cm^2. An Ag 45+ beam with varying intensity (10^6 sec^{-1} to 10^8sec^{-1}) was incident on Au target of thickness 2.5 mm. The spill structure as obtained from the GEM hits with time (in 10

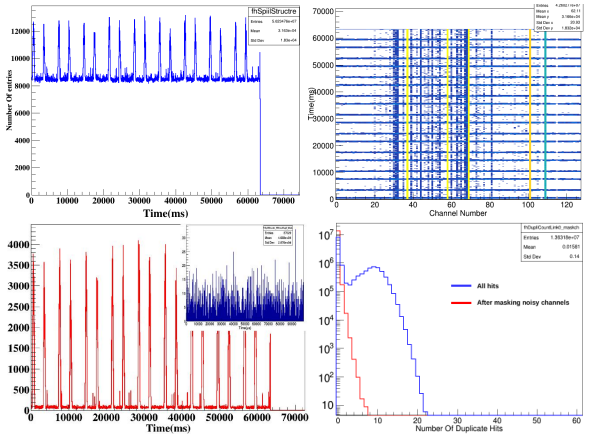

Figure 4: Top Left: Spill structure plot for all hits from one FEB (in 10 ms bins). Top Right: Variation of duplicate hits time with the channel number. Bottom Left: Spill structure after removing duplicate hits and noisy channels and the inset is for 1μs bin size. Bottom Right: Distribution of consecutive duplicate hits

ms bins), is shown in Fig.4 (top left). A spill length of ∼700 ms is observed. Two consecutive spills are seen to be separated by ∼2300 ms or ∼3400 ms. Owing to an stsXYTER-chip bug, a large number of duplicate hits bearing identical time-stamps and channel numbers were observed in data. This contributed to the online spill structure. The distribution of these duplicate hits time with channel number is shown in Fig.4 (top right). A few of the channels is seen to be very noisy, while others fire mostly during on-spill. The distribution of the total number of consecutive duplicate hits is shown in Fig.4 (bottom right), the blue colour being for all hits, and the red color after removing the noisy channels. The spill structure in 10 ms bin size, after filtering the duplicate hits and noisy channels is shown in Fig. 4 (bottom left). In the inset is shown the spill structure in finer time-bin(1μs), which reveals the substructure in the beam. The time correlation spectra from detector between one channel to another channel within a FEB is shown in Fig. 7 (left). The correlation spectra peaks around ∼0 ns which is expected. The time correlation spectra between GEM and one of the TOF detector in time slice is shown in Fig. 7 (right). Fig. 5 (left) shows the pulse height spectra from the detector. The average particle rate as calculated from the spill structure by integrating the spill count (after all filtering) divided by the spill-time and detector area, comes out to be ∼4.2 kHz cm^{-2}. This is underestimated as there are sub-structures in the beam, and the actual instantaneous rates are higher.A consecutive hit time distribution for any particular channel and fitted to an exponential function, as shown in Fig. 5 (right) gives a better estimate of the incident particle rate on the detector. The average value thus calculated for every channel in the FEB, is shown in Fig. 6. The dimensions of the pads vary from ∼5.20 mm to ∼6.17 mm.

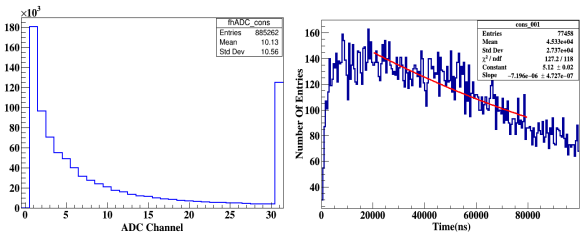

Figure 5: Left: Distribution of pulse height histogram. Right: Consecutive time difference distribution for one channel (channel 2)

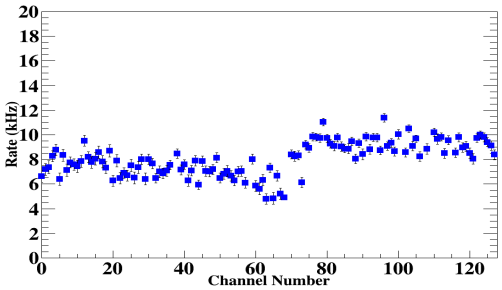

Figure 6: Rate (kHz) for each channel of MUCH-XYTER

$$R = N_B N_A \rho \frac{d}{A} \sigma \quad (1)$$

The event rate for Ag + Au collisions at beam intensity of 10^7sec^{-1} has been calculated using equation (1) and it comes out ∼7.5 x 10^5sec^{-1}. Where N_B is the beam particles/s, N_A is Avagadro number, ρ is the density, d is thickness and A is atomic mass number of the target, and σ is the cross-section. CBMROOT simulations with the actual test setup was carried out. The average number of particle per event falling on the GEM1 acceptance is ∼4.542. The particle rate (taking into account the event rate and area of the detector) from simulation comes out ∼1.793 kHz cm^{-2}.

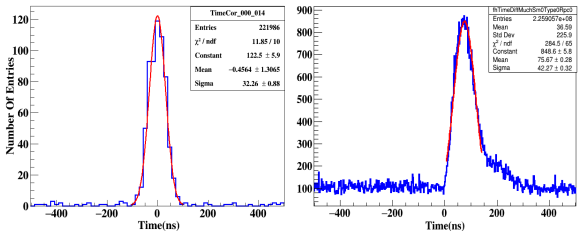

Figure 7: Left: Time difference spectra between one channel to another channel within one FEB. Time difference spectra between GEM and one of the RPC detector (run 48)

In summary, we tested the GEM detector with Ag + Au collision and estimated the particle rate. Simulation has been performed to verify the results. Detailed data analysis and simulation is under process. We want to thank GSI colleagues for their help and support during the entire beam time.

References

[1] http://sympnp.org/proceedings/61/G69.pdf
[2] http://sympnp.org/proceedings/61/G30.pdf

Fabrication of Mv2 module for mCBM experiment and first test with optocoupler based HV biasing

A. Kumar[1,2], *A. K. Dubey*[1], *J. Saini*[1], *V. Negi*[1], *and S. Chattopadhyay*[1]
[1]Variable Energy Cyclotron Centre, Kolkata, India; [2]HBNI, Mumbai, India

GEM (Gas Electron Multiplier) based detector technology will be used for the first two stations of MUCH (Muon Chamber). Fabrication of large size triple GEM module with realistic design (Mv1) for the first station of CBM-MUCH using NS-2 (glue-less) technique has been already discussed in the report[1]. In the present report, we discuss the fabrication of Mv2 module and its test (with X-ray) with new optocoupler based HV biasing. The main difference between old design and the new design is the gap configuration and the HV biasing scheme, while the size of the active area being only slightly different. The gap configuration for Mv1 was 3-1-1-1.5 mm, and Mv2 is 3-2-2-2 mm. A larger gap greatly reduces the mechanical sagging effects. A ceramic resistive divider has been used to power the GEM foils. Such customised ceramic dividers are also used by various GEM detector groups in the world.

While for Mv1 design, a single resistive chain was used to power all the 24 segments in GEM foil, for the new layout (Mv2), each segment has independent connection. One of the main challenges in operating large size triple GEM detectors is how to handle the segments which may develop shorts (for whatever reasons), especially during long term operation. The research on this aspect is ongoing. For our Mv2 case, we have adopted and designed an optocoupler based HV bias to serve this purpose. The advantage of such a scheme is that any problematic segment can easily be isolated, whenever required.

Having all the 24 segments of the triple GEM powered individually means routing 72+3=75 such HV lines on the PCB surface. HV lines were etched on the outer plane of the drift PCB, and the connection to the foil-segments was maintained using spring contacts. In this respect, the drift board design of Mv2 was completely different as compared to Mv1 case. Each of these HV lines coming from the foil was then connected to the resistive chain via an optocoupler as shown in the Fig.1 (left) and the zoomed picture of the optocoupler & its control is shown in the Fig.1 (right). The idea is that during normal operation, the switches for controlling optocouplers will be on, allowing the voltages to be relayed to the corresponding GEM segments. And during the operation, say at some point the branch current shows an abnormally high current (quite higher than the pulsed current), then this would possibly indicate the occurrence of a problematic segment. On careful and iterative debugging, the appropriate optocoupler will be switched off restoring the detector to stable condition. Development of FPGA based control system for controlling optocoupler is under process.

The fabrication of the chamber is shown in Fig.2 (a to d). The readout consists of pads with progressively increasing pad sizes from ∼3mm to ∼17mm, shown in the Fig.2(a) and the picture of the segmented GEM foil and its leakage current test is shown in the Fig.2 (b). After testing the GEM foils, we place the foils together with a gap of 2 mm, which is shown in Fig.2(c). Fig.2(d) shows all the assembled foils stacked together inside the edge frame.

Two such real-size (∼80 cm x ∼ 40 cm) trapezoidal shaped triple GEM chambers using NS-2(glue-less) technique were fabricated and tested with the Fe^{55} source at VECC. These modules were installed in the mCBM[3] experiment at GSI. Fig.3(a) shows the test setup at VECC. The Fe^{55} spectra obtained from this detector is shown in Fig.3(b).

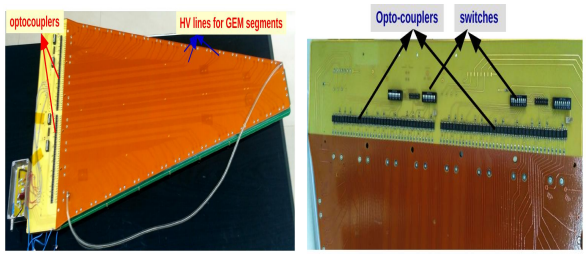

Figure 1: Left: Drift PCB and HV layout. Right: Zoomed picture of optocouplers

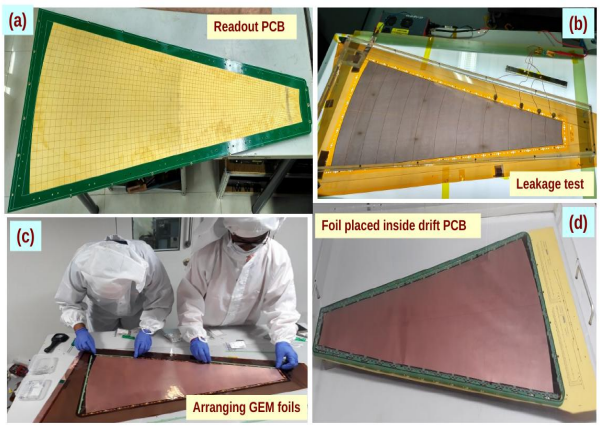

Figure 2: a) Picture of large size readout PCB. b) Picture of GEM foil and leakage test. c) Placing GEM foils with a gap of 2mm. d) Stack of GEM foils placed inside the drift PCB. Thanks to CPDA lab of VECC for providing a clean room.

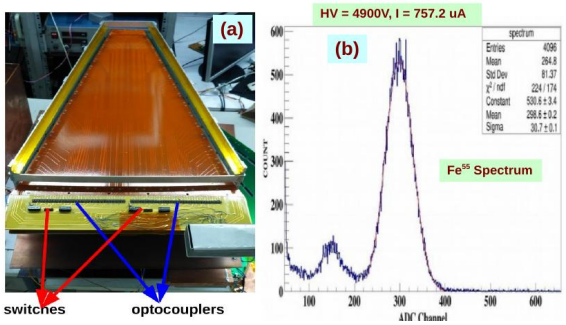

Figure 3: a) Test setup at VECC lab b) Fe^{55} spectrum

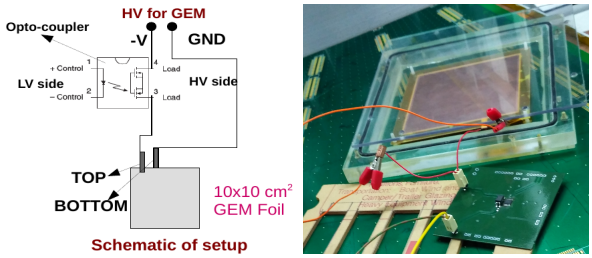

Figure 4: Left: Schematic of test setup for optocoupler Right: Picture of the test setup in lab

Test with opto-couplers

These components should be tested for its radiation hardness, stability towards sparks in the GEM foil, short segment and its effect on detector gain before the use in final design. The radiation hardness test of these optocoupler has been already reported[4]. Here we discuss the other tests.

Short segment test

To mimic the effect of a short-segment, we manually shorted one of the segments of the GEM foil and tested the operation of optocouplers. At HV = 4550V branch current I = 688μA at normal condition. After shorting one of the segments, the current increased to 754 μA. We switched off the optocoupler for the corresponding segment and observed that the current restored to its normal value (I = 688 μA). In this way, we will be able to isolate the faulty segments of GEM foil.

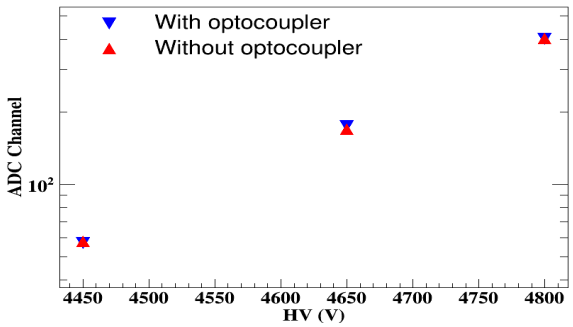

Figure 5: Variation of photo-peak ADC channel with high voltage

Effect of sparks in GEM foil on opto-couplers

Gas detectors are prone to sparks. So we need to test the stability of these optocoupler devices towards the sparks in GEMs. The schematic and picture of the experimental setup are shown in Fig.4. We used a single 10 cm x10 cm GEM foil for the test. The high voltage to the GEM foils has been given through optocoupler, and the number of sparks has been measured for a given period. The GEM voltages and the number of sparks are summarised in Table.1. The leakage current of optocoupler before and after the spark test was measured and the current in both the cases was found to be similar ($\sim$3nA at 600 V), implying no change in the optocoupler properties. For the triple GEM detector, the operating GEM voltages are $\sim$100 V lower as compared to that applied in these tests with single GEM. So the number of sparks should also be less. This test validates the robustness of the optocouplers towards sparks.

Table 1: Table for sparks test of opto-coupler

ΔV_{GEM}(V)	Time (min)	No. of sparks
530	35	22
550	178	48
570	200	45
590	153	260

Gain of detector with and without opto-couplers

Another important parameter is to study the effect of optocoupler on the detector gain. A 10 cm x 10 cm triple GEM detector was used for this study. The photo-peak position from Fe^{55} spectra for with and without optocoupler configuration has been measured, for three different GEM voltages, as shown in Fig.5. The two gains remain identical as observed from the figure.

In summary, we have assembled and tested (with Fe^{55}, X-ray source) two large size triple GEM modules with optocoupler based new biasing scheme. Robustness against sparks and no adverse effect on detector gain has been demonstrated. Further operational performance and issues with this new biasing scheme will be known from the ongoing mCBM tests.

References

[1] CBM Progress Report 2013, 2014.

[2] http://www.sympnp.org/proceedings/61/G30.pdf

[3] https://www.gsi.de/work/forschung/cbmnqm/cbm/activities/mcbm.htm

[4] CBM Progress Report 2017.

QA of GEM foils: Measuring hole dimensions and pitch

A. Agarwal[1,2], *A. Kumar*[1,2], *and A. K. Dubey*[1]
[1]Variable Energy Cyclotron Centre, Kolkata, India; [2]HBNI, Mumbai, India

GEM foils consists of a regular array of tiny holes of size $\sim$50μm with a pitch of about 140 μm spread accross its entire area. Measurement of geometrical parameters such as the hole-diameters and pitch, is necessary for assessing the quality of foil-production. Manual measurements of each such hole thorughout the foil will be extremely time consuming and just impossible. So as an alternative approach multiple high resolution images of the foil were taken and measurement done using software fits. Fig.1 shows the schematic picture of the real size trapezoidal GEM foil with several image-locations indicated. The images were taken using an optical microscope.

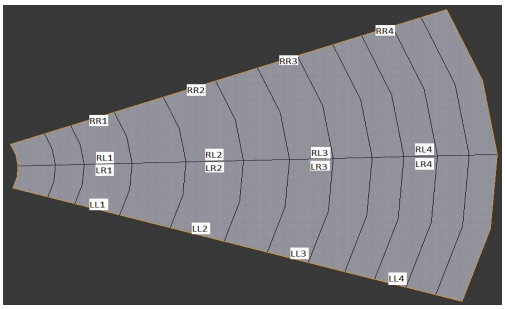

Figure 1: Different areas for which photos were taken (along with their codes)

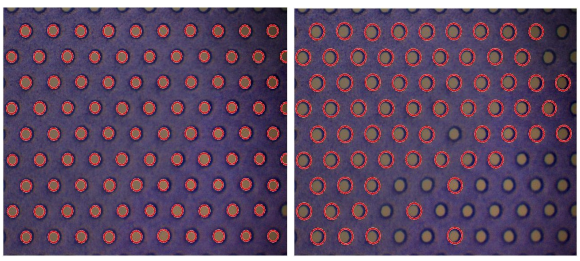

Figure 2: Left: MATLAB measurement of inner radii. Right: measuring outer radii

These images were processed using MATLAB circle-finding algorithm. This can separately identify the inner circles and outer circles as indicated in Fig.2(left and right, respectively), and give the respective radii and co-ordinates of the centres. These three data namely, inner radii, outer radii (in units of pixels) and co-ordinates of centres of the circles were saved. An image of a straight wire of known thickness was also taken for obtaining the appropriate calibration ratio in terms of μm/pixels. Using this calibration, these data were accordingly converted to dimensions in μm. A distribution of the inner and outer diameters and pitch measured at a particular position is shown in Fig.3.

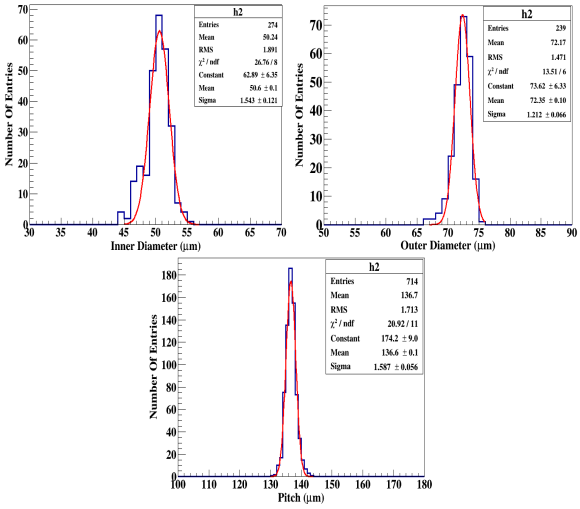

Figure 3: Top Left: Plot for inner diameter for LL1. Top Right: Plot for outer diameter for LL1 Bottom:Plot for pitch for LL1

Table 1:

Position	Inner Dia(μm)	Outer Dia(μm)	Pitch(μm)
LL1	50.24	72.17	136.7
LL2	50.25	72.17	136.7
LL3	51.17	75.08	136.6
LL4	51.63	74.05	136.7
LR1	51.28	73.03	136.7
LR2	52.65	73.88	136.7
LR3	52.70	75.47	136.7
LR4	53.22	79.00	136.7
RL1	52.01	75.24	136.6
RL2	52.25	75.24	136.7
RL3	52.40	77.77	136.6
RL4	53.07	no data	136.8
RR1	52.53	75.93	136.7
RR2	52.29	76.16	136.7
RR3	52.34	77.58	136.7
RR4	52.62	78.16	136.7

Figure 4: Different areas for which photos were taken (along with their codes)

For each position indicated in Fig.1, at least 3 photographs were taken with slight variation around indicated positions to increase the statistics of the number of holes scanned. After doing the necessary calculations, histograms for inner diameter, outer diameter and pitch were plotted. The corresponding means extracted from gaussian fits to the distribution, have been tabulated in Fig.4. The inner and outer diameters show slight variations from one end to the other, increasing along one of the principle diagonals of the foil (connecting LL1 to RR4). The pitch however is almost consistent throughout. Effect of systematics such as focusing, alignment, planarity etc. on these measurements is under study.

First GEM detector tests using MUCH-XYTER

C. Ghosh[1], *G. Sikder*[3], *A. Kumar*[1,2], *J. Saini*[1], *A.K. Dubey*[1], *and S. Chattopadhyay*[1]
[1]Variable Energy Cyclotron Centre, Kolkata, India; [2]Homi Bhabha National Institute, Anushaktinagar, Mumbai, India;
[3]University of Calcutta, Kolkata, India

nXYTER based self triggered readout electronics has so far, been the main electronics used for testing all our gem detector prototypes for Muon Chambers(MUCH). However, for the final experiment, a specially designed radiation hard ASIC called MUCH-XYTER will be used for reading out signals from the first two stations of MUCH. This ASIC has 128 analog front end channels with a dedicated 5-bit ADC per channel for processing the charge pulses from the GEM detector. It can accept both positive and negative charge with configurable e-link and each e-link has a maximum data transmission rate of 320 Mbps. For GEM detectors, we use the negative-pulse configuration. In this paper, we report the first test results of a 10 cm X 10 cm triple GEM detector, with a gap configuration of 3-2-2-2 mm, using the first version of MUCH-XYTER(v2.0) front end board(FEB). A ceramic resistive chain was used for powering the GEMs. The test setup at VECC is shown in Fig.1. It consists of the entire DAQ chain including the FEB, AFCK and FLIB (First level interface board).

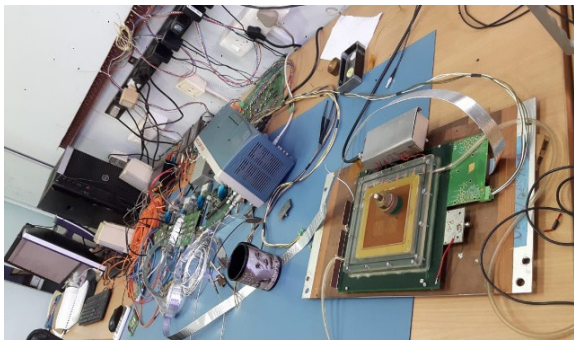

Figure 1: Experimental setup

The triple GEM detector was tested with X-rays from ^{55}Fe sources with Ar/CO2 (70/30) gas mixture. A typical pulse height spectra as obtained is shown in Fig.2. The 32 comparators corresponding to the 32 ADC channels in each of the 128 analog channels were calibrated from 6 fC to 81 fC with a step of 2.5 fC. The peak corresponds to the major X-ray peak of 5.9 keV from ^{55}Fe source. The spectra is rather wide as compared to those measured with nXYTER, as expected due to coarser ADC resolution. Hence, the argon escape peak is barely visible. Data were taken for varying range GEM voltages to study the gain variation. The detector gain has been obtained by extracting the number of electrons from the measured peak positions in fC(femto Coulombs) and then dividing it by the number of primaries. Fig 3 shows the variation of this detector gain with high

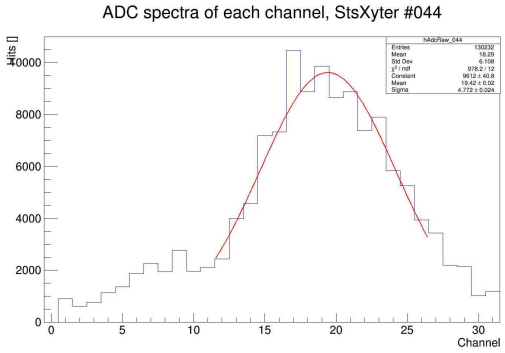

Figure 2: Fe55 ADC spectra at HV=4450V

voltage(HV).

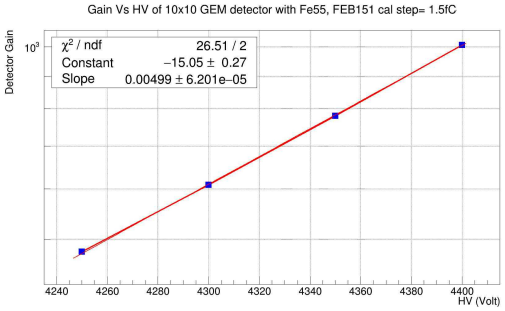

Figure 3: Gain vs HV at calibration step of 1.5 fC

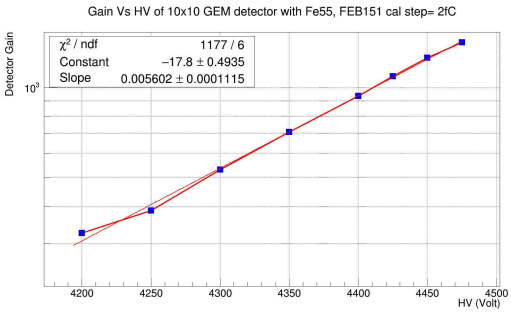

Figure 4: Gain vs HV at calibration step of 2 fC

The effect of calibration on detector gain has been studied by calibrating one FEB at three different sets of calibration steps namely, 1.5 fC, 2 fC and 2.5 fC, with the

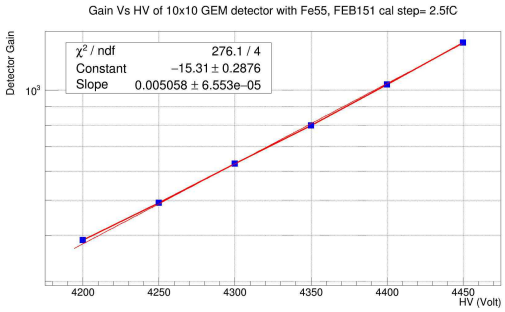

Figure 5: Gain vs HV at calibration step of 2.5 fC

threshold charge being set to 6 fC for all cases. For each of the cases, the detector charge corresponding to the peak position of the spectra was measured. It is observed that at any particular HV, the gain value for the three different calibration remains almost the same, confirming that the FEB reads correct charge from the detector irrespective of its calibration step. Fig 3, Fig 4 and Fig 5 show the gain vs HV spectra at 3 different calibration steps. Detector response from two different FEBs calibrated at the same bias settings was studied. It was observed that both the FEBs showed almost same pulse height characteristics for the same bias settings and same detector parameters, as evident from Fig 6 and Fig 7.

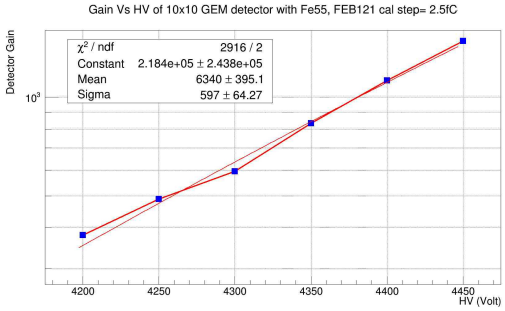

Figure 6: Gain vs HV of FEB no:121

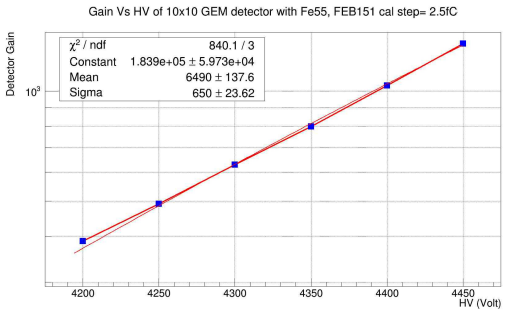

Figure 7: Gain vs HV of FEB no:151

Timing information using MUCH XYTER coupled to GEM detector has also been studied. For this, a coincidence test setup using two scintillators and a 10 cm x10 cm GEM detector sandwiched between them was carried out. A β source (^{90}Sr) was placed on top of one scintillator. The coincidence signals of the two scintillators was put into one channel of the MUCH-XYTER FEB, while signals from detector was acquired by another FEB. Both FEBs were connected to one AFCK, which is supposed to maintain the time synchronization. Fig 8 shows the preliminary results for the time correlation spectra measured at 4700 V. The sigma of this distribution seems to be of the order of 30 ns which is rather high compared to the previous results with nXYTER. The gain dependence study of this time correlation spectra is under progress.

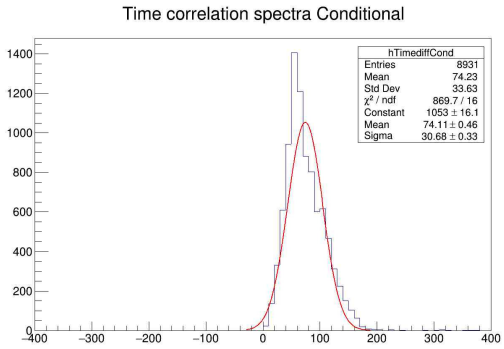

Figure 8: Time Correlation spectra

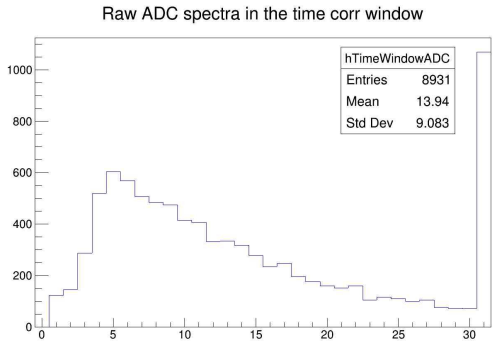

Figure 9: ADC spectra wihin 400 ns time window

On some occasions, two peaks were observed in the time correlation spectra. This is yet to be understood. One reason could be that the time synchronization gets disturbed during the course of data taking. Further investigation is on to address this issue. Fig 9 shows the pulse height spectra from all the channels combined for a time window of 400 ns after each scintillator trigger.

Feasibility of operating Resistive Plate Chambers in low charge production mode for their possible use in MuCh

A. Jash, V. K. S. Kashyap, and B. Mohanty
School of Physical Sciences, National Institute of Science Education and Research, HBNI, Jatni - 752050, Odisha, India

Introduction

The NISER group is involved in studying the feasibility of using Resistive Plate Chambers (RPCs) [1] in the 3rd and 4th stations of Muon Chambers (MuCh) in CBM [2]. The required particle rate handling capability for RPCs is about 15 kHz cm^{-2}. A standard RPC with 2 mm gas gap, low resistive electrodes ($\sim 10^{10}$ Ω cm) and operating in avalanche mode can handle a rate upto $\sim$1 kHz cm^{-2} with more than 90% efficiency [3, 4]. The RPC rate capability (RC) is given by [4] $RC = V/(\rho Q_{\rm m} t)$ where, ρ is the bulk resistivity of electrodes, t is their thickness, V is the voltage drop across the electrodes and $Q_{\rm m}$ is the mean produced charge in the gas gap. Lowering any or all of the parameters in the denominator of the relation can increase the rate capability of an RPC. Reduction of electrode resistivity or its thickness could have adverse effects such as increase in leakage current, ageing and reduced mechanical stability of the chambers. So, these parameters cannot be reduced to very low values. The best way to increase the rate capability would be to operate the detector in low charge production mode. Substituting $\rho = 3\times10^{10}$ Ω cm, $Q_{\rm m} = 100$ fC, $V = 10$ V and $t = 2$ mm, in the above relation, rate capability can be increased to $\sim$15 kHz cm^{-2}. We performed simulations and experiments on a glass RPC to find the conditions to operate it within desired limits using a gas mixture containing $C_2H_2F_4$, 4.5% i-C_4H_{10} and different fractions of SF_6 ranging from 0.0% to 2.0%.

Method

Simulation: GARFIELD++[5] has been used to simulate the current generated on the readout strip of RPC due to passage of 1000 muons, each of energy 2 GeV passing through the detector with randomly varying directions (zenith angle, $\theta = 5^\circ - 25^\circ$, azimuthal angle, $\phi = 0^\circ - 360^\circ$) corresponding to the acceptance of RPC in MuCh. An RPC of dimension 30 cm $\times$ 30 cm with 2 mm gas gap and 3 mm thick electrodes has been modeled. The electric field within the detector was calculated separately using COMSOL Multiphysics [6] and supplied manually to the simulation whereas, the primary ionization and transport properties of the electrons have been calculated using C++ versions of HEED [7] and Magboltz [8], respectively. The current signals generated by GARFIELD++ were then analyzed to obtain the charge and related parameters.

Experiment: A 30$\times$30 cm^2 glass RPC was sandwiched between two scintillators, each of size 8 cm $\times$ 8 cm in coincidence with one of the readout strips (2.8 cm $\times$ 30 cm) of RPC. The gas gap of the RPC is made of 3 mm thick glass electrodes ($\rho \sim 10^{12}$ Ω cm) separated by a gap of 2 mm using perspex spacers. Float glass for the electrodes were procured locally. The conductive coating on the electrodes has a surface resistivity of $\sim$250 k$\Omega/\square$. Foam based polycarbonate readout panels of thickness 5 mm are of area 30$\times$30 cm^2. They have strips of dimension 2.8$\times$30 cm^2 with a pitch of 2 mm. The coincident signals from the two scintillators (2-fold, 2F signal) was used as trigger to a 1 GHz oscilloscope (Teledyne LeCroy WaveSurfer 510) having 10 GS s^{-1} sampling rate. In presence of the 2F trigger, raw signals from the RPC were recorded after amplifying it 100 times using a NIM based fast amplifier (CAEN N979). Data was acquired for 2 hours for a fixed voltage setting and a fixed gas mixture. The voltage signal at each instant was divided by 50 Ω (characteristic impedance of the readout strip) and the amplification factor (100) to obtain the corresponding current values. The current signals were then analyzed to obtain the charge distribution and related characteristic parameters.

Analysis of RPC signals

Identical method has been followed to analyze the current signals induced on the RPC readout strip, as obtained from simulation and experiment to find the produced charge and detector efficiency. Each current signal was integrated within a 50 ns window to find the charge induced on the readout. A typical charge distribution obtained for 1000 events from simulation is shown in Fig. 1. To have

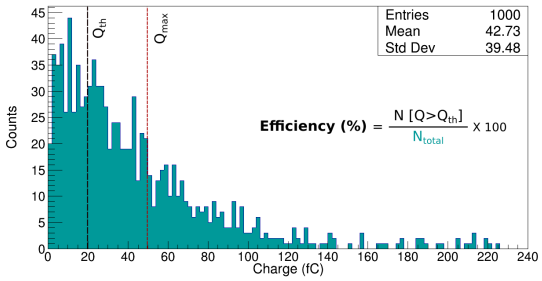

Figure 1: A typical charge distribution obtained from simulation and scheme of calculating the detector efficiency.

common electronics for the MuCh subsystem, XYTER [2] has been proposed for RPC frontend. It restricts the measurement of charge within a maximum value, $Q_{\rm max}$ (50 fC currently) above which it will not be able to retain the charge information. However, details of the signal such as

timing, and position information may still be available. By observing the traces recorded for all the pulses, we have used a voltage threshold of 30 mV on the average amplitude of the signals within the charge integration window to remove noise. A minimum threshold, $Q_{\rm th}$ on the produced charge can also be imposed to further suppress detector noise. Fig. 1 depicts the scheme to calculate the efficiency in crossing a charge threshold, $Q_{\rm th}$ (20 fC in figure). If $N_{\rm total}$ is the total number of 2F triggers among which $N_{\rm detect}$ is the number of events producing charge greater than $Q_{\rm th}$ then the ratio $\frac{N_{\rm detect}}{N_{\rm total}} \times 100$ gives the efficiency.

Results

The variation of mean charge produced within RPC gas gap with the applied field, as found from simulation is shown using a black dashed line in Fig. 2 for the gas mixture containing 0.3% SF_6 along with 4.5% i-C_4H_{10} and 95.2% $C_2H_2F_4$. To get the mean produced charge less than ($Q_{\rm max}$=) 100 fC the detector needs to be operated at a field of 39.58 kV cm^{-1} (HV$\sim$7.9 kV). The variation of detector efficiency in crossing different charge thresholds with the applied field is also shown in Fig. 2. Simulation assumes that the noise is completely suppressed and is an ideal case. In our experiment, value of $Q_{\rm th}$ =30 fC or higher depending on the noise level. Initial experimental

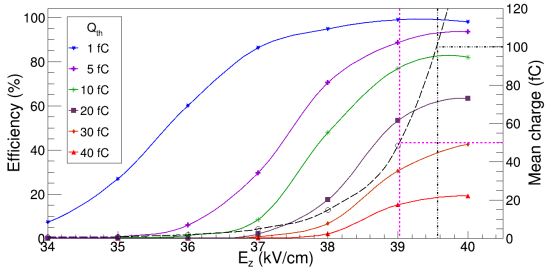

Figure 2: Simulated result on variation of RPC efficiency (solid lines) with the applied field with gas mixture containing 0.3% SF_6. The black dashed line shows the variation of mean charge.

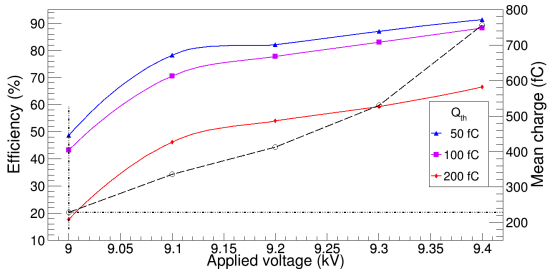

Figure 3: Experimental result on variation of RPC efficiency (solid lines) with the applied voltage for the gas mixture containing 0.3% SF_6. The black dashed line shows the variation of mean charge.

investigations have shown that it is difficult to operate the detector with mean charge production within 100 fC limit. Fig. 3 shows the variation of mean charge (black dashed line) with the applied voltage when the detector is operated with the standard gas mixture containing 0.3% SF_6. Mean produced charge is $\sim$220 fC even when the applied voltage is $\sim$9 kV. We could not proceed to lower voltages as RPC signals beyond the noise level of $\sim$ 30 mV were very less. Variation of detector efficiency is also shown in the same Fig. for different values of $Q_{\rm th}$. About 50% efficiency is achievable with $Q_{\rm th}$= 220 fC.

Conclusion & Outlook

Simulated results show that RPC in principle can be operated at charges as low as 50 fC by operating the detector at low voltage. The effect of detector noise or streamer fraction is not included in the current simulation. Experimentally, we find that it is rather difficult to operate the detector at the predicted voltages/fields unless (i) the noise level is kept at the lowest and (ii) electronics with lower noise and better amplification is used. Our, initial experimental results have shown that it is possible to operate the detector with a mean charge of 220 fC albeit with efficiency $\sim$50%. As an outlook, we plan to do the following: (a) with the recently procured properly sized scintillator paddles perform experiments and obtain more accurate results, (b) perform studies with low resistive electrodes (bakelite, semiconductive glass etc.), (c) experiment with better low noise high gain electronics and explore multigap configurations, and (d) investigate and improve other characteristic parameters such as time resolution and cluster size of RPC.

Acknowledgments

We would like to thank the INO group at TIFR, India for providing us honeycomb readouts and conductive graphite paint to construct the RPCs. We would also like to thank the MuCh group at VECC, India for discussions. NISER and DAE, Govt. of India are acknowledged for funds.

References

[1] R. Santonico and R. Cardarelli, NIM A 187 (1981) 377.

[2] CBM Collaboration, Technical Design Report for the CBM : Muon Chambers (MuCh),GSI-2015-02580, (2015)

[3] C. Bacci et. al, NIM A 352 (1995) 552.

[4] R. Arnaldi et. al, NIM A 456 (2000) 73.

[5] H. Schindler, R. Veenhof, https://garfieldpp.web.cern.ch/

[6] COMSOL Multiphysics, https://www.comsol.co.in/

[7] I. B. Smirnov, NIM A 554 (2005) 474.

[8] S.F. Biagi, NIM A 273 (1988) 533.

Rectangular straw tube detector prototype for CBM

G. D. Kekelidze, V. A. Kramarenko, V. P. Ladygin, and V. M. Lysan
LHEP-JINR, Dubna, Russian Federation

Straw tube detectors are considered as the option for the 3-rd and 4-th stations of CBM Muon Chamber [1]. The full size octagonal straw module prototype has been produced and tested at LHEP JINR [2]. The straw detector with the rectangular shape [3] can be also used at CBM to reduce the cost and to improve the quality of the muon tracker.

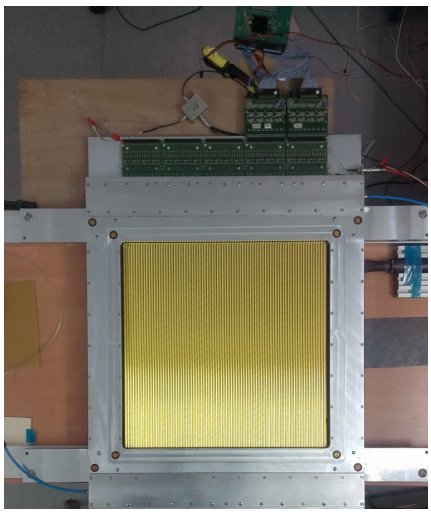

Figure 1: The general view of the rectangular straw chamber prototype.

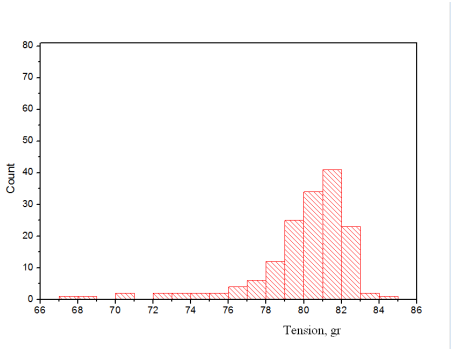

Figure 2: The signal wires tension distribution.

A small rectangular chamber prototype with the working area of 500×500 mm has been produced at LHEP JINR. It consists of two layers, each of them contains 80 straws. The diameter of the straws is 6 mm. The anodes of the chamber is a gilded tungsten wire with a diameter of 30 μm. The thickness of the straw walls is about 60 μm. The walls of straws are its cathode. The wall of straw consists of two layers of the polyimide film. The inner layer is covered with a graphite coating. The cathodes of straw have a relatively resistance about 0.85 Ohm/square. The general view of the rectangular straw chamber prototype is shown in Fig.1

High-voltage measurements were carried out at 2000 V with the air. The value of the current is 5 nA. The gas volumes of all tubes of the chamber and gas manifold are 9.5 l and 2 l, respectively. The test of the gas leakage was carried out in the air. The leaks were less than 10 cm^3/min. The results of the measurement of the signal wires tension is shown in Fig.2. The average value of the tension is ∼80 g.

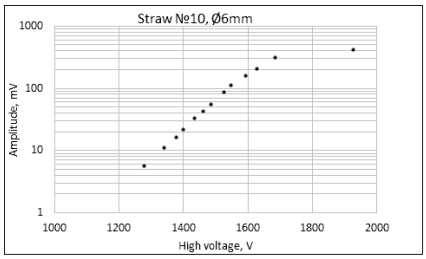

Figure 3: The dependence of the signal amplitude on the high voltage.

The gas gain test was performed using 80%Ar + 20% CO_2 gas mixture and ^{55}Fe radioactive source. Nonuniformity of the amplitude is 5% in the corners of the chamber. This corresponds to the eccentricity of the signal electrodes less than 100 μm. The amplitude of the signals is ∼45 mV at 1440 V. This corresponds to the gas gain of ∼2·10^4. The dependence of the amplitude on the voltage for one of the straw tubes is shown in Fig.3.

The produced rectangular straw chamber prototype can be used for the tests at mCBM.

References

[1] The CBM Collaboration, "Technical Design Report for the CBM Muon Chambers", GSI-2015-02580, Darmstadt, 2015.

[2] G.D. Kekelidze *et al.*, "Straw tube prototype for the CBM muon detector", CBM Progress Report 2016 (2017) 91.

[3] V.N. Bychkov *et al.*, "The large size straw drift chambers of the COMPASS experiment", Nucl.Instrum.Meth. in Phys.Res. A**556** (2006) 66.

Front-end electronics for the straw tube detector

G. D. Kekelidze[1], *V. A. Kramarenko*[1], *V. P. Ladygin*[1], *V. M. Lysan*[1], *A. A. Solin*[2], *and A. V. Solin*[2]
[1]LHEP-JINR, Dubna, Russian Federation; [2]INP BSU, Minsk, Belarus

Di- muon measurement in heavy-ion collisions is one of the priorities of the scientific program at CBM. Rather low particle multiplicities behind the last muon absorbers allows to use straw tube detectors for the 3-rd and 4-th stations of CBM Muon Chamber [1].

Front-end electronics board for straw tube detector with 32- charge- sensitive amplifiers based on AST-1-1 chip [2] is shown in Fig.1. These chips are specially designed to read the signals from straw detectors. Each AST-1-1 chip processes signals from eight straw tubes providing eight LVDS outputs to the TDC.

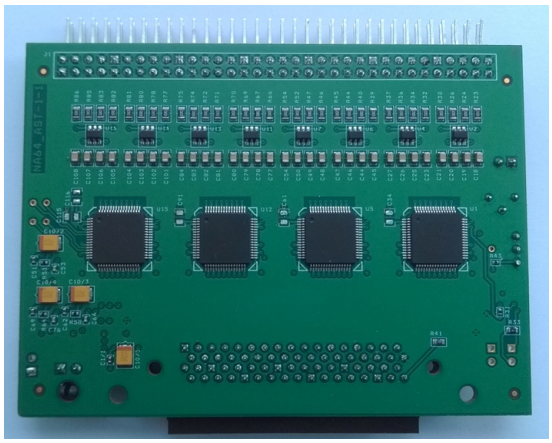

Figure 1: Front-end electronics PCB.

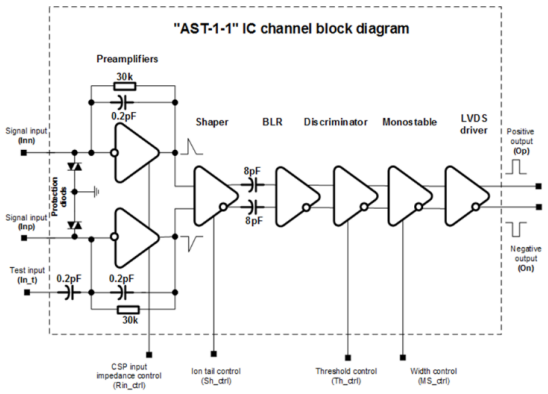

Figure 2: AST-1-1 ASIC block diagrams.

The main features of the AST-1-1 ASIC are eight signal channels, control of input resistance of preamplifier, adjustment of the ion signal tail, BLR, two modes of discriminator operation: time over threshold (ToT) and control of the output signal width, LVDS driver, presence of the ninth channel for monitoring and signal shaping from the straw. The block diagram of the signal channel is given in Fig.2. The preamplifiers has charge sensitive configuration. Preamplifiers, shaper, BLR are bipolar circuit, while discriminator, monostable and LVDS drivers have CMOS schematic solution. The minimum operating voltage for the AST-1-1 ASIC is 2.5 V. The optimum combination of parameters and power consumption is achieved at a supply voltage of 2.8 V.

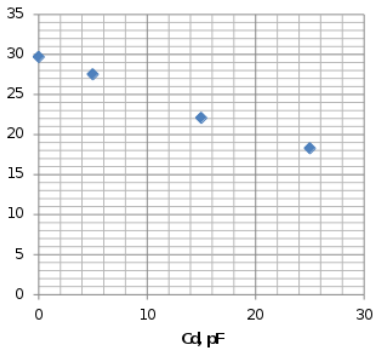

Figure 3: Differential gain of the BLR vs detector capacitance.

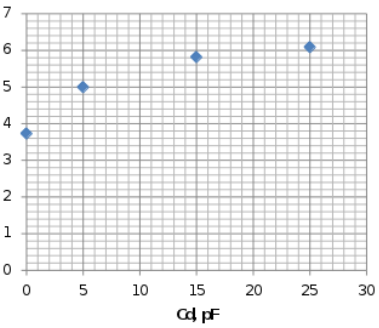

Figure 4: Peaking time of the BLR vs detector capacitance.

The dependencies of the differential gain and the peaking time of the BLR on the detector capacitance at a supply voltage of 3.3 V are shown in Fig.3 and Fig.4, respectively. The measurements were performed with the default pream-

plifier input impedance of R_{in}= 120 Ohm and Q_{in}=10 fC. The values of the differential gain and the peaking time at C_d=15 pF are ∼22 and ∼6 ns, respectively.

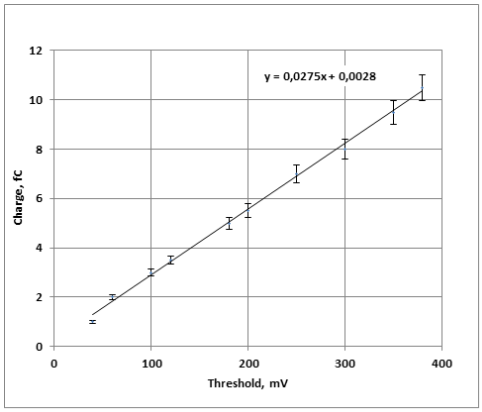

Figure 5: Threshold characteristic of the AST-1-1 ASIC.

The threshold characteristic of the AST-1-1 ASIC shown in Fig.5 was studied using the rectangular pulse generator with a signal leading edge less than 1 ns. The channel gain calculated as the inverse value of the fit parameter in Fig.5 is ∼36.7 mV/fC.

The matching of the straw tubes impedance can be done by the changing preamplifier input resistance by the soldering of resistors on the board. The compensation for the ion tail of the straw signals can be provided by the soldering of the resistors on the amplifier board. The nominal of the resistors depends on the design features of the straw chamber and the used gas mixture and can be defined when testing straw chambers.

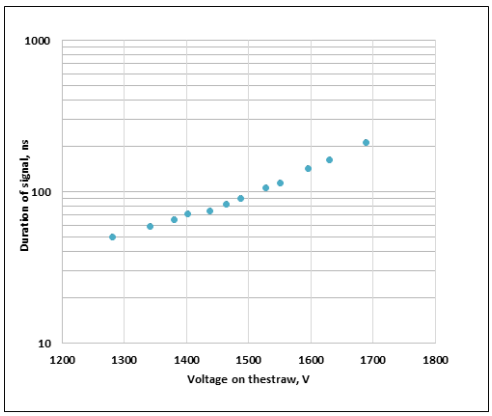

Figure 6: Output LVDS signal width for the ToT option vs the anode voltage.

There is a possibility to provide the option when the output signal width depends on the amplitude of the signal from the straw detector (ToT). The dependence of the output LVDS signal width on the anode voltage at the straw detector is shown in Fig.6. The width of the LVDS signal is ∼100 ns at 1500 V. Another option is the fixed width of the output LVDS signal. The rate capability of the FEE has been checked using a generator signal with a duration of 20 ns and an amplitude of 10 mV fed to 32 channels of the board through 1 kOhm. The maximal rate allowed is ∼10 MHz for the width of the LVDS signal width of 60 ns and a threshold setting of 100 mV.

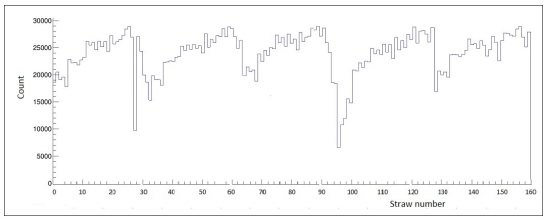

Figure 7: The counts profile from the straw chamber FEE.

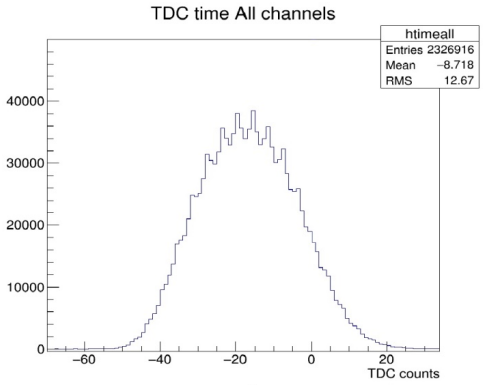

Figure 8: Drift time for 32 straws.

The developed FEE has been associated with the 500×500 mm^2 straw detector consisting of 160 straws produced at LHEP JINR. The chamber was irradiated using ^{106}Ru radioactive source. The counts profile from the straw chamber FEE is shown in Fig.7. The distribution non-uniformity is caused by the radioactive source irradiation. The drift time for 32 straws associated with one FEE board is demonstrated in Fig.8.

The developed board based on the AST-1-1 ASIC can be used as a FEE for straw detector of CBM MuCH [3].

References

[1] The CBM Collaboration, "Technical Design Report for the CBM Muon Chambers", GSI-2015-02580, Darmstadt, 2015.

[2] A.V.Solin *et al.*, "Development of the readout electronics for new experiments in particle physics and at high energies", Bull.Found.Bas.Res. **3 (73)** (2015) 59.

[3] G.D. Kekelidze *et al.*, "Straw tube prototype for the CBM muon detector", CBM Progress Report 2016 (2017) 91.

Performance of a prototype bakelite RPC in low gain mode for 3^{rd} and 4^{th} stations of CBM-MuCh

M. Mondal, J. Saini, Z. Ahammed, and S. Chattopadhyay
Variable Energy Cyclotron Centre, Kolkata, India

Introduction

Resistive plate chambers (RPC) are proposed as the active detector for the 3^{rd} and 4^{th} stations of CBM-MuCh where the maximum particle rate with modified MuCh absorber thickness will be 16 kHz/cm^2 and 5.6 kHz/cm^2 respectively in 8 AGeV central Pb-Pb collision. The prototype single gas gap (2 mm) RPC (area 30 x 30 cm^2) made of low resistive (3.5×10^{10} Ω-cm) bakelite plates has shown 95% efficiency with a low dark count rate ($\sim$ 40 nA) at the cosmic ray test setup of VECC using current sensitive front end electronics (FEE). It was planned to use MuCh-XYTER as the final FEE for RPCs which are being used for GEM detetctor in the 1^{st} and 2^{nd} stations of CBM-MuCh. The RPC has been tested with a commercial charge sensitive preamplier 142IH to test the effectiveness of using charge senstive electronics, i.e., MuCh-XYTER. The detector has subsequently been tested at the Gamma Irradiation Facility (GIF++) of CERN in presence of muon beam of energy 100 GeV.

Test of the RPC at VECC

The prototype bakelite RPC has shown $> 95\%$ efficiency in detecting cosmic muons at 10.5 kV [1] using the following current sensitive electronics, NINO and PADI-6. The detetctor has been operated in avalance mode with the gas mixture ratio of R134a : iC$_4$H$_{10}$: SF$_6$ :: 94.2 : 4.7 : 1.1. To test the feasibility of using charge sensitive FEE, i.e., MuCh-XYTER, as a first step the detector has been operated with the same gas mixture by using a commercial charge senstive preamplier 142IH as shown in Fig.1. In this case, we could get 95% efficiency at a lower voltage of 9.9 kV. The charge sepctra of the detetctor has also been measured at 9.8 kV using MANAS based electronics [2] and the maximum measured charge was $\sim$ 270 fC as shown in Fig.2.

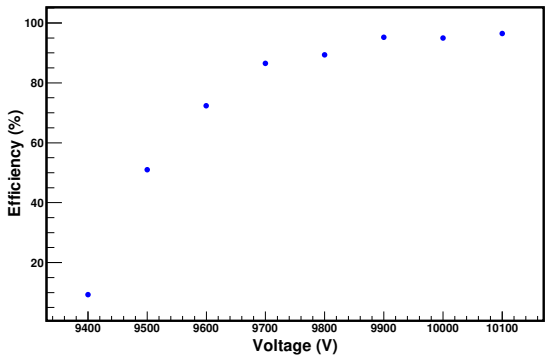

Figure 1: Measured Efficiency with respect to high voltage using commercial CSA 142IH.

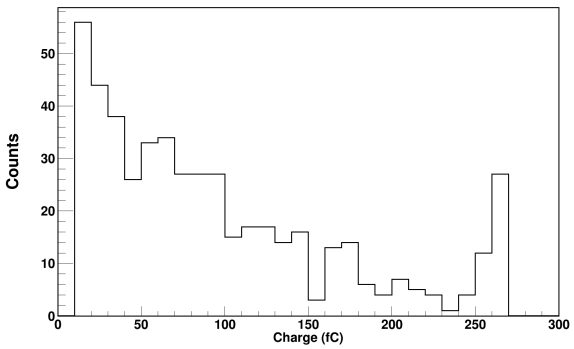

Figure 2: Measured Charge Spectrum using MANAS DAQ.

GIF++ Beam Test Setup

To test the detetctor in high particle rate environment, it has been tested at GIF++ facility situated at CERN. It was irradiated with high energy photons (mainly 662 keV) produced by a Cs^{137} isotope with 13.9 TBq activity. At the same time, the detector has been exposed to a high energy muon beam (100 GeV/c) provided by the CERN SPS H4 test beamline. The flux of the muons per spill (4 sec) has been around 10^5 and the core of the beam fell upon an area of around 10 cm x 10 cm. An attenuator system, each consisting of an array of 3x3 convex lead filters was installed to vary the gamma flux on the two sides of the source independently. The filters have the nominal attenuation factors 1 (A1,B1,C1), 1.5 (B2), 2.2 (C2),4.6 (C3), 10 (A2) and 100 (A3, B3). By adjusting the value of these three filters, the total attenuation factor ranging from 1 to 46415 can be set via the GIF++ control system.

Readout of the detetctor has been done by 11 copper pickup strips, each of 2.3 cm wide, from anode side only. The pick up panel (30 cm x 30 cm) is made of 1.5 mm FR4 sheet sandwiched between two 35 μm copper layers. For the readout electronics, we have used the MuCh-XYTER FEE board along with AFCK and FLIB based stand alone DAQ setup. MuCh-XYTER board have a 100 fC dyanmic range and the board has been calibrated for 60 fC to 160 fC. The chamber was flushed with the available CMS-RPC gas mixture at GIF++, i.e., R134a : iC$_4$H$_{10}$: SF$_6$ :: 95.2 :

4.5 : 0.3. The experimental setup is shown in Fig.3. The RPC was placed 1.67 m downstream the Cs^{137} source behind two CBM-TRD detetctors. A finger scintillator (3 cm x 12 cm) has been placed in front of the TRD detectors so that it's projection completely overlapped with the prototype RPC detector. Two big size (30 cm x 40 cm) scintil-

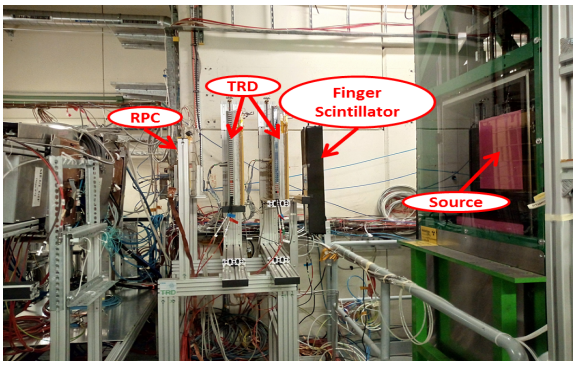

Figure 3: Detetctors setup and position of Cs^{137} source in GIF++

lator detectors was placed outside the GIF++ cave to count muon flux. We have taken RPC data without any online trigger. A digital signal cosisting of the coincidences of the big scintillator GIF++ paddles and the finger scintillator has been fed to another channel of MuCh XYTER FEE for using as offline trigger. We have done the high voltage scan when source was OFF, only in the presence of muon beam. Data has also been taken in source-ON-condition with different attenuation factors.

GIF++ Beam Test Results

As shown in Fig.4, the detetctor shows a muon efficiency $> 95\%$ at 9.1 kV in source OFF condition. We have also

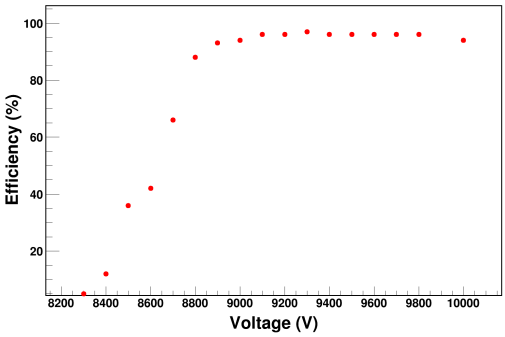

Figure 4: Efficiency of muon detetction of the prototype RPC in source OFF consition as a function of high voltage in GIF++.

calculated the hits on RPC shown in Fig.5. The left peak is pedestal peak and the right one is the muon peak. The core of the muon beam is 100 cm^2 and the detector area is

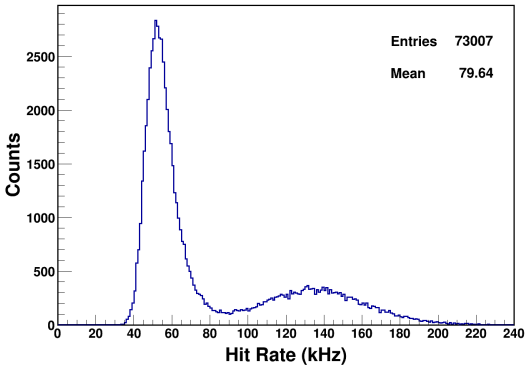

Figure 5: Hit Rate of muon beam on the whole RPC detector at 9200V in source OFF condition.

900 cm^2. The average muon rate therefore falling on the chamber is $\sim$ 1.4 kHz/cm^2.

Fig.6 shows the efficiency with high voltage in presence of gamma background. The photon flux falling on the detector has been calculated for diffferent attenuation factors. The efficiency is seen to be reduced in presence of gamma. At 9.6 kV the detector has shown > 90 % muon efficiency when the photon flux is 40 kHz/cm^2. Further analysis of the test beam results is ongoing.

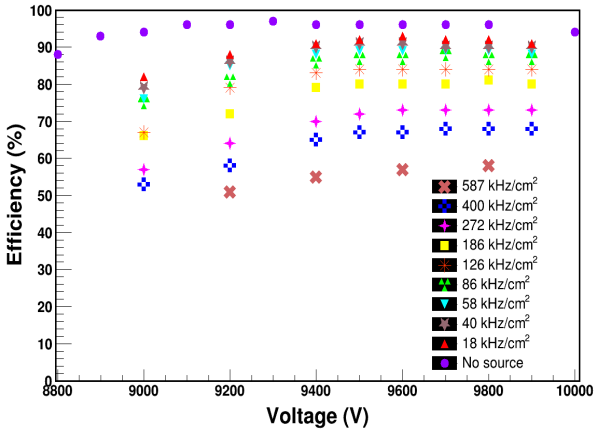

Figure 6: Efficiency of the detetctor for detecting muons in highly irradiated gamma background.

References

[1] M. Mondal et. al,Testing of Low Resistive RPC detector for 3^{rd} and 4^{th} station of CBM-MuCh, CBM Progress Report 2017.

[2] V. Chambert for Alice Collaboration,The electronics of ALICE Dimuon tracking chambers.

Stability and uniformity study of triple GEM detector

S. Chatterjee[1], *S. Roy*[1], *S. Chakraborty*[1], *S. Rudra*[2], *S. Shaw*[3], *R. P. Adak*[1], *S. Biswas*[1], *S. Das*[1], *S. K. Ghosh*[1], *S. K. Prasad*[1], *and S. Raha*[1]

[1]Department of Physics (CAPSS), Bose Institute, Kolkata, India; [2]Seacom Engineering College, West Bengal, India; [3]Vidyasagar University, West Bengal, India

Introduction

Triple GEM chambers will be used as a tracking device in the 1^{st} and 2^{nd} stations of CBM Muon Chamber (MUCH). Long-term stability test and uniformity check [1, 2] have been carried out using a 10 cm $\times$ 10 cm double mask triple GEM detector with Argon/CO_2 gas mixtures in 70/30 ratio. The study of stability in terms of the gain and energy resolution of the prototype has been done using a strong Fe^{55} X-ray source. Also the variation in the characteristics of the prototype in terms of its gain, energy resolution and count rate over the central active region have been studied using the same source. The drift, transfer and induction gaps of the prototype are kept 3 mm, 2 mm and 2 mm respectively. The high voltage to the drift plane and to the individual GEM foils have been applied through a voltage divider resistor chain. The signal is collected using a sum-up board from 9 readout pads each having area 9 mm $\times$ 9 mm and fed to a charge sensitive preamplifier (VV50-2) having gain and shaping time of 2 mV/fC & 300 ns respectively. The preamplifier output has been fed to a linear Fan-in-Fan-out (FIFO) module and used both for measuring the count rate as well as for energy spectra. The analog signal from the linear FIFO has been connected to a Single Channel Analyser (SCA) to measure the counts of the incident particles. The SCA has been operated in integral mode and the threshold is set at 0.1 V to reject the noise. Typically, at HV of - 4150 V with 0.1 V threshold the noise rate has been found to be 45 Hz. The discriminated signal from the SCA, which is TTL in nature, has been put to a TTL-NIM adapter and the output NIM signal was counted using a NIM scaler. The signal count rate of the detector in Hz is then calculated. Another output of the linear FIFO was fed to a Multi Channel Analyser (MCA) to obtain the energy spectra [2]. The method of measurement and test results are discussed in this report.

Stability study

In this stability test a collimator of diameter 8 mm has been used to irradiate a particular area ($\sim$ 50 mm^2) of the detector, with Fe^{55} X-ray of rate $\sim$ 350 kHz, for the entire duration of the study i.e. the equivalent rate per unit area is 0.7 MHz/cm^2. The same source has been used to irradiate the chamber and also to obtain the spectrum at a constant ΔV of $\sim$ 378.7 V to each foil. The gain of the detector has been calculated by fitting the 5.9 keV peak of Fe^{55} X-ray spectrum with a Gaussian distribution. The % energy resolution has been calculated from the relation $\frac{sigma \times 2.355}{mean} \times 100\%$, where mean and sigma are obtain after the Gaussian fitting of the spectra. The spectra are stored automatically using ORTEC MCA at a regular interval of 10 minutes and CuteCom software package has been used for continuous monitoring of the temperature and pressure around the chamber. The measurement of gain and energy resolution has been carried out uninterruptedly for a period of >1200 hours. Figure 1 shows the variation of measured gain, energy resolution and $\frac{T}{p}$ as a function of time.

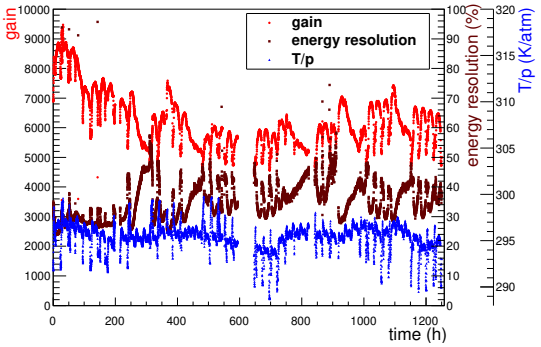

Figure 1: Variation of gain, energy resolution and T/p as a function of time

During this period the accumulated charge has been calculated using the relation $\frac{dq}{dA} = \frac{r \times n \times e \times G \times dt}{dA}$, where r is the measured rate (in Hz) incident on a particular area of the detector, n is the number of primary electrons for a single X-ray photon, e is the electronic charge, G is the gain of the detector, dt is the time in second and dA (50 mm^2, as mentioned in the previous paragraph) is the irradiated area of the chamber. The average gain and energy resolution have been found to be 6385 with a variation of 15% and 34.6 with a variation of 20% respectively for a continuous operation of 1200 hours, which is equivalent to an accumulated charge of $\sim$6.5 mC/mm^2.

Uniformity study

The uniformity study has been carried out at an applied high voltage of - 4150 V corresponding to ΔV $\sim$ 385.9 V across each GEM foil. The active area of the chamber has been divided into 100 zones of 1 cm^2 area. The variation in gain, count rate and energy resolution are measured in the central part in 5$\times$4 array i.e. in 20 zones because the readout pads are located only in the central region. Figure 2 shows the variation of gain, count rate and energy reso-

lution over the central active area of the chamber. From figure 3, it is clear that the measured value of the parameters are not uniform over the active area of the detector. The variation in gain is around $\sim$ 10% and for the energy resolution and count rate it is around $\sim$ 20%. A few percentage of variation in the characteristics in terms of the measured parameters of the prototype is possible because of the intrinsic inhomogeneity in their characteristics due to the variation in GEM geometry and also due to the inhomogeneity in the gap between individual GEM foils.

Since it is not possible to scale all the measured parameters for a large area triple GEM detector, it is in our future plan to fabricate a large area triple GEM detector and to perform the stability and basic characteristics study of the detector.

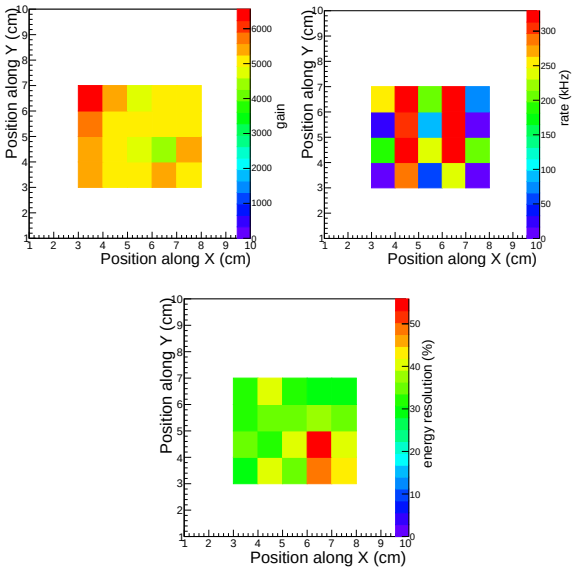

Figure 2: Gain (top left), count rate (top right), energy resolution (bottom), at 20 different places on the detector

Acknowledgements

We would like to thank Dr. Christian, J. Schmidt and Mr. Jörg Hehner of GSI Detector Laboratory for valuable discussions and suggestions in the course of the study and providing some components. This work is partially supported by the research grant SR/MF/PS-01/2014-BI from DST, Govt. of India and the research grant of CBM-MUCH project from BI-IFCC, DST, Govt. of India

References

[1] S. Roy et al. Nucl. Instr. and Meth. A https://doi.org/10.1016/j.nima.2018.10.060.

[2] S. Chatterjee et al. Nucl. Instr. and Meth. A https://doi.org/10.1016/j.nima.2018.08.068.

Development of RPC with low resistive material for CBM-MUCH

S. Chakraborty[1], *A. Sen*[1], *S. Chatterjee*[1], *S. Roy*[1], *A. Roy*[*2], *S. Biswas*[1], *S. Das*[1], *S. K. Ghosh*[1], *S. K. Prasad*[1], *and S. Raha*[1]

[1]Department of Physics (CAPSS), Bose Institute, Kolkata, India; [2]Department of Particle Physics and Astrophysics, Weizmann Institute of Science, 7610001 Rehovot, Israel

Introduction

The possibility of using single gap Resistive Plate Chamber (RPC) in the 3^{rd} and 4^{th} stations of the CBM-MUCH detector are currently being explored. RPC detector technology is widely used in high energy physics experiments, for trigger and tracking purposes, due to its excellent efficiency ($> 90\%$) and time resolution (1-2 ns). The maximum particle flux on the 3^{rd} and 4^{th} stations of CBM-MUCH have been estimated to be 15 kHz/cm^2 and 5.6 kHz/cm^2, respectively, for minimum bias Au–Au collisions at 8 AGeV. Therefore, the inexpensive RPC's, known for their moderate rate handling capacity ($\sim$ 1-2 kHz/cm^2, depending on the resistivity of the material used), are being considered for the CBM. We are currently investigating the possibility of using low-resistive materials for RPC fabrication that will ensure stable operation at higher rates ($\sim$ 10 kHz/cm^2) in the avalanche mode.

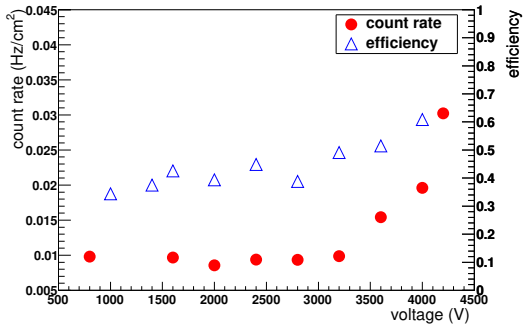

Figure 1: Noise rate and Efficiency Vs. voltage

Detector description and experimental set-up

We have fabricated a 15 cm $\times$ 15 cm prototype RPC with a carbon-loaded Polytetrafluoroethylene (PTFE) material commonly known as Teflon of thickness 1 mm [1]. This particular sample is 25% carbon-filled having a bulk resistivity of $10^5\Omega$-cm. The volume resistivity of Carbon-loaded materials (like the PTFE sample used) can be tuned according to requirements, by modifying the carbon/graphite content. The measured surface resistivity of the carbon-loaded PTFE has been found to be 20 k$\Omega/\square$. The material has not been coated with graphite for high voltage distribution as the surface resistivity of carbon-loaded PTFE is very low. As the surface of the material has been found to be smooth by visual inspection, we have not used oil coating in this case. 100% R-134a (Tetrafluoroethane) has been used as the sensitive gas for the chamber. Differential voltage has been applied to the chamber to produce the electric field inside the gas gap. A charge sensitive preamplifier (VV50-2) with gain 2 mV/fC and shaping time 300 ns has been used for the signal collection. Due to impedance mismatch there was always a reflected negative part in each signal however this negative part was useful to discriminate the signal from noise using a leading edge discriminator (LED). For efficiency measurement a cosmic ray trigger set-up is used keeping two plastic scintillator detectors of dimension 20 cm $\times$ 20 cm and 2 cm $\times$ 10 cm above the chamber and one with dimension 10 cm$\times$ 10 cm below it. The un-triggered discriminated RPC signals are also counted to measure the noise rate.

Results

The three-fold scintillator trigger signals, four-fold (3-fold $\times$ RPC signal) signals and the singles from the RPC are counted for 30 minutes for each voltage setting. The singles count rate has been divided by the area of a strip and the count rate per unit area is shown as a function of voltage in Figure 1. Noise rate increases with voltage. The ratio of the four-fold count rate to the three-fold count rate is the efficiency and that as a function of voltage is also shown in Figure 1. The efficiency increases with increasing applied voltage. At a voltage of 4 kV typical values of efficiency and noise rate are found to be 60% and 0.02 Hz/cm^2 respectively. This value of efficiency is quite low considering a typical single gap RPC efficiency of 90%. However for this detector discharges occur beyond the high voltage of 4 kV. These are preliminary results with a Carbon-loaded PTFE sample of very low resistivity. Investigations are ongoing to understand the drawbacks of this prototype detector, compared to existing glass/bakelite RPC results. Recently an R&D has been started with locally available bakelite plate and the plan is to operate the new RPC at low gas gain with Ar/CO_2 mixture.

Acknowledgements

We would like to thank Dr. C.J. Schmidt and Dr. W.F.J. Müller of GSI, Germany for valuable discussions and suggestions in the course of the study. This work is partially supported by the research grant of CBM-MUCH project from BI-IFCC, DST, Govt. of India.

References

[1] S. Chakraborty, et al., Nucl. Instr. and Meth. A (2018), https://doi.org/10.1016/j.nima.2018.08.058.

*Now at Nuclear Engineering Unit, Faculty of Engineering Sciences, Ben-Gurion University of the Negev, P.O.B. 653, Beer-Sheva, 8410501, Israel

Aging studies of Straw tube detector

S. Roy[1], *S. Chatterjee*[1], *S. Chakraborty*[1], *A. Sen*[1], *S. Biswas*[1], *S. Das*[1], *S. K. Ghosh*[1], *S. K. Prasad*[1], *S. Raha*[1], *V. D. Peshekhonov* [*2], *V. M. Lysan*[2], *G. D. Kekelidze*[2], *and V. V. Myalkovsky*[2]

[1]Department of Physics (CAPSS), Bose Institute, Kolkata, India; [2]LHEP-JINR, Dubna, Russian Federation

Introduction

Straw tube detectors are widely used for large-area tracking because of reduction of material budget. We are exploring the possibility of using straw tubes for the 3^{rd} and 4^{th} stations of CBM Muon Chamber (CBM-MUCH) [1, 2]. Because of high particle rates at the 3^{rd} and 4^{th} stations of MUCH (15 kHz/cm^2 and 5.6 kHz/cm^2, respectively, for central Au-Au collisions at 8 AGeV), aging of the active detectors is a concern. At a chosen gain of 10^4, for MIP the charge accumulated along the length in the straws at the 3^{rd} station for three months of operation is estimated to be 8.4 mC/mm ($number\ of\ primary \times electronic\ charge \times gain \times rate \times straw\ diameter \times time = 60\ e \times 10^4 \times 15 \times 10^3\ Hz \times 0.6\ cm \times 10^7\ s$), which sets the goal for aging studies. Characteristics study of straw tube detector and rate handling capability has been reported earlier [3]. Long-term study of the straw tube detector with high radiation has been performed using ^{55}Fe X-ray source by monitoring the gain and energy resolution of the detector continuously with time.

Experimental set-up

The straw tube detector prototype used in this test has diameter 6 mm and length 20 cm filled with Ar/CO_2 premixed gas in the volume ratio 80:20 at a constant flow rate of 3 lt/hr. To irradiate the detector, a collimated X-ray from ^{55}Fe radioactive source has been used. In order to accumulate a charge of 8.4 mC/mm within a reasonable time, we set a particle rate of 40 kHz/mm and a realistic gas gain of 1.4 $\times$ 10^4 which was obtained at anode voltage of 1550 V. The spectra are stored automatically using ORTEC MCA at a regular interval of time. Ambient temperature and pressure are simultaneously measured with a data logger made in house and recorded online using CuteCom software package.

Results

The gain and T/P as function of time is shown in Figure 1. The measured gain is normalised by the theoretically obtained gain $G(T/p) = Ae^{B\frac{T}{p}}$. The normalised gain is shown in the figure 2 as a function of accumulated charge. The accumulated charge has been calculated using the relation $\frac{dq}{dl} = \frac{r \times n \times e \times G \times dt}{dl}$, where r is the measured rate (in Hz) incident on a particular area of the detector, n is the number of primary electrons for a single X-ray photon, e is the electronic charge, G is the gain of the detector, dt is the time in second and dl is the irradiated length of the straw. The mean normalised gain has been found to be 0.99 with a rms of 0.01 and during this time the energy resolution obtained varies between 18.5% to 20% for a continuous operation of 120 hours, which is equivalent to an accumulated charge per unit length of ∼9 mC/mm. No deterioration in gain or energy resolution of the detector has been observed.

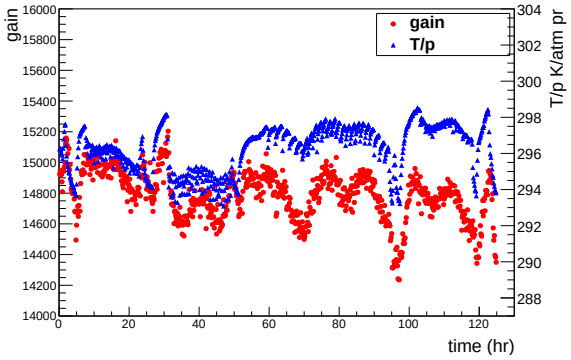

Figure 1: Variation of gain and T/p as a function of time

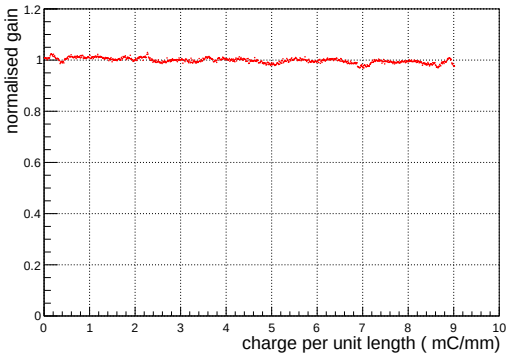

Figure 2: Variation of normalized gain as a function of accumulated charge

References

[1] http://www.fair-center.eu/for-users/experiments/cbm.html .

[2] http://www.fair-center.eu/ .

[3] S. Roy et al. Nucl. Instr. and Meth. A (2018), https://doi.org/10.1016/j.nima.2018.08.056

[4] S. Roy et al. Nucl. Instr. and Meth. A (2018), https://doi.org/10.1016/j.nima.2018.10.060.

[*] deceased

Automated calibration of STS/MUCH XYTER ASIC in MUCH Mode followed by voltage scan and online power control and monitoring system

G. Sikder[1], J. Saini[2], C. Ghosh[2], A. Chakrabarti[1], S. Chattopadhyay[2], A. Bhattacharyya[1], and C. Schmidt[3]

[1]University of Calcutta, Kolkata, India; [2]VECC, Kolkata, India; [3]GSI, Darmstadt, Germany

The new dual gain STS/MUCH-XYTER is a 128 channel highly configurable ASIC with dedicated 5-bit flash ADC for each individual channel. This ADC have 31 comparators which can be trimmed for a particular reference voltage controlled by a 8-bit Digital to Analog Convertor (DAC). Each bit needs to be calibrated for a particular input charge which can be either linear or non-linear within its dynamic range. A known charge is injected for any given ADC-channel and then trimming offset of that particular channel is set such that ADC decoder output shows the targeted channel only. A counter feedback algorithm is also developed to digitally adjust the comparator offset to minimize the deviation from the expected value. To calibrate 31 comparators of an ADC of all 128 channels in the MUCH mode, it was required to inject the known charge at the input of the channel. This charge was injected using a voltage to charge convertor circuit controlled by a pulse generator. If manually done, this is a time taking process which required at least 31 time interventions to complete the calibration. Therefore we have developed an automated comparator calibration technique which includes automation of several equipment used in this setup.

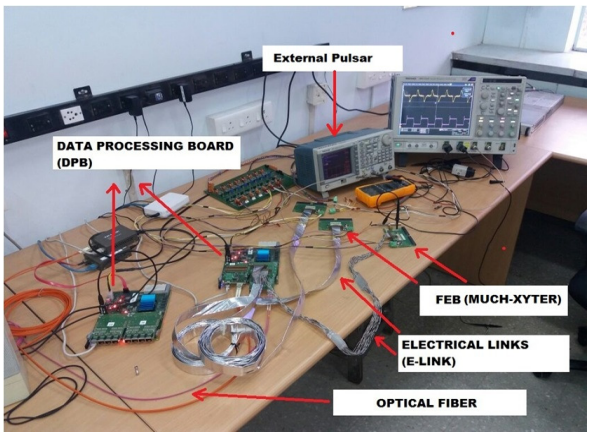

Figure 1: Test Bench Setup for Calibration at VECC

Calibration test-bench setup

To perform this calibration on the MUCH-XYTER ASIC, a known charge is injected in all 128 channels of the ASIC for which, Tektronix arbitrary function generator (AFG) 3000 is used to inject a pulse of a definite height, which is then converted to charge using a common 50 Ohm terminator followed by a series 1 pF capacitor for each individual channel. In Figure 1, the test bench setup picture is shown and in Figure 2, the picture of MUCH-XYTER FEE board and compact connector with charge injection circuit for individual channel is also there at top of the image. Other components includes a Kintex-7 FPGA based data processing board. Back-end of this board has an IPbus interface via which we control and readback all the trimming commands as well as data. After a defined charge is injected to all the channels, data is readback from the output buffer register of all the individual ADCs. A counter feedback mechanism is then used to digitally adjust the comparator's offset which is controlled by a trimming register so that the offset is minimized from the desired value. Apart from the ADC calibration, we have also developed a Voltage Scanning procedure to determine proper bias settings to calibrate MUCH-XYTER ASIC.

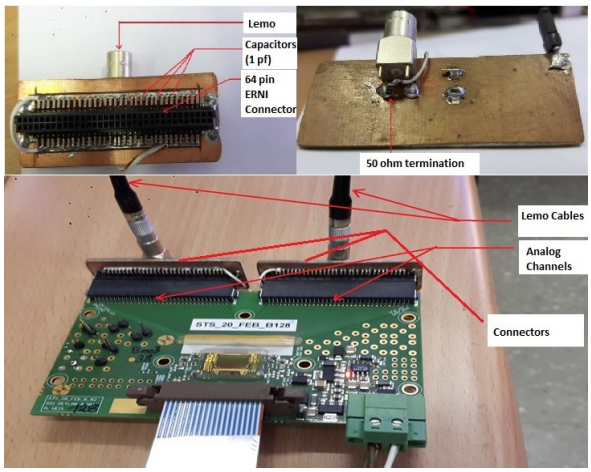

Figure 2: FEE Board with MUCH-XYTER ASIC and connector for charge injection

Automation of instruments used in the calibration setup

Tektronix AFG 3000

To automate the Tektronix AFG 3000, a control script has been developed using Python 2.7. This setup requires python package called Py-VISA and backend library called Py-VISA-py to access the external pulsar from the host computer. In the auto-calibration software, these scripts are called several times on a regular basis with varying parameters to automatically change the pulse output from the

AFG function generator.

Agilent power supply

There are several occasion when the power cycle is required for some particular channel of LV. Apart from lab testing, during the beam time, these low voltage power supplies are generally housed close to the detector which are not accessible during the beam time and required to be accessed frequently for a clean start of the readout chain. Hence, an automated Control System and Constant Power Monitoring System has been developed by which we can control power and current of the power supply. We can even monitor the status of currents and voltages of all individual channels of the power supply. Same as the Tektronix function generator, python package called Py-VISA and backend library called Py-VISA-py has been used to develop this Control and Monitoring setup. A Python script has been written using module specific GPIB commands to access this Agilent power supply for its each channel. A separate text file exists where the list of voltage and current values are written in accordance with each channel and the power system channels are controlled using the these scripts by fetching the values of voltage and current from this file. The values in the text file can be changed as per the requirement. A screen shot of sample power monitoring system is given in Figure 3.

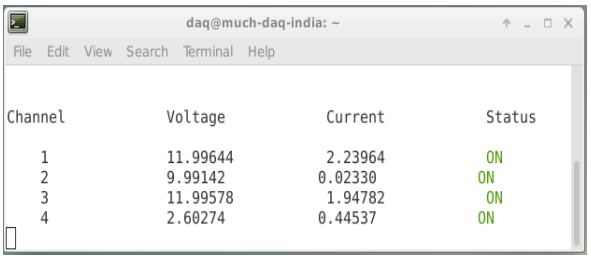

Figure 3: Online Power Monitoring System for Agilent Power Supply

Voltage Scanning Procedure to determine required bias settings for calibration

Voltage Scanning is a procedure by which we can determine the proper bias settings (VrefN, VrefP and VrefT) for a given calibration. The 5 bit Flash ADC of an analog channel has 31 comparators and there is a 12 bit counter associated with each and every comparator. A known pulse height of a given frequency is injected, the 31 counters store the number of times the associated comparator gets fired based on a certain trim value. In this procedure, a particular analog channel is selected, the pre-calibrated trim values are uploaded. Then charge is injected in that channel from minimum limit (e.g. 5 fC) to maximum limit (e.g. 67 fC) which may or may not be same as per the pre calibrated file parameters. However, incremental charge step size should remain same as per the calibration file parameter (e.g. 2 fC in general) which is governed by AFG 3252 function generator and charge injector circuit on the mating connectors of the FEE boards as shown in Figure 2. After injecting these charges periodically for a pre defined time (e.g. 1 second), all the counter values associated with 31 comparators of that channel are read back via IPBus protocol. Then an ADC linearity plot is generated using the

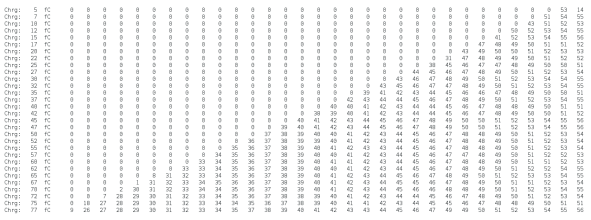

Figure 4: ADC linearity output after voltage scan

counter readback values. Different bias settings (VrefN, VrefP, VrefT) are used to find the bias setting to accommodate the ADC linearity range. If some of the channels are not able to calibrate or are out of the biasing range, then these bias parameters are readjusted to put back the ADC linearity within the range. In this way, we can also offset the range i.e, 5 fC to 67 fC can be changed to 10fC to 72fC or any other range in a certain biasing limit of the ASIC. However, step sizes cannot be altered with this procedure. To alter the step size, we need to re-trim the full ASIC with new step size. A screen shot of a sample ADC linearity plot is given in the Figure 4.

References

[1] P Senger and the Cbm Collaboration. The cbm experiment at fair. Journal of Physics:Conference Series, 50(1):357,2006.

[2] H. Okada, Y. Hashimoto, K. Sakata, T. Tsukada, and K. Ishibashi,“Offset calibrating comparator array for 1.2-V, 6-bit, 4-Gsample/s flash ADCs using 0.13μm CMOS technology,” in Proc. ESSCIRC’03 Sep.2003, pp. 711-714

[3] Chun-Cheng Huang, Student Member, IEEE and Jieh-Tsorng Wu, Member, IEEE, “A Background Comparator Calibration Technique for Flash Analog-to-Digital Converters”, IEEE TRANSACTIONS ON CIRCUITS AND SYSTEMS—I: REGULAR PAPERS, VOL. 52, NO. 9, SEPTEMBER 2005

Low Voltage and sensor control system for m-CBM Experiment

V. S. Negi, J. Saini, A. K. Dubey, and S. Chattopadhyay
Variable Energy Cyclotron Centre, Kolkata, India

Introduction

The first prototype of LVDB had been developed with 12V, 6A input and 15 output channels. Each channel can be controlled and monitored individually with the adjustable voltage from 0.8 to 5.5V with 3A output current capability. In spite of using switch (Logic 0 or 1), driver current of converter were controlled using 8 bit variable resistance. This unique control scheme gives the six fold coincident reliability which enhances the radiation tolerant itself capability of LVDB.

The LVDB board with its components is shown in figure 1. One of its Channel will be used for optocoupler control rest of all for powering FEE boards of GEM detector. Pressure sensor, humidity sensor and temperature sensor are mounted to detect any leak in the detector.

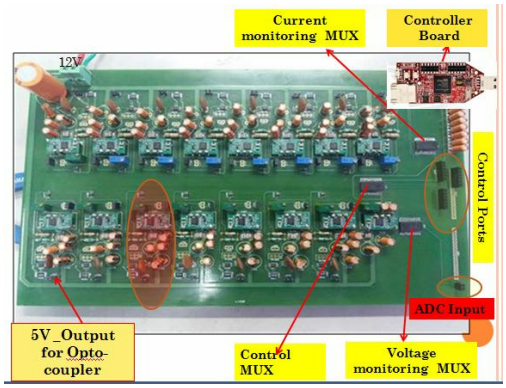

Figure 1: LVDB for mCBM

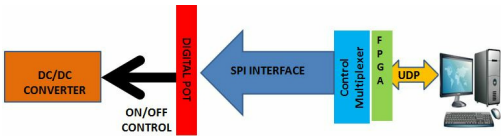

Figure 2: Simplified Control Scheme

DEVICES	REFRESH RATE	SEUS	SIZE
FPGA BOARD	10MINS	398 (MAX)	15mm X 15mm
FPGA BOARD	2MINS	42 (MAX)	15mm X 15mm
FPGA FLASH	12 HOUR	NIL	4mm X 6mm
DIGITAL POTS	2 HOURS	NIL	1.6mm X 2.9mm

Figure 3: SEUs count of memory devices

Control System in mini-CBM

Low cost FPGA were chosen for control and monitoring of LVDB channels and various sensors. Control scheme for one channel had been shown in fig.2 . LVDB got commands via Ethernet backend. Individual channels can be aimed by selecting the dedicated multiplexer channel. Once channel is selected control system invoke SPI communication and program the 8 bit variable resistor that leads to enable and disable of channel. The control topology includes three level of radiation protection

Scrubbing of FPGA via FLASH memory

We had tested the FPGA board with neutron flux 1000 time more than the real experiment and upsets were recorded with different scrubbing rates shown in fig 3 . With the Scrubbing of few minute we will landed with negligible SEUs.

Redundancy in the control logic via Digital pot

This logic not only gives six-fold coincident protection (radiations need to flip at least six bit then only it affects the status of the channel) but also limits the dependency of LVDB on controller.

Limited control by FPGA

Control pins of FPGA are electrically isolated from LVDB once it is programmed while the monitoring pins are remain intact. If the whole program in the controller (before periodic scrubbing) get alter or erased completely, since digital pot is a memory device itself it will remember the previous state of converter or channel. Digital pot not only gives reliability and granularity but also shown outstanding reluctance towards SEUs as mentioned in table2. Unlike FPGA based controller, effect of every bit flip in digital pot can be estimated and mitigated accordingly.

Conclusion

First prototype of LVDB and sensor board with all the controls and UDP interface has been developed and ready to be used in mCBM. At present GUI has been developed on MAT-LAB for control and monitoring process.

Acknowledgment

Authors like to thank Dr. Abhijit Saha and Dr S.C Gadkari and their team members from UGC-DAE CSR, Kolkata and TPD group BARC for their support and cooperation.

Transition Radiation Detector

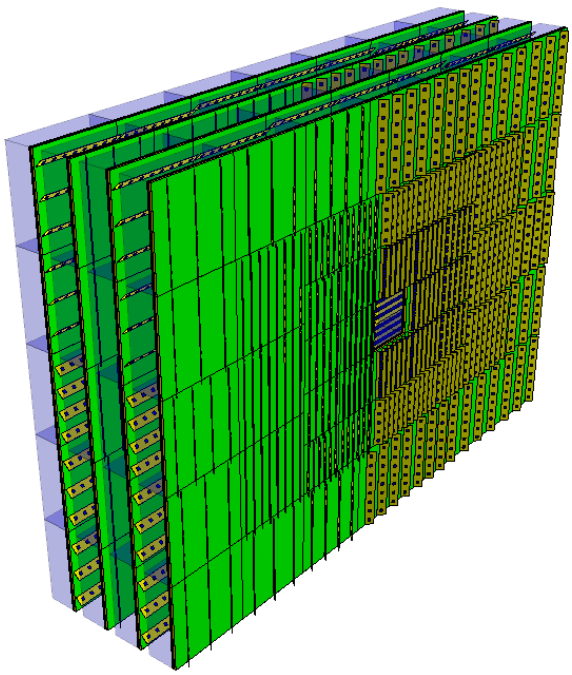

Summary on the TRD project

C. Blume and the CBM-TRD working group
Institut für Kernphysik, Frankfurt am Main, Germany

Introduction

The main task of the Transition Radiation Detector (TRD) is to identify electrons above momenta of 1 GeV/c and thus to extend the electron identification capabilities of the Ring Imaging CHerenkov (RICH) detector above momenta of $p \sim 5$ GeV/c. In this region the TRD should provide a pion suppression factor in the range of 10 – 20 at an electron efficiency of 90 %, in order to allow for a high quality measurement of dielectrons in the mass range from below the ρ and ω masses to beyond the J/ψ mass. Due to its capability to identify charged particles via their specific energy loss, the TRD in addition will provide valuable information for the measurement of fragments. A new, detailed study of the decisive role of the TRD in physics topic of hypernuclei has been performed in the last year [1].

These requirements can be fulfilled with a Xe/CO_2 based Multi-Wire Proportional Counter (MWPC) detector in combination with an adequate radiator. The default MWPC design is composed of a symmetric amplification area of $3.5 + 3.5$ mm thickness, complemented by a 5 mm drift region to enhance the TR-photon absorption probability in the active gas volume. This geometry provides also efficient and fast signal creation, as well as readout, with timescales below 250 ns per charged particle track. The performance of the detector is maximized by reducing the material budget between radiator and gas volume to a minimum.

The baseline design for the TRD at SIS100 will consist of one station, composed of four detector layers. It will be positioned between the RICH and the Time-Of-Flight (TOF) detector and thus will help to reduce the background in the TOF resulting from track mismatches by providing additional position information between RICH and TOF. The TRD will also be used as tracking station behind the last absorber of the MUCH detector in the muon configuration of CBM.

Technical design report

The technical design report has been evaluated by the referee appointed by the FAIR Expert Committee Experiments (ECE). Based on the suggestions and comments of the referee, a revision of the report was prepared and finally approved by the ECE on its 10$^{\text{th}}$ meeting on Oct. 9., 2018 [2]. After successfully completing this decisive step, the TRD project can now move from its R&D-phase into the production stage.

Concerning the design of the ten innermost modules, which will be exposed to the highest particle rates, work on an addendum to the design report is progressing. It is planned to finalize this in the course of summer 2019.

Front-end electronics and readout

An extensive evaluation of the SPADIC 2.0, as it has e.g. been used during the beam test at DESY [3], a test batch of the improved version, SPADIC 2.1, was ordered. Unfortunately, this submission turned out to be faulty, as due to an error of the manufacturer, the ASICs were produced without RAM. It was therefore decided to directly move ahead to version SPADIC 2.2, which is supposed to be the final implementation of the ASIC, featuring all bug fixes (e.g. a solution to a synchronization problem inherited from the XYTER backend) and the final data protocol. A first batch of this chip (8633 ASICs) has already been produced as part of a CBM-wide ASIC-submission and packaged. Currently, Front-End Boards (FEBs) are being equipped the ASICs and will be tested in the next weeks.

Concerning the FASP-based readout, a new version of the ASIC, FASP v03, is being prepared [4]. This version will have an improved analog circuitry and a new processing logic for neighbor readout and is supposed to be used in the mCBM-setup. For the readout of the ASIC, FASPRO (FASP Read-Out) boards have been designed and tested.

Further developments concern the data format using in the FASP readout and long term tests of the GETS (General Event Time-stamping Serializer) FEE [5].

Online data reduction on the FGPA stage is an important component of the TRD readout chain. A thorough understanding of the performance achievable with different algorithms is here mandatory and has been studied within a simulation [6].

Laboratory and beam tests

High rate tests have been performed at the CERN Gamma Irradiation Facility in 2018. A first analysis was able to demonstrate that the MWPCs exhibit a stable performance up to hit-rates of at least 12 kHz/cm^2 [7]. For the first time, a trigger on the muons delivered by the SPS was implemented, which will allow to investigate the development of the signal quality with increasing detector load and which is the subject of an ongoing analysis.

The chambers, which are intended to be used in the inner zone of the TRD, have been exposed to high-intensity x-rays in the Bucharest laboratory. These setup allowed to

perform extensive measurements of the energy resolution and the gas gain in dependence of the anode voltages [8].

Another test, performed in the Münster laboratory, investigated the humidity intake into the TRD counting gas via different detector components. It was found, that a significant amount of humidity can diffuse through the Kapton entrance window foil [9].

In the summer 2019 a second beam test at DESY is planned. The purpose is the qualification of the final radiator design with electron beams at different momenta and incidence angle. This data will also serve as a reference for tuning the simulation and particle identification.

TRD in mCBM

Two large (i.e. 95×95 cm^2 TRD chambers have been integrated into the mCBM setup and are fully operational. They are instrumented with quad-FEBs, equipped with SPADIC 2.0, which allow to read out a substantial fraction of the active detector area. Unfortunately, the development of the firmware for the C-ROB based readout had to be put on hold, as the expert left for a position in industry. Therefore, the TRD cannot be part of the data stream during the current mCBM beamtime. However, the work on this topic has already been taken up again and the integration of the TRD will be finished as soon as possible. In the meantime, the TRD chambers in the mCBM setup can in principle be used to perform detector related studies, such as the HV stability with and without capacitors on the HV distribution boards.

For the next year, it is planned to add one TRD prototype of the Bucharest version with FASP readout to the setup. The preparations are progressing quickly [4, 5, 8, 11].

Software developments

Substantial work has been made in the simulation framework for the TRD. The major change is the move of the digitizer to the four-dimensional approach, but also many detailed improvements in the description of the detector response have been made. For instance, the time distribution of the ionization processes and the response of the SPADIC 2.2 is now realistically implemented [10].

Also, for the chambers of the inner detector region the digitization scheme has been refined to provide a realistic response for the triangular pad plane and the characteristics of the FASP-based readout [11].

Summary and outlook

Generally, a lot of progress towards the final detector design has been made. While the layout of the TRD modules is essentially complete, the ongoing developments focus on infrastructure elements, such as details of the support structure, cooling and LV distribution. For the latter, all required power supplies have already been procured. As the mass production of the modules is supposed to start by the end of the year, the corresponding planning of the production schedules, as well as equipment and installations at the involved institutions need to be worked out. In order to progress on the corresponding planning, a retreat meeting of all groups involved in the TRD-project will be held in Mar. 27. – 29. at Schloß Waldthausen in Mainz, Germany.

References

[1] S. Gläßel et al., “Identification of hypernuclei via energy loss measurements with the TRD”, this report.

[2] C. Blume et al. (CBM Collaboration), “Technical Design Report for the CBM Transition Radiation Detector (TRD)”, CBM Technical Design Reports, GSI, Darmstadt, DOI:10.15120/GSI-2018-01091 (2018).

[3] A. Meyer-Ahrens et al., “SPADIC baseline in 2017 DEST test beam data”, this report.

[4] A. Bercuci et al., “FEE readiness of Bucharest TRD chamber for mCBM”, this report.

[5] A. Bercuci et al., “Data format and long term tests for FASP/GETS FEE in view of mCBM integration”, this report.

[6] F. Roether et al., “Data reduction by feature extraction”, this report.

[7] P. Kähler et al., “TRD high-rate test beam at the CERN Gamma Irradiation Facility 2018”, this report.

[8] A. Bercuci et al., “Energy resolution and gain measurements for the TRD chamber configuration proposed for the inner zone of the CBM-TRD”, this report.

[9] R. Weber et al., “Humidity in the gas system of the CBM-TRD”, this report.

[10] E. Bechtel et al., “Simulation developments for the CBM-TRD”, this report.

[11] A. Bercuci et al., “Realistic response of the Bucharest TRD for mCBM simulations at top rates.”, this report.

Identification of hypernuclei via energy loss measurements with the TRD

S. Gläßel and C. Blume
Institut für Kernphysik, Frankfurt, Germany

An important part of the CBM physics program is a high statistics measurement of double-Λ hypernuclei. Since up to now only very few double-Λ hypernuclei events have been identified, this measurement is considered a breakthrough in this field of physics [1].

The Transition Radiation Detector (TRD) will significantly extend the number of accessible hypernuclei states. The m/Z measurement of their decay products (hadrons) alone, as provided by the Time of Flight detector (TOF), is not able to distinguish between two different charge states. The TRD contributes to the separation of charged hadrons with a measurement of their specific energy loss [2].

For the identification of ${}^{6}_{\Lambda\Lambda}$He, which decays as ${}^{6}_{\Lambda\Lambda}$He $\rightarrow {}^{5}_{\Lambda}$He + p + π^- and subsequently as ${}^{5}_{\Lambda}$He $\rightarrow {}^{4}$He + p + π^-, the separation of d and ^{4}He is particularly important. In fact, without clearly separating these two nuclei, it is not possible to distinguish the ${}^{5}_{\Lambda}$He-decay from the decay of the hypertriton: ${}^{3}_{\Lambda}$He $\rightarrow$ d + p + π^-. As the expected production rate of ${}^{3}_{\Lambda}$H ($1.7 \cdot 10^{2}$ per central Au-Au collision at 8 AGeV [3, 4]) is significantly higher compared to the production rate of ${}^{6}_{\Lambda\Lambda}$He ($4.8 \cdot 10^{-8}$ per event), a high background is expected. Figure 1 shows the distribution of wrongly identified ${}^{5}_{\Lambda}$He (in blue) in 10^7 simulated UrQMD-events, each containing one ${}^{3}_{\Lambda}$H and six d [4], but neither ${}^{5}_{\Lambda}$He nor ${}^{6}_{\Lambda\Lambda}$He. With a TOF mass-cut $\Delta m = \pm 3\ \sigma$ around the ${}^{5}_{\Lambda}$He-mass (in violet) the number of wrongly identified ${}^{5}_{\Lambda}$He is around 1,000. The TRD provides a suppression of nearly all misidentified ${}^{5}_{\Lambda}$He (in orange).

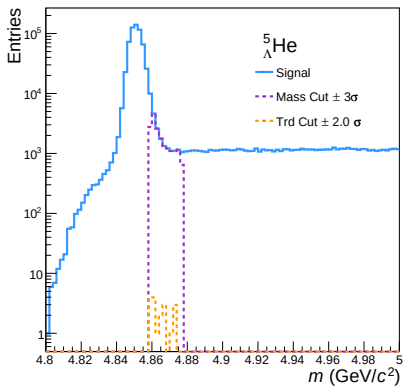

Figure 1: Mass distribution of wrongly identified ${}^{5}_{\Lambda}$He for 10^7 simulated UrQMD-events with embedded ${}^{3}_{\Lambda}$H and d.

At the same time, the efficiency $\epsilon = n_{sig}^{MC}/n_{sim}$, i.e. the ratio of correctly identified particles n_{sig}^{MC} to simulated particles n_{sim}, is hardly effected by a $\langle \mathrm{d}E\mathrm{d}x \rangle$-cut. Fig. 2 shows the mass distribution of ${}^{6}_{\Lambda\Lambda}$He for 10^6 simulated ${}^{6}_{\Lambda\Lambda}$He-events embedded in UrQMD-events with d. The reconstructed signal (in blue) is compared to the cases with mass-cut (in violet), the reconstructed particles with correct MC-Id (in red) and with TRD-cut (in orange). The suppression of correctly identified ${}^{6}_{\Lambda\Lambda}$He via a 2σ-$\langle \mathrm{d}E\mathrm{d}x \rangle$-cut is on a negligible level.

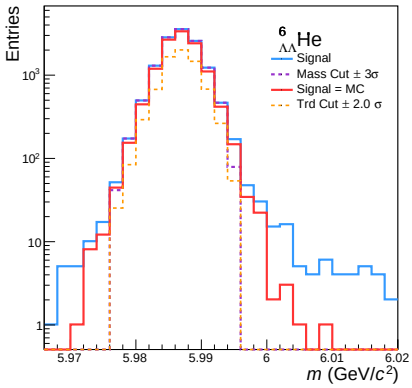

Figure 2: Mass distribution of ${}^{6}_{\Lambda\Lambda}$He for 10^6 simulated UrQMD-events with embedded ${}^{6}_{\Lambda\Lambda}$H and d.

Simulations that combine ${}^{3}_{\Lambda}$H and ${}^{6}_{\Lambda\Lambda}$He in a realistic yield ratio (${}^{6}_{\Lambda\Lambda}$He/${}^{3}_{\Lambda}$H = $2.8 \cdot 10^{-6}$) were performed to study the effects of a $\langle \mathrm{d}E\mathrm{d}x \rangle$-cut on the purity of the measurements $P = n_{sig}^{MC}/n_{sig}$, i.e. the ratio of correctly identified particles n_{sig}^{MC} to the reconstructed signal n_{sig}. As the hypernuclei ${}^{6}_{\Lambda\Lambda}$He is an extremely rare particle, quantitative conclusions are difficult to make, due to statistical limitations. Still, there is a clear evidence, that the TRD significantly improves the purity of the reconstructed ${}^{6}_{\Lambda\Lambda}$He-signal.

References

[1] T. Ablyazimov et al. (CBM Collaboration), "Challenges in QCD matter physics - The scientific programme of the CBM experiment at FAIR", Eur. Phys. J **A53** (2017) 60.

[2] P. Bhaduri et al., CBM Progress Report 2017, Darmstadt, 2017.

[3] A. Andronic at al., "Production of light nuclei, hypernuclei and their antiparticles in relativistic nuclear collisions", Phys. Lett. **B697**, 2011, 203.

[4] A. Andronic, private communication, 2018.

SPADIC Baseline in 2017 DESY test beam data

A. Meyer-Ahrens, A. Andronic, F. Fidorra, P. Kähler, C. Klein-Bösing, M. Kohn, H. Morgenweck, P. Munkes, P. Schneider, and R. Weber

Institut für Kernphysik, Münster, Germany

Baseline calculation

In 2017, test beam measurements with several CBM-TRD prototypes were conducted at DESY with electron beams at momenta ranging from 1 to 4 GeV/c [1]. As absolute trigger thresholds were used during the whole measurement campaign, a precise knowledge about position, width and time behaviour of the baseline is crucial. For this purpose, the three following methods to determine the baseline in this larger setup-size have been tested:

1. First sample of self-triggered messages (sample[0])
2. Second sample of self-triggered messages (sample[1])
3. Last sample of neighbour-triggered messages with small maximum ADC values (sample[31])

The positions of the named samples are fixed to the relative position of the pulse via the trigger condition, and thus, all carry information about the baseline. While method 1 is the default, the other two were used mainly as reference values to distinguish between real changes in the baseline and noise. ADC spectra of the used samples are plotted in Fig. 1. As can be seen, the spectra of sample[0] and sample[1] nearly coincide. Since, in most cases, sample[2] will be still beneath the lower trigger threshold and the signal shape has a short peaking time of 240 ns (= 3.84 TS), it was to be expected that the signal does not rise significantly between sample[0] and sample[1]. On the right side of both of these spectra, there is a "shoulder" of values considerably higher than the calibrated baseline. This is caused by triggering on the falling tail of a previous signal. With the SPADIC's hit logic, a signal coming from above and falling between the thresholds for just one or two samples can also fulfil the trigger condition. As the first and second samples of these signals do not carry any information about the baseline, the Gaussian fit is only applied in the range of -256 to -205 ADC.

A fit over sample[31] always gives a slightly higher baseline position, since the value of sample[31] is correlated with the maximum ADC of the signal, as can be seen in Fig. 2.

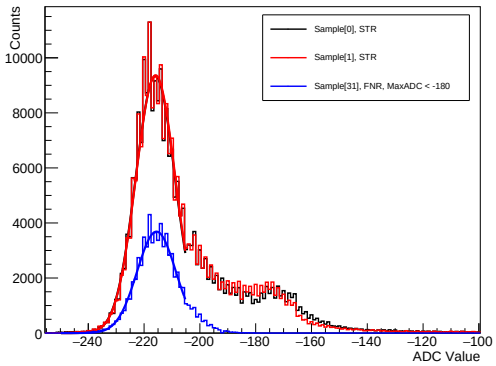

Figure 1: ADC spectra of the samples used for the three proposed methods for baseline determination, each fitted with a Gaussian function (Xe/CO_2(80:20), Anode HV = 2000 V).

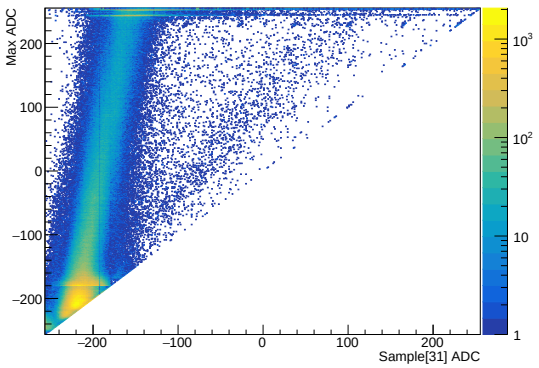

Figure 2: Maximum ADC value plotted against the ADC value of sample[31] for self or neighbour triggered messages on all channels (Xe/CO_2(80:20), Anode HV = 2000 V).

Baseline behaviour with time

As a next step, the fit results for 46 consecutive TSA files have been compared. We define the width of the baseline here as two times the sigma of the fitted Gaussian. The calculated baseline positions and widths can be seen in Fig. 3. Evidently, the baseline position does change over time, even though this change is very small (about 1 ADC), but as the results of all three methods are correlated, they are interpreted here as actual baseline shifts.

In the lower panel of Fig. 3 three clear discontinuities, in which the baseline width drops significantly, can be seen, located at around 100 s, 450 s and 780 s, respectively. In the time of recording of these three TSA files, a "PETRA III top-up" [2] happened, resulting in almost no incoming

beam for half of the time recored in these files. As a TSA file is limited in data size and not in time of recording, these three files span over longer time than the other files, as indicated by the larger horizontal error bars. Why the baseline position and especially its width drops significantly at a PETRA III top-up is not yet fully clear. While it could also be a reconstruction artefact, it would otherwise suggest a load dependence, though a verification of this is non-trivial. If a higher load, quantified by an increased hit rate, would raise baseline position and width, so would a raised baseline position and width increase the hit rate, as absolute thresholds were used. For a disentanglement of these two effects, more refined measurements and analysis have to be conducted. A test setup, specifically for in depth baseline measurements, is currently being installed in the laboratory in Münster.

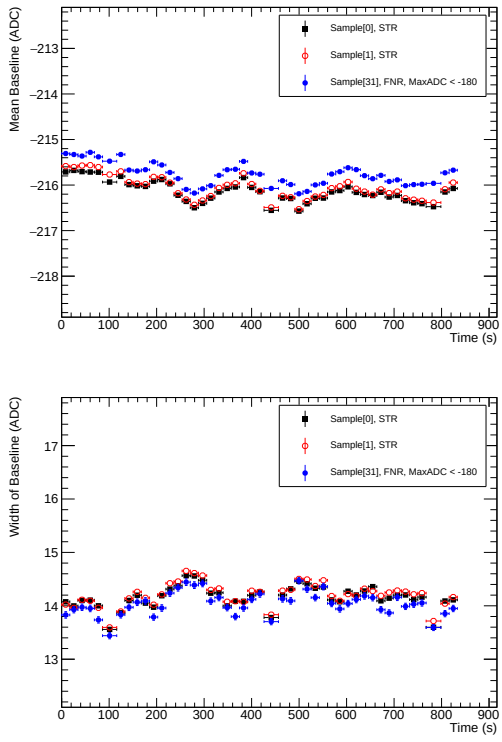

Figure 3: Baseline positions (upper panel) and widths, determined as 2σ of the Gaussian fit (lower panel) of channel 6 determined by Gaussian fits for the sample[0], sample[1] and sample[31] methods plotted against time (Xe/CO_2(80:20), Anode HV = 2000 V).

Correlation of different channels

To check for correlations between different channels, the baseline positions and widths determined by using sample[0] on four channels have been plotted in Fig. 4. Since the channels 5 and 7, as well as the channels 4 and 6 behave very similarly to each other, one can conclude that the baselines of neighbouring pads are correlated. As channel 4 and 6 were located in the beam spot, thus receiving higher statistics, they have generally less statistical fluctuations, but are affected more strongly by the PETRA top-ups. Generally, the width of the baseline needs to be reduced substantially to achieve the design value. We note that a good detector energy resolution was measured in the lab with a ^{55}Fe source [3].

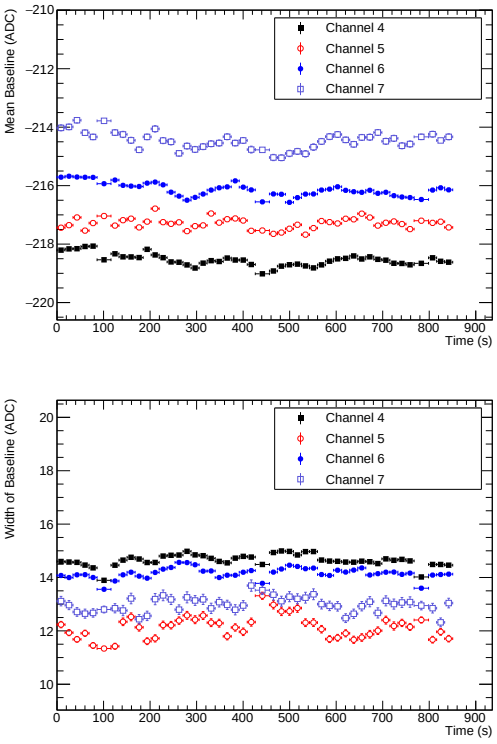

Figure 4: Baseline positions (upper panel) and widths, determined as 2σ of the Gaussian fit, (lower panel) of the channels 4 to 7, calculated with the sample[0] method plotted against time. The channels 4 and 6 were located in the beam spot, the channels 5 and 7 outside of it (Xe/CO_2(80:20), Anode HV = 2000 V).

References

[1] F. Roether et al., “Electron test beam campaign of the CBM-TRD at DESY”, CBM Progress Report 2017, p. 93.

[2] R. Diener et al., “The DESY II Test Beam Facility”, 2018, https://arxiv.org/abs/1807.09328.

[3] J. Beckhoff, ”Automated Test Stand Setup and Signal Reconstruction for the CBM-TRD”, Masters Thesis, 2018.

FEE readiness of Bucharest TRD chamber for mCBM

A. Bercuci, V. Cătănescu, M. Petrovici, L. Radulescu, and C. Schiaua
National Institute for Physics and Nuclear Engineering (IFIN-HH), Hadron Physics Department, Bucharest, Romania

The most inner 10 TRD modules of each layer of the TRD wall in the CBM experiment are exposed to high rates of particles often in pile-up regime. To disentangle individual hits and reconstruct incident position and energy deposit, the Bucharest-prototype is designed around two features: triangular-shaped pad-plane for 2D position sensitivity and non-diagonal self-triggered singled-value read-out ASIC - FASP (Fast Analog Signal Processor) [1] for optimal data load. An almost exact replica of the CBM modules will be installed in the mCBM setup [2] at SIS18. The prototype of 59×59 cm^2 with 2880 readout channels is operated by 180 FASPs mounted on 30 FASPRO boards. For the mCBM experiment a new FASP version ($v03$) is prepared and a 6-FASPs FASPRO (FASP Read-Out) board has been produced and tested ($v02$).

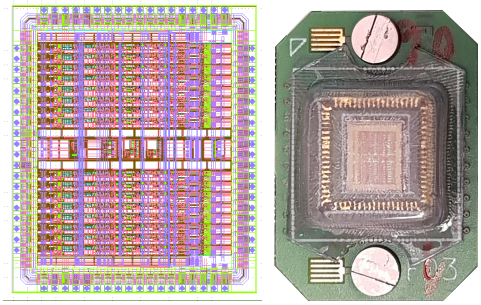

Figure 1: The third version of the FASP ASIC prepared for mCBM test in the design phase (left) and after bonding and ready for integration (right).

The FASP $v03$ prepared to be used at mCBM has improved analog circuitry and most notably a new processing logic for neighbor readout. This is a DCS selectable feature of FASP which can be used to process channels which do not self-trigger but are neighbors of such a channel. This feature is used in tracking optimized applications to improve position resolution by increasing the cluster size by two. A key feature of the FASP (available also on $v02$), related to the triangular-shaped read-out pad, is the neighbor input channels summation yielding the geometrical rectangular and tilt pairing of the pads with application in 2D position sensitivity. The ASIC in the CADENCE implementation is presented in Fig. 1 left and, respectively on the right, after being bonded on its board. Particularly the FASP board is handy as it can be used on a variety of integration boards for testing, calibration or production, via an $interposer$ [3].

The FASP $v03$ was tested on a test board already available from the previous version. The analog and digital processing of the chip are transparent from the curves in Fig. 2. A step like signal of 80 mV amplitude @1 kHz is injected on the 10$^{\text{th}}$ input (top panel). The internal pairing of the FASP will produce $in(9) + in(10) \rightarrow out(10)$ and $in(10) + in(11) \rightarrow out(11)$. As $in(9) = in(11) = 0$ in our test, the amplitudes on $out(10)$ and $out(11)$ are equal and synchronous as can be seen in the middle panels of Fig. 2. The self and neighboring trigger mechanism is shown in the bottom panel. The signals labeled *"CS-Ch10"* and *"CS-Ch11"* are self-triggers on the output channels $out(10)$ and $out(11)$, with signal over threshold. Additionally, neighbor-triggers appear on the 9$^{\text{th}}$ and 12$^{\text{th}}$ channels, delayed wrt. to the self-triggers, which mark the digitization gate for under-threshold signals (if any). For completion the digital signals for the second order neighbors, the 8$^{\text{th}}$ and 13$^{\text{th}}$ channels, are also included to show that no signal is generated outside the requested range.

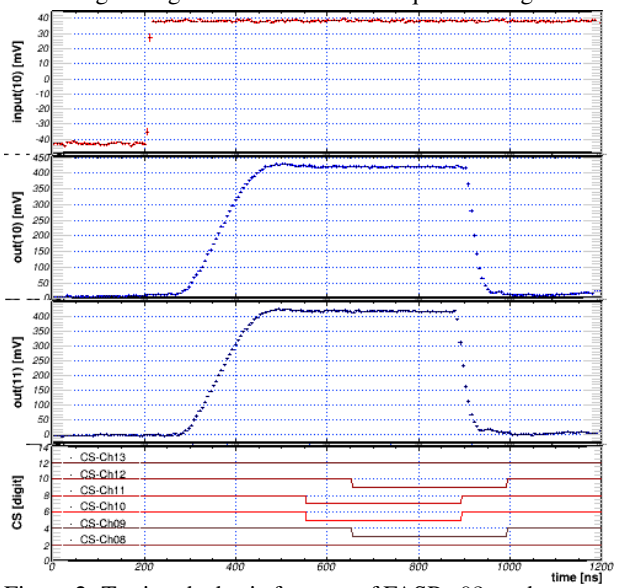

Figure 2: Testing the basic features of FASP $v03$ on the test board during 1.2 μs. From top to bottom: the input on pad entry 10, the summed analog output on channels 10 and 11 and the digital self-trigger signals on channels $8 - 13$.

The FEE operation of the Bucharest-prototype for mCBM is based on integrating six FASP chips on a FASPRO board, chaining three by three FASPs on two rows (see Fig. 3). Signal digitization happens on board steered by FASP channel-wise triggers, on commercial ADCs (one for each FASP output channel). The FEE runs at a 80 MHz clock frequency, double relative to the old $v02$ FASP, successfully tested on laboratory as seen in Fig. 4. The first

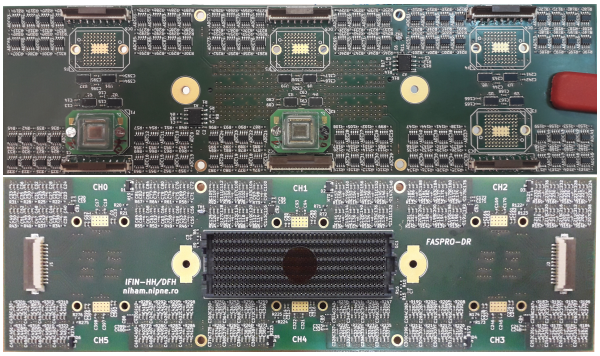

Figure 3: The 6-FASPs FASPRO board ($v02$) prepared for mCBM integration; its back-side toward the detector, housing the FASPs (top) and its front-side towards GETS board housing the Samtec™ ASP connector (middle) and board-to-board connectors (left/right) (bottom picture). Two FASP chips are mounted on the bottom row slots during local testings (top).

batch of 10 boards were delivered by company and dedicated tests are in progress in our laboratory. Although conclusive tests on the fully equipped board can be only performed using the GETS (General Event Time-stamping Streamer) (not ready yet), some qualitative tests were already performed. One such test is the chip-to-chip communication on both the analog and digital lines, a test which was impossible on the test board used to characterize individual ASICs.

For the FASP-FASP communication tests only two chips were mounted on the bottom row as presented in Fig. 3/top while the rest of FASP slots were left empty. In absence of the GETS board the FASPRO was operated by providing all LV values and clock from outside. The reading of the signals was done directly on the board using the oscilloscope.

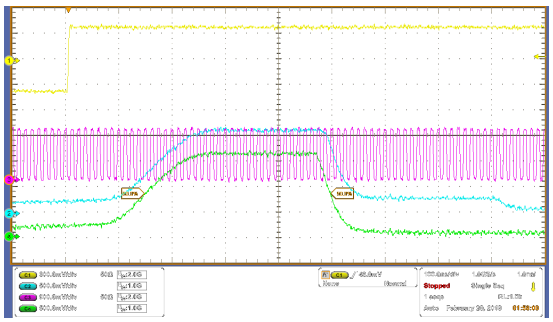

Figure 4: Testing FASP-FASP communication on the FASPRO board from Fig. 3. The input on $FASP-0/ch-15$ (yellow) is seen on the output $FASP-0/CH-15$ (green) and $FASP-1/CH-0$ (blue). The FEE operates at 80 MHz clock rate (magenta).

In Fig. 4 a snap-shot of 1 μs is taken with the oscilloscope. The input signal (yellow-top, label *C1*) is injected on the 15^{th} (last) channel of $FASP-0$ (bottom left in Fig. 3). It generates the direct output (green signal - label *C4* in figure) on the 15^{th} output channel of $FASP-0$ but also the indirect, blue signal (labeled *C2* in figure), registered on the first output channel of $FASP-1$. As one can see, the chip-to-chip communication is proven as both signals are of equal amplitude ($\approx$ 1 V) without noise. A second order communication is also present in our FEE, the board-to-board one, which is designed over the left/right connectors on the front-side of FASPRO (see 3/bottom) not tested yet.

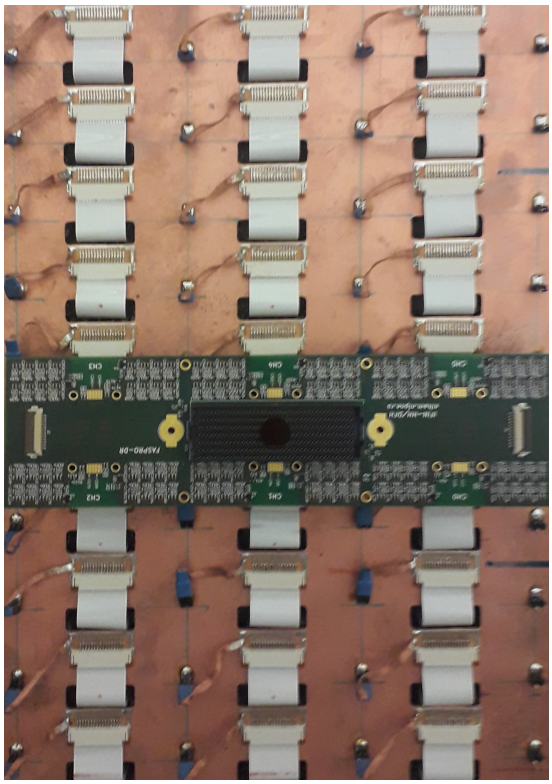

Figure 5: A region on the back-side of the Bucharest-prototype to be installed at mCBM. A FASPRO board is also mounted on the FC connectors for the first mechanical integration tests.

A region of the back-side of the TRD module to be installed at mCBM is presented in Fig. 5. The FASPRO board was tested mechanically on the module, as can be seen in the figure. The supporting structure of the FASPRO/GETS boards on the back-panel of the detector is in progress.

References

[1] G. Caragheorgheopol et al., CBM Progress Report 2015, (88) 2016.

[2] L. Radulescu et al., CBM Progress Report 2016, (176) 2017.

[3] A. Bercuci et al., 32^{nd} CBM Collaboration Meeting, https://indico.gsi.de/event/5863/session/25/contribution/28.

Data format and long term tests for FASP/GETS FEE in view of mCBM integration

A. Bercuci, V. Cătănescu, M. Petrovici, L. Radulescu, and C. Schiaua
National Institute for Physics and Nuclear Engineering (IFIN-HH), Hadron Physics Department, Bucharest, Romania

The free-running DAQ is just started to be explored by the physics community and complex tests are used to understand its potential. The CBM experiment at FAIR is going to operate at very high interaction rates using such a DAQ. A minimalistic clone of the CBM experiment, tagged as mCBM (mini CBM), having nevertheless the complexity of the final set-up, is installed at SIS18 facility of GSI. Testing the free-running DAQ of a heterogeneous detection system is a keyword in the mCBM program.

Long-term FASP/GETS stability

A TRD system proposed by the Bucharest TRD subgroup for the inner zone, around the beam-pipe of the TRD wall, is currently undergoing the final in-house tests before being integrated in the mCBM set-up. The DAQ used for operating the detector is based on the FASP (Fast Analog Signal Processor) ASIC [1] and its digital companion GETS (General Event Time-stamping Serializer) [2]. Here we report on the long-term stability of this system using a telescope of two small TRD Bucharest-prototypes mounted inside the laboratory. Several runs of Cosmic Rays (CR) of up to 48 hours were recorded in order to asses system stability, data format optimization and error management.

A particular interesting run was recorded on the 5^{th} of September[1]. The event (signal cluster) rates for each detector, labeled "TRD A" and "TRD B", are shown in Fig. 1 (top) as a function of time. For clarity, the time on the horizontal axis, is expressed as *day.month hour:min* and the moments of interest will be further referred as such. As expected, the rate registered by the bottom detector ("TRD B") is ≈ 1 Hz lower than the top one due to extra shielding. A rate of ≈ 1.5 Hz is recorded for the synchronous registration of hits in both chambers produced by through going CR tracks. The run was started around 15:00 before applying HV which can be seen in the null hit rate registered by both detectors in the first approx. 30 min of data taking. Afterward, for almost 20 hours, a flat profile is registered for the time dependence of the rate in both chambers and also for their synchronous detection. A peculiar deviation from this trend is registered on 6.09 at 11:00 (see Fig. 1/top - last approx. 30 min of data taking) which manifest itself as both an increase in the "TRD B" rate and a decrease in the CR tracks rate.

The TRD system prototyped here has, by construction, a build-in self time-correlation [3] mechanism obtained by

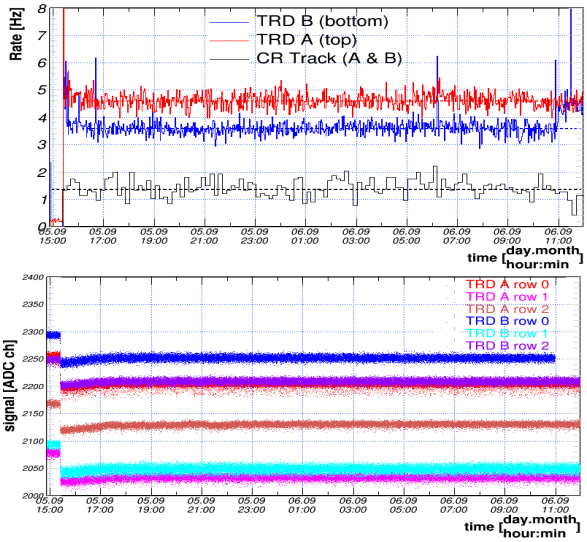

Figure 1: Long run CR rate measurements using a TRD telescope operated with FASP/GETS FEE (top). Monitoring the DAQ synchronization and capturing the clock skew on the curve labeled "TRD B row 0" on 6.09 at 11:00 AM local time (bottom).

feeding a constant rate fixed-amplitude signal through the anode wires in parallel with time registration of the signal front ($sync$ signal) on the DAQ. As both, the signal induced in the TRD read-out and the $sync$, are registered using the (same) DAQ clock their correlation provide a method of checking the synchronization of all GETS in the acquisition. Several other applications for detector control are also build on this synchronization system but they were discussed elsewhere. Using this feature of the Bucharest-prototype detector/FEE, the correlation from Fig. 1 (bottom) is obtained. For each GETS in the CR set-up, data from an (arbitrarily selected) output channel is recorded as function of time (in the same format as for the rate (top)) $only$ for events which are produced by the pulser, synchronous with the Master $sync$ signal. It is observed in the figure, that the GETS identified in the figure as "TRD B row 0" looses sync (stops) with the system. By comparing the top and bottom representations of the run one can see that the two events (rate modifications and sync loss) coincide in time and can be assumed cause-effect related by the following facts: if by $chance$ there is a clock skew on one GETS, the system will get back in sync with the DAQ clock automatically. Nevertheless the re-synchronization procedure will take same time and there-

[1]Thanks to Teodora-Maria Filip, Mihaela Marinescu and Lyudmil Ninyo from University of Birmingham which helped this work during their summer student internship.

fore the local timer (which defines the event time-label) will be off wrt. global DAQ. The signals broadcast by it, from this moment on, will have a time label shifted in the past with the re-synchronization time and thus unusable for the global event builder.

The situation described here, perfectly possible in any global clock driven system, spoils completely the free-running data. Synchronization loss in some out of many parts in a system driven by a global clock is a feature of such systems. Capturing and correcting such occurrences has to be done by adding redundant synchronization elements (e.g. our pulser) in the system. For a large system as the CBM, a standard mechanism for detecting and correcting such events is mandatory.

Rate optimized data format for FASP/GETS

The TRD Bucharest-prototype which will be installed at mCBM will have 2880 read-out channels. At an average signal rate of ≈ 0.5 MHz/channel the amount of data can easily explode to values which are non-sustainable in terms of costs/channel. A different problem appears at low rates (e.g. CR) where the amount of signals is low. In both cases one has to find the equilibrium between the amount of signal data (positive load) and the amount of data used to describe the time of their occurrence (used in signal matching). A common approach used in the CBM DAQ is to use a short-lived time-label attached to the signal itself and a long-lived signal-independent time-label (usually called "epoch") which extend the event time identification by marking the reset of the $signal$ time counter. Global time is recovered by contextual analysis of the message chain ($epoch$ and $signal$). Optimally, the ratio between $epoch$ to $signal$ messages should be constant and low as function of different data rates.

We have developed a data driven model for the network protocol and the data format which should scale with the rate. For our uniform message length of 64 bits the $signal$ time is expressed on 7 bits (i.e. 127×12.5 ns) while the epoch time counter is expressed on 21 bits and covers an interval of approx. 3.3 s. The $epoch$ message are defined at ASIC level and are send **only** when conditioned by the existence of data (in the current epoch) and not by any signal time counter resets. The GETS firmware is responsible to send only data for which also the epoch message can be safely written or otherwise an error message is send describing the number of epoch lost. The epoch time counter reset is send always as it is used in higher processing steps (CROB board) to issue the "super epoch" message.

In Fig. 2 a snap-shot of the GETS data flow was captured for exemplification. Additionally, the built-in synchronization mechanism described in the previous section is transparent in this figure. The first message in Fig. 2 is of $signal$ type ("messFASP") and contains the index of the FASP on the GETS (1 GETS operates 2 FASPs) id (here 1) and the FASP channel ch (here 11). It is followed by the signal time label tl (here 80) and the ADC value measured on the flat-top, $data$ (here 2234). The last information is an error code wrt. to ADC reading (here 0 no error). The message is followed by 9 other signal messages which are very similar to it as far as the tl and $data$ are concerned. This identifies a pulser event of synchronous, quasi-equal signal values in all channels (see Fig. 1 bottom). Since both FASP had data during current epoch, an epoch message is issued at the end (see label "messEpoch"). Following the pulser signal the data flow contains a reading of 4 $signal$ messages issued by FASP $id = 0$ on 4 adjacent channels and having the similar time-label $tl = 124$. This is identified as a cluster produced by a CR. Since the cluster is fully contained in FASP 0 only its $epoch$ message is send. The epoch counter of both FASPs is reset at the value 2097151 (to be compared with the epoch counter of the first CR hit 1860169 and last 130926). The "super epoch message" is issued there and the "super epoch counter" $SEpoch$ is incremented. Last 6 messages are a second CR hit happening with 5 signal messages and the corresponding epoch message at the end.

Figure 2: The data flow of GETS for CR detection with emphasizes on different type of messages and their time correlation.

The data format model implemented in GETS coupled with FASP analog signal processing assure the lowest data load on the transport lines for the TRD and easily scale with the rate. The format was tested for various incident rates ranging from CR to X-ray tube irradiation, i.e. above 10^5 photon/cm^s/s [4]. In all cases a scaling of data volume to incoming particle rate is observed.

References

[1] G. Caragheorgheopol et al., CBM Progress Report 2015, (88) 2016.

[2] A. Bercuci et al., CBM Progress Report 2016, (114) 2017.

[3] A. Bercuci et al., TRD TDR Review, https://indico.gsi.de/event/5809/contribution/12.

[4] A. Bercuci et al., 31st CBM Collaboration Meeting, https://indico.gsi.de/event/5862/session/21/contribution/38.

Data reduction by feature extraction

F. Roether[1], *C. Blume*[1], *E. Bechtel*[1], *and P. Kähler*[2]
[1]Institut für Kernphysik, Frankfurt, Germany; [2]Institut für Kernphysik, Münster, Germany

The data rate produced by the final CBM experiment of up to 2 TB/s will be a challenging task regarding data processing and storage. To reduce the raw data coming from the TRD, it is vital to extract only the necessary information. In this article different methods in the first stage of the feature extraction are compared.

Data flow in the final experiment

The Self-triggered Pulse Amplification and Digitization asIC (SPADIC) [1] is the centrepiece of the Front-end Electronic Boards (FEB) [2] and responsible for digitizing the analog signals coming from the detector. On a TRD module, up to 20 SPADICs are connected via e-links to a Readout Board (ROB) which aggregates the data streams and sends them via optical links towards the Data Processing Board (DPB). The DPB processes the data of multiple ROBs by a high performance FPGA.

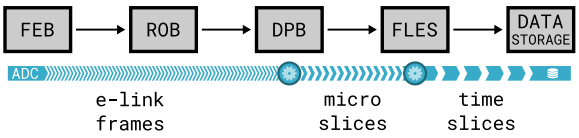

Figure 1: Data acquisition chain of the final experiment along with the data format used at different stages.

The goal is to utilize the FPGA for feature extraction and thereby to reduce the data volume as early as possible in the DAQ chain (see Fig. 1). After processing, the data is packed into micro-slices which are send to the First-level Event Selector (FLES). The FLES system performs online track reconstruction in 4D and full event reconstruction. All interesting events are selected and stored to disc.

Data reduction

The SPADIC is capable of digitizing all incoming signals, which are fulfilling the trigger condition with up to 32 samples. Under the high loads expected at SIS100, the data rate would exceed the available e-link bandwidth, leading to a loss of data. As the signal height is the only usable information to extract available the energy loss of a charged particle passing the detector, not all 32 samples are required. A configurable selection mask allows to control, which samples are read out. Simulations suggest that at SIS100, a selection mask with 7 samples should not exceed the available bandwidth. Figure 2 shows a single hit message on one channel. Due to the geometry of the detector chamber, the majority of physical hits will produce 3 to 4 spatially adjacent hit messages.

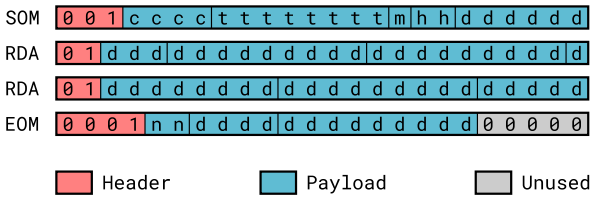

Figure 2: Example of a hit message with 7 samples. Since version 2.2 the SPADIC encodes the data in 24-bit frames.

For a configuration with 7 samples, this results in a total payload of 80 bits per hit message. The feature extraction process can be subdivided into separate stages (see Fig. 3). The first stage extracts the charge and refines the time information for each hit message individually. After this step, assuming that, besides 4 bits for the channel number, only time and charge information with 12 bits each is forwarded, the payload is reduced to 28 bits corresponding to a reduction of 65 %. At the second stage a cluster finding algorithm selects all hit messages which most likely belong to a single physical hit.

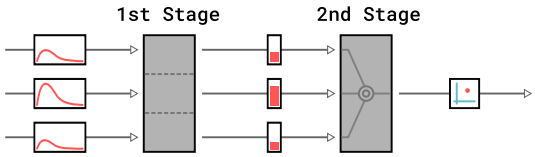

Figure 3: The two separate stages of the feature extraction process. In this example a hit resulting in three hit messages is reconstructed.

Based on the charge distribution on the different pads, the clusterizer can reconstruct the position according to the pad response function down to a resolution of 300 μm. 14 bits are needed to encode the extracted position information. Together with the time and charge information, this would sum up to 38 bits corresponding to a reduction of 54 % for a three pad cluster, respectively of 66 % for a four pad cluster. For both stages combined, this will result in a total data reduction of more than 80 %.

Feature extraction methods in the first stage

To evaluate different feature extraction methods under different conditions like noise and signal amplitude, signals where simulated according to the first order shaper implemented in the SPADIC 2.2:

$$f(t) = A \cdot \frac{t}{\tau} \cdot \exp\left(-\frac{t}{\tau}\right) \quad (\text{for } t > 0)$$

As a basis for the simulation, an intrinsic energy resolution of the detector of 10 % and a noise level of $\sigma_{\mathrm{ADC}} = 1$ was assumed. Figure 4 shows different methods used to extract the signal height of the simulated signals.

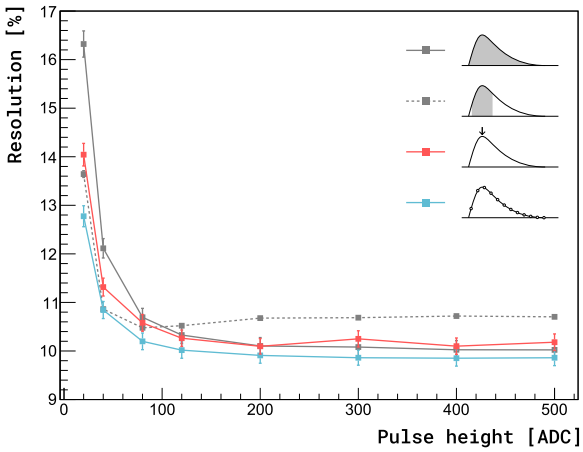

Figure 4: Comparison of the performance of different feature extraction methods.

The gray continuous line shows the methods in which the total charge is calculated as the sum over all 32 samples of the signal. As the full readout of all samples is unfeasible in the final experiment, an alternative method was tested, which is shown as the gray dotted line. This method uses just 7 samples around the peak of the signal.

An alternative approach, which shows good results, takes the maximal ADC-value (red line). The last method shown here applies a fit to the signal shape (blue line). Even though this concept yields the best results, an implementation on the FPGA of the DPB is not feasible, and serves only as an ideal benchmark for comparison. Towards smaller amplitudes, the signal to noise ratio deteriorates and presents a challenge for all feature extraction algorithms. In Fig. 5, the influence of the noise on the max-ADC method is shown. This demonstrates how important it is to minimize the noise as much as possible.

Conclusion and outlook

The saving potential on the data rate by the implementation of feature extraction algorithms on the DPB and the performance of even simple feature extraction methods are promising. Currently, more complex approaches, which

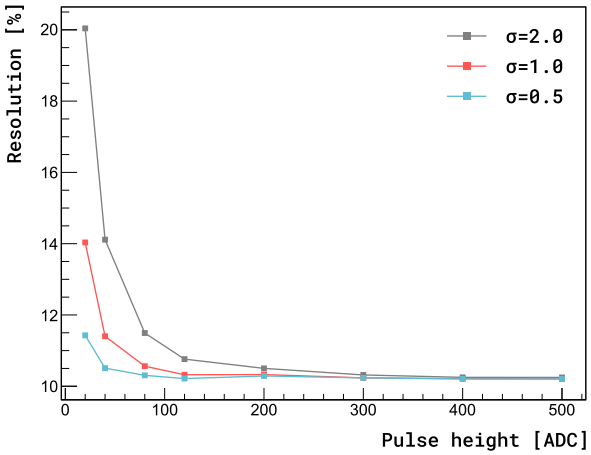

Figure 5: Influence of noise on the max-ADC method.

are still suitable for the implementation on an FPGA, are under investigation. Further methods to achieve a finer time resolution as well as cluster finding algorithms are under development.

References

[1] P. Fischer and M. Krieger, “Development of new SPADIC versions 1.1 and 2.0”, CBM Progress Report 2016, p. 109.

[2] F. Roether et al., “Front end board development for TRD”, CBM Progress Report 2017, p. 105.

TRD high-rate test beam at the CERN Gamma Irradiation Facility 2018

P. Kähler[1], F. Roether[2], A. Andronic[1], J. Beckhoff[1], C. Blume[1], D. Bonaventura[1], F. Fidorra[1], N. Heine[1], C. Klein-Bösing[1], A. Meyer-Ahrens[1], P. Munkes[1], and R. Weber[1]

[1]Institut für Kernphysik, Münster, Germany; [2]Institut für Kernphysik, Frankfurt, Germany

TRD setup at the CERN-GIF

In October 2018, measurements with CBM-TRD MWPCs have been conducted at the CERN Gamma Irradiation Facility (GIF^{++}) [1], during which the detectors have been exposed to the γ flux of a 14 TBq ^{137}Cs source and μ beam at the same time. Two modules were aligned in 1:1 coverage with respect to the passing μ beam. As μ reference counter, two scintillators of the GIF have been used, which are permanently installed outside the GIF cave and thus are shielded from the GIF source irradiation field, but passed by the μ beam only. A third scintillator has been installed directly in front of the TRD MWPCs, matching the active (recorded) area of the tested detectors. A sketch of the different detectors is shown in Figure 2.

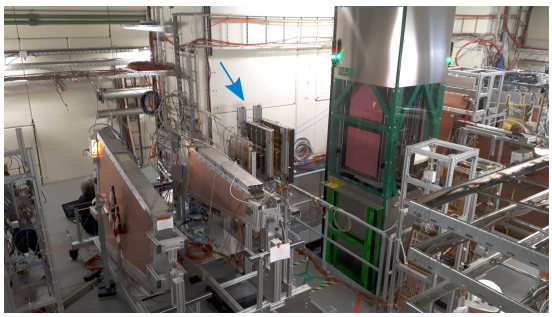

Figure 1: Two TRD MWPCs (arrow) installed in the downstream field of the GIF irradiator, and in-line with the μ beam from CERN-SPS/T2/H4.

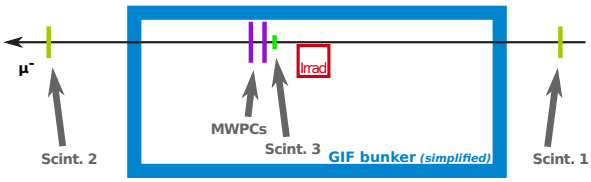

Figure 2: Sketch of the setup, showing relative distances. The inner red box marks the position of the GIF ^{137}Cs irradiator, while the μ beam is sketched as a black line.

NIM coincidence units have been used to detect, in a first coincidence level, μ passage through the outer scintillators. For a second level, coincidence of all three scintillators has been required. Both coincidence signals were injected in the SPADIC/FLES system using a SPADIC 2.0 FEB with LEMO connectors and analogue signal adaption. This signal routing has been checked by comparing the SPADIC measurement with one performed with the NIM μ counting system of the GIF, with noted deviations all below 0.7 %. Expected routing latencies have been documented.

Measurements

The MWPCs have been operated with Xe/CO_2(85:15) at an anode voltage of 1850 V (530 V/mm). Oxygen contamination and humidity of the detector gas have been monitored continuously in the gas return line. Measurements have been taken with SPADIC 2.0 at 16 MHz sampling frequency in self-triggered mode plus forced-neighbour readout on the adjacent detector pads. The front-ends were directly connected to one AFCK board running in *SimpleMicroslice* mode. Default setting for the transmitted samples per trigger was a selection mask 0–2–4–6–7–8–10–12, resulting in a SPADIC word pattern `SOM TSW RDA CON CON CON CON EOM` and thus 8×16 bit transported in 8×24 bit-frames per channel per trigger. The readout settings and in particular the mentioned selection mask have been chosen based on experiences from the GIF campaign in 2017 as a compromise between low/effective e-link usage and full information content concerning the detector signals.

It was possible to record FLES data at GIF attenuator settings from 460 up to 10, thus providing a wide range of load on the detectors, with μ reference signals in the same data stream. It has been found, that the radiation level seen by our detectors in the downstream field depends also on the attenuator setting for the upstream field, which is believed to be caused by backscattering directly in the upstream attenuation filters and maybe also by materials in this field. In case other users were granted a change in the upstream settings, we tried to achieve measurements of both situations (before/after) with constant downstream settings to enable a direct evaluation of the upstream influence.

For each attenuator setting, two levels for the drift field in the MWPCs have been set.

Analysis and first results

In a first step of analysis, a hit rate determination from the recorded data has been approached. To ensure independence from the efficiency of clusterisation algorithms, this analysis has been implemented on single message (pad) level. The frequency as estimator for the detector load from the GIF irradiator is determined then by hit counting in fixed time windows, off-spill of the μ beam. In case of self-triggered hits, with only accompanying neighbour-triggered pads, direct counting is done; while for more than

one pad fulfilling the trigger condition in a group of adjacent, the number of hits is divided by the mean size of such objects. Stabilisation against the known loss effects in the SPADIC 2.0 message builder still can and has to be increased: due to conditions in the chip-internal signalling, up to two consecutive SPADIC words can erroneously be considered as corrupted and will therefore finally not be sent by the e-link interface of the chip [2]. In the SPADIC unpacking as currently implemented in CbmRoot, affected messages with missing words are consequently being discarded. A careful treatment of canonically unexpected word patterns in the unpacker code would enable to win back the time information and/or originating pad coordinate in most of the cases. So far, the expected effect is considered in the uncertainty estimation of the hit rate determination.

Figure 3 shows anode and drift currents as measured with the supplying HV units in dependence of the mean counting rates per pad, which corresponds to a counting rate per $1\,\mathrm{cm}^2$ of detector surface. The found current scaling is compatible with a linear description, which is interpreted as stable detector gain in the tested detector loads.

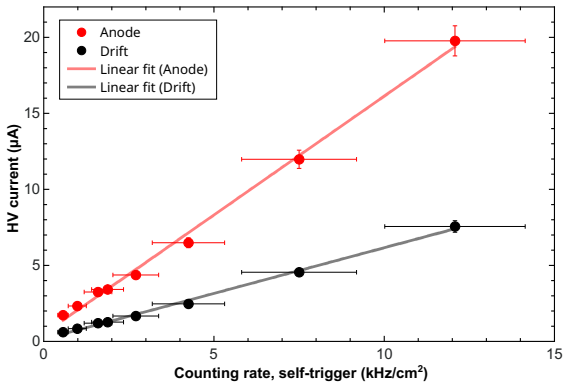

Figure 3: Measured HV anode and drift currents wrt. counted hit-rates per per pad ($1\,\mathrm{cm}^2$). Anode voltage of $1850\,\mathrm{V}$ and drift voltage of $500\,\mathrm{V}$. The current scaling is found to follow a linear correlation up to the highest measured detector load.

After this linearity is being found, the anode currents are seen as a measure for ionisation in the active gas volume, and therefore expected to be the decisive absolute descriptor for detector load. A comparison of the primary energy deposition per event in this measurement and as expected in the CBM is currently being prepared.

Furthermore, the μ detection efficiency is to be determined with respect to the detector load from the recorded data. To do so, the selection of μ events in the data streams of the both MWPCs in correlation with the scintillator is targeted.

References

[1] M.R. Jäkel *et al.*, "CERN GIF^{++}: A new irradiation facility to test large-area particle detectors for the high-luminosity LHC program", PoS(TIPP2014)102, 2014.

[2] M. Krieger, "SPADIC design review", Talk, SPADIC 2.2 Submission Review, GSI, 2018.

Energy resolution and gain measurements for the TRD chamber configuration proposed for the inner zone of the CBM-TRD

A. Bercuci, V. Cătănescu, M. Petrovici, L. Radulescu, and C. Schiaua
National Institute for Physics and Nuclear Engineering (IFIN-HH), Hadron Physics Department, Bucharest, Romania

The TRD (Transition Radiation Detector) of the CBM experiment is instrumental in complementing the TOF (Time of Flight) detector for particle tracking and PID. Particularly, for the regions close to the beam drain (forward rapidity), where particle rates can reach values up to 10^5 cm^{-2}s^{-1}, a good energy resolution has to be coupled with position separation capabilities to disentangle time-space overlapping particles. The 2D position reconstruction capabilities of the Bucharest-prototype coupled with an efficient and minimalistic data readout can provide a serious candidate for a TRD implementation in this region. The PID performance of the detector was tested in various situations before [1] but a systematic study of the actual detector+FEE system wrt. energy resolution was lacking. Here we present the results obtained in laboratory conditions using X-ray induced signals from a 3.7 GBq ^{55}Fe radioactive source. The detector was operated using FASP (Fast Analog Signal Processor) /GETS (General Event Time-stamping Serializer).

In this study, which lacks an operational NE (Neighbor Enable) feature, the 02 version of FASP was used. The third version of the ASIC, including an operational NE, is produced, tested and ready for integration at mCBM [2]. Such feature on the FEE coupled with a larger conversion range will have positive implications on the energy resolution.

The method of cluster reconstruction using the data from the TRD Bucharest-prototype was described elsewhere [3]. It was shown that position information perpendicular to the anode wires can be obtained using triangular pads and the FASP readout by identifying the anode wire where the amplification avalanche takes place. Such position information is mandatory in selecting the photons which interact in the middle of the row and generate a signal fully contained in one pad row, avoiding systematic effects happening at row boundaries. A correlation between anode index and position wrt. to center of a rectangular coupled signal is observed also with the cluster size. All these systematic effects were included in a differential analysis of the reconstructed energy spectrum as a function of cluster size, maximum signal type ("T" *tilt* and "R" *rectangular* coupled signal) and anode wire id (4 being in the middle of the row). In Fig. 1 (top) the reconstructed energy spectrum is shown for a selection of clusters of size 5 being localized within an area of 3 columns ($\approx$ 2.2 cm) on the middle row on the anode wire 5 and maximum signal of type tilt paring "T" (label "Raw spectrum" in figure).

The energy calibration procedure is based on identifying the structures observed in the measured spectrum with energy deposits based on ^{55}Fe decay BR and X - $ArCO_2$ interaction. We have considered the following Fe lines $K_\alpha = 5.895$ keV (89%), $K_\beta = 6.492$ keV (11%). Considering only the photoelectric effect on the Ar K-shell (binding energy 3.2 keV) and the Auger electron of 2.7 keV and emission probability of 88% one can model a 4 spectral components with the following energies and theoretical abundances: 5.992 keV (9.7%), 5.395 keV (9.7%), 3.292 keV (1.2%) and 2.695 keV (9.8%). The spectral decomposition of the reconstructed energy spectrum is presented in the figure under the label "Model components"; the 5.992 keV component in red and the 5.395 keV component in blue. The sum of the 4 components is shown in green under the label "Model 4Gauss". The difference between the reconstructed spectrum and the theoretical 4 components spectrum is shown as "Residual spectrum".

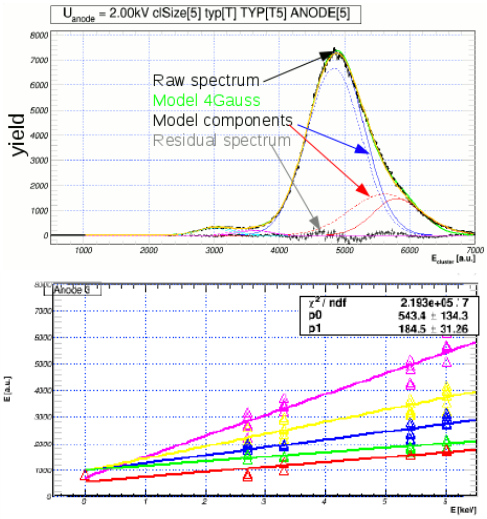

Figure 1: Spectral deconvolution of the ^{55}Fe spectrum using four components for selected clusters based on readout topology (top). Energy calibration for a range of 5 anode voltages (bottom).

The relative amplitude and the flatness of this last graph demonstrate the quality of the fit. In Fig. 1 (bottom) the results of spectral deconvolution for a variety of cluster shapes is shown for five anode voltages, in the order of decreasing slope, 2.00, 1.95, 1.90, 1.85 and 1.80 kV. For each anode voltage a linear correlation is found between the theoretical energy of the spectral component (horizontal axis) and the measured value of the peak defined as the mean of the Gauss model. The slope of the fit is proportional to the detector gain and the intercept at origin is a

measure of the FEE baseline and amounts for the spectrum shift upwards.

Due to various systematic effects in cluster reconstruction, estimations as presented in Fig. 1 (bottom) were repeated for all 9 anode wires serving one pad row. The values for the slope obtained for each pair $(U_{anode},\ ID_{anode})$ (excepting the anode wires which are on the row boundaries), are represented in Fig. 2 (after a common offset was forced on all energy calibration fits) as function of the U_{anode}. For each ID_{anode} an exponential fit is performed. Excepting two outliers, all exponential model describing the gain dependence on the applied polarization have similar parameters thus proving the method consistency.

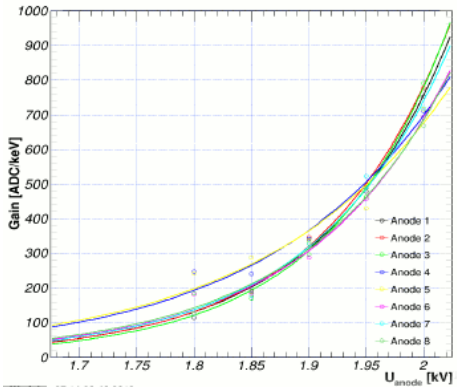

Figure 2: The exponential model (continuous lines) describing the TRD gas gain dependency on the anode voltage fit through the energy calibration slopes of 7 out of 9 anode wires.

A uniform description of the TRD energy calibration is obtained from the fits in Fig. 2 from the expression: $E[\text{keV}] = (E[\text{a.u.}] - E_0)/G$ and $G = \exp(a + b \times U_{anode}[\text{kV}])$ with E_0, a and b being the parameters describing the TRD detector for all polarization conditions.

To test the gain calibration procedure we present the results obtained on the 2 kV anode and 0.8 kV drift polarizations in Fig. 3. The measured spectrum, the hatched area, is obtained after the cluster reconstruction procedure, selecting only clusters which are fully contained in one pad-row (middle) and having anode ID in the middle 12 mm of it. A spectral decomposition procedure is applied using 4-Gauss components, each centered on the theoretical value but having the width (σ_G) and the relative yield ($\mathcal{Y}$) as free parameters. The four components are presented in the figure legend, identified for the main (E) and escape (e) peaks and the two ^{55}Fe lines α and β. Beside each component the resolution, $\sigma[\%] = \sigma_G[\text{keV}]/E[\text{keV}]$ is indicated. The quality of the spectral decomposition is also suggested by including the residual spectrum (dark shaded). Several statistics are also presented in the figure regarding the relative yields of the four spectral components:

- *Main Peak :* K_α is $\mathcal{Y}(E_\alpha)/\mathcal{Y}(E_\beta)$. Estimated value is 4% under the theoretical value (green label 89%) which can be explained by considering the residual spectrum which suggest both an underestimation for E_α and overestimation for E_β.
- *Escape Peak :* K_α is $\mathcal{Y}(e_\alpha)/\mathcal{Y}(e_\beta)$. Estimated value is $\approx 30\%$ under the theoretical value which may be explained by a drop in efficiency reconstruction for the $\approx$ 2.7 keV component. See next item also.
- *Auger*$_\alpha$ is $\mathcal{Y}(E_\alpha)/\mathcal{Y}(e_\alpha)$. The estimation exceed the theoretical value of 88% by 7.5% suggesting a drop in reconstruction efficiency at low energies by incomplete charge recording (threshold effects).
- *Auger*$_\beta$ is $\mathcal{Y}(E_\beta)/\mathcal{Y}(e_\beta)$. In good agreement with estimation given the systematic errors on the two yields.
- *Auger*$_{data}$ is $[\mathcal{Y}(E_\alpha) + \mathcal{Y}(E_\beta)]/[\mathcal{Y}(e_\alpha) + \mathcal{Y}(e_\beta)]$. The estimation in good agreement (3% difference) with theoretical value (can be explained by a decreasing efficiency at low energy deposits).

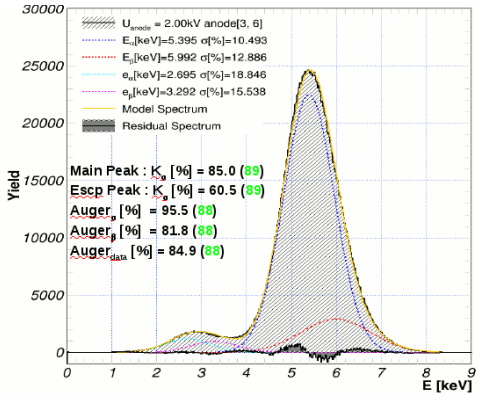

Figure 3: Reconstructed ^{55}Fe spectrum measured at 2 kV anode voltage for the four most central anodes and various measured statistics of yields for the spectral components as compared with the theoretical values (green).

The results presented in this report describe the method of energy calibration for the Bucharest-prototype of the TRD chamber for all polarization conditions during data taking. The calibration is tested, using a systematic free procedure, by comparing various statistics obtained based on a four component decomposition of the measured ^{55}Fe spectrum with their theoretical values. Preliminary results based on FASP version 02 are very promising. New measurements/calibrations for the new FASP, version 03, are in progress and the slightly lower efficiency observed for the 2.7 keV peak is supposed to be corrected.

References

[1] M. Petris et al., Nucl. Instrum. and Meths., A732 (2013) 375.

[2] A. Bercuci et al., "FEE readiness of Bucharest TRD chamber for mCBM", this report.

[3] A. Bercuci et al., 32nd CBM Collaboration Meeting, https://indico.gsi.de/event/5863/session/25/contribution/31.

Humidity in the gas system of the CBM-TRD

R. Weber, P. Kähler, A. Andronic, J. Beckhoff, F. Fidorra, C. Klein-Bösing, M. Kohn, A. Meyer-Ahrens, H. Morgenweck, P. Munkes, and P. Schneider
Institut für Kernphysik, WWU Münster, Germany

Measurements on humidity in the detector gas of a CBM-TRD module have been conducted [1]. Diffusive and storage-like components of materials in contact with the gas have been disentangled. For these measurements, a setup of a small-size TRD prototype ($57 \times 57\,\mathrm{cm}^2$) and polyamide hoses has been used, which is a realistic representation of current in-house and in-beam TRD measurements.

These efforts lead to the conclusion that regularly used polyamide hoses contribute to a large amount of humidity in the gas system. Concerning the detector modules, diffusion of humidity through parts of the detector material has also been found. In the following their overall contribution is being investigated. The detector gas humidity and contributions from system components are important knowledge relevant for the design of CBM-TRD gas system.

Measurements

The setup used for the investigations (see Fig. 1) consisted of an acrylic hood, enabling the creation of a humidity-controlled atmosphere around the TRD module. The module and parts of the supplying detector gas lines were positioned inside this volume. The ambient humidity inside the hood was influenced using a dry air supply. Every part of the tubing outside the hood and upstream of the sensors was made of steel. The ambient temperature and humidity were logged, as was the flow of the used gas (*Sagox* 18: Ar/CO_2 (82/18)), the humidity and oxygen concentration inside the gas system and the pressure difference between in- and outside of the system.

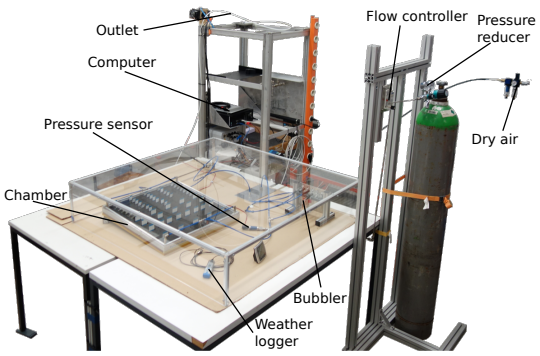

Figure 1: A picture of the experimental setup.

The fraction of humidity induced by the polyamide hoses is measured right before and right after a measurement with the investigated TRD module. This development of the humidity concentration was fitted using a function based on a similar situation described in [2, p. 72].

Basic tightness of the installation is ensured by monitoring the oxygen concentration which is sufficiently low at the order of magnitude of 40 ppmV at a gas flow of 3 l/h. A measurement with the TRD module was conducted over a period of several weeks in which the ambient humidity and the flow were changed. A change of temperature took place in this period of time.

In the first 186 h of the measurement the humidity concentration decreased continuously for stationary conditions of the system. After 186 h, the humidity concentration was nearly constant at around 3760 ppmV.

Subsequent to this first decrease, the ambient humidity was reduced rapidly. After this reduction, the humidity in the gas system is around 1150 ppmV (after 400 h of measurement time, see Fig. 2). This decrease of humidity is due to a drying of the chamber, since all materials without the chamber have been shown to be constant under change of ambient humidity before.

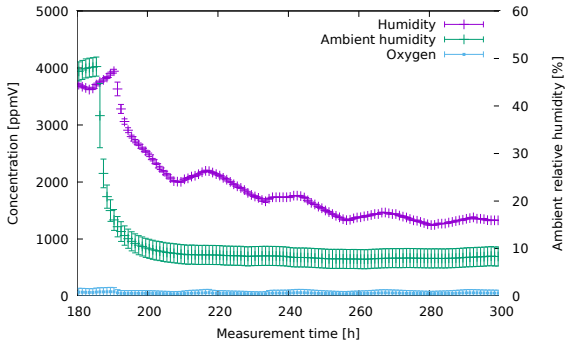

Figure 2: The development of the humidity concentration inside the gas system after drying the acrylic hood, beginning at 186 h measurement time, and the ambient relative humidity.

In a next step, the detector gas flow has been doubled to approximately 6 l/h. The measured humidity values did decrease from around 1170 ppmV (at 405 h measurement time) to around 630 ppmV (at 450 h). This concentration is approximately constant until the next step at 548 h measurement time.

After approximately 548 h the gas flow gets reduced to its original value of 3 l/h. The result is a jump of

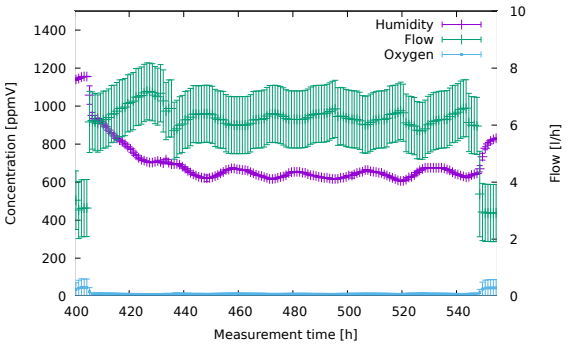

Figure 3: The development of humidity and oxygen concentration and the ambient gas flow.

the humidity concentration from 650 ppmV (at 548 h) to 830 ppmV (at 555 h, see Fig. 3). An increase was expected, since constant diffusive humidity contributions are less diluted in the lower flow rate. On the other hand, the overall falling trend with time continued, which is attributed to continued drying of storage-like components.

In the last step of the measurement, the hood is lifted from the setup (at 862 h measurement time) leading to the gas system being exposed to room conditions again. As a result the humidity concentration inside the gas system jumps up from around 830 ppmV at 861 h measurement time to around 1550 ppmV at 875 h measurement time. Since this increase is induced purely by the increased ambient humidity, it is interpreted as diffusion of humidity into the chamber.

Besides the dependency of the ambient humidity a dependency on the ambient temperature can be observed in this part of the measurement.

Conclusion

The rate at which humidity enters a $57 \times 57\,\mathrm{cm}^2$ prototype depends on the ambient humidity and the ambient temperature. After 1196 hours of measurement the rate at which humidity enters the gas system via the chamber is $1.57 \pm 0.66\,\mathrm{ml/h}$, while the ambient humidity is $(35.8 \pm 2.0)\,\%$ and the ambient temperature is $(20.5 \pm 0.3)\,^\circ\mathrm{C}$.

The entrance window made of aluminum coated (50 nm) *Kapton* foil is suspected to be the responsible component for water diffusion into the chamber [3]. This assumption is based on the observation of such diffusion also in other measurements [4].

A measurement with specific control on the environmental air volume contacting the entrance window is currently being prepared.

References

[1] R. Weber: *Feuchtigkeit im Gassystem des Übergangsstrahlungsdetektors im CBM-Experiment*, Bachelors-Thesis, Institut für Kernphysik, WWU Münster, Sept. 2018.

[2] M. Wutz, H. Adam, W. Walcher: *Handbuch Vakuumtechnik* Theorie und Praxis der Vakuumtechnik. Sechste Auflage, Vieweg, Braunschweig, 1997.

[3] Dupont™: *Dupont™ Kapton® Summary of Properties*, 2017.

[4] L. Murray: *The Impact of Foil Pinholes and Flex Cracks on the Moisture and Oxygen Barrier of Flexible Packaging* Alcan Packaging, Neenah Technical Center, 2006.

Simulation developments for the CBM-TRD

E. Bechtel and C. Blume
Institut für Kernphysik, Frankfurt am Main, Germany

The TRD will deliver particle identification crucial for the investigation of rare dilepton channels and will be able to separate charge states for the hypernuclei program. For the best understanding of the detector it is necessary to simulate all effects as realistic as possible, in order to get the best overview of all expected performances and possible issues. By implementing the front-end electronic algorithms in the simulation it is now possible to study all detector aspects in more detail. Since the Monte-Carlo information generated by Geant only contains the total charge deposition, but does not calculate the ionization at specific positions inside the gas volume, this has to included in the digitization step, e.g. to account for statistical fluctuations in the ionization process. The charge is now distributed according to the Bethe-Bloch curve for Xe [2] (see Fig. 1) to calculate the integrated probability for an ionization to happen at a certain distance using Eqs. 1 and 2.

$$P(s) = \frac{1}{D} \exp\left(-\frac{s}{D}\right) \tag{1}$$

$$D = \frac{1}{\langle N_{prim} \rangle \cdot f(\beta\gamma)} \tag{2}$$

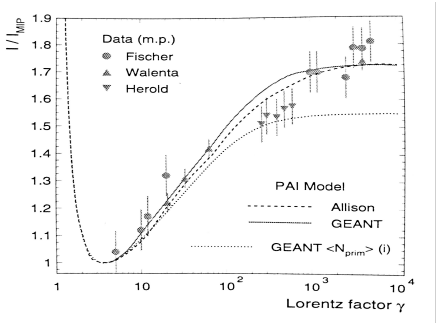

Figure 1: Relative energy loss in Xe [2].

Afterwards, the charge is distributed to different read out channels via the Pad-Response-Function (PRF) based on the Mathieson formula (see Fig. 2). With these steps we get multiple little ionizations at different positions along the track of the particle, together with their induced charges on each read out channel around its original position. In reality the ion drifts, which are collected by the front-end electronics, are formed into pulse shapes corresponding to the shaper function in Eq. 3 [1],

$$g(t) = A \cdot \left(\frac{t}{\tau}\right)^2 \cdot \exp\left(-\frac{t}{\tau}\right) \tag{3}$$

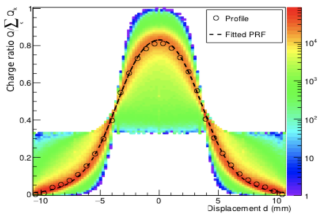

Figure 2: Measured charge distribution of a charged particle passing through the detector and creating a signal on three adjacent readout channels [1].

where τ is the peaking time and A is a calibration factor.

The calculation of the actual pulses and the conversion of their charge values into ADC channels allows for realistic investigations of energy resolutions with different reconstruction methods, precise studies of trigger behaviour and better handling of correlated and uncorrelated noise, as well as crosstalk between the channels. The resulting simulated pulses are shown in Fig. 3.

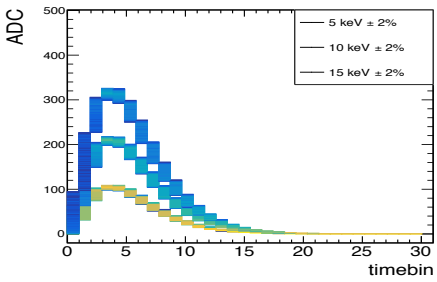

Figure 3: Self-triggered pulses for different ranges of energy deposition in the detector, simulated using the SIS100 electron setup and UrQMD events at 8 A GeV.

References

[1] CBM-TRD Technical Design Report, DOI:10.15120/GSI-2018-01091 (2018).

[2] ALICE-TRD Technical Design Report, ISBN 92-9083-184-7, (2001).

Realistic response of the Bucharest TRD for mCBM simulations at top rates

A. Bercuci, V. Cătănescu, M. Petrovici, L. Radulescu, and C. Schiaua
National Institute for Physics and Nuclear Engineering (IFIN-HH),Hadron Physics Department, Bucharest, Romania

The particle rates expected for the TRD modules at $\approx$ 5 m from target, close to the beam drain, are reaching average values of $10^5/\mathrm{cm}^2/\mathrm{s}$ at the top CBM intensities. The challenge facing detector modeling and reconstruction is to correctly estimate the signal rate and to infer particle position and energy. The average trace of each particle on the readout plane of the Bucharest TRD prototype [1] is $\approx$ 6 channels[1] for 1 pad-row signal topologies. Additionally, in $\approx$ 50% of the cases, particles can produce signals in two pad-rows if the incident position is close enough (here a value of $\approx$ 7 mm is considered) to pad-row boundary. Thus, an average channel-wise signal-rate close to 0.9 MHz is considered for uncorrelated (space-time) incoming particles on the detector surface. Due to fluctuations in the particle rate, as well as particle-particle time-space correlation, the instantaneous signal-rate per channel can easily exceed 1 MHz. At such rates overlapping signals become a reality and the FEE [3] response has to be modeled accordingly.

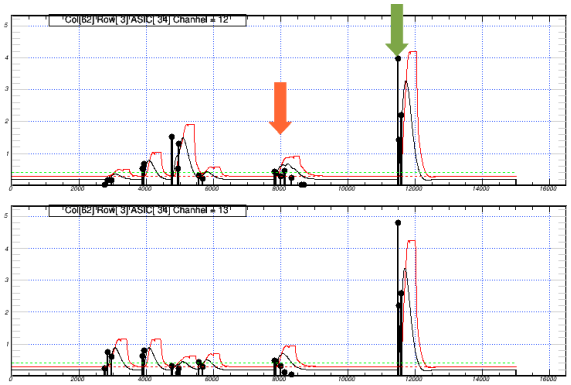

Figure 1: Example of modeling the response of BuchTRD+FASP for the mCBM set-up; physical signal fronts (black markers), amplified/shaped signals generation (thin black) and FASP analog output (thin red) on two adjacent channels (12 and 13) out of 2880.

In Fig. 1 the correlation of the signal generated by incoming particles and the FASP analog processing is shown for a time window of $16k \times 12.5$ ns$= 200\mu$s. Each incident particle generates at most three signals due to the detection mechanism: the prompt and the delayed anode signals depending on the inclination of the trajectory and the TR signal (usually the latest of the three). Such signal configuration is clearly seen on the two adjacent channels from figure, e.g. around $time \approx 11500$ clk (marked by green arrow) and their sharp fronts are marked in thick black. The FASP amplified/shaped response is calculated based on convoluted singled value CADENCE estimates and marked by the thin continuous black curve. The analog output of FASP is marked in thin red, where the flat top marks the ADC converted value of the input charge and the small indentation, before the plateau, the moment of self-trigger. A complex read-out structure, generated by pile-up (more than three signal fronts), is shown in the same figure at e.g. $time \approx 8000$ clk (marked by red arrow). The shaped FASP signal, especially for the channel 12 (top), becomes wriggled, the self-trigger is delayed wrt. prompt signal and its amplitude lowered, both design features of the ASIC in pile-up conditions, correctly reproduced by the simulation.

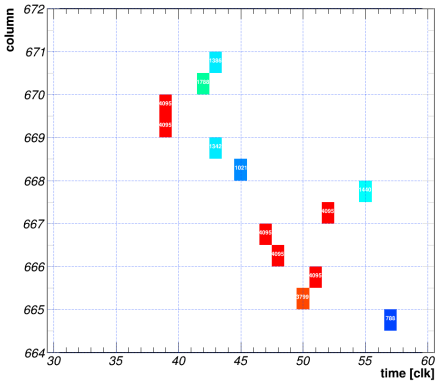

Figure 2: FASP-digits representation of TRD response to top rate interactions in the mCBM set-up. The time on the horizontal axis is measured in FASP clocks of 12.5 ns.

In Fig. 2 the result of TRD+FASP modeling is shown for mCBM set-up at 10^7 Au+Au interactions. For a time window of 375 ns the moment and the digital value (CbmRoot digit) of the charge/channel registration are marked as labeled rectangles. On the vertical axis the geometrical correlation between FASP channel and geometrical position (pad column) on the detector surface is emphasized. The time profile of signal wrt. the spatial coordinate, implicit in the "column" index, is a measure of particles space-time pile-up with which the detector/FEE has to cope.

References

[1] A. Bercuci et al., TRD TDR Review, https://indico.gsi.de/event/5809/contribution/12.

[2] A. Bercuci et al., "FEE readiness of Bucharest TRD chamber for mCBM", this report.

[3] A. Bercuci et al., 32nd CBM Collaboration Meeting, https://indico.gsi.de/event/5863/session/25/contribution/31.

[1] True for FASP read-out mode with *Neighbor Enable* feature [2].

Time-of-Flight Detector

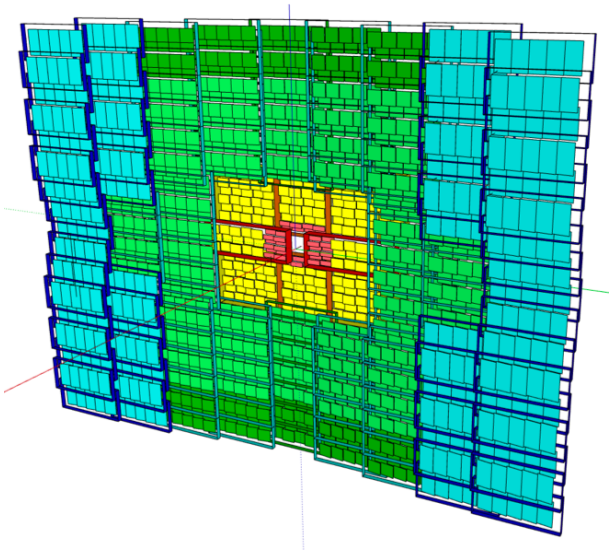

TOF - Summary

Ingo Deppner[1], *Norbert Herrmann*[1], *and the CBM TOF working group*
[1]Ruprecht-Karls-Universität Heidelberg, Heidelberg, Germany

The CBM TOF group can look back on a very successful year 2018. Here we report on the progress made in the TOF FAIR phase 0 programs [1, 2] and on the detector R&D for CBM TOF.

Even though a pre mass-production for the TOF FAIR phase 0 program of about 150 MRPC3a/b counter is finished [3, 4, 5] the MRPC R&D especially for the inner TOF region is still ongoing. The development of the ceramic single cell MRPCs, foreseen for the Beam Fragmentation T0 Counter (BFTC), is well progressed and test beam results are presented here [6]. The R&D for this type of counter will continue till 2021 and will be finalized based on test beam results at Rossendorf and mCBM. In the same time frame the PDR of the inner TOF wall is intended. The R&D regarding electrode materials and final design of this counter type (MRPC1a-c) is ongoing aiming at tests of the latest prototype [7] in the mCBM beam time 2019. The counter R&D for the intermediate and outer region is mostly concentrated on the HV electrode and the FDR will be based on the mCBM beam time in 2020.

Figure 1: mTOF wall at mCBM (left plot) and eTOF wheel at STAR (right plot).

The major attention in 2018 however draw the TOF FAIR phase 0 program. For mCBM [2] a mTOF wall was constructed (see Fig. 1). The mTOF wall comprises 5 full size CBM TOF modules with 5 MRPC3a high rate capable counters each. The conditioning happened in the December 2018 beam time at mCBM and first results can be seen here [8].

The biggest effort however was put in the TOF FAIR phase 0 program at STAR/BNL. Here a so called eTOF wheel was build comprising 36 modules arranged in 12 sectors contributing to the STAR detector upgrade program. The 108 counters were read out by our current CBM standard free streaming DAQ based on the AFCK and portions of data selected based on the STAR trigger token were send to the STAR event builder. That this approach was successful is demonstrated in Fig. 2 [9]. The upper row of plots shows the PID capability of eTOF while the plots of the lower row show the phase space distribution of the various hadrons. The data providing this plots were obtained during the beginning of the Beam Energy Scan campaign (BESII) in 2019. Dedicated data analysis show a system time resolution in the order of 85 ps [10] which allows a separation of kaons from pions up to 1.8 GeV/c. In order to reach such PID quality a sophisticated calibration is required [11].

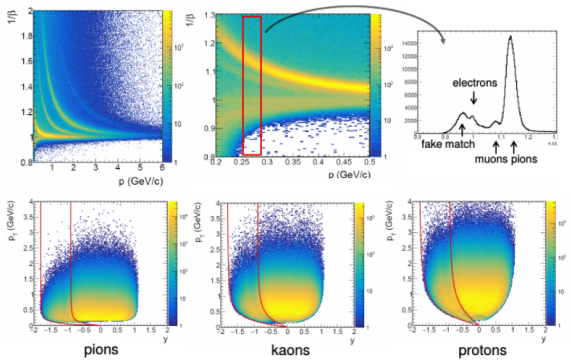

Figure 2: Particle identification capability of eTOF demonstrated at STAR (upper plots) and phase space distributions for pions, kaons and protons (lower plots).

References

[1] I. Deppner *et al.*, CBM Progress Report 2017, p. 192
[2] Ch. Sturm *et al.*, CBM Progress Report 2018, this report
[3] P. Lyu *et al.*, CBM Progress Report 2017, p. 104
[4] D. Hu *et al.*, CBM Progress Report 2017, p. 194
[5] J. Zhou *et al.*, CBM Progress Report 2018, this report
[6] R. Sultanov *et al.*, CBM Progress Report 2018, this report
[7] M. Petriş *et al.*, CBM Progress Report 2018, this report
[8] Q. Zhang *et al.*, CBM Progress Report 2018, this report
[9] F. Seck, private communication
[10] P. Lyu *et al.*, CBM Progress Report 2018, this report
[11] P. Weidenkaff *et al.*, CBM Progress Report 2018, this report

Testing the BFTC RPC cells with a new version of readout electronics

R. Sultanov[1], A. Akindinov[1], R. Beyer[2], J. Dreyer[2], X. Fan[2], R. Greifenhagen[2], B. Kämpfer[2], S. Kiselev[1], R. Kotte[2], A. Laso Garcia[2], D. Mal'kevich[1], L. Naumann[2], V. Plotnikov[1], M. Prokudin[1], D. Stach[2], S. Shirinkin[1], and K. Voloshin[1]

[1]Institute for Theoretical and Experimental Physics, Moscow, Russia; [2]Helmholtz-Zentrum Dresden-Rossendorf, Dresden, Germany

The results of the two beam sessions conducted in 2017 showed that in case of using PADI readout (versions VI and X) the efficiency of the ceramic RPCs with resistivity values in the orfer of $10^9\Omega \cdot cm$ of floating electrodes is lower comparing to case of using electronics based on a MAXIM 3760 amplifier. In addition the efficiency has been measured for different types of TDC (CAEN and VFTX) while using PADI [1, 2]. In the 2018 we were continuing the adaptation of the mini-module design and coupling it with the PADI readout electronics, aiming at understanding the reason of a low registration efficiency.

Since the signal from the chambers of the mini-module is differentiated and shaped to have a pulse length not more than 5 ns for operation under high counting rates, the results of 2017 beam-tests lead us to the assumption, that the tested TDCs are not sensitive to very short signals (< 5 ns) and this causes the loss of efficiency. In order to fix this issue we implemented an external board for signal stretching. The outputs of this stretcher increases the duration of the input signal by 3.7 ns. To test this solution, a beam session was conducted at the ELBE accelerator (HZDR) in April 2018.

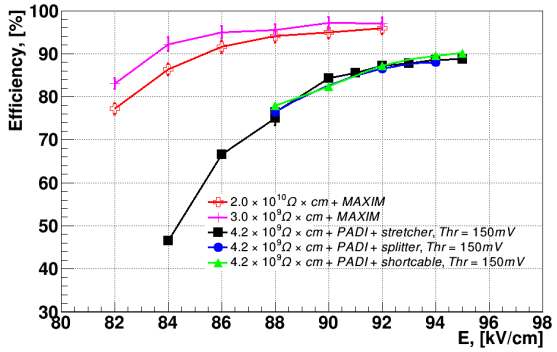

Figure 1: Efficiency as function of electric field strength for three RPC cells and different types of used readout electronics.

The results obtained after the beam test are presented on Fig. 1. Adding a stretcher, as well as reducing the length of the cable connecting mini-module and TDC, did not improve the detecting efficiency. In Fig. 2 one can see the effect of the stretcher on the Time-over-Threshold spectrum (ToT), enhancing the region of low values of ToT, but the spectrum does not reach the expected width of 5 ns even for the lowest values of the signal discrimination threshold. The correlations of the arrival time of a signal and its ToT value are typical for this type of detector. It does not have spikes or gaps, which ensures the impedance matching of the connection mini-module to PADI.

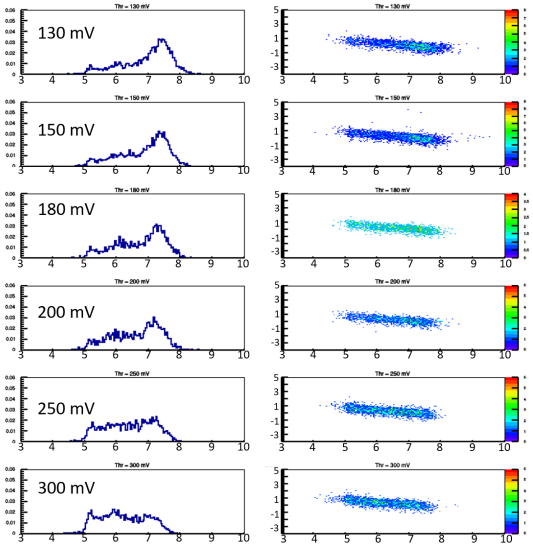

Figure 2: ToT spectra (left row) and ToT-to-time correlations (right row) of channel 4 for different values of the discrimination threshold indicated on the left. Minimodule is connected to the TDC via a signal stretcher. All time scales in ns.

To confirm the mini-module proper operation it was decided to perform tests with use of NINO readout electronics, developed for ALICE TOF detector, which has the function of stretching the length of the output signal inside the chip. In the spring of 2018, an additional beam test was conducted at the PS accelerator at CERN with NINO electronics and standard HPTDC [3], which is used in the ALICE experiment. As a first test several hundreds of signals from the beam particles (π^- at 5 GeV/c) were digitized with an oscilloscope when triggered by a system of scintillation counters. A typical signal from one of the mini-module RPCs is shown in Fig. 3. The pulse amplitude is sufficient for working with standard thresholds of both NINO and PADI electronics, and the pulse duration corresponds to that obtained with simulations of the differentiating chain operation.

After these measurements, the NINO electronics was connected to the mini-module. Since the design of the mini-module does not provide the connection interface for this electronics, a temporary adapter from the PADI board

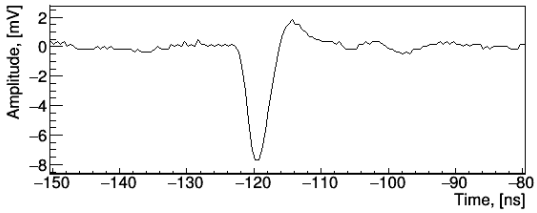

Figure 3: Typical MIP signal from the RPC of the mini-module.

connection format to the NINO board format was made. Such an adapter is not resistant to noise interference and should not be used for accurate timing measurements. The results of the efficiency measurements and comparison to those obtained with PADI and MAXIM electronics are shown in Fig. 4. The results for NINO agree well with the MAXIM 3760 results. It should be noticed, that during this measurements due to high noise level the threshold value was set almost twice as high as that used in ALICE measurements. Furthermore, the width of the ToT spectrum, which is shown in Fig. 5, exactly matched to the pulse length of 5 ns. In addition, the shape of ToT spectra agrees well with spectra of the ALICE TOF strip RPCs, obtained using the same electronics during ALICE R&D [4]. The time resolution, shown on Fig. 6 as function of the field strength in the gaps, amounts to 87 ps across the working plateau of the chamber.

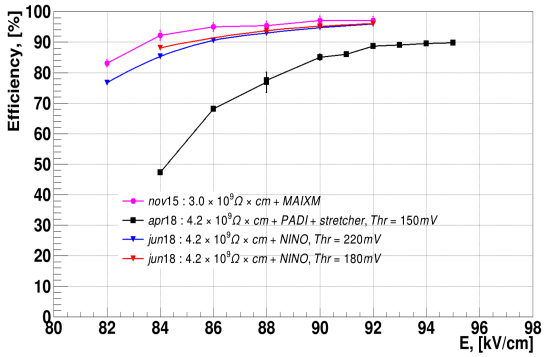

Figure 4: Registration efficiency versus field strength in a chamber for connecting discrete electronics based on a MAXIM 3760 amplifier (magenta curve), NINO electronics (blue and red curves) and PADI electronics (black curve)

For further investigation of the efficiency loss the mini-module and the single chamber with single ended readout are installed to the cosmic stand at HD University, where the readout chain is similar to that used in the mCBM facility.

References

[1] R. Sultanov, CBM Progress report 2017

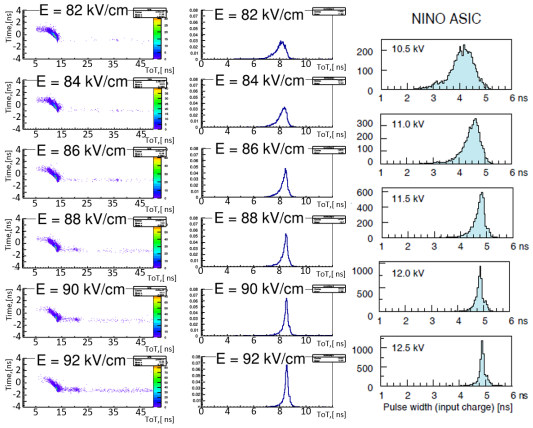

Figure 5: Tot-to-Time correlation (left row) and ToT spectra (middle row) of the BFTC mini-module in comparison to the pulse-width spectra of ALICE strip RPCs obtained with NINO electronics for different values of the field strength in the gas gap (applied voltage in the case of ALICE data).

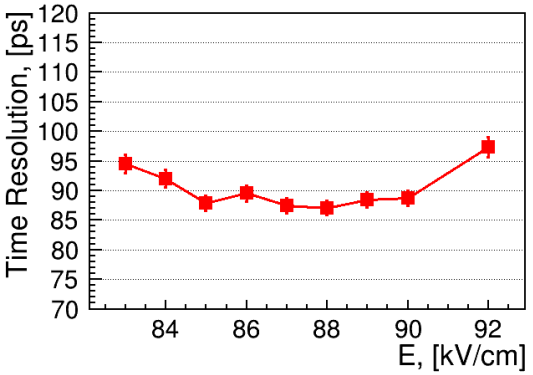

Figure 6: Time resolution of the mini-module RPC cell number 4 in case of using NINO electronics as function of the field strength in the gas gap.

[2] R. Sultanov et. al., "A Timing RPC with low resistive ceramic electrodes", arXiv:submit/2287539 [physics.ins-det] 7 Jun 2018

[3] A. Akindinov et. al., "Design aspects and prototype test of a very precise TDC system implemented for the Multigap RPC of the ALICE-TOF", NIM Section A, Vol. 533 (2004) p.178-182,

[4] F. Anghinolfi et. al., "NINO: an ultra-fast and low-power front-end amplifier/discriminator ASIC designed for the multigap resistive plate chamber", NIM Section A, Vol. 533 (2004) p.183–187

High granularity timing RPC prototype for the inner zone of the CBM TOF wall

D. Bartoş , M. Petriş , M. Petrovici , L. Rădulescu , and V. Simion*
NIPNE, Bucharest, Romania

A MGMSRPC prototype with 32 readout channels was designed and built as basic cell for the inner zone of the CBM-TOF wall. The aim is to exploit efficiently both the active area of the detector as well as the 32 channels of a single front-end electronics baseboard for CBM-TOF. The inner architecture of the detector is the same as for RPC2015DS prototype [1], successfully tested in two in-beam test campaignes in both triggered [2] and free streaming mode operation [3]. The strip width of the readout electrode was obtained using the method described in [4]. A readout strip width of 1.27 mm corresponds to 100 Ω characteristic impedance of the differential transmission line for the present architecture. The obtained readout strip width is very close to the value of the strip width of RPC2015DS. However, in order to exploit efficiently the maximum available size of the low resistivity glass, the strip width of the high voltage electrode increased from 5.6 mm to 7.37 mm. Consequently, the strip pitch, the same for both HV and readout electrodes, increased from 7.2 mm to 9.02 mm. The 60 mm strip length corresponds to the counters of the CBM-TOF inner zone with the highest granularity. After

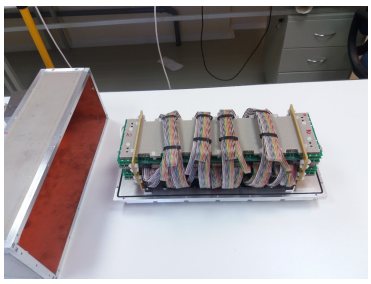

Figure 1: The two identical MGMSRPCs with 100 Ohm impedance mounted on the back pannel of the housing box.

assembling, the two prototypes were preliminary tested in the detector laboratory. A pulser signal was split in two, one of the signals being used to trigger the oscilloscope, the other one being split again, one of these being inverted. The negative signal was injected in the anode and the positive one in the cathode readout strips, at one end, and recorded at the other end directly on the oscilloscope. The measured propagated signals through the transmission line did not reveal any significant reflections. A cross talk test was also performed, injecting both polarity signals on the main strip (CH1 and CH2) and recording the signals of the first neighbour strip (CH3 and CH4), at the same side where the signal was injected, the oposite side being closed and matched to 50 Ohm. As can be observed in the screen capture shown in Fig.2, the cross talk is negligible.

* mpetris@nipne.ro

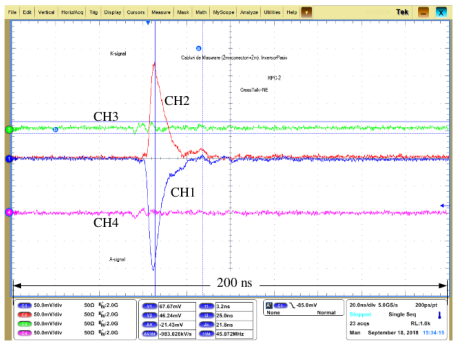

Figure 2: CH1 and CH2 - injected signals; CH3 and CH4 neglijible cross-talk in the first neighbour.

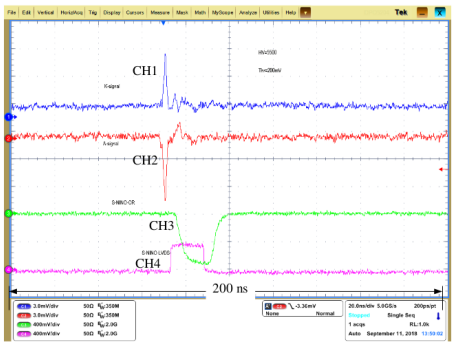

Figure 3: Snap-shot of real cosmic ray signals.

We conditioned the detector applying gradually the high voltage up to the nominal value (2 × 5.5 kV). Real signals produced by cosmic rays were recorded. A snapshot of the signals from both cathode (CH1) and anode (CH2) readout strips recorded directly from the detector at one end of the strip and the output of the NINO FEE [5] i.e the LVDS signal (CH4) and the logic OR (CH3), recorded at the other end, are presented in Fig.3. As can be seen, one does not observe reflections on a time scale of 200 ns (20 ns/div).

References

[1] V. Aprodu et al., CBM Progress Report 2015 (2016) 97
[2] M. Petriş et al., Nucl. Instrum. Meth. A 920 (2019), 100.
[3] M. Petriş et al., CBM Progress Report 2017 (2018) 102
[4] D. Bartoş et al., Rom. Journ. Phys. 63, 901, (2018)
[5] F. Anghinolfi et al., Nucl. Instrum. Meth. A 533 (2004) 183.

Simulated data analysis in a high track-multiplicity reaction environment

C. Simon[1], *N. Herrmann*[1], *I. Deppner*[1], *P.-A. Loizeau*[2], *D. Sauter*[1], *and Ph. Weidenkaff*[1]
[1]Ruprecht-Karls-Universität Heidelberg, Heidelberg, Germany; [2]GSI, Darmstadt, Germany

To validate the algorithms used for evaluating CBM ToF beamtime results [1] with Monte Carlo information, the time-based ToF digitization scheme described in [2] and in [3] with intrinsic track-interference handling and field-recovery memory has been extended to allow for heavy-ion collision simulations on a production scale. The spray of particles impinging on the setup after each collision represents a challenge both to the detectors and to the analysis software. Multiple particles traverse a single counter within an $\mathcal{O}(\mathrm{ns})$ time interval and interfere with each other in the detector response, i.e. a reconstructed hit contains information from several original tracks.

For demonstrating purposes, a $30\,\mathrm{AGeV/c}$ Au beam hits an $8\,\%$ Au target ($4\,\mathrm{mm}$ Pb equivalent) in the "*tof_v15e*" geometry at a constant beam intensity of $1.3{\times}10^6\,\mathrm{Hz}$ in spills of $10\,\mathrm{s}$ duration. The simulated setup corresponds to the "upper level" in Figs. 2 and 3 of [1] and the selected beam intensity results in an external particle flux of about $1\,\mathrm{kHz/cm^2}$ on the detector indexed with 3 which serves as DUT. Detectors indexed with 1, 6, 7 and a diamond start counter serve as tracking stations to identify the best "selector track" in an event to which a hit from each station contributes (except for the DUT). The X, Y, and T coordinates of an expected hit on the DUT are inferred from an interpolation along the selector track line in time and space.

Finding a meaningful selector track if—on average—8 external particles trigger a response in each large-area counter per collision requires strict hit selection and track fitting criteria. Besides the number of secondary tracks which do neither directly nor direction-wise originate from the target also the significant e^+/e^- pair production from primary π^0 decay gammas in the relatively thick target (cf. Fig. 1, left plot) complicates selector track finding due to multiple scattering. At the cost of statistics, e.g. by dropping $99\,\%$ of about 1 million events in spill via cuts, a selector track purity (every hit in the track can be primarily attributed to the same physical particle) of $98\,\%$ is achieved and in another $98\,\%$ of cases the underlying particle originates from the target. In addition, e^+/e^- are chosen as selector tracks relatively less often (cf. Fig. 1, right plot).

With a selector track at hand, the nearest-neighbor DUT hit to the predicted position is considered a match (and the counter efficient) if a given limit on a χ^2-like distance measure between hit and track in X, Y, and T is met. While in $99\,\%$ of events in which a selector track is found *some* hit is available on the DUT, a proper χ^2 limit is needed to suppress impure matches, i.e. DUT hit and selector track do not result from the same particle. Figure 2 shows the simulated χ^2 acceptance and purity as a function of the applied

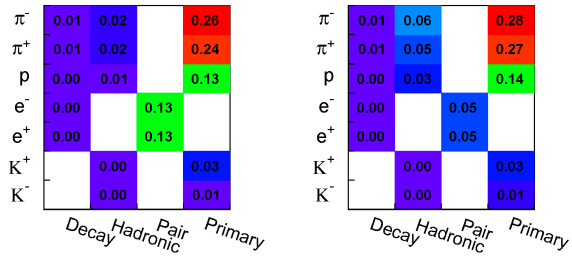

Figure 1: Particle species vs. production process of all (left plot) simulated charged particles created in the target volume which traverse all tracking stations and of those only which a selector track has been matched to (right plot).

χ^2 limit. With an $8\,\%$ maximum chance of a mismatch in a multi-track environment (left plot) compared to a clean single-track reference scenario (right plot; obtained with a muon generator) this method bias needs to be taken into account for efficiency determination in the data analysis.

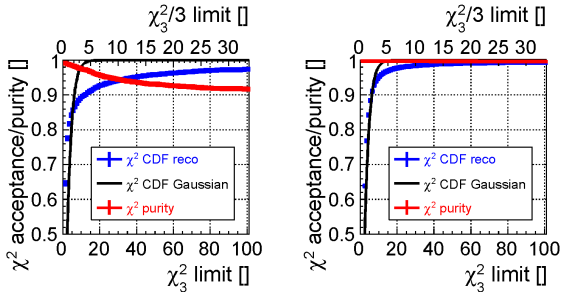

Figure 2: Matching acceptance (blue curve) and purity (red curve) of DUT hits with selector tracks as a function of the (reduced) χ^2 distance measure limit in a multi-track (left plot) and in a single-track (right plot) environment. As a point of reference, the χ^2 acceptance of a purely Gaussian response function with 3 degrees of freedom (black curve) is given.

References

[1] C. Simon *et al.*, CBM Progress Report 2015, p. 90
[2] C. Simon *et al.*, CBM Progress Report 2016, p. 133
[3] C. Simon *et al.*, CBM Progress Report 2017, p. 141

The first beam test of mTOF at GSI

Q. Zhang[*1], *I. Deppner*[2], *and N. Herrmann*[2]
[1]Tsinghua University, Beijing, China; [2]Heidelberg University, Heidelberg, Germany

Structure of mTOF

mTOF is one of the sub-systems in the mCBM experiment [1], designed to measure the time of flight of charged particles. It features 5 modules (cf. Fig. 1 right) covering an total area of 1.25 m × 1.5 m. During the commissioning beam-time in December 2018 the mTOF wall was rearranged in order to allow quality assurance of the detectors. Therefore 2 stacks of 2 and 3 modules each (as shown in Fig. 1) were positioned at an angle of 25° with respect to the beam axis and 234 cm from the target. Each module contains five high rate MRPCs called MRPC3a [2], which contains low resistive glass sheets [3]. The high rate capability and good time resolution of these detectors are crucial for particle identification in high rate experiments. The first stack (module 4 and 5 in Fig. 1) of mTOF contains two modules, overlapping in the z-axis direction. It is located closer to the beam pipe and therefore exposed to higher particle fluxes. With this stack the aim is to test the rate capability of the MRPC3a counters. However, it is not trivial to get the efficiency of the counters reliably well with only one additional reference. Therefore the information of a T0 (diamond counter) is needed. The situation is better for the second stack with three modules (module 1,2 and 3) overlapping in the z-axis direction. With tracks traversing all three modules, the efficiency of the MRPCs can be obtained more easily due to one more layer as reference detector.

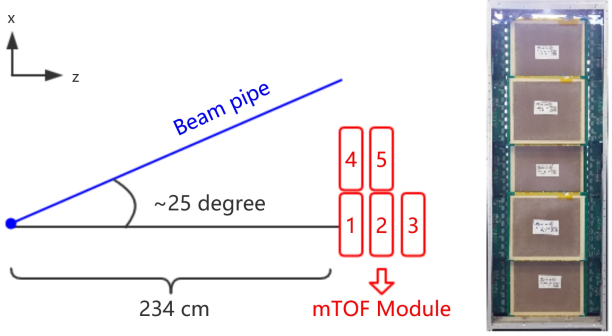

Figure 1: The mTOF experimental set-up and module structure. Left: The mTOF experimental set-up. It is located 234 cm away from the target, positioned under an angle of 25° with respect to primary beam. Right: One mTOF module. Each module contains five MRPC3as.

* zhangqn17@tsinghua.org.cn

The mTOF readout chain and data aquisition

The free-streaming mTOF readout chain is composed of the PADI10 preamplifier, the self-triggered GET4 Time to Digital Converter (TDC), the GBTX based readout board (ROB) and the FPGA based Data Processing Board (DPB) AFCK as shown in Fig. 2. The data from mTOF are sent to the FLES (a high-performance online computer farm) located in the Green IT Cube where they are combined with the data from other sub systems and stored to a file system. The so called tsa-files which contain the raw information were unpacked during the December beam-time for TOF the first time in the FAIR MQ framework producing a root file which can be analyzed by the CBM root framework.

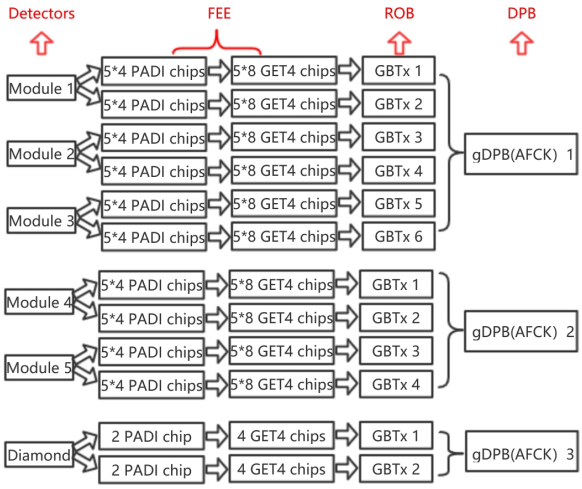

Figure 2: Readout chain of mTOF.

mTOF beam test

The performance of mTOF was firstly tested in beam during mCBM commissioning run in Dec. 2018 carried out at SIS18 in GSI. The beam was generated by 1.2 AGeV Ag hitting 10% Au target, whose total thickness is 0.1 cm with 0.5 cm in diameter. The working gas mixture for mTOF is 90 % $C_2H_2F_4$ (R134a), 5 % i-C_4H_{10} and 5 % SF_6. Due to a malfunction of the gas distribution panel, the five modules had to be daisy-chained, flowed by the gas mixture for 15 days at the speed of only 93 ml/min for the beam test. It turned out that this was not sufficient to have the same gas quality in all modules. Consequently, the high voltage (HV) of five modules could be set to ± 5300 V, ± 5300 V,

$\pm$ 5200 V, $\pm$ 5000 V, $\pm$ 4900 V respectively instead of the working value $\pm$ 5400 V. Subsequent detectors in the gas flow process had lower HV. PADI threshold was set at $-$ 400 mV during the beam time for all counters.

First results of the data analysis for mTOF

Good quality data for mTOF was obtained during almost the whole beam test. The first and preliminary analysis results of mTOF were obtained for RUN 49 were all participating sub-systems were combined. Fig. 3 shows the average cluster size (ACS) for all 25 counters (grouped in 5 modules with different colors). The average of each module is indicated by the black dashed line. It decreases from about 1.2 to 1.1 depending on the applied HV which is in all cases kind of small due to the insufficient applied working voltage. In addition a trend of the average cluster size is seen in each module. The MRPCs located on the top of the "hanging" module shows the largest ACS. The further down the counter is, the lower the ACS. The most probable reason for this observation could be the temperature gradient but also the pressure gradient in the module.

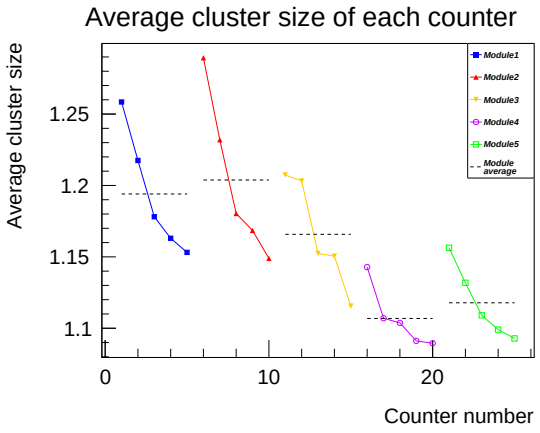

Figure 3: The average cluster size of each counter in mTOF. Each point represents a counter. The gas flowed through counters from counter 1 to counter 25 in sequence. The dotted line is the average cluster size of five counters in each module.

Fig. 4 shows the hit distribution along the strip on each MRPC after the calibration. The 5 rows indicate the 5 modules with 5 MRPCs in each module. The x-axis denotes the strip number (32 per MRPC) while the y-axis denotes the strip length. The boarder of the MRPC is sharp and clearly notable which demonstrates the quality of the obtained data. However, structures on the distribution are visible. For example few strips (about 3) are barely populated and one strip is fully missing which indicates a bad or loose contact to the preamplifier. In addition bands of 4 strips (GET4 chip granularity) with less statistics indicate a synchronization loss of the GET4 chip which recovers after a short period of time.

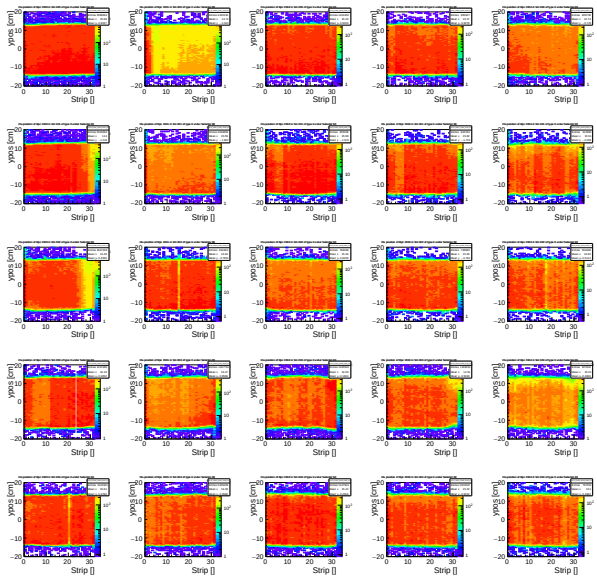

Figure 4: The cluster position of all counters of mTOF. More information see text.

This first results demonstrate that all in all the mTOF system worked reliably well. However, the readout leaves room for improvements. Next steps are the analysis of all taken runs in terms efficiency and time resolution of the counters at different rates for the triple stack modules.

References

[1] The CBM collaboration, "A CBM full system test-setup for high-rate nucleus-nucleus collisions at GSI / FAIR", mCBM proposal 2017 34

[2] N. Herrmann et al. "CBM-TOF Technical Design Report", http://repository.gsi.de/record/109024/files/, October 2014

[3] J. Wang, et al., "Development of multi-gap resistive plate chambers with low-resistive silicate glass electrodes for operation at high particle fluxes and large transported charges". Nucl Instrum Meth A'621, September 2010, p. 151

Performance of CBM MRPC3a running on STAR-eTOF in 2018

P. Lyu[1], *Y. Wang*[1], *F. Seck*[2], *P. Weidenkaff*[3], *D. Brandenburg*[4], *F. Geurts*[5], *and D. Tlusty*[5]

[1]Department of Engineering Physics, Tsinghua University, Beijing, China; [2]IKP, Technical University Darmstadt, Darmstadt, Germany; [3]PI, Heidelberg University, Heidelberg, Germany; [4]Department of Physics, Brookhaven National Laboratory, USA; [5]Physics & Astronomy Department, Rice University, Houston, USA

In 2018, we have managed to produce 73 high-rate MRPC3a counters with low-resistive glass electrodes at Nuctech in Beijing and tested them [1-2]. They were all delivered to Heidelberg University and assembled into modules there. As part of the CBM FAIR phase 0 programs [3], 48 of these MRPC3a counters together with 60 MRPC3b from USTC are finally installed, commissioned and operated as the endcap TOF system (eTOF) at the east pole tip of the STAR experiment. The eTOF project is also part of the BES-II detector upgrade at STAR. It will provide particle identification in the extended pseudorapidity range provided by the iTPC upgrade to the main tracking chamber [4]. For STAR experiment, the eTOF upgrade will bring compelling new physics capabilities to the RHIC BES-II prgram. On the other hand, CBM also benefits from STAR-eTOF by providing a large-scale integration test of the CBM-TOF hardware and software system.

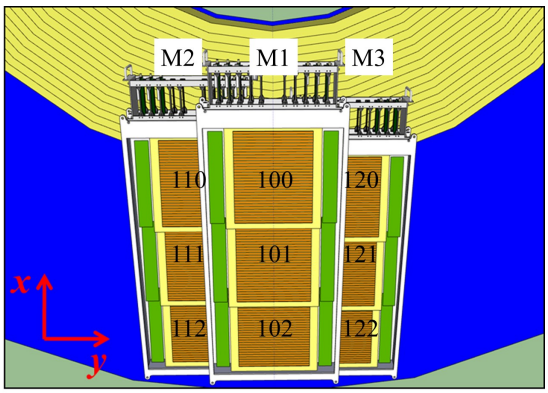

Figure 1: The sketch of the only one eTOF sector installed in STAR Run18.

In STAR Run18, only one sector containing 3 modules were mounted in the 6 o'clock position of the east-side end-cap of the magnet. As shown in Fig.1, the 3 counters from module1 are MRPC3b, and the rest 6 counters are MRPC3a. These counters formed the eTOF system in Run18 and were included in the calibration production for Au + Au at 27 GeV. About 2 million events were obtained in total, and after firmware fix 600 thousand events with good timing eTOF information were available.

The eTOF software team established an offline reconstruction chain based on the STAR software framework in order to reconstruct tracks from DAQ information, verify reliability of the system, and realize particle identification. In the first step, the DAQ files are read in and unpacked. After the mapping from electronic address to the geometry identifiers is applied, a series of calibrations, including local position calibration, gain correction, walk correction and T0 offset correction, are carried out on the raw digis. Then the calibrated digis from different sides of the same detector strip are matched into single strip hits, and the hits are further merged into clusters. The well calibrated information make it possible for us to analyze the counters' timing performance in Run18.

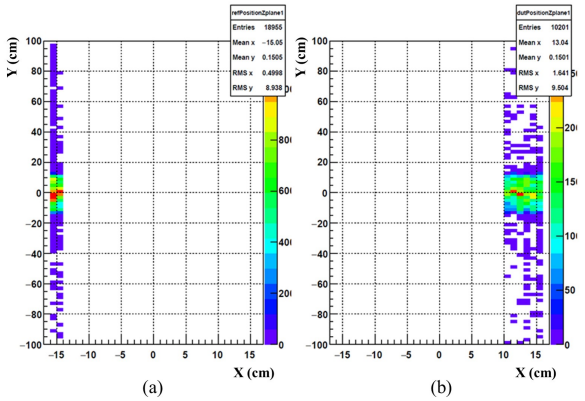

Figure 2: (a) The XY position of the hits located at the first 2 strips of counter 101. (b) The XY position of the hits located at the last 6 strips of counter 100 while it also passes through the first 2 strips of counter 101.

The first analysis method makes use of the 2 overlapping strips of the adjacent counters in the same module. If a hit passes through the 2 counters at the same time, the time resolution can be got from the time difference. We first get a list of hits located at the first 2 strips in Ref, shown in Fig.2(a), then look for hits in the last 6 strips in Dut from the corresponding events. The two lists of hits are built into hit pairs if the Chi2 is within the limit. From the time difference distributon of hit pairs, an intrinsic time resolution below 100 ps is obtained.

The disadvantage of the overlapping strip analysis is that only small part of the counter is taken into consideration. Moreover, the strips on the edge are most noisy. Thus it is nessary to include the whole counter into the analysis. With help of tracking from TPC, the eTOF resolution can be achieved from the time difference with VPD's T0 information. We need to get a list of eTOF detector hits and another of track intersections with active eTOF volumes. Similarly, match candidates are built if the intersection and

detector hit are on the same detector, and the local distance in X and Y is smaller enough. By subtracting the eTOF arrival time and VPD start time of the match candidates the time-of-flight is got.

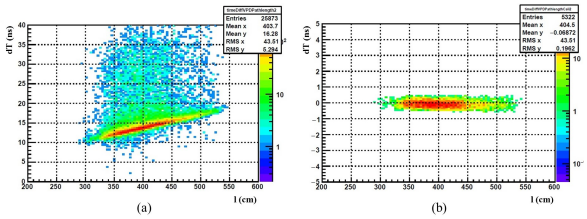

Figure 3: The dT between eTOF and VPD as a function of pathlength. (a) before calibration. (b) after calibration.

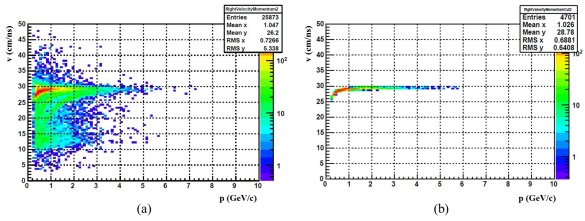

Figure 4: The particle flight velocity as a function of its momentum. (a) before calibration. (b) after calibration.

The raw dT distributon is pretty wide, because the flight time is related to several factors which should be calibrated out to acquire the intrinsic eTOF counter's time resolution. As shown in Fig.3(a), the time difference is proportional to the pathlength. This relation needs to be corrected by a linear fit. Fig.4(a) shows the flight velocity's relation with momentum, from which the 3 bands of pions, kaons and protons are clear. Apparently we only want pions in the analysis to ensure all the particles have similar flight velocity. By comparing the expected pions' time-of-flight and the measured value, the pions band is selected shown in Fig.4(b). A narrow cut on momentum is applied additionally to the dT distribution. After all of these calibrations and selections, the average correlated time resolution between VPD and 3 eTOF modules is about 90 ps, shown in Fig.5. Since VPD's resolution in 27 GeV Au + Au collision is 60 ps, we get an eTOF resolution on a level of 60 ps through this analysis method.

With the momentum and flight time information of the match candidates, the PID at end-cap region is realized with help of the eTOF counters. Shown in Fig.6, the seperation of π/K reaches 1.6 GeV/c, and seperation of K/p reaches 3 GeV/c. eTOF will provide additional information to separate pions from kaons and protons where energy loss along from TPC can no longer differentiate.

The application of MRPC3a counters at STAR is the first-time large-scale running of the high rate MRPCs in large physics experiments. It is proved that these counters have kept a promising 60 ps time resolution from Run18

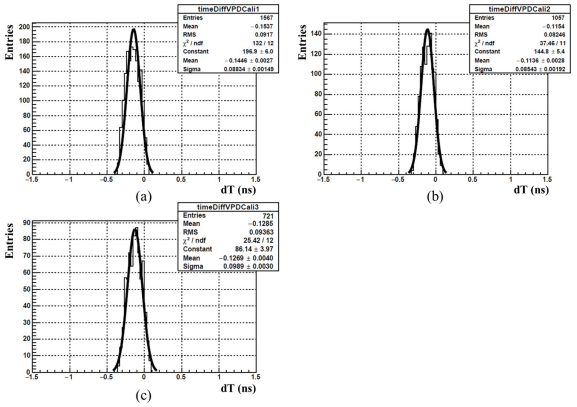

Figure 5: The calibrated time difference distribution between VPD and eTOF: (a) counter 102. (b) counter 112. (c) counter 122.

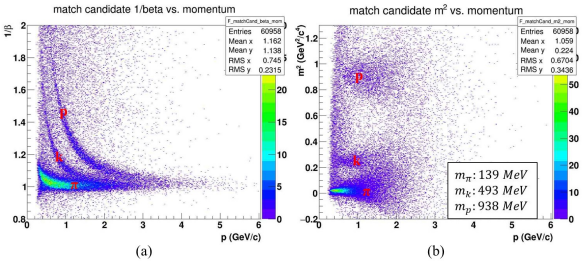

Figure 6: The PID plots achieved by eTOF. (a) The match candidates' 1/beta as a function of momentum. (b) The match candidates' m^2 as a function of momentum.

analysis. It's also the first time that the low-resistive glass MRPC realize the particle identificaiton. The whole eTOF wheel with all 12 sectors were installed and is now taking data in STAR 2019 running [5]. These experience will be very helpful to the preparation for day one experiment at FAIR.

References

[1] I. Deppner and N.Herrmann, et al. CBM Progress Report 2017, 99.

[2] P. Lyu, et al. CBM Progress Report 2016, 126.

[3] P. Lyu, et al. CBM Progress Report 2017, 104.

[4] The CBM Collaboration eTOF Group. Physics program for the STAR/CBM eTOF upgrade. 2009. https://arxiv.org/abs/1609.05102.

[5] I. Deppner and N.Herrmann, et al. CBM Progress Report 2018.

Quality control in MRPC3b mass production for CBM/STAR eTOF

J.Zhou, X.Wang, D.Hu, and Y.Sun
USTC, Hefei, China

Hadron identification at CBM is provided by measuring the momentum and the time of flight of the respective particles [1]. With the excellent performance, Multi-gap Resistive Plate Chamber (MRPC) is a very suitable candidate for CBM-TOF at affordable costs. MRPC3b is a prototype used for the outer part of the TOF wall [2]. On the other hand, the STAR-eTOF project is a joint project between CBM and STAR collaboration. It is part of the BESII detector upgraded at STAR. It comprises the installation, commissioning and operation of CBM TOF modules positioned at the east pole tip of the STAR apparatus during the BESII campaign.

In general, MRPC3b is a double-stack and double-end strip readout detector. The MRPC3b mass production formally started in March 2018 after all the standards in mass production had been established. For the purpose of the quality control of the CBM-TOF MRPC, A FPGA-based TDC and DAQ system is designed by the Fast Electrical Laboratory of USTC, as illustrated in Figure1. Due to the limited time for the mass production, only 30% of the counters were measured with noise rate and took sufficient statistics for the efficiency and time resolution analysis. The batch testing of the MRPC3b started in April 2018. By the end of September, 80 MRPC3bs have been produced and tested and sent to Heidelberg University in several batches for module installation.

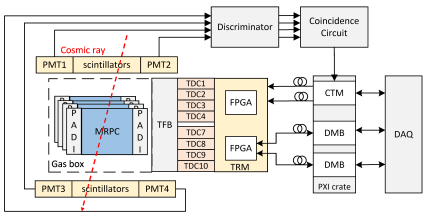

Figure 1: DAQ system.

Figure2 shows the test results. The anode dark currents of all tested MRPC counters are below 100nA. The reasons for the high dark current may be due to the absence of SF6 in the gas mixture and the high humidity in Hefei in summer. The noise rate of all testing counters are lower than 3 Hz/cm^2. The average efficiency of each counters is about 95% and the average time resolution of each counters is about 55ps. Most MRPC counters have excellent performance.

Another TRB3 TDC and DAQ system provide by GSI is also under running. Figure3 shows the preliminary results of the TRB3 system. The efficiency is better than 92% and time resolution is about 55ps. More test will continue in the future. The MRPC3b counters have been installed on the STAR-eTOF by November 2018.

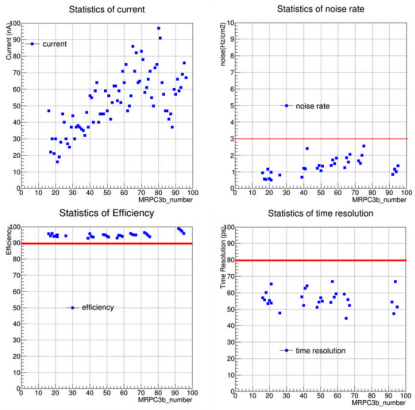

Figure 2: Test results.

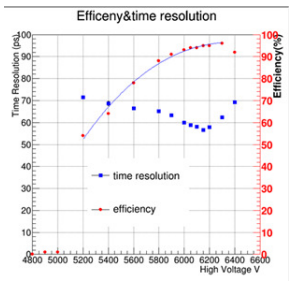

Figure 3: MRPC voltage plateau curve.

In summary, the mass production of the CBM-STAR eTOF project has been done. The assembly procedures and QA&QC methods have been established and qualified by this pilot process.

References

[1] Williams M C S. Particle identification using time of flight[J]. Journal of Physics G: Nuclear and Particle Physics, 2012, 39(12): 123001.

[2] Deppner I, Herrmann N, Gonzalez-Diaz D, et al. The CBM time-of-flight wall[J]. Nuclear Instruments and Methods in Physics Research Section A: Accelerators, Spectrometers, Detectors and Associated Equipment, 2012, 661: S121-S124.

Hit building and calibration of CBM-ToF detectors in the StRoot framework for Phase-0 activities

Ph. Weidenkaff[1], *I. Deppner*[1], *N. Herrmann*[1], *P. Lyu*[3], *and F. Seck*[2]

[1]Ruprecht-Karls-Universität Heidelberg, Germany; [2]Technische Universität Darmstadt, Germany; [3]Tsinghua University, Beijing, China

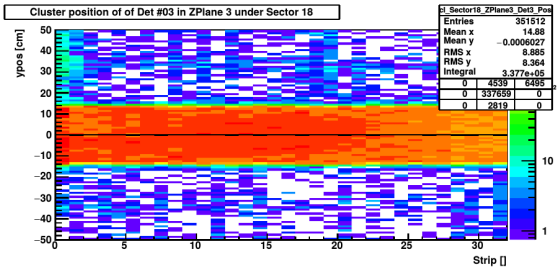

Figure 1: Example hit distribution over the surface of a detector after position offset calibration.

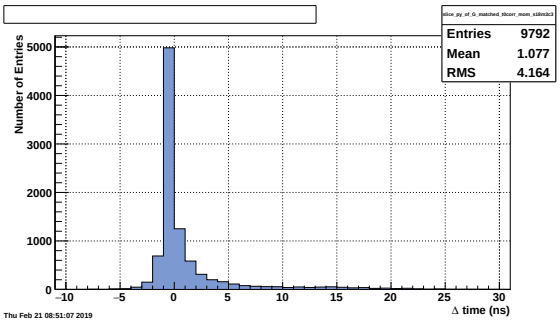

Figure 2: corrected distribution of matched track time-of-flight - expected time of flight for pions.

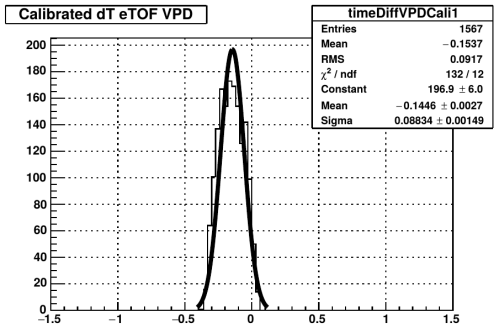

Figure 3: system time resolution of eToF and VPD start time. With courtesy of P. Lyu.

Algorithms for hit-reconstruction and calibration of MRPC data have been ported to the StRoot-framework to be used for the data taken in the Beam Energy Scan II program at STAR. The lessons learned at STAR in 2019 and forward will help to improve our understanding of the impact of algorithms on physics observables.

In order to make the raw data of eToF physically meaningfull, multiple calibration steps have to be done.

A dataset from the 2018 STAR Au+Au physics run at $27\,GeV$ have been used as test data for this procedure.

The mayor effects that have to be taken into account to calibrate eToF data are:

- Time offsets between front-end electronic (FEE) channels, leading to position deviations of hits
- Time offsets with respect to the STAR main clock, leading to time-of-flight deviations
- The time walk/slewing effect, leading to time-over-threshold depending delays of the signal dependence

In the inital steps of the calibration procedure, the time offsets between opposing FEE channels connected to the same RPC strip are corrected by shifting the mean position of hits along the strip to the center of the strip. The result (see 1 is a homogeneous hit distribution over the surface of the detector, as it is expected from the physical illumination of the detector. Few reconstructed hits outside of the physical detector area point to a low fraction of wrongly reconstructed hits.

In the next step, the global time offsets between each eToF detector and the STAR start time is corrected. In order to do this, TPC tracks are spacially matched to the now correct positions of eToF hits. Under the assumption that most particles are pions, the expected time of flight is calculated from the known track momentum and helix path length. To calculate a starting time, the time information from the STAR vertex position detector is used. The time offset is then determined such that the peak of this distribution (corresponding to pions with a velocity close the light-speed) is shifted to zero.

At last, the time walk effect is corrected out. This is done in multiple iterative steps which are alternated with position correction steps in order to minimize distortions on the hit position due to the time walk correction. Similar to the global time offsets, the time difference between the measured ToF and the expected ToF is calculated, but now as a function of the ToT. The correction is calculated with a finer granularity and separately for each FEE channel on each detector.

After these corrections, a combined time resolution of eToF and VPD $\leq 90\,ps$ was obtained.

Calorimeters

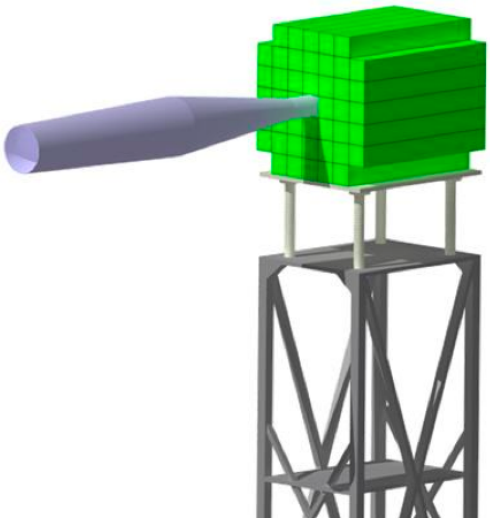

Projectile Spectator Detector - Summary

F. Guber
INR RAS, Moscow, Russia

The CBM PSD project has made substantial progress in various fields in 2018 as will be presented in the following articles. Few beam tests of the PSD supermodule assembled as array 3x3 from 9 modules produced at INR for PSD CBM have been done at CERN T9/T10 beam lines during 2017-2018 years. Two pipe-line ADC64s2 64-channel 12-bit 62.5 MS/s boards [1] have been used to read-out fast signals from MPPCs in these tests. These boards measure signal waveforms with precision of 16ns. The PSD supermodule response has been studied for protons in the energy range of 2-9 GeV. It was demonstrated [2] that obtained dependence of energy resolution as function of proton energy can be fitted by function with stochastic term of about $0.54/\sqrt{E}$ while the constant term of about 4.5% which agrees well with simulation results.

A new method for fitting fast PSD signals based on the Prony least squares method is developed. It allows one to determine the amplitude and time of arrival of the signal more reliably. The advantages of the method make it possible to work with small signals near the noise level, in particular, the method will be used to calibrate calorimeter sections on cosmic muons. Another advantage of this method is the high speed of the new fitting procedure, which requires three orders of magnitude less machine time than standard minimization package in the ROOT environment. At present, this new fitting procedure is implemented in analysis of the PSD signals obtained on test beams in order to improve the energy resolution at low energies.

After 2 months of the CBM operation with beam rate 10^8 gold ions per second and 1% gold target, the maximum neutron fluence at MPPCs position behind PSD is expected on the level of 2×10^{11} n/cm^2. During the test runs on T10 at CERN in 2018 the response of one of PSD modules equipped with 10 preliminary irradiated MPPCs with 2×10^{11} n/cm^2 has been studied as well. It was shown that energy resolution is dropped only slightly (on level of 10%) at this neutron fluence. Several special beam tests have been done also in 2018 for the study of single module response by use another prototypes of readout electronics. In particular, current version of PaDiWa ADC has been tested and it was demonstrated that additional improvements of this board are needed to satisfy CBM PSD requirements. Another prototype of ToT board with 8 channels has been designed in INR (Moscow) and tested at CERN. This ToT board with TRB3 is proposed to use for readout fast signals from new quartz forward hodoscope at HADES Ag+Ag experiment in March 2019.

In 2018 significant activity was aimed to preparation of the use of already constructed PSD CBM modules at mCBM, BM@N and NA61 experiments during FAIR-Phase-0. In particular, the optimization of PSD CBM modules position in the upgraded hadron calorimeters in NA61 and BM@N experiments has been done taken into account allowed level of radiation estimated by Fluka simulations (details in A.Senger article in the chapter "Radiation hardness studies"). For the first time the response of one PSD module was studied at BM@N run in spring 2018 on Ar beam with energy 3.5 AGeV. The obtained energy resolution of about 12% and the hadron shower profile are in a good agreement with MC simulation. To study the mPSD response at mCBM [3] in 2020 under realistic experiment conditions up to top CBM interaction rates of 10 MHz and in the full free-streaming data acquisition system some preparation work started already in 2018. In particular, the FEE PSD board with MPPCs dedicated to collect light from mPSD module and scintillation plates mounted directly on MPPC has been prepared at the end of 2018 to test during mCBM beam run in March 2019. For the first time the ADC PANDA ECAL board [4] will be used for MPPCs signal readout in the beam tests in standalone mode. This board uses LTM9011 sampling ADC that allows to take signal waveforms with rates up to 125MS/s. Currently only pre-production version of ADC board with rate of 80MS/s is available and will be used in beam tests. Integration of this board in the mCBM DAQ will be started immediately after March 2019 mCBM beam run. Optimization of PSD CBM geometry was one of the PSD group activity in 2018. Physics performance of the PSD CBM with different beam holes has been studied. This work is continued in 2019. Very important task in 2018, which was successfully done, is the development of construction of PSD support structure for the PSD CBM. The platform should be constructed and shipped to GSI at the end of 2019.

References

[1] http://afi.jinr.ru

[2] D. Finogeev at al., 2018, The PSD CBM supermodule response study for hadrons in momentum range 2-6 GeV/cat CERN test beams, in The 3rd International Conference on Particle Physics and Astrophysics, KnE Energy & Physics, pp 333-339. DOI 10.18502/ken.v3i1.1763

[3] mCBM@SIS18 http://www.fair-center.eu/fileadmin/fair/experiments/CBM/documents/mcbm-proposal2GPAC-WebVersion0619-SVN7729.pdf

[4] Technical Design Report for the PANDA Forward Spectrometer Calorimeter https://indico.ph.tum.de/event/1063/ https://ieeexplore.ieee.org/document/5402172

Summary of PSD supermodule response study at CERN test beams

A.Ivashkin[1], *D. Finogeev*[1,2], *M.Golubeva*[1], *F.Guber*[1], *A.Izvestnyy*[1], *N. Karpushkin*[1], *S.Morozov*[1,2], *and O.Petukhov*[1]

[1]INR RAS, Moscow, Russia; [2]MEPHI, Moscow, Russia

The centrality and the reaction plane orientation in heavy ion collisions at CBM will be measured by the Projectile Spectator Detector (PSD) which is the forward hadron calorimeter. The PSD will measure the energy of projectile spectators and produced particles in the range 1-11 GeV. It includes 44 individual modules with the beam hole in the center. More details about the PSD module design can be found in [1]. The longitudinal division into 10 sections ensures the uniformity of the light collection along the module. Ten Hamamatsu MPPCs S12572-010P are used as photodetectors in each module. The light yield measured with cosmic muons is about 50 ph.e per each section.

To check the performance of the PSD a compact supermodule was constructed and tested at the beam energies 1-10 GeV. A PSD supermodule consists of 9 individual modules with the transverse sizes of 20x20 cm^2 assembled in a 3x3 array.

Read-out of PSD supermodule

The Front-End-Electronics (FEE) used for the MPPC readout includes the amplifier and shaper of the differential signals, see photo of FEE board in Fig. 1. Due to the shaper, the signal lengh is about 0.5 μs and is about one order longer of the original signal widths after the phtotodetectors.

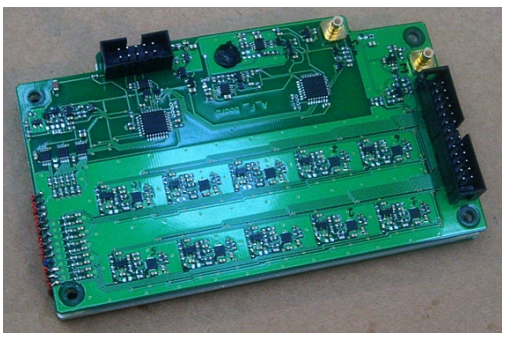

Figure 1: 10 channels FEE board with differential outputs used in beam tests.

A few option of PSD readout were tested. Pipe-line ADC is the main proposed method to read-out fast signals from MPPCs. Current version of electronics is presented with ADC64s2 board manufactured at Dubna company AFI Electronics [2], see Fig. 2. The ADC64s2 is a 64-channel 12-bit 62.5 MS/s ADC device with signal processing core and Ethernet interface. This board measures signal waveform with precision of 16ns.

A ToT method is an another alternative for the measurement of signal amplitudes. In this approach the initial pulse from MPPC is directed to shape generator. Then the shaped signal is discriminated with some threshold and time pulse is produced. This FEE is designed for work with TRB3 board.

The results below were obtained with first version of the readout.

Figure 2: Photo of ADC64s2 board.

PSD supermodule performance at hadron beams

The PSD supermodule response was studied at the T9/T10 beam lines of Proton Synchrotron (PS) at CERN [3]. This beam lines provides secondary beams of pions and protons with a momentum in the range of 2– 10 GeV/c. The identification of beam particles was carried out by the Cherenkov detectors installed upstream of the PSD supermodule with use of TOF method at T10 beam line or the threshold method at T9.

The energy calibration of all longitudinal sections in supermodule was performed by the muons contaminated in the hadron beams. These muons are born in the in-flight decays of pion during the transportation through the beam line. The identification of muons was done using the two-dimensional correlation between the energy depositions in the first half of the module (first five sections) and the last half of the module. These energy depositions for the muons should be practically the same, while the hadrons deposit main fraction of energy in the first half of the module. The mean value of the amplitude distribution in single longitudinal section corresponds to the muon energy loss of about 5 MeV in 6 layers of scintillators with the total thickness of

24 mm. It allows to establish the correspondence between the signal amplitude and the deposited energy for any types of the particles detected in the calorimeter.

During the tests the scan of the beam momenta was done to measure the PSD supermodule response in available energy range. For each beam momentum the spectrum of the deposited energies in the PSD supermodule was recorded. The mean values and the width of these spectra allow the determination of the energy resolution.

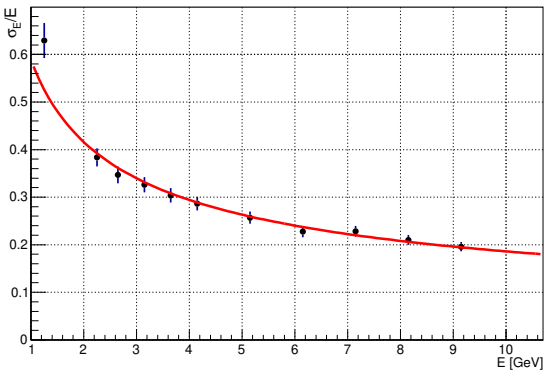

Figure 3: Energy resolution of the PSD supermodule for protons as a function of beam energy.

The dependence of energy resolution on the proton energy is presented in Figure 3. The obtained energy resolutions at different proton energies were fitted by the two term function. The stochastic term is about 54%, while the constant term is about 4.5%.

The longitudinal segmentation of the PSD modules into 10 sections makes possible to check the longitudinal shower profile at different proton energies. For this purpose the summary energy deposition in each section was normalized to the number of detected protons. Figure 4 presents the dependence of the normalized energy depositions on the number of the longitudinal section. One can see, that for the minimum proton momentum of 2 GeV/c almost full energy is contained in first 6 sections. It is explained by the fact that 2 GeV/c protons lose the energy mainly via the ionizing losses process and can pass through the lead absorber in these section only. For 10 GeV/c protons the situation is much different. Here a significant part of the energy is deposited in the hadron shower. And all 10 longitudinal sections are obligatory to absorb the full proton energy.

Note that the fits of the obtained energy resolutions with more complicated functions, including the noise and constant terms do not change the stochastic term notably and the nose term is negligibly small.

Conclusion

The results of the PSD supermodule tests for the protons in the energy range of 2 - 9 GeV have been presented. The obtained energy resolution is in a good agreement with the simulation prediction. It was shown, that the PSD module length is optimum for the dedicated energy range. These results demonstrate that the calorimeter based on lead/scintillator sampling and with the selected light readout using silicon photomultipliers satisfies the requirements of the CBM experiment.

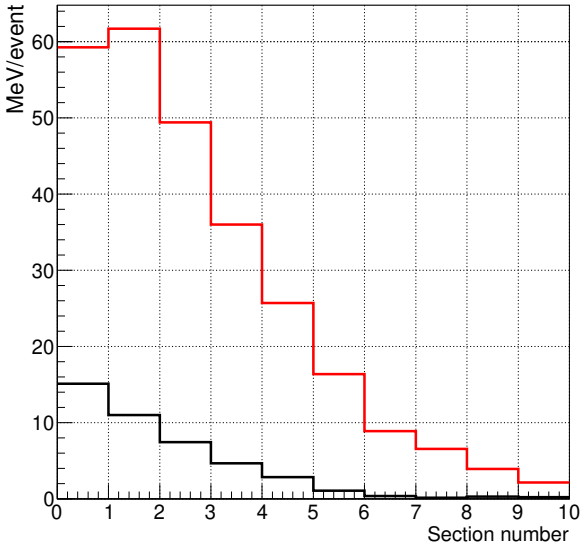

Figure 4: Longitudinal profile of deposited energies from protons. The black and red lines correspond to proton momentum 2 GeV/c and 10 GeV/c, respectively.

References

[1] Technical Design Report for the CBM Projectile Spectator Detector (PSD), 2015.

[2] http://afi.jinr.ru

[3] D. Finogeev at al., 2018, “The PSD CBM supermodule response study for hadrons in momentum range 2 – 6 GeV/c at CERN test beams” in The 3rd International Conference on Particle Physics and Astrophysics, KnE Energy & Physics, pages 333–339. DOI 10.18502/ken.v3i1.1763

Status of mPSD front-end and read-out electronics development

F. Guber[1], *A. Ivashkin*[1], *D. Finogeev*[1,2], *and S.Morozov*[1,2]
[1]INR RAS, Moscow, Russia; [2]NRNU MEPhI, Moscow, Russia

Mini PSD (mPSD), as part of mCBM [1], has been designed to study the prototypes of the PSD front-end and readout electronics developed for the CBM [2] experiment as well as the software packages under realistic experiment conditions up to top CBM interaction rates of 10 MHz. Important task is to study the mPSD operation and response in the full free-streaming data acquisition system including the data transport to a high-performance computer farm located at the Green IT Cube. One PSD module will be used for mPSD setup. The module is ready at INR (Moscow). It was tested on cosmic muons in order to study the response of each section to MIP like particle. It will be delivered to GSI for installation at mCBM cave at the end of April 2019 together with support platform which is constructed at INR (Moscow) as well.

Tests of mPSD FEE and read-out electronics on mCBM setup in March 2019

It is proposed to test FEE PSD board with MPPCs dedicated to collect light from mPSD module and to study readout electronics during the mCBM beam test in March 2019. The ADC PANDA ECAL board [3] will be used for MPPCs signal readout in the beam tests in standalone mode. In order to simulate light generation without mPSD module scintillation plates will be mounted directly on MPPC diodes on FEE card. Prepared FEE with slow control box is shown in Fig. 1. View of the ADC PANDA ECAL board is presented in Fig. 2.

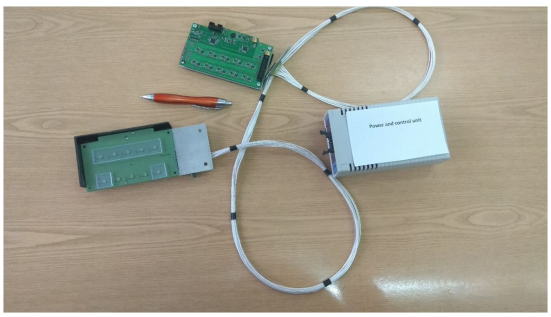

Figure 1: FEE board with scintillators glued to MPPCs and HV control box

PANDA ECAL ADC module

At mCBM beam test in March 2019 the PANDA ECAL ADC board provided by PANDA Collabotration will be used. This board uses LTM9011 sampling ADC that allows to take signal waveforms with rates up to 125MS/s. Currently only pre-production version of ADC board with rate of 80MS/s is available and will be used in beam tests. Signal measurement has 14 bit resolution with 2 Vpp range. 64 channels are combined to pairs with low and high amplification gain to increase dynamic range. Measured waveforms are calculated on the fly using on-board FPGA Kintex 7. This allows one to apply digital filters decreasing a noise level as well as signal processing algorithms for signal tail reconstruction and pile-up recognition. Therefore each channel generates a 128bit value that can be readed out with desired rate up to 1 MHz with bandwidth 4.8 Gbit/s. Readout topology of ECAL detector at PANDA experiment is shown in Fig. 3. Slow control is integrated in SODAnet system based on TRBnet and the SODAnet [4] provides a clock distribution as well. The SODAnet is distributed via HUBs to Data Concentrators (DC) that connected to FEE ADCs. The DCs distribute clock and control commands to FEE and send collected data for event building to network via optical cables with 10b8 protocol.

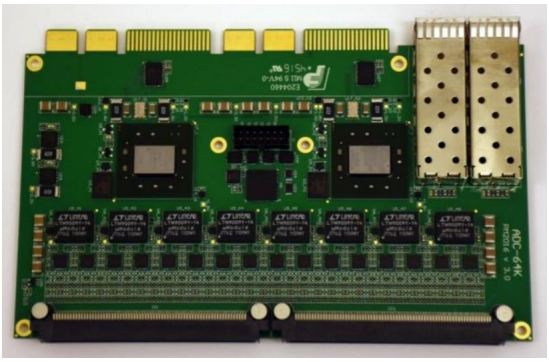

Figure 2: ADC PANDA ECAL board

Workbanch for mPSD read-out beam test at mCBM in March 2019

Topology of ECAL ADCs readout in PANDA is represented in Fig. 4. SODAnet, DC and UDP converter implemented on FPGAs of TRB3 board. Data collected by DC forwarded to PC server via UDP data converter. Only one ADC (ADC0) will be used in beam tests. ADC configuration based on TRBnet commands addressed to central FPGA of TRB board. Also LabView project is developed for slow-control by GUI via TRB DIM server. View of

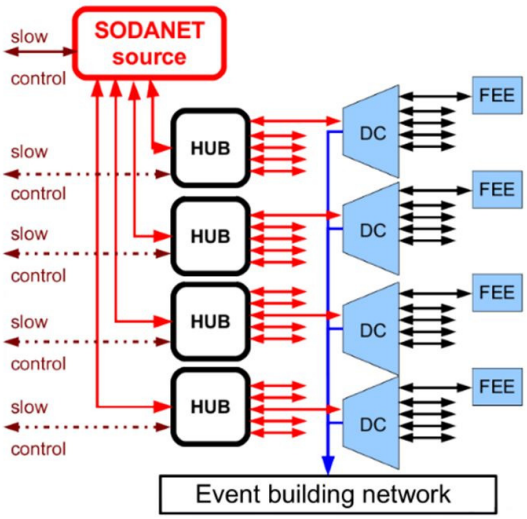

Figure 3: Readout topology of ECAL PANDA ADC

TRB3 board configured to work with PANDA ECAL ADC is shown in Fig. 5. Similar readout set-up will be used at GSI while beam test at mCBM cave in March. System will be assembled on the table to take data from cosmic muons then the detector will be installed in mCBM cave to take beam data. Main aim of the test is to check the readout at high readout rate and under radiation condition. Now ADC board needs all parts of PANDA readout chain: SODAnet and DC. As PANDA configuration based on TRBnet, clock distribution implemented in SODAnet and data transmitted via standard GTX protocol 10b8, the best way of ADC integration into CBM DAQ is using GBT-FPGA module what applied in CBM readout system. Main points of ADC integration are: GBT integration in ADC FPGA project using on board clock, DAQ clock distribution to ACD, ADC configuration procedure. This work will be started after test beam at March 19.

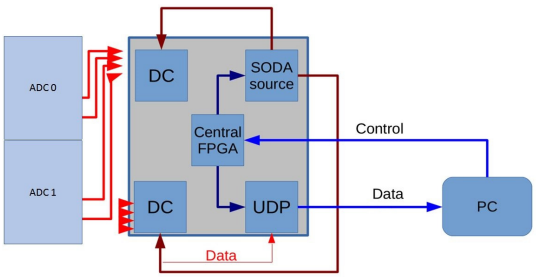

Figure 4: Readout ADC workbench schematic

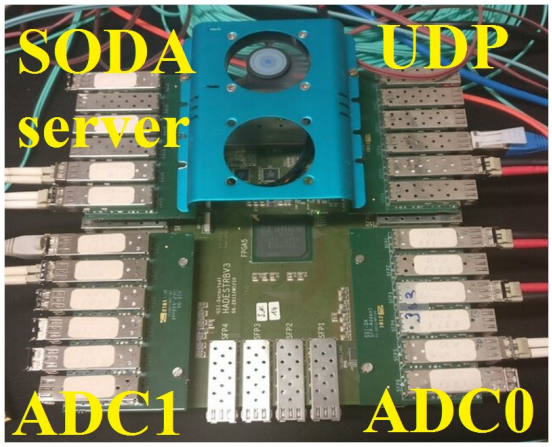

Figure 5: TRB3 based DAQ for PANDA ECAL ADC

References

[1] http://www.fair-center.eu/?leadmin/fair/experiments/CBM/documents/mcbm-proposal2GPAC-WebVersion0619SVN7729.pdf

[2] CBM collaboration, Technical Design Report for the CBM Projectile Spectator Detector (PSD), GSI Darmstadt 2015

[3] Technical Design Report for the PANDA Forward Spectrometer Calorimeter https://indico.ph.tum.de/event/1063/ https://ieeexplore.ieee.org/document/5402172

[4] I. Konorov et al., NSS/MIC Conf. Rec., 2009 IEEE, DOI 10.1109/NSSMIC.2009.5402172

New method of fast PSD signals analysis based on the Prony least squares method

N. Karpushkin, F. Guber, and A. Ivashkin
INR RAS, Moscow, Russia

Introduction

To analyze signals from the calorimeter sections obtained during tests on cosmic muons and hadron beams at CERN the ADC64s2 board with sampling interval of 16 nsec has been used. Usually the procedure of signal fitting uses a universal minimization package in the ROOT environment which requires considerable machine time and is not applicable for processing large amounts of data. New method of fast PSD signals analysis based on the Prony least squares method that uses minimization with functionality reflecting a specific waveform is proposed. Since the shape of the scintillation signal is characterized by the rising and falling components of the pulse [1] with durations τ_r and τ_d, respectively:

$$A(t) = k\left(1 - \exp\left(-\frac{t}{\tau_r}\right)\right)\exp\left(-\frac{t}{\tau_d}\right) \qquad (1)$$

it becomes possible to use a fitting procedure based on the Prony least squares method. The use of this procedure has reduced the time required for signal processing by more than three orders of magnitude.

Digitizing an analog signal using an ADC results in a sampling of the signal. In this case, the sum of several ADC samples for a short time interval is taken as the signal charge value. It is clear that the charge calculated in this way (signal area) will be strongly fluctuating. Therefore, the use of the integration method (summation of ADC samples) of fast signals negatively affects the obtained resolution. The developed procedure of signal fitting allows to obtain more accurately the area (charge) under the signal. Moreover, fitting signals with a known function allows us to isolate weak signals comparable to the level of electronic noise, and to obtain undistorted information about them. Since the noises are random, fitting them with a fixed function gives a low probability of identifying noise as a valid signal. This property is especially useful when performing muon calibration of calorimeter sections, since the signals from muons have a low amplitude, comparable to the noise level. Finally, the fitting procedure makes it possible to select events with signal overlaps (pile up), which is important when working at a high event count rate.

Prony LS method

The Prony method was discussed in detail by S.L. Marple [2], therefore only a brief overview of the method procedure is given here. Suppose that there are N complex samples of data x [1], ..., x [N]. Then the Prony method allows us to estimate x[n] using some p-term model of exponential components:

$$\hat{x}[n] = \sum_{k=1}^{n} A_k \exp[(\alpha_k + j2\pi f_k)(n-1)T + j\theta_k] \qquad (2)$$

for n = 1, 2, ..., N, where $j^2 = -1$, and T is the sampling interval. The objects of estimation are: amplitudes of complex exponentials A_k, attenuation parameters α_k, harmonic frequencies f_k and phases θ_k. Finding the parameters A_k, α_k, f_k, θ_k that minimize the sum of squared errors

$$\rho = \sum_{k=1}^{n} (|x[n] - \hat{x}[n]|)^2 \qquad (3)$$

is a difficult non-linear least-squares approximation problem. To solve it, various iterative algorithms can be used that require large computational costs and do not always converge to the global minimum. An alternative suboptimal solution, which uses solutions of two systems of linear equations, is based on the Prony least squares method.

Application to waveform analysis

The Prony method includes three basic steps. At the first stage, the linear prediction parameters, which correspond to the available data, are determined by solving a system of linear equations. At the second stage, a polynomial is formed from the linear prediction coefficients and its roots are determined. These roots give estimates of the attenuation coefficients and sinusoid frequencies for each exponential term. At the third stage, the solution of the second system of linear equations is sought, which gives estimates of the amplitudes of the exponentials and initial phases. The relationship between the linear prediction and autoregressive parameters allows the first and second stages to be interpreted as a procedure for finding the poles of some autoregressive process.

The AFI ADC64s2 board is a 64-channel 12-bit device with a sampling frequency of 62.5 MHz. Waveforms of ADC are one-dimensional arrays of 200 samples. Signal shaper used in FEE boards, generates a signal with a duration of about 350ns. In the CBM experiment it is proposed to measure signals with a duration of about 60 ns without shaper by 125 MHz ADC board.

The Prony least-squares fitting algorithm is implemented as a C++ class. After the waveform information is transmitted to the class object, the model order (in this case 2) and the range of samples in which the signal lies are set. The Prony method has a convenient division into stages, in particular, the determination of amplitudes can be implemented using known frequencies and attenuation parameters of the corresponding exponential components. Therefore, the Prony method is implemented in two iterations: on the first, the correct arguments of the exponential components are determined using all steps of the Prony method, on the second iteration, the specified arguments are used to find the corresponding amplitudes using only the third stage of the method. Such a splitting into iterations allows to select the correct arguments of the exponential components in the files, a priori containing a large number of low noise signals, and then use them at the second iteration.

The Prony method has no information about the start time of the signal, so at the first iteration the start time is determined by the linear spline of the leading edge of the signal. After calculating the attenuation coefficients and the corresponding amplitudes, good events are selected by applying the Pearson criterion. Correctly determined attenuation coefficients are entered into the ROOT histograms. The second iteration of signal processing consists in the implementation of the third stage of the Prony method, with an indication of the average values of the attenuation coefficients determined at the first iteration. The start time of the signal t_0 is determined by the maximum signal time and the known attenuation coefficients:

$$t_0 = t_{MAX} - \tau_r * ln\frac{\tau_r + \tau_d}{\tau_r} \quad (4)$$

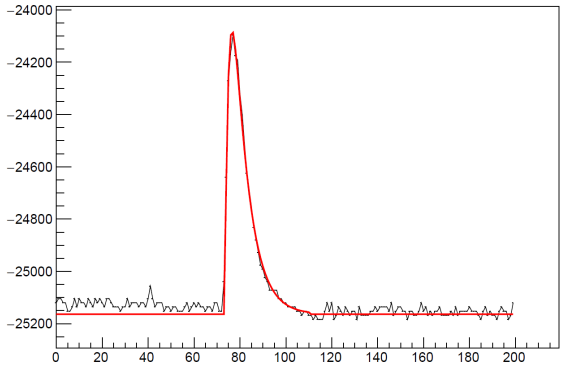

Figure 1: An example of waveform (black) and superimposed fit (red).

Figure 1 shows the characteristic waveform and superimposed fit. The obtained chi square values, normalized to the number of degrees of freedom, are shown in Figure 2, depending on the signal area under the fit. One can see a good separation of the muon spot located near the 3000 ADC channel and noise events grouped around 0. At the same time, the chi square selection also makes it possible to reliably separate these two groups of events.

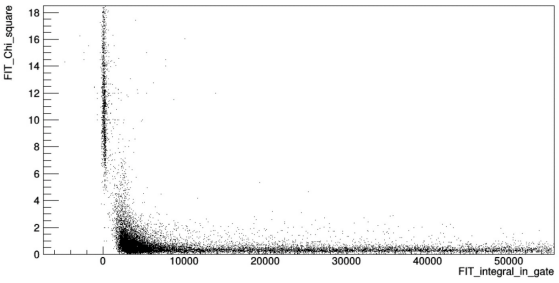

Figure 2: Normalized chi square as a function of signal charge.

Conclusion

A new method for fitting fast PSD signals based on the Prony least squares method has been proposed. This method allows to determine the amplitude and time of arrival of the signal more reliably. The advantages of the method make it possible to work with small signals near the noise level, in particular, the method will be used to calibrate calorimeter sections on cosmic muons. This was made possible largely due to the high speed of the new fitting procedure, which requires three orders of magnitude less machine time than standard minimization package in the ROOT environment. Work is underway to apply a new fitting procedure to the PSD signals obtained on test beams in order to improve the energy resolution at low energies.

References

[1] J.Glodo, W.W.Moses, W.M.Higgins,E. van Loef, P.Wong, S.Derenzo, M.J.Weber, K.S.Shah. Effects of Ce concentration on scintillation properties of LaBr3:Ce. Nuclear Science, IEEE Transactions vol.52, no.10, pp.1805–1808, 2005.

[2] S.L. Marple Jr. Digital Spectral Analysis with Applications. Acoustical Society of America Journal, 86(5), 1989. DOI: 10.1121/1.398548.

Status of PSD CBM platform development

M. Janda, F. Lopot, and V. Vacek
CTU, Prague, Czech Republic

Introduction

The PSD platform (see design study overview in Fig. 1) consists of three independent frames for movement of PSD in X and Y and Y rotation. Z movement is realized on the support structure the PSD platform is sitting on and it is not part of the PSD platform design. The PSD platform support structure design is going to be realized as soon as a CBM cave rails system is defined.

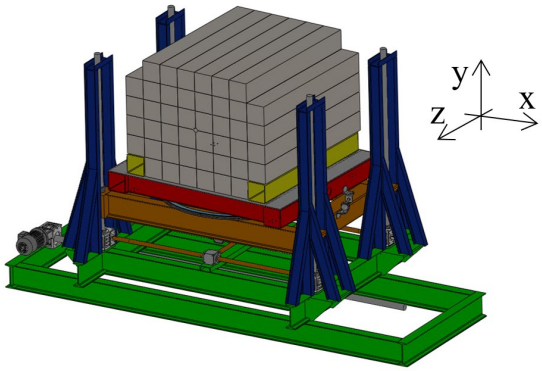

Figure 1: PSD Platform Design Study Overview.

Development

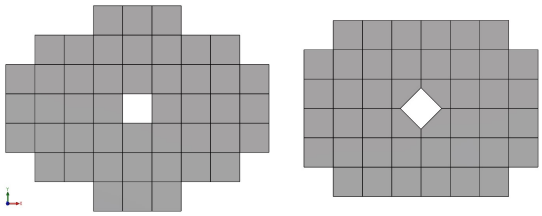

Figure 2: PSD Layouts (7x9 modules layout on left side, 6x8 modules layout on right side).

Very first idea of the PSD platform with movements in directions X and Y was presented at CBM week in GSI in March 2018. The presented idea was agreed by coordinators but with request to allow also Y rotation of PSD. The development team continued with modifying the design of the platform. There were selected drives with required parameters and all other purchased component such as linear guides, gearboxes etc. during this period.

Modified design of the platform was presented at autumn CBM Week at GSI in October. All modifications were agreed but two new requirements appear. 1. PSD modules should be kept in structure (=cage) which must allow to move with them by crane. 2. The cage must be able to accommodate two different PSD layouts (see Fig. 2).

Conclusion

The PSD platform 3D model is shown in Fig. 3. The developed platform allows to move with PSD in ranges +/- 900mm along X axis, +/- 700mm along Y axis and to rotate with PSD in range +/- 3deg along Y axis. The cage (in yellow) is able to accommodate two different PSD layouts as requested and allows to move with it by crane independently on the rest of the platform. Total weight of PSD and platform is approx. 29tons (23tons PSD + 6tons the platform).

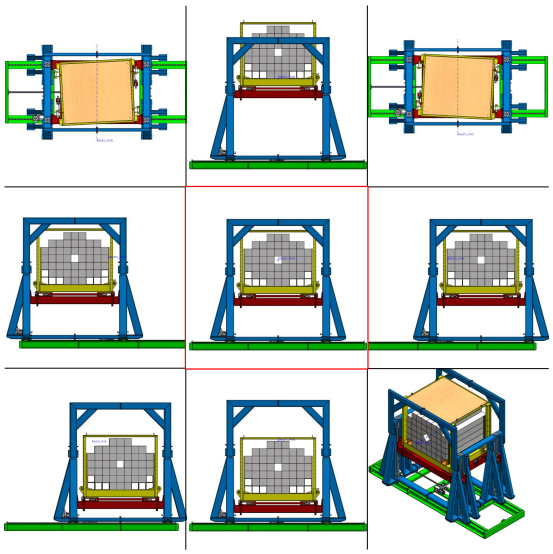

Figure 3: Reachable positions of PSD platform (all pictures show 7x9 modules PSD layout).

Pictures in top left and right corners show rotation along the Y axis. Picture in the middle shows a working position of PSD. Picture in bottom left corner shows a parking position of PSD and picture in bottom right corner shows an ISO view of 6x8 PSD layout mount on the platform.

Summary of PSD performance under radiation conditions

V. Mikhaylov[1,2], *A. Kugler*[1], *V. Kushpil*[1], *S. Morozov*[3,4], *O. Svoboda*[1], *and A. Senger*[5]

[1]NPI of CAS, Řež, Czech Republic; [2]CTU, Prague, Czech Republic; [3]INR RAS, Moscow, Russia; [4]MEPHI, Moscow, Russia; [5]GSI, Darmstadt, Germany

The Projectile Spectator Detector (PSD) of the CBM experiment is a compensating lead-scintillator calorimeter designed to measure the energy distribution of the forward going projectile nucleons and nuclei fragments (spectators) produced close to the beam rapidity [1]. High intensity beams at FAIR SIS100/300 up to $10^6/10^7$ interactions/s lead to the high radiation emission to the PSD making it act as a spallation target producing the high neutron fluence accompanied by the ionizing radiation.

PSD versus the ionizing radiation

The calorimeter irradiation was simulated with the FLUKA code for 2 months of the CBM run with Au+Au collisions on a 1 % interaction Au target at beam energy of 10 AGeV at the beam rate of 10^8 ions/s. Fig. 1 shows that the absorbed dose in the PSD does not exceed 1 kGy. Damage by the ionizing dose which is the most crucial for the scintillator tiles was studied in details for calorimeters of LHCb experiment [2]. The relative light yield of the LHCb tiles degraded by 25 % after 2.5 kGy irradiation, and then slowly decreased further by 20 % after irradiation up to 14 kGy. Therefore, scintillators and WLS-fibers of PSD are not expected to degrade significantly. Moreover, the modular structure and the longitudinal segmentation of PSD coupled with the regular calibration will ensure the stability of transverse and longitudinal uniformity of the light collection. Scintillator irradiation tests are being discussed to study their degradation in details.

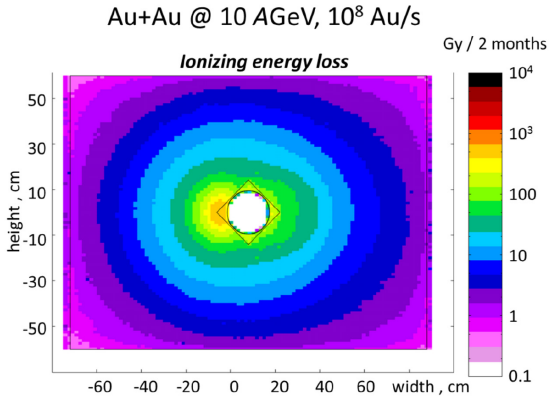

Figure 1: Distribution of ionizing energy loss in transverse plane at 20 cm depth from the PSD module front.

Radiation reduction techniques for PSD

To avoid a high radiation load in the central modules, there is a beam hole in the center of PSD. Three different beam hole shapes were considered, namely round with a 3 cm radius, quadratic- and diamond-shaped of 20×20 cm^2 size. Fig. 2 illustrates the reduction of non-ionizing energy loss by factor of 2 at the distance of 10 cm from the beam axis for the enlarged beam hole. Diamond-shaped hole design was chosen because it provided additional reduction to the ionizing dose compared to the quadratic-shaped design [3]. Another safety measure in form of a dedicated neutron shielding based on 8 cm thick polyethylene blocks with 3 % of boron is introduced reducing the fluence up to factor of five.

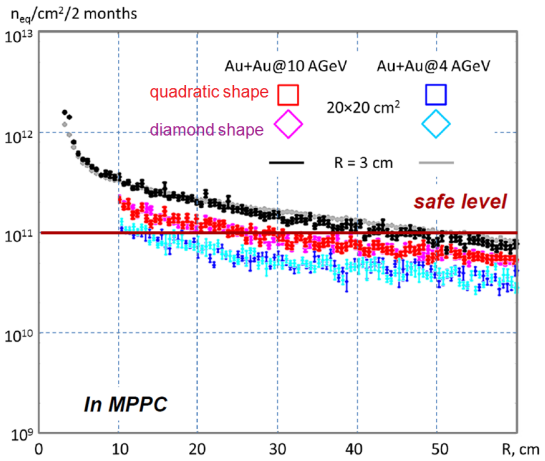

Figure 2: Non-ionizing energy loss vs radius at transverse plane where MPPCs are located for different configurations of the beam hole.

PSD versus the non-ionizing radiation

Non-ionizing energy loss is important for semiconductor readout electronics and most crucial for the Silicon Photomultipliers or Multi-Pixel Photon Counters (MPPCs) which have a fine pixel structure of 10×10 μm^2. 1 MeV equivalent neutron fluence at the very end of the calorimeter where the MPPCs are located is below 2×10^{11} n_{eq}/cm^2 for inner calorimeter modules (see Fig. 2). To study the effect of neutron fluence on MPPCs several samples were irradiated at the cyclotron of NPI with a broad (from thermal up to 34 MeV) neutron spectrum and total fluences in the

wide range of $6 \times 10^{10} - 9 \times 10^{12}$ n_{eq}/cm^2. After irradiation with 2×10^{11} n_{eq}/cm^2 MPPC dark current increased by 3 orders of magnitude and reached 10 μA [4]. This resulted in the increase of noise by 1 order of magnitude and consequent drop of signal to noise ratio down to ~ 50.

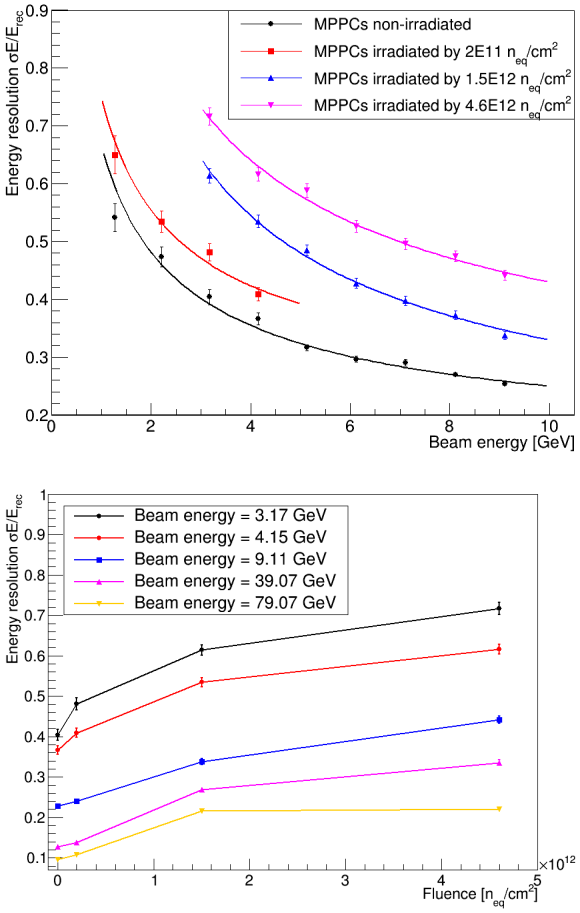

Figure 3: Single module proton energy resolution vs beam energies for different neutron fluences acquired by MPPCs (top) and vs fluence for different beam energies (bottom).

To study the calorimeter performance degradation due to the MPPC irradiation single PSD module was consequently equipped with 3 batches of irradiated photodiodes. The neutron fluences accumulated by MPPCs were 2×10^{11}, 1.5×10^{12} and 4.6×10^{12} n_{eq}/cm^2. Single module response to proton beams measured inside the PSD supermodule in the momentum range of 2 – 10 GeV/c is showed in Fig. 3 (top). Another test was performed with beams of up to 80 GeV/c momentum at calorimeter of NA61 experiment in CERN which has similar module design as CBM PSD. Detailed information on this test can be found at [4]. It is important to note, that only first 5 sections of the module were measured for MPPCs irradiated by 1.5×10^{12} and 4.6×10^{12} n_{eq}/cm^2. Dark currents of these photodiodes increased up to a few mA after irradiation, thus external voltage supply had to be used which introduced additional noise. Therefore, achieved performance for these highly irradiated MPPCs shall be regarded as the upper limit and expected to be much better in reality if such doses will ever be reached in the experiment.

Summary of the energy resolution degradation for both tests is presented in Fig. 3 (bottom). PSD module energy resolution drops only slightly after irradiation by 2×10^{11} n_{eq}/cm^2. Furthermore, inner calorimeter modules are located closer to the beam and typically detect higher signals which enhances signal to noise ratio and energy resolution. On the other hand, modules located further from the beam will achieve significantly lower dose which again improves energy resolution.

Conclusion

Overview of the recent investigations on the CBM PSD radiation performance is presented. Due to the harsh radiation conditions a 20×20 cm^2 beam hole and endcap neutron shielding are incorporated in design reducing the radiation load by factor of 10. Estimated absorbed ionizing dose below 1 kGy is expected to be safe for the operation, while further tests on the subject are being planned. High neutron fluence of 2×10^{11} n_{eq}/cm^2 results in slight deterioration of energy resolution due to degradation of the MPPC photodiodes. Achieved results are as well of interest for MPD and BM@N experiments at NICA and NA61 experiment at CERN where very similar calorimeter design including the MPPCs light readout is utilized.

References

[1] CBM collaboration, Technical Design Report for the CBM Projectile Spectator Detector (PSD), GSI Darmstadt 2015

[2] A. Alves et al. (LHCb collaboration), The LHCb Detector at the LHC, JINST 3, S08005 (2018).

[3] A. Senger, Simulation of PSD irradiation with enlarged beam hole, presentations at 29th – 32nd CBM Collaboration Meetings (2017 – 2018).

[4] V. Mikhaylov et al., Radiation hardness of Silicon Photomultipliers for CBM@FAIR, NA61@CERN and BM@N experiments, NIM A 912 241 (2018).

Test of PSD modules at the BM@N experiment

A.Ivashkin[1], *D. Finogeev*[1,3], *M.Golubeva*[1], *F.Guber*[1], *A.Izvestnyy*[1], *N. Karpushkin*[1,2], *S.Morozov*[1,3], *and A.Strizhak*[1,2]

[1]INR RAS, Moscow, Russia; [2]MIPT, Moscow, Russia; [3]MEPHI, Moscow, Russia

BM@N experiment

The BM@N experiment has unique possibility to investigate hot and dense nuclear matter in heavy ion collisions at Nuclotron beam energies between 2 and 6 AGeV [1]. The density of nuclear matter created in the collision zone at these energies exceeds the saturation nuclear density by a factor of 3-4 for gold-gold collisions [2].

Schematic view of the BM@N experimental setup is shown in Fig. 1. The momentum measurements of produced charged particles is performed with high precision track measurements by central tracker based on two-coordinate triple GEM detectors located downstream of the target inside the magnet and the drift/cathode pad chambers (DCH/CPC) of the outer tracker placed behind the magnet. BM@N dipole magnet has the gap around 1 m between the poles. The maximum magnetic field of the magnet is up to 1.2 T and can be varied to get the optimal BM@N detector acceptance and momentum resolution for different processes and beam energies. Particle identification is done by TOF measured between T0 detectors and multi-gap resistive plate chambers (mRPC) with a strip read-out. The TOF detectors provide time resolution about 80 psec. and allow to discriminate hadrons (π, K, p) as well as light nuclei with the momentum up to few GeV/c produced in multi-particle events. To measure the collision centrality in nucleus-nucleus collisions the ZDC is used. This hadron calorimeter is placed at the end of BM@N beam line on distance 9 m from the target.

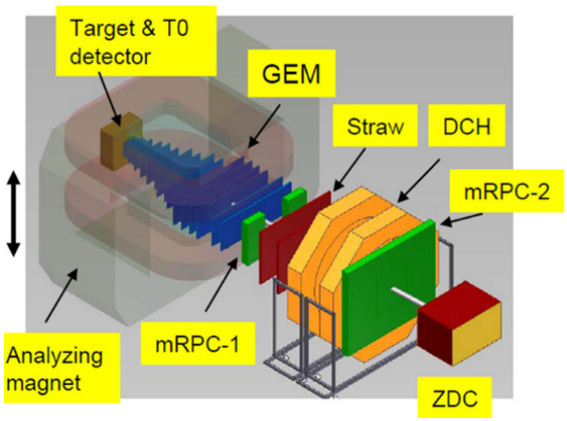

Figure 1: Schematic view of the BM@N set up.

New FHCal for the BM@N heavy ion experiments

Starting from 2020 new heavy ion experiments at BM@N are planned. It was shown by FLUKA simulations, that the radiation doses from ionizing and non-ionizing particles in central part of the present ZDC expected for gold beam at energy 4 AGeV and beam rate 2x10^6 ions per second will be too high and the light output in central modules will be decreased due to radiation damage.

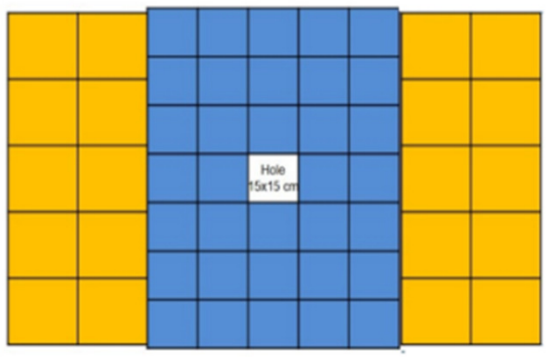

Figure 2: Proposed geometry of new FHCal BM@N. Yellow modules are from PSD CBM. Blue modules are shorter MPD/NICA ones.

To avoid the above problems, a new configuration of the hadron calorimeter was suggested. Twenty PSD CBM modules for outer modules of FHCAL BM@N will be used. The modules have transverse sizes of 20x20 cm^2 and active length corresponding to 5.6 nuclear interaction lengths. They have sampling structure and consist of 60 lead/scintillator layers with sampling ratio 4:1 (the thicknesses of the lead plates and scintillator tiles are 16 mm and 4 mm, respectively). Light readout from each scintillator is provided by WLS-fibers embedded in groove in the scintillator plate. The WLS fibers from each 6 consecutive scintillator tiles are combined together and connected to a single photodetector at the end of the module. The longitudinal segmentation of modules into 10 sections allows to avoid the effect of non uniformity of the light collection along the module. Ten Hamamatsu MPPCs S12572-010P with active area 3x3 mm^2 are used as photodetectors in each module. The light yield measured with muon beam is about 40-50 p.e./section.

For inner part of new calorimeter 34 modules of FHCAL MPD will be used. They have transverse sizes of 15x15

cm^2 and are shorter length of 7 longitudinal sections. Total length of inner modules corresponds to about 4 nuclear interaction lengths. Schematic view of new FHCAL is shown in Fig. 2.

In spring 2018 one PSD CBM module was installed in BM@N experimental area during the ^{40}Ar beam run, see Fig. 3. It was an unique chance to check the PSD module response to heavy fragments. The readout of module was integrated to the general data acquisition system of BM@N experiment. It allow one to use the beam counters for the selection of useful events. The beam energy was 3.5 $AGeV$ with the total ion energy of 140 GeV. Note, that the visible energy in PSD module is only about 2%, because the most part of the hadron shower is absorbed in the lead plates.

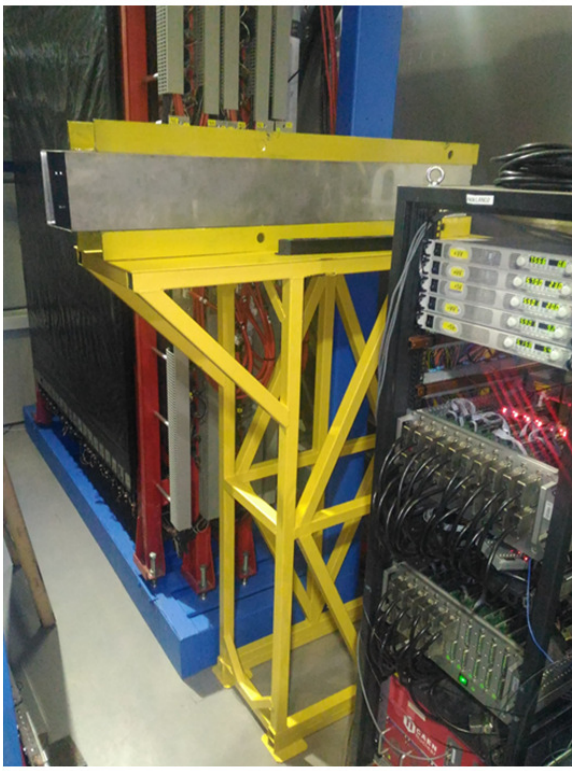

Figure 3: Photo of PSD module installed at BM@N beam line.

The amplitude spectrum of deposited in PSD module energies from ^{40}Ar ions is shown in Fig. 4. One can see, that the energy resolution for these heavy fragments is about 12% and is in good agreement with MC simulation.

Due to the longitudinal segmentation of PSD module to 10 section, it is possible to measure the longitudinal shower profile, see Fig. 5. One can see, that the maximum energy deposition is in the first section. It is explained by the very low energy of ^{40}Ar ions. Also, the hadron shower in module is rather short with almost no energy deposition in the last three sections.

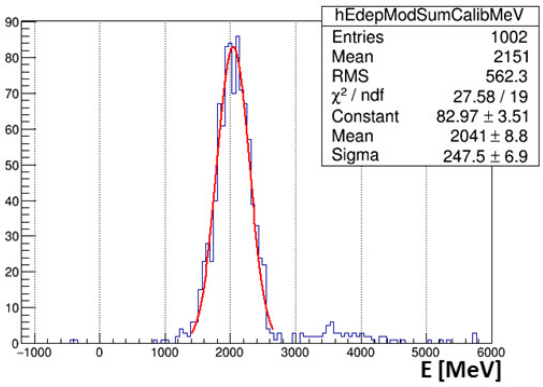

Figure 4: The amplitude spectrum of deposited in PSD module energies from ^{40}Ar ions.

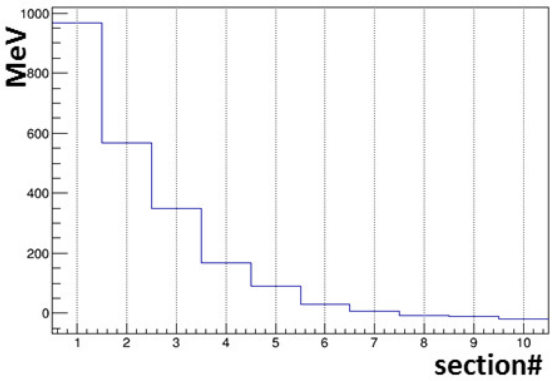

Figure 5: The longitudinal shower profile in PSD module for 3.5 $AGeV$ ^{40}Ar ions.

Conclusion

For the first time the response of PSD module was checked at heavy ^{40}Ar ion beam at BM@N experiment. The amplitude spectra and the shower profile were studied. The obtained energy resolution of about 12% and the hadron shower profile are in in good agreement with MC simulation.

References

[1] Ablyazimov T.O. et al. (BM@N Collaboration) Conceptual Design Report of BM@N. http://nica.jinr.ru/files/BM@N/BMN-CDR.pdf

[2] B. Friman, W. Norenberg and V.D. Toneev, Eur. Phys. J. **A3** 165-170 (1998)

Radiation damage and activation of CBM-PSD modules after use in FAIR-Phase0 experiments.

A. Senger and the CBM collaboration
GSI, Darmstadt, Germany

Within the CBM Phase 0 program various modules of the CBM Project Spectator Detector (PSD) will be used in the several experiments: in the fixed-target Baryonic Matter experiment at the Nuclotron (BM@N), in the Heavy Ion and Neutrino Experiment NA61 (Shine) at SPS, and in the mCBM experiment at SIS18. The geometries of the different PSD versions are shown in figure 1 for the BM@N experiment (top, CBM modules in yellow), and for the NA61 experiment(bottom, CBM modules in red). The CBM PSD module used in the mCBM setup at SIS18 is shown figure 2 together with the other detectors.

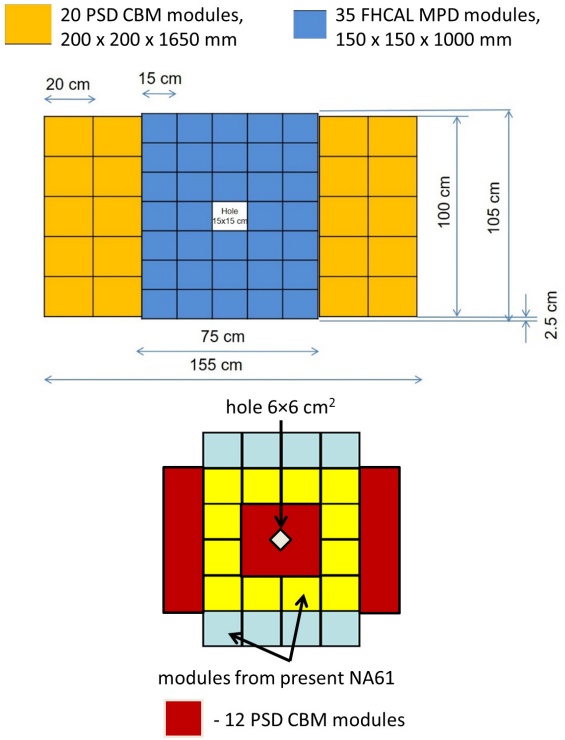

Figure 1: The geometries of the different PSD versions in BM@N (top, CBM modules in yellow) and NA61 (bottom, CBM modules in red).

Three important qualities have been calculated using the FLUKA code: (i) the ionising dose in the CBM PSD modules, (ii) the neutron equivalent dose in the photo-counters at the rear end of the modules, and (iii) the activation of the modules after the beam time. The geometry of the CBM PSD as implemented in FLUKA is shown in figure 3.

The PSD modules will be used under different experimental conditions:

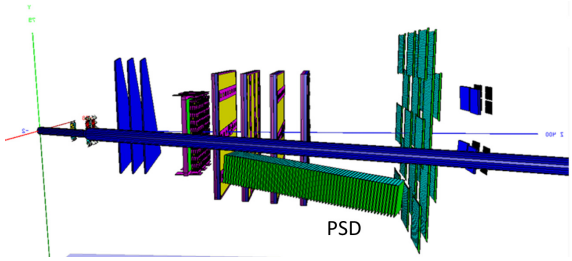

Figure 2: The mCBM setup with the PSD module (GEANT3 picture).

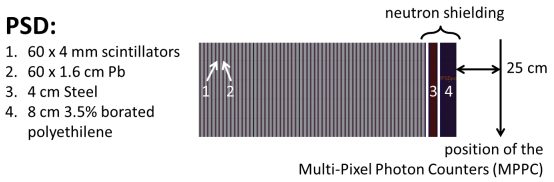

Figure 3: The geometry of the PSD as implemented in FLUKA.

- BM@N: Au beam @ 4 AGeV + 100 μm Au target, beam 2×10^6 Au/sec;
- NA61: Pb beam @ 150 AGeV + 210 μm Pb target, beam 2.5×10^4 Pb/sec;
- mCBM@SIS18: Ag beam @ 1.65 AGeV + 4 mm Ag target, beam 10^8 Ag/sec.

The results of the FLUKA calculations for the expected ionizing dose after typical experimental run times are as follows:

- BM@N: 100 Gy for a detector configuration without beam hole (v1), and less than 1 Gy for the detector arrangement with a beam hole of size 15×15 cm^2 (v2) after 2 months of beam time;
- NA61: 200 Gy after 1 month of beam time;
- mCBM@SIS18: 20 Gy after 1 week of beam time.

It is expected that the relative light yield of the scintillator tiles will degrade above ionization doses of 1 kGy. The simulation results indicate, that for operation of the PSD

modules in the CBM experiment, where the beam intensities are at least two orders of magnitude higher as at the Nuclotron, a beam hole of size 15×15 cm^2 might be required, in order to prevent serious performance losses due to radiation effects. A detailed study of the radiation damage of CBM scintillator tiles will be performed using the proton beam of NPI-CAS in Rez at the end of March 2019.

The neutron equivalent dose distribution in the place of photon-counters is shown in figure 4 for the various experimental conditions discussed above. Tests of counters have demonstrated that the internal noise increases after irradiation with doses above 10^{11} n_{eq}/cm^2. It is worthwhile to note, that the non-ionizing dose for the modules to be used in the BM@N experiment differ only about a factor of 2 for the detector configurations with hole (v1) and without (v1), whereas for the ionizing dose the difference was a factor of 100.

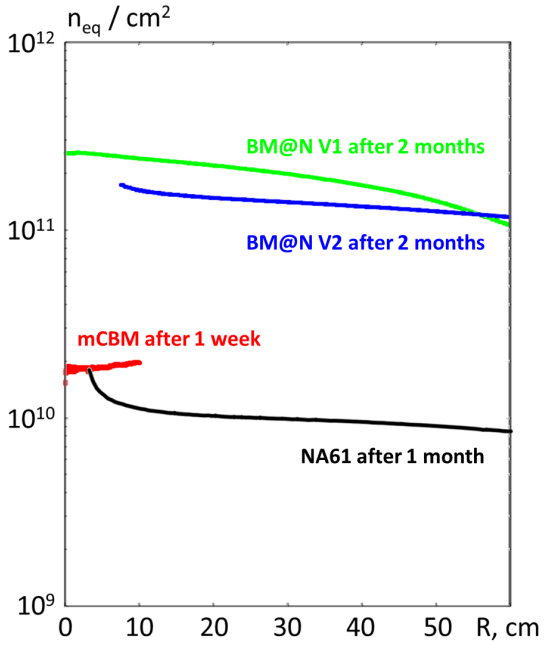

Figure 4: Non-ionizing dose in MPPC of CBM PSD in FAIR Phase0 experiments.

The CBM-PSD modules will be transported back from CERN or JINR to GSI after operation. Therefore, the activation of the modules is of importance. FLUKA predicts the following dose rates due to the activation of the PSD modules:

- BM@N: up to 2 μSv/h in neutron shielding after 1 month of beam shutdown for detector without beam hole;
- NA61: up to 10 μSv/h in regions closed to the beam hole and in the region of neutron shielding.

According to the German radiation safety regulations (Strahlenschutzverordnung StrlSchV), the maximum value of the dose rate has to be lower than 0.5 μSv/h if the modules will be transported or handled outside a radiation protection zone. Therefore, a decay time after irradiation longer than mentioned above might be required.

Magnet

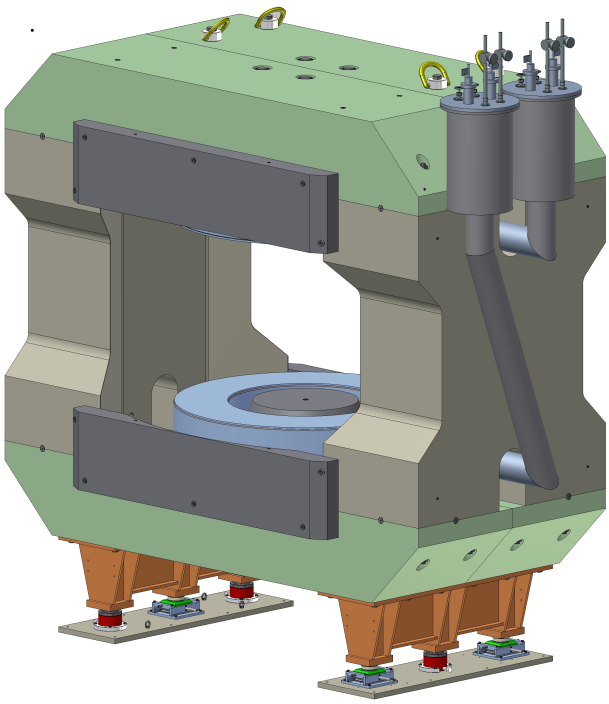

The superconducting dipole magnet of the CBM experiment.

P. Senger and the CBM collaboration
GSI, Darmstadt, Germany

Magnet design

The magnet has a free aperture of 1.44 m vertically and 3.0 m horizontally in order to accommodate the STS detector system with a polar angle acceptance of 25 degrees and a horizontal acceptance of 30 degrees. The 3D magnetic field calculations were made with two different codes (Mermaid and ANSYS), whereas the forces on the coils and the poles were calculated with the ANSYS 3D model. The results of the two codes for the magnetic field distribution along the beam are shown in figure 1. The maximum field in the centre of the magnet is 1.08 T (Mermaid) and 1.12 T (ANSYS).

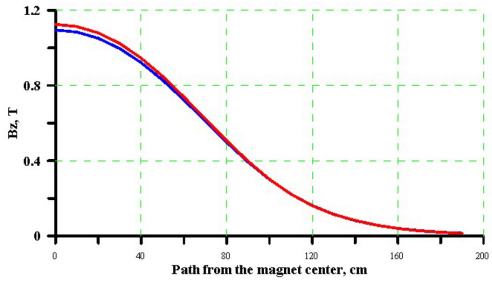

Figure 1: Magnetic field distribution along the beam starting in the center of the magnet. Blue line: Mermaid calculation. Red line: ANSYS calculation.

It was found that the calculated stresses in the coil structure and inside the windings are found to be well below acceptable stresses in stainless steel, copper, and the NbTi superconductor. The cross section of the iron yoke is shown in figure 2. The iron yoke serves as a construction frame for the magnet and systems of the detector. The total mass of the iron yoke is about 140 tons. It has special tools for adjusting its position in all directions. The magnet comprises two separated superconducting coils symmetrically placed close at the top and bottom blocks of the iron yoke. The coils are placed around the cylindrical pole shoes of the magnet.

The upper coil with the support struts is shown in figure 3. The main components of the coils are superconducting cables, the copper and the stainless steel cases, and the support struts. The design of the coil has been modified in 2018 according to the suggestions of the external expert committee. The coil still is cooled indirectly via the copper case and a liquid Helium cooling tube. However, the cooling tube now is located at the outer circumference of the coil, in order to provide pressure between copper case and

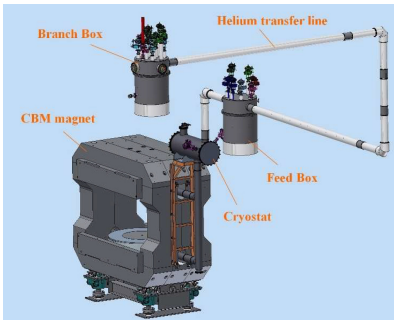

Figure 2: General view of the CBM magnet including cryogenics provided by BIBP.

coils while cooling down. The tube will be imbedded in the copper case such that the exit end of the tube is placed at a higher position than the inlet end of the tube (see figure 3). In this case the helium bubbles will accelerate the total helium flow along the tubes. Additional heaters at the outlet of the tubes will provide a forced flow, ensuring the function of the thermosyphon cooling concept. Moreover, the copper case now covers 4 sides of the coil, and the number of the support struts has been increased from 6 to 8 in order to distribute the forces more homogeneously on the steel case. Each coil will be made of two pieces of superconducting cable each with a length of about 4.5 km. The design includes the complete cryogenic system including the branch box, helium transfer line, the cryostat and the feed boxes, as well as the power supply and the quench detection and protection system.

The Conceptual Design Report has been approved in April 2018. The manufacture of the superconducting cable and of the iron yoke has started. The magnet will be provided by the Budker-Institute for Nuclear Physics (BINP) in Novosibirsk.

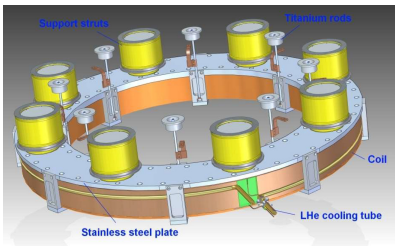

Figure 3: The superconducting upper coil with supports struts.

Magnetic field calculations with the volume integral equation method for CBM dipole magnet

P.G. Akishin[1], *A.A. Sapozhnikov*[1], *and V.P. Ladygin*[2]
[1]LIT-JINR, Dubna, Russian Federation; [2]LHEP-JINR, Dubna, Russian Federation

The CBM superconducting dipole magnet [1] with the enlarged vertical aperture up to 1440 mm has to provide the vertical magnetic field with a bending power of ∼1 T·m on the length 1 m from the target. The volume integral equation method (VIEM) [2] was used to calculate the magnetic field of CBM dipole magnet with BINP design to have a cross check of the TOSCA [3] simulation.

The following integral equation can be written for the intensity $\bar{H}(\bar{a})$ and the magnetization $\bar{M}(\bar{a})$ of the magnetic field in the point $\bar{a}$

$$\bar{H}(\bar{a}) = \bar{H}^S(\bar{a}) + \frac{1}{4\pi}\nabla_{\bar{a}} \int\limits_G \left(\bar{M}(\bar{x}), \nabla_a \frac{1}{|\bar{x}-\bar{a}|} \right) dv_{\bar{x}}$$

, where $\bar{H}^S(\bar{a})$ is the magnetic field from the current winding, G is the area filled by iron. The field $\bar{H}^S(\bar{a})$ can be found according to the Biot-Savart law

$$\bar{H}^S(\bar{a}) = \frac{1}{4\pi}\mathrm{Rot}_{\bar{a}} \int\limits_{R^3} \frac{\bar{J}(\bar{x})}{|\bar{x}-\bar{a}|} dv_{\bar{x}},$$

where $\bar{J}(\bar{x})$ is the current density.

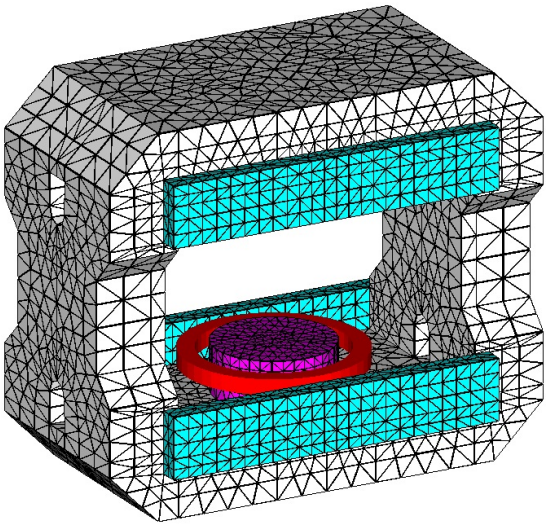

Figure 1: 3D model of CBM dipole magnet.

The method of volume integral equations with the linear approximation of magnetization [4] has been used for the CBM dipole magnet calculation. The symmetry of magnetic field has been taken into account, that allowed to reduce the number of unknown parameters in 8 times. $1/8$-th of the magnet has been divided into 12841 tetrahedrons. The total number of vertexes was 3128. 3D model of CBM dipole magnet is presented in Fig.1.

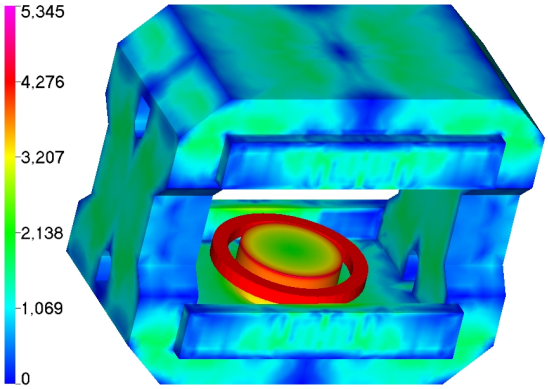

Figure 2: The CBM magnet saturation picture.

The magnet field saturation inside the CBM magnet is shown in Fig.2. Maximal field saturation is at the poles.

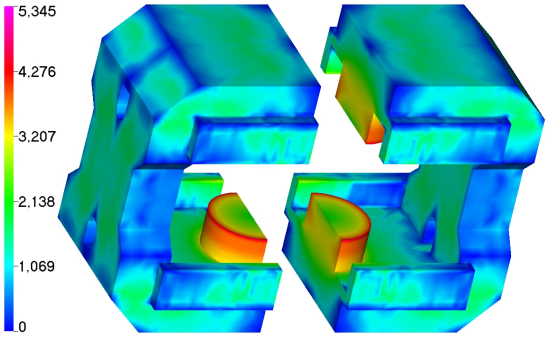

Figure 3: Field distribution inside the CBM dipole magnet obtained by VIEM [4].

Field distribution inside the yoke and poles of CBM dipole magnet obtained by VIEM [4] is shown in Fig.3.

The comparison of the vertical magnetic field component B_y distribution along the beam direction obatined by TOSCA [3] and VIEM [4] is presented in Fig.4. z position is given in mm. The field integrals are ∼0.995 T·m and ∼0.996 T·m for the current in one coil of 1.2 MA for the TOSCA [3] simulation and VIEM [4], respectively.

VIEM approach has been used for the calculations of the magnetic field for BINP version of the CBM dipole magnet. These calculations confirm the calculations performed

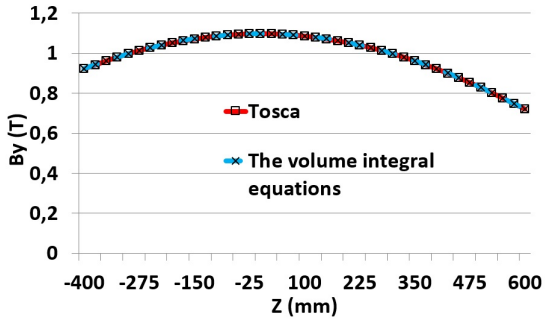

Figure 4: The comparison of the results obtained by VIEM [4] and with TOSCA [3] for the vertical component of the magnetic field.

using TOSCA and ANSYS.

References

[1] The CBM collaboration, "Technical Design Report for the CBM Superconducting Dipole Magnet", Darmstadt, 2014.

[2] C.W. Trowbridge, "Progress in magnet design by computers", Proc. 4-th Int. Con. Magnet Tech., 1972, p. 555.

[3] J. Simkin and C.W. Trowbridge, "Three dimensional non-linear electromagnetic field computations using scalar potentials", IEE Proc. B **127**, 1980, p.368.

[4] P. Akishin, A. Sapozhnikov, "Linear Approximation of Volume Integral Equations for the Problem of Magnetostatics", EPJ Web Conf. **173**, 2018, 03001.

Magnetic field calculations for RICH detector

P.G. Akishin[1] *and V.P. Ladygin*[2]
[1]LIT-JINR, Dubna, Russian Federation; [2]LHEP-JINR, Dubna, Russian Federation

The CBM superconducting dipole magnet has to provide the bending power of ∼1 T·m and quite low stray magnetic field in the region of RICH [1]. The magnetic field in the vicinity of the RICH photodetector has been calculated for BINP design of the CBM magnet. The 3D- model of CBM dipole magnet with RICH photodetector without z- symmetry for the TOSCA [2] simulation is presented in Fig:1.

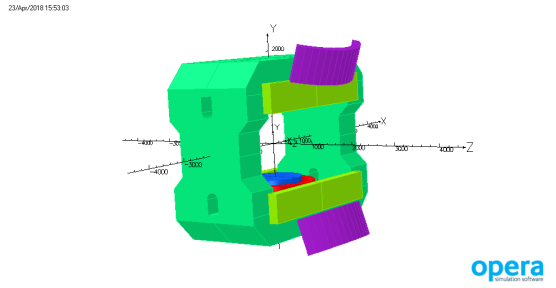

Figure 1: 3D model of CBM dipole magnet with RICH photodetectors.

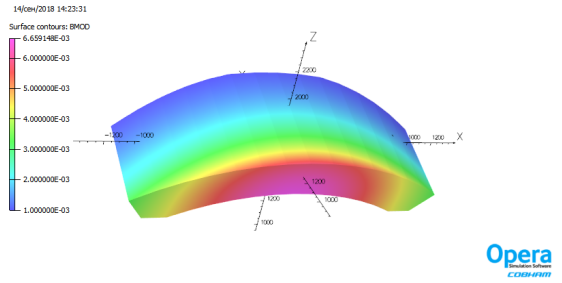

Figure 2: The field distribution in the area of RICH detector.

The field distribution in the RICH region is shown in Fig:2. The value of the stray field approaches about 6-7 mT in the region of RICH photodetectors, that requires the use of the shielding box. The appropriate shielding box must to block the field penetration in the RICH photodetector region. It should also not to reduce the angular acceptance of CBM and the RICH acceptance itself.

The main problem in the construction of the shielding box is very short distance between the RICH photodetectors and the magnet. The possible shielding box design for reducing the stray field level in the region of photosensors is shown in Fig:3. The shielding box holes should have the holes for high-voltage, low-voltage, signal cables and electronic air cooling for the RICH photodetector operation.

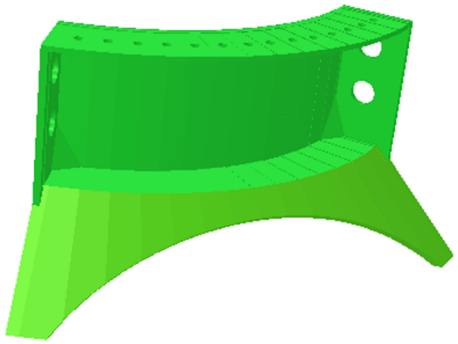

Figure 3: The shielding box of the RICH photodetector.

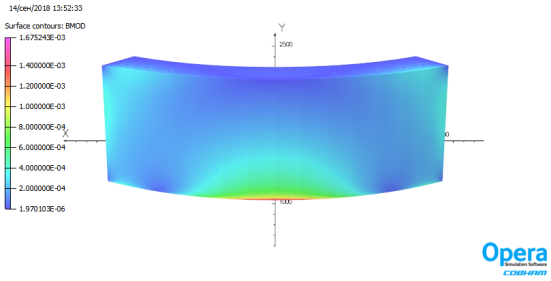

Figure 4: Distribution of the magnetic field in the area of the RICH shielding box.

The holes break the screening field from the dipole magnet into the box. This is the reason to locate the holes on the box sides and top where the field value is less. The volume of the present shielding box is ∼0.215 m^3.

Fig.4 shows the distribution of the absolute value of magnetic field inside the shielding box for the BINP ver-

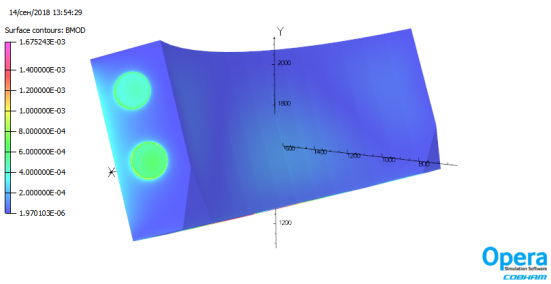

Figure 5: View of the magnetic field distribution in the area of the RICH shielding box from the side.

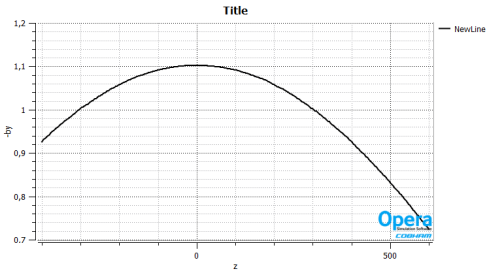

Figure 6: The distribution of B_y magnetic field component along z axis for the electron version of the CBM detector. z position is given in mm.

sion of the CBM magnet. The calculation demonstrates the significant decrease of the magnetic field in the photocatode plane. The field value does not exceed 1 mT. View of the magnetic field distribution in the area of the RICH shielding box from the side is shown in Fig.5.

The vertical magnetic field component B_y distribution along the beam direction is shown in Fig.6. The maximal value of the B_y component is $\sim$1.1 T with the field integral of $\sim$1.00028 T·m for the current in the coil of 1.209 MA.

The authors are grateful to C.Höhne, Ch.Pauly and E.V.Ovcharenko for their interest in this study, helpfull discussions and the technical support.

References

[1] The CBM collaboration, "Technical Design Report for the CBM Superconducting Dipole Magnet", Darmstadt, 2014.

[2] J. Simkin and C.W. Trowbridge, "Three dimensional nonlinear electromagnetic field computations using scalar potentials", IEE Proc. B **127**, 1980, p.368.

3D- simulation for new design of the CBM superconducting dipole magnet

P.G. Akishin[1], Yu.V. Gusakov[2], A.V. Bychkov[2], and V.P. Ladygin[2]
[1]LIT-JINR, Dubna, Russian Federation; [2]LHEP-JINR, Dubna, Russian Federation

BINP design of the CBM superconducting dipole magnet with the enlarged vertical aperture up to 1440 mm is shown in Fig.1. It has few differences from the initial one [1], namely, the cylindrical poles, 4 flat vertical beams and 6 narrow horizontal beams. The materials of the poles and yoke are the ARMCO and the SA1010 steel, respectively. Magnetic and stress analysis for BINP design was made with the ANSYS [2] and TOSCA [3].

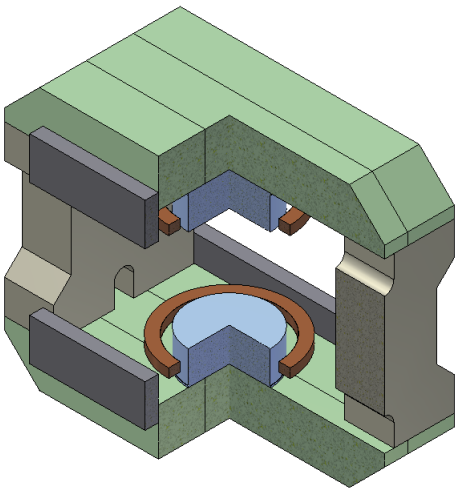

Figure 1: BINP design of the CBM magnet.

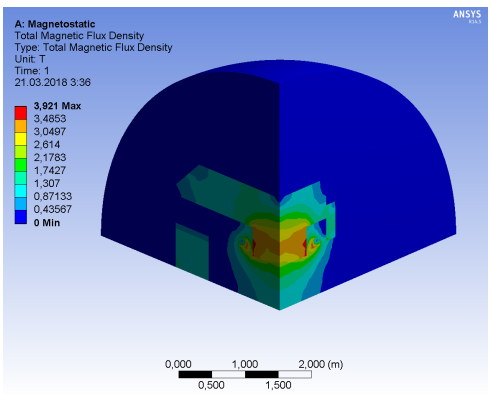

Figure 2: Total magnetic flux density in the CBM magnet.

The total magnetic flux density in the magnet and in the superconducting coil calculated using ANSYS workbench [2] are presented in Fig.2 and Fig.3, respectively. The current in the coils is 1.2 MA (686 A). The maximal magnetic field in the coils is 3.9 T. The vertical forces acting on the coils are ∼311 tons. The field integral is 1.001 T·m.

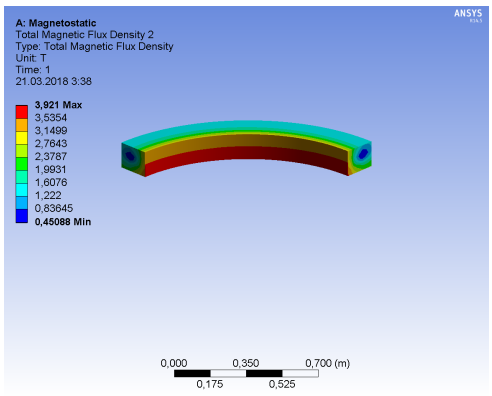

Figure 3: Total magnetic flux density in the CBM magnet coil.

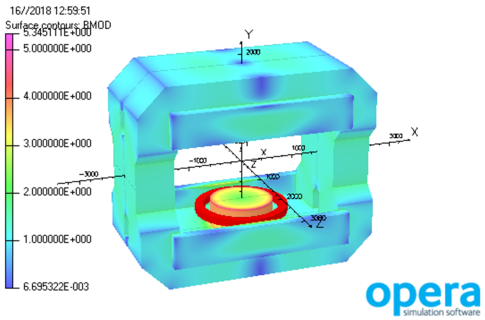

Figure 4: The CBM magnet saturation picture.

TOSCA [3] was used for 3D modelling. The current in one coil is 1.2 MA. The CBM magnet saturation picture and the vertical magnetic field component B_y distribution along the beam direction are shown in Fig.4 and Fig.5, respectively. The maximal value of the B_y component is ∼1.1 T with the field integral of ∼0.995 T·m. The results are consistent with the ANSYS calculations [2]. The additional investigation has been performed for the current in the coil of 1.209 MA. In this case the field integrals are ∼1.0002 and ∼1.0001 for muon and electron versions of the CBM magnet, respectively.

3D magnetic field maps for all models have been calculated and provided for CBMRoot.

The expertise of the BINP design of the CBM supercon-

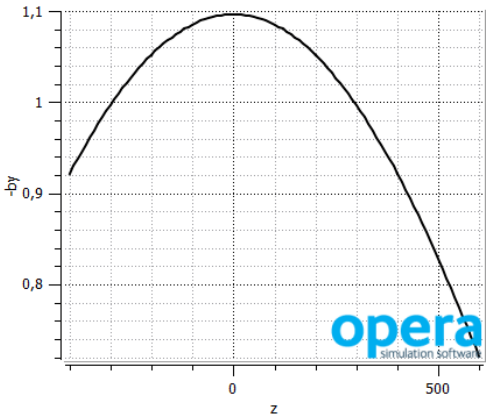

Figure 5: The vertical component of the magnetic field distribution for the muon version of the CBM detector. z position is given in mm.

ducting magnet has been performed using ANSYS [2] and TOSCA [3]. It is shown that the current version of the magnet satisfies to the TDR requirements [1].

References

[1] The CBM collaboration, "Technical Design Report for the CBM Superconducting Dipole Magnet", Darmstadt, 2014.

[2] "Finite Element Simulation", http://www.ansys.com

[3] J. Simkin and C.W. Trowbridge, "Three dimensional nonlinear electromagnetic field computations using scalar potentials", IEE Proc. B **127**, 1980, p.368.

Infrastructure

Radiation from beam dump of the CBM experiment

A. Senger and the CBM collaboration
GSI, Darmstadt, Germany

Introduction

This report is based on the CBM Internal Technical Note 19001. This note describes the results of simulations performed with the FLUKA transport code concerning secondary radiation sources in the CBM experiment: backscattering of particles (mainly neutrons) from beam dump during the measurements, and radiation in the cave due to activation of the iron beam dump after beam shut down. To reduce the yield of backscattered neutrons from the beam dump, a shielding device is proposed. The same device can be used to reduce the radiation from the activated beam dump after beam shut down.

The CBM beam dump

The CBM beam dump was designed for high-intensity heavy-ion beams from SIS300, i.e. Au beams with a kinetic energy of 30 A GeV and an intensity of 10^9 ions/s. Cross sections of the CBM cave and the beam dump are shown in figure 1. The dump consists of an iron core (4000 tons) surrounded by a concrete shielding (5000 tons). The total length of the dump is approximately 30 m with a width and height of about 10 m, the entrance window has a size of 2 x 2 m^2.

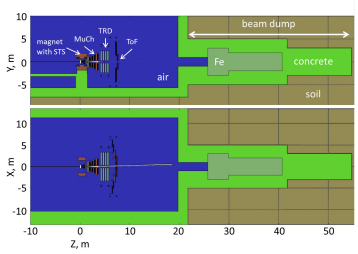

Figure 1: Side view (upper panel) and top view (lower panel) of the CBM cave and the beam dump (see text).

Radiation from beam dump

The horizontal distribution of the non-ionizing dose in the CBM cave produced by particles backscattered from the beam dump during the measurements is shown in figure 2. The FLUKA calculation was performed without shielding for an Au beam with kinetic energy of 2A GeV and an intensity of 10^9 ions/s over 2 months for a 1% interaction Au target and 50% of the nominal magnetic field. During beam operation, large areas of the TOF detector and its electronics will be irradiated with a total dose between about 5×10^10 and 5×10^11 neq/cm^2. It is important to note, that in this calculation the vertical opening of the beam dump already has been reduced to a height of 20 cm only by concrete blocks of 1 m thickness, as illustrated in figure 4.

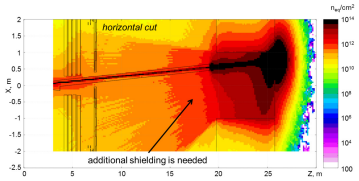

Figure 2: Horizontal distribution of the non-ionizing dose in the CBM cave without shielding (see text).

Figure 3 illustrates the horizontal distribution of dose rate due to the activation of the iron beam dump and the target 1 day after beam shut down. The FLUKA calculation has been performed for an Au beam with kinetic energy of 2A GeV and an intensity of 10^9 ions/s over 2 months for a 1% interaction Au target and 50% of the nominal magnetic field. The dose rate downstream the TOF wall increases from about 5 μSv/h up to about 50 μSv/h close to the beam dump entrance.

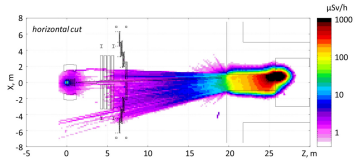

Figure 3: Horizontal distribution of the dose rate in the CBM cave due to the activation of the beam dump and the target 1 day after beam shut down (see text).

Proposal for a beam dump shielding

The dose rate limit for occupationally exposed persons (OEP) is 3 Sv/h, and should not exceed a value of 100 μSv for a one-time exposure. In order to reduce the radiation in the cave after beam shut down, the beam dump should be shielded. Figure 4 illustrates a possible shielding scenario for the beam dump. The 2 x 2 m^2 entrance window should be permanently filled with concrete blocks leaving open only a slit of about 20 cm height for the beam

pipe. The horizontal width of the slit is required for moving the beam pipe according to the beam deflection. After beam shut down, the slit will be completely closed by two movable paraffin wax blocks. During the experiment, the paraffin blocks will be shifted in order to open space for the beam pipe. The paraffin shielding will reduce the radiation level due to backscattered particles during beam operation.

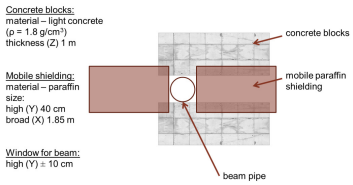

Figure 4: Front view of the beam dump window with concrete and paraffin shielding during beam operation. Please note that the figure is not to scale. The concrete blocks cover the 2 x 2 m^2 large opening of the beam dump, except for the window for the beam, which has a width of 2 m and a height of 20 cm. After beam shut down, the hole for the beam will be closed by the mobile paraffin blocks (see text and figure description).

In order to estimate the required thickness of the paraffin blocks, FLUKA calculations have been performed for an Au beam with a kinetic energy of 11A GeV, and a beam intensity of 10^9 ions/s integrated over a beam time of 2 months. Figure 5 depicts the dose rate in front of the shielding 1 day after beam shut down for different thicknesses of the paraffin blocks. Assuming a thickness of 60 cm for the paraffin shielding, the dose can be reduced by a factor of about 100 down to a value below 3 μSv/h in front of the paraffin blocks.

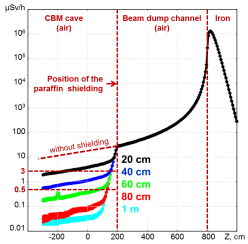

Figure 5: Distribution of the dose rate in the CBM cave due to the activation of the beam dump for different thicknesses of the paraffin shielding calculated with FLUKA 1 day after beam shut down (see text).

Backscattering of neutrons during the measurements with and without beam dump shielding

Figure 6 illustrates the rate density of particles in the horizontal plane in the CBM cave during the measurements without paraffin beam dump shielding. The FLUKA calculation was performed for an Au beam with kinetic energy of 2A GeV and an intensity of 10^9 ions/s. The upper and lower panel of figure 6 depicts the rate density of charged particles and neutrons, respectively. The profiles of the particle distributions indicate that the charged particles are emitted predominantly from the target region, whereas the neutrons stem from the beam dump. This scenario is supported by figure 7 which presents the same distributions as in figure 6 but with paraffin beam dump shielding of 60 cm thickness. The charged particle density in the cave is not affected by the beam dump shielding, whereas the neutron radiation is reduced by shielding the dump.

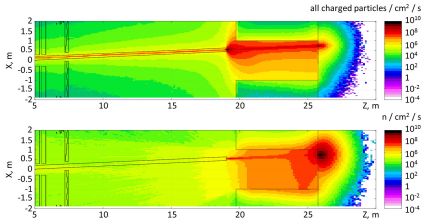

Figure 6: Rate density of charged particles (upper panel) and neutrons (lower panel) in the CBM cave during the measurements without paraffin beam dump shielding (see text).

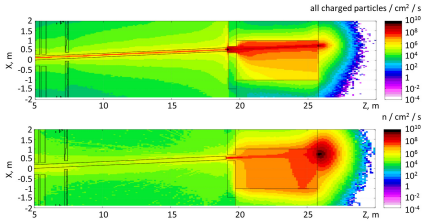

Figure 7: Rate density of charged particles (upper panel) and neutrons (lower panel) in the CBM cave during the measurements with a 60 cm thick paraffin beam dump shielding (see text).

Conclusions

In order to reduce the radiation in the cave during and after beam operation, it is proposed to install movable paraffin beam dump shielding, which consists of two blocks of 40 cm height and 185 cm length. During beam operation, the two blocks leave space for the beam pipe, whereas after beam shut down this gap will be closed to shield the activated beam dump. With a paraffin thickness of 60 cm, the dose due to activation is reduced by a factor of about 100 down to a value below 3 μSv/h in front of the shielding blocks. During beam operation, the total neutron flux through the TOF within an area of about 4 x 1 m^2 can be reduced by about a factor of 10 by the paraffin beam dump shielding of 60 cm thickness.

Design simulations of beam pipe and radiation studies for the CBM experiment

A. Senger and the CBM collaboration
GSI, Darmstadt, Germany

Introduction

This report is based on the CBM Internal Technical Note 18001. This note describes the conceptual design of a vacuum beam pipe for the CBM experiment based on simulations of the beam using the transport codes FLUKA and GEANT3. The task of the beam pipe is to guide a high-intensity beam of up to 10^9 Au ions/s to the beam dump without producing significant background radiation in the various detector stations, taking into account the broadened beam profile due to multiple scattering in the target, and the deflection of the beam in the field of the CBM dipole magnet. The beam profile defines a certain minimal diameter of the beam pipe, and the deflection of the beam requires - depending on beam energy and Z/A ratio - a variable bending of the beam pipe provided by a bellow. In principle, the beam pipe could be bend with a fixed angle, which then would require to adapt the magnetic dipole field to the rigidity of the beam. However, this solution would prevent the possibility to optimize the magnetic field, and, hence, improve the momentum resolution, in particular for beams with high rigidities such as protons or nuclei with equal number of protons and neutrons. A particular challenge for the beam pipe design represents the Projectile Spectator Detector which has a hole for the passage of the beam. This hole has to be sufficiently wide to reduce the flux of scattered beam particles into the active detector area, but on the other hand should be narrow to detect beam fragments produced in the target.

Simulation framework and input

The simulations have been performed using the transport codes FLUKA and GEANT3. Gold beams with kinetic energies between 2A and 10A GeV have been used to study the interaction of the beam with the target, the detector materials, the proposed beam pipe and the beam dump. For the design of the beam pipe and the beam dump the beam profile after the target has to be considered. The typical size of the SIS100 Au beam hitting the target is $\Delta x = \Delta y = 0.6$ mm with a divergence of 1.7 mrad [1]. Figure 1 depicts the horizontal profile of an Au beam with an energy of 2A GeV at a distance of 1.6 m behind a 250 μm thick Au (1% interaction) target as calculated with FLUKA for a typical SIS100 beam (red) and for a point-like beam (blue). The comparison clearly demonstrates that the beam profile is generated by multiple scattering in the target. The deflection of the beam is due to the magnetic field which was assumed to be 100% (BL = 1 Tm).

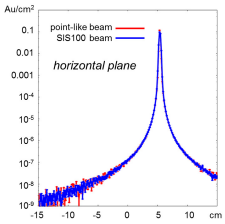

Figure 1: Horizontal profile of an Au beam with kinetic energy 2A GeV at a distance of 1.6 m downstream a 250 μm thick Au target for full magnetic field calculated with the FLUKA code assuming a typical SIS100 Au beam with $\Delta x = \Delta y = 0.6$ mm and a divergence of 1.7 mrad (blue histogram) compared to a point-like beam (red histogram).

The deflection of a gold beam due to the magnetic field of the CBM dipole is illustrated in the left panel of figure 2 left for beam kinetic energies between 2A and 8A GeV and the full magnetic field integral of 1 Tm. For energies above 6A GeV the beam still hits the iron core of the beam dump, while for lower energies this is no longer the case. This situation already requires to reduce the magnetic field for low Au beam energies. Low-energy beams with a larger Z/A ratio than Au, in particular protons, require even more reduced magnetic fields. The calculations show already that the position of the PSD has to be adjusted to the beam deflection. The right panel of figure 2 right depicts the beam profile at the entrance of the beam dump for Au beam kinetic energies between 2A and 10A GeV for scaled magnetic fields. The scaling factors for the different beam energies were taken from the Technical Design Report of the PSD. The 6A GeV beam (green line) would still be well within the iron core of the beam dump if the scaling factor of 60% would be increased to 80% or 90%.

Beam pipe concepts

The beam pipe within the STS has been designed and a prototype has been built. The technical drawing is shown in figure 3 [2]. This beam pipe, which consists of carbon fiber of 0.5 mm thickness, has been used in the FLUKA calculations. After testing the mechanical stability of the carbon pipe, the thickness has been increased to 1 mm, while the window for the particles still remains 0.5 mm thick. According to FLUKA calculations, the increased thickness of the pipe does not generate more background in the detectors.

The STS beam pipe ends with a flange (see figure 3) and

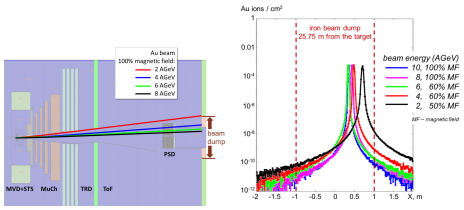

Figure 2: Left: Deflection of Au beams with kinetic energies between 2A and 8A GeV by the magnetic field with an integral of BL = 1 Tm (= 100%). Right: Horizontal profiles of Au beams with kinetic energies from 2A to 10A GeV at the entrance of the beam dump traversing a 250 μm hick Au target for different scaling factors of the magnetic field as proposed in the TDR of the PSD. The distributions are normalized to one Au ion.

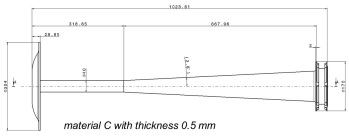

Figure 3: Beam pipe within the STS.

is followed by the beam pipe within the RICH or the MuCh detector. These two beam pipes have to fulfil very different requirements concerning material budget, and will be designed for each detector separately. However, these beam pipes should agree in their general shape in order to fit to the upstream STS beam pipe and to the downstream TRD and TOF beam pipe. For the following design considerations and corresponding calculations it is assumed that the RICH/MuCh beam pipe continues like the conical part of the STS beam pipe, resulting in a radius of R = 7.47 cm at a distance of 170 cm downstream the target, and a radius of R = 16.16 cm at a distance of 370 cm. The beam profile at 370 cm is shown in figure 4. For the calculations it is assumed that the beam pipe consists of carbon fiber with 0.5 mm wall thickness.

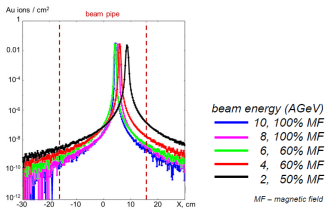

Figure 4: Au beam profiles for kinetic energies between 2A and 10 A GeV at a distance of 370 cm behind the 250 μm thick Au target for scaled magnetic fields. The distributions are normalized to one Au ion.

It can be seen in figure 4 that at a distance of 3.7 m downstream the target the beams are displaced from the center of the beam pipe, and one tail of the beam distributions starts to hit the beam pipe. Moreover, when continuing with a conical beam pipe, it would not fit into the inner holes of TRD, TOF and PSD. Therefore, it is assumed for the following simulations that the beam pipe will continue with a cylindrical shape, which is tilted to confine the beam in the center until it reaches the beam dump. Figure 5 depicts two beam pipe options with a bellow between RICH/MuCh and the TRD detector. One concept is a cylindrical beam pipe with a radius of R = 16.16 cm up to the entrance of the PSD, where the radius is reduced to R = 9.5 cm in order to fit into the hole of the PSD. The reduction of the radius is accompanied by a shift of the beam pipe in order to keep the beam in the center of the smaller pipe. The other concept assumes the reduction of the radius to R = 9.5 cm and the re-centering of the pipe directly behind the bellow. For both beam pipe options the bellow has to provide a kink angle between 0.7 and 1.8 degrees for Au beams with energies of 10A and 2A GeV, respectively. The tilt of the beam pipe according to the beam rigidity requires the corresponding movement of the mechanical structures of the pipe including pumps, and of the PSD. For the following simulations it is assumed that the beam pipes consists of carbon fiber with 0.5 mm wall thickness.

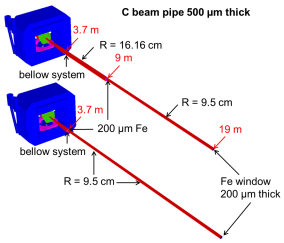

Figure 5: Models of the two beam pipe versions in CBMroot.

Conclusion and next steps

Two options for the CBM beam pipe have been proposed. According to the FLUKA calculations both beam line options show the same performance concerning the background radiation level in the detectors and in the cave. The next step is to use the beam pipe models for physics simulations, in order to study the influence of the additional background radiation on the performance of global track reconstruction and particle identification. Particularly important is the study of the performance of the PSD concerning event plane reconstruction which might suffer most from the additional radiation background. In order to prepare these simulations, the two beam line options have been implemented into CBMroot.

References

[1] Sebastian Ratschow, private communication

[2] Wolfgang Niebur, private communication

Web and ROOT interfaces to FLUKA calculation results for the CBM cave

A. Senger and the CBM collaboration
GSI, Darmstadt, Germany

Introduction

This report is based on the CBM Internal Technical Note 18013. FLUKA calculations of the ionizing dose, non-ionizing energy loss, and hadron fluxes in all areas of the CBM cave have been performed for min. bias Au+Au collisions with a beam kinetic energy of 11A GeV, a 1% interaction target, and a running time of 1 month. A beam intensity of 10^9 ion/s was assumed for the muon setup, which comprises the STS, the MuCh, the TRD, and the TOF. A beam intensity of 10^8 ion/s was chosen for the electron setup, which consists of the MVD, the STS, the RICH, the TRD, the TOF, and the PSD. The bin size of the data depends on the area: $1\times1\times1$ m^3 for the cave, $50\times50\times50$ cm^3 for the E10 service area, and $10\times10\times10$ cm^3 for the magnet gap. The FLUKA results can be accessed by a Web and a ROOT interface. The latter one also allows to modify the beam intensity and the running time. The location of the interfaces can be found in the internal note.

Web interface

Figure 1 depicts the web page with FLUKA results, which were converted into the ROOT format. Users have access to the predefined ROOT histograms for an Au beam with a kinetic energy of 11A GeV, with an intensity 10^9 Au/s, and 1 month of running for the muon setup of CBM. For the electron setup of CBM, the beam intensity is 10^8 Au/s. The interface uses JSROOT (https://root.cern.ch/js/) for handling the ROOT files. The upper panel of figure 1 illustrates the geometries of the three areas for which the FLUKA calculations were performed: cave (left), E10 service area (middle), and magnet gap (right). The same area names were used for ROOT file. For each area three different quantities were calculated: ionizing dose, non-ionizing energy loss, and the flux of hadrons with energy > 20 MeV. In order to draw a histogram, the user has to click on the histogram name. The canvas with the selected histogram will be produced.

The grid of the histograms is for

1. The cave: $1\times1\times1$ m^3;
2. The magnet gap: $10\times10\times10$ cm^3;
3. The E10 service area: $50\times50\times50$ cm^3.

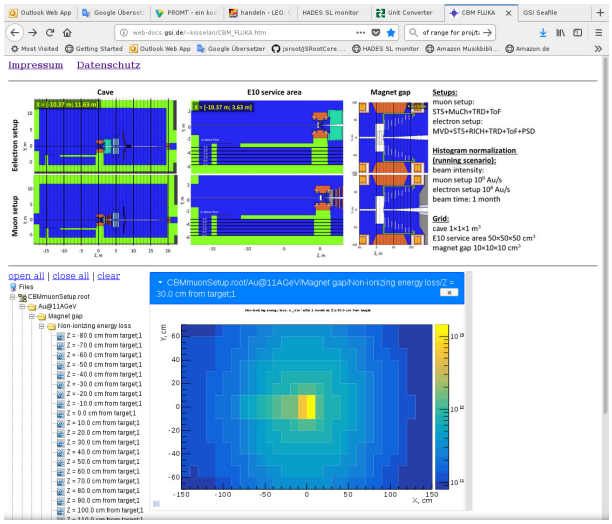

Figure 1: Web interface for the FLUKA results.

ROOT interface

The ROOT interface is a ROOT based GUI and has to be used on LINUX. It is a ROOT macro. There are two possibilities to run the GUI: the user has to copy all the files needed into his home directory, and run GUI without connection to GSI. Alternatively, the user can run the macro after connection to GSI on the LINUX server. The full paths to the files are presented in the note. The ROOT interface provides more possibilities as the Web interface (see below). Figure 3 shows the GUI after running the macro. The window comprises 2 parts: input parameters on the left side, and FLUKA results on the right side.

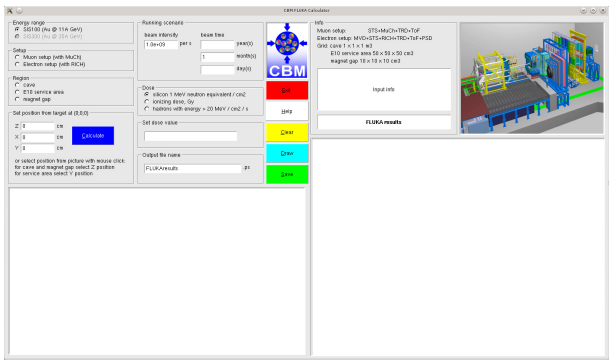

Figure 2: GUI after run ROOT macro.

Set input data.

The user has to set the following input information:

1. Selection of CBM setup (muon or electron/hadron setup);

2. Selection of the region of interest (cave, E10 service area or magnet gap);

3. Set running scenario (beam intensity and beam time in days, months and years);

4. Selection of the quantity of interest (ionizing dose, non-ionizing energy loss, and hadrons with energy $>$ 20 MeV);

Draw geometry of selected area.

After selection of the area in the "Region" group, the corresponding geometry will be shown automatically.

Calculation of the parameters in fixed position.

The user has to put the X, Y, Z coordinate of the equipment relative to the target position into "Set position from the target at (0,0,0)" group and press "Calculate" button. The results will be presented in the "FLUKA results" window with errors.

Draw 2D histogram for selected position and get values from the histogram.

The user can select with a mouse click the position of the equipment from the geometry picture: Z position in case of cave and magnet gap, and Y position for E10 service area. The corresponding coordinate will be updated in the "Set position..." group. After pressing the "Draw" button, the 2D histogram for the selected region will be presented in the window. With a mouse click the user can select a bin of interests, and the value from this bin will be shown in the "FLUKA results" window with errors. An example is shown in figure 3.

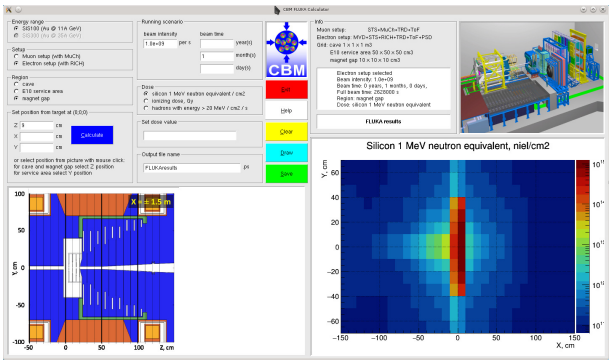

Figure 3: GUI with geometry of selected area and 2D histogram for selected Z position.

Draw 2D histogram above safety limit.

The user can set the safety limit for equipment in "Set dose value" window. After pressing the "Draw" button the 2D histogram with values above limit will be presented in window (see figure 4).

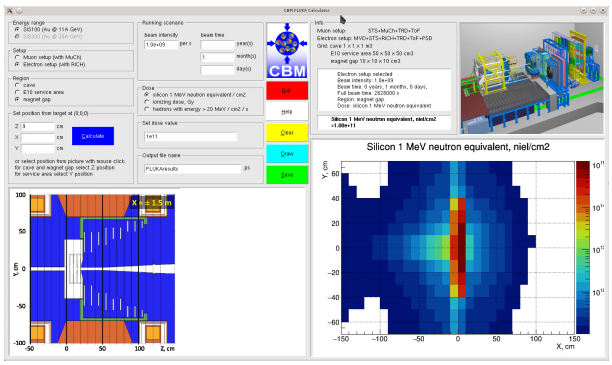

Figure 4: The same window, as in Figure 3, but with setting of safety level for NIEL.

Save the results.

The user can save the results in the *.ps file. The name of the output file could be put into "Output file name". After pressing the "Save" button, the ps-file will be saved.

Buttons.

"Calculate" to calculate the parameter in the selected point. "Clear" to clean all windows and settings. "Draw" to draw 2D histogram of selected area. "Exit" to close ROOT session. "Help" to see information about GUI handling. "Save" to save the information into ps-file.

Radiation level below the CBM service platform

A. Senger and the CBM collaboration
GSI, Darmstadt, Germany

Introduction

This report based on CBM internal Technical Note 18002. This note presents results of FLUKA calculations of the radiation level, i.e. the non-ionizing dose, the ionizing dose, and the hadron flux below the CBM service platform, where racks with experiment electronic and power supplies will be located. The calculations have been performed for an Au beam with kinetic energy of 11A GeV, and an intensity of 10^9 ions/s, impinging on an Au target with a thickness of 250 μm corresponding to 1% interaction length. The doses are integrated over 1 month.

Cave geometry and materials

The 3D CAD view (figure 1) shows the area below the CBM service platform and the neighbouring parts of the CBM setup, especially magnet foundation, CBM dipole and CBM RICH and MUCH detectors. Figure 2 shows the anticipated locations of service electronics racks, the two main rack rows are also indicated in the CAD view (in dark violet). Based in the CAD model a FLUKA geometry was created, only containing the geometry and the materials relevant for radiation calculations. Figure 3 shows the Z-X and the Z-Y views.

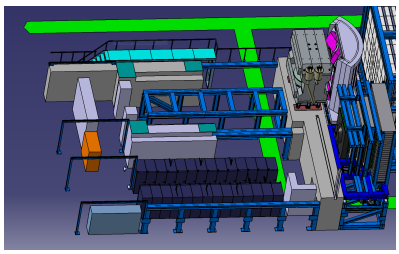

Figure 1: 3D CAD view of the space below CBM service platform.

Radiation field maps

The radiation field maps presented in the note have been calculated in the horizontal X-Z plane, corresponding to the upper panel of figure 3, for 5 different Y-values, i.e. for 5 vertical steps of 0.5 m each, starting from the floor of the cave, up to the concrete roof of the platform (see upper panel figure 3). The figures 4-6 presents one example for maps of ionizing and non-ionizing doses and hadron flux.

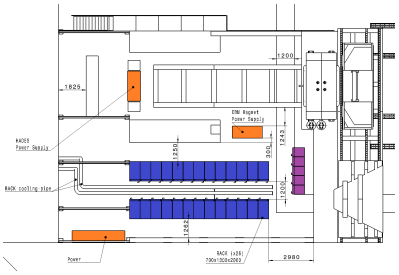

Figure 2: Very preliminary planning of rack positions in the service area.

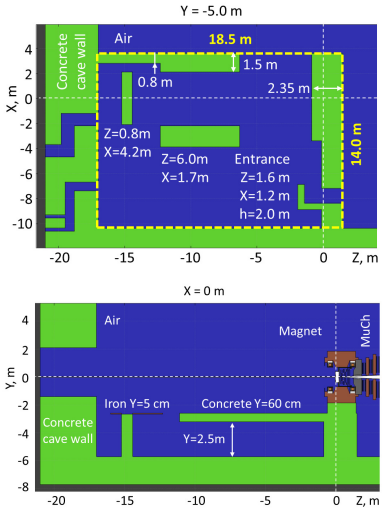

Figure 3: Upper panel: Room below the service platform in the X-Z plane at Y = - 5m, which is 0.7 m above the floor of the cave. Lower panel: Cross section in the Y-Z plane vertical to the beam.

Summary

In order to estimate the radiation level in the room below the CBM service platform, FLUKA calculations have been performed for an Au beam with kinetic energy of 11A GeV, an intensity of 10^9 ions/s, and an Au target with a thickness corresponding to 1% interaction length. The doses are integrated over 1 month. The following maximum values have been found, mostly in the vicinity of the openings in the concrete walls: Non-ionizing dose: about 10^9 1MeV n_{eq}/cm^2 Ionizing dose: 1 Gy Hadron flux: 100 hadrons/cm^2/s.

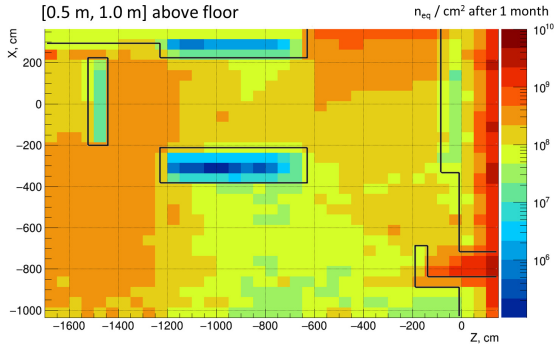

Figure 4: Non-ionizing dose after one month of beam integrated over Y from 0.5 to 1.0 m.

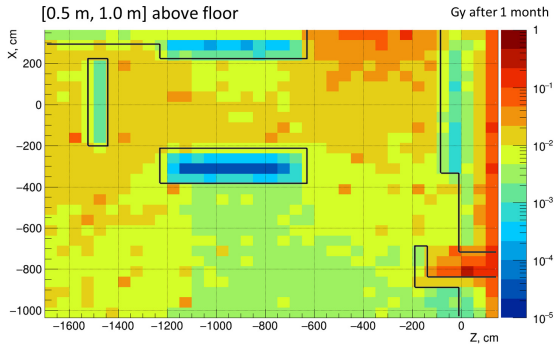

Figure 5: Ionizing dose after one month of beam integrated over Y from 0.5 to 1.0 m.

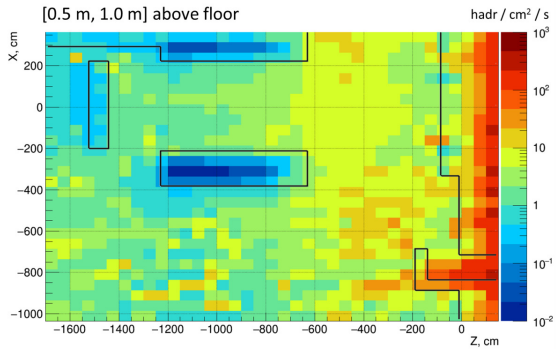

Figure 6: Hadron flux per cm2 and sec integrated over Y from 0.5 to 1.0 m.

Radiation from target of the CBM experiment

A. Senger and the CBM collaboration
GSI, Darmstadt, Germany

Introduction

This report is based on the CBM Internal Technical Note 19001. This note describes the results of simulations performed with the FLUKA transport code concerning secondary radiation sources in the CBM experiment. In this report, the radiation from the activated target after beam shut down is discussed. The dose rate close to the activated target might require a dedicated concept of target handling/shielding after beam shut down.

Dose rate from target activation

Figure 1 depicts the dose rate close to the target for different times after shutdown of an Au beam which bombarded the Au target with a kinetic energy of 12A GeV and an intensity of 10^9 ions/s over one month. Even one day after shut down, the dose rate in the magnet gap exceeds a value of 5 μSv/h, in particular in front and inside the target box. In figure 2 the dose rates are shown in a smaller scale, indicating that dose rate values of the order of 1000 μSv are reached in the close vicinity of the target still one day after beam shutdown. In order to reduce the radiation level when working at the target or close to the target box shortly after beam shutdown, a target shielding device is recommended. After removal of the target, the dose rate is drastically reduced as can be seen in figure 3.

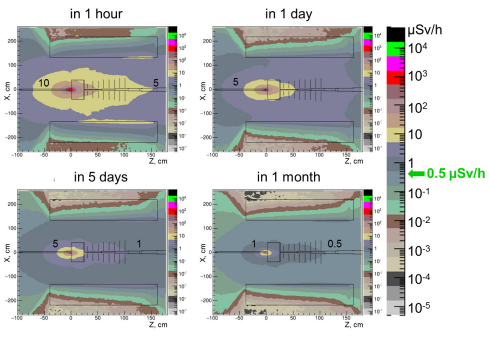

Figure 1: Dose rate distributions in the horizontal plane in the gap of the dipole magnet at different time steps after shutdown of the beam. The Au target was irradiated by an Au beam with an energy of 12A GeV and an intensity of 10^9 ions/s over one month.

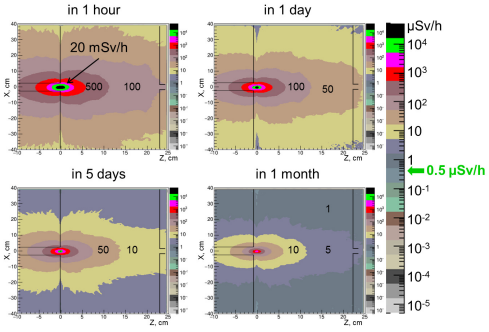

Figure 2: Dose rate distributions in the horizontal plane close to the target at different time steps after shutdown of the beam (see text).

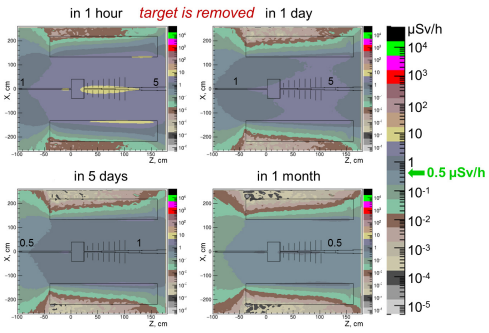

Figure 3: Dose rate distributions in the horizontal plane in the gap of the dipole magnet after removal of the target at different time steps after shutdown of the beam (see text).

Conclusions

In order to study possible problems of target handling due to activation after beam shut down, FLUKA calculations have been performed for an Au beam bombarding a 1% interaction Au target with a kinetic energy of 12A GeV, and an intensity of 10^9 ions/s over one month. It turns out, that one day after beam shut down the dose rate in the close vicinity of the target, i.e. at a distance of below 5 cm, reaches values of up to 1000 μSv/h. In the magnet gap outside the target box, where the Silicon Detector System is located, the dose rate is about 5 Sv/h, both with target and with target removed. A target shielding device is recommended when working very close to the activated target shortly after beam shut down.

Data Acquisition and Online Systems

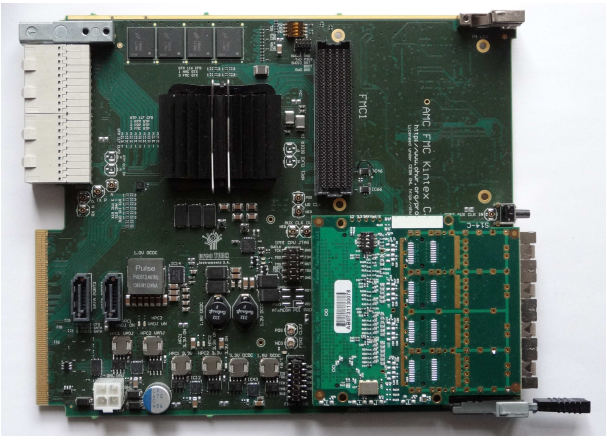

DPB/CRI firmware development

W. Zabolotny, A. Byszuk, M. Guminski, G. Kasprowicz, M. Kruszewski, K. Pozniak, and R. Romaniuk
Warsaw University of Technology, Institute of Electronic Systems, Warszawa, Poland

Support for the GBT-based readout

The GBT-based readout requires support for CROB boards capable to connect multiple FEBs, with different configurations of SMX2 chips. The structure of the DPB firmware was reorganized as shown in Fig. 1. The main

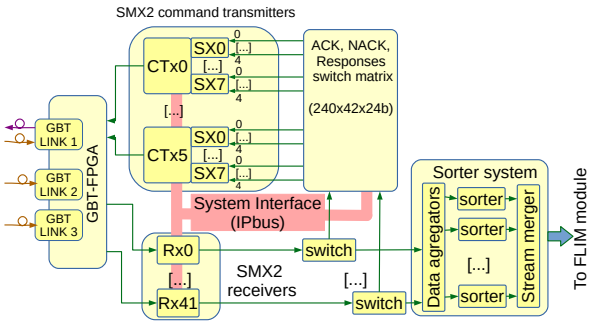

Figure 1: Block diagram of the CROB-oriented DPB firmware (modified figure from [1]).

object is the CROB controller, controlling multiple downlinks via SMX2 command transmitters. Each transmitter may control up to 8 SMX2 ASICs. The responses from those ASICS are received independently and routed to the right command transmitter via a switchable response routing matrix. Precompiled routing settings for different STS and MUCH configurations were prepared.

A necessity to support the parametrized number of CROB controllers, with the parametrized number of downlinks and number of SMX2 chips required improvement of the register address allocation system. An automatic address table generator [2] was adopted for that purpose.

Further improvements in the E-Link based DPB firmware

The diagnostic features in the DPB firmware have been extended with detection of errors in the E-Links and possibility to read raw data via a dedicated FIFO. The data sorting algorithm improved reconstruction of timestamps in high occupancy conditions when the SMX2 data are heavily delayed.

A few special diagnostic versions of the E-Link based DPB firmware have been prepared. The first one with software-switchable E-Link clock (160/80/40 MHz) to aid debugging of problems related to SMX2 communication, other ones for testing the quality of multi-gigabit FMC links and the FLIM link.

Additionally, a special version of E-Link based firmware, imitating the CROB-functionality has been prepared for cooperation with JINR in Dubna.

Preparations for CRI

It was necessary to select the hardware platform for the final CRI board. Two main candidates were the commercially available HTG-Z920 board [3], and the FLX-712 board [4] developed for ATLAS experiment at CERN. The finally chosen FLX-712 didn't require significant hardware modifications for use as CRI, and its suitability for similar applications has been verified by CERN teams. Applicability of that board as the CRI was also successfully tested by the compilation of a special "mock-up" version of the firmware, obtained by quick porting of the DPB firmware to the UltraScale FPGAs and multiplication of the CROB-controller blocks [4].

The CRI firmware is even more complicated than the CROB-oriented DPB firmware. That required finding a better method to provide a control interface for a multilevel hierarchical system of independently developed IP blocks. As a solution, the open system for automatic generation od address maps and Wishbone bus infrastructure [5] has been proposed.

References

[1] W.M. Zabolotny et al.,"GBT oriented firmware for Data Processing Boards for CBM", TWEPP 2018, accepted for Proceedings of Science, https://indico.cern.ch/event/697988/papers/3056462/files/8079-WZab_CBM.pdf

[2] W.M. Zabolotny, "adr_gen - automatic address generator", https://github.com/wzab/wzab-hdl-library/tree/master/addr_gen

[3] W.M. Zabolotny et al., "CRI board for CBM experiment: preliminary studies", Proc. SPIE 10808 (2018) 108083X, doi:10.1117/12.2501415

[4] W.M. Zabolotny et al., "FELIX board as a CRI platform - frmware development based on hardware features", presentation on 32nd CBM Collaboration Meeting,

[5] W.M. Zabolotny, M.Guminski,"adr_gen_wb.py - register access for hierarchical Wishbone connected systems", https://github.com/wzab/addr_gen_wb

Preparation of the GBTX emulator

W. Zabolotny[1], A. Byszuk[1], M. Guminski[1], G. Kasprowicz[1], M. Kruszewski[1], K. Pozniak[1], R. Romaniuk[1], and C.J. Schmidt[2]

[1]Warsaw University of Technology, Institute of Electronic Systems, Warszawa, Poland; [2]GSI, Darmstadt, Germany

Proposal of the GBTX emulator

GBTx is a radiation tolerant ASIC used to control front end electronics (FEE) and to concentrate readout data. It uses multiple copper E-Links for FEE connection and 4.8 Gb/s optical link for uplink. Unfortunately, due to radiation-hard technology, GBTx is submitted to export restrictions and can't be used in certain countries involved in the development of the CBM and similar experiments. The GBTxEMU should emulate the GBTx functionality in a commercially available FPGA.

Hardware platform for GBTxEMU development

The development of the GBTxEMU has been started basing on the commercially available TE0712 [1] and TEBA0841 [2]. It allowed verifying the basic concepts, but it was necessary to supplement the boards with the external 100 Mb/s Ethernet PHY and with the breakout cable for connection of the FEB-B board.

The dedicated board for the GBTxEMU is currently being developed at GSI. It is equipped with hardware jitter-cleaner based on Si5344 chip and may support up to two GBT links.

The GBTxEMU firmware

The block diagram of the GBTxEMU firmware is shown in Fig. 1. The reference clock is produced by the GTP receiver connected to the GBT link. The recovered clock is cleaned in a firmware-based jitter-cleaner using the Si5338 chip. The cleaned clock is used to drive the GTP transceiver, the GBT-FPGA block [3] (modified for Artix 7 FPGA) and the E-Links controller.

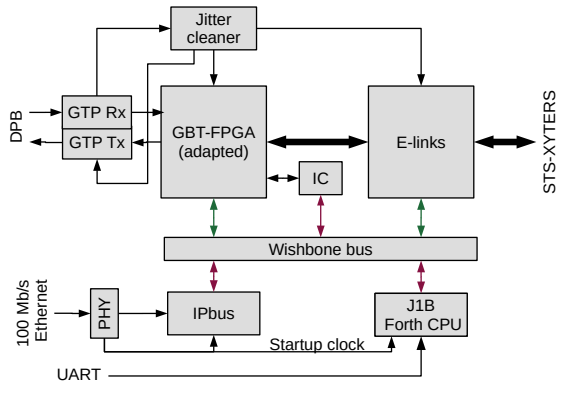

Figure 1: Block diagram of the GBTxEMU firmware.

The internal bus in the GBTxEMU is the Wishbone bus. It may be controlled by three masters. The first of them is the IPbus (modified for operation via 100 Mb/s Ethernet [4]). The second is the modified IC controller connected to the GBT link. The third is the Forth J1B CPU [5], that may be used for interactive testing or debugging, but is also capable to perform a complex initialization routine after power-up.

The current state of development

Currently, the modified GBT-FPGA block, the jitter-cleaner, and the J1B CPU blocks are implemented and tested. Successful communication with the AFCK-implemented DPB via the GBT link has been achieved. The connection of the control and status registers in all blocks to the bus is provided by a system providing the automated generation of address map and bus glue-logic [6]. The E-Links block is partially implemented and is awaiting integration with the GBT-FPGA. The IC controller is currently under development.

References

[1] "FPGA Module with Xilinx Artix-7 XC7A100T-2FGG484C", https://shop.trenz-electronic.de/en/TE0712-02-100-2C-FPGA-Module-with-Xilinx-Artix-7-XC7A100T-2FGG484C-1-GByte-DDR3-4-x-5-cm

[2] "TEBA0841 - Simple base for TE0841 and TE0741", https://shop.trenz-electronic.de/en/TEBA0841-02-TEBA0841-Simple-base-for-TE0841-and-TE0741

[3] J.M. Mendez et al., "Firmware dedicated to the communication with the GBTx ASIC", https://gitlab.cern.ch/gbt-fpga/gbt-fpga

[4] W.M. Zabolotny, "IPbus on FPGA board with 100Mbps Ethernet", https://svnweb.cern.ch/trac/cactus/ticket/2256

[5] W.M. Zabolotny, "AFCK_J1B_FORTH - Forth based system for AFCK board initialization and diagnostics",https://github.com/wzab/AFCK_J1B_FORTH

[6] W.M. Zabolotny, M.Guminski,"adr_gen_wb.py - register access for hierarchical Wishbone connected systems", https://github.com/wzab/addr_gen_wb

Towards the new FLES read-out architecture

D. Hutter, J. de Cuveland, and V. Lindenstruth
FIAS Frankfurt Institute for Advanced Studies, Goethe-Universität Frankfurt am Main, Germany

The First-level Event Selector (FLES) is the central event selection system in the CBM experiment. Its task is to select data for storage based on online analyses including a complete event reconstruction. Latest developments for the FLES focus on performing the shift of the CBM read-out and FLES architecture towards a new two cluster solution. While many elements will be adopted from the current architecture this also requires new developments, especially with respect to the timeslice building network.

One goal for the new architecture is implementing the approximately 600 m long connection between the FLES entry and processing clusters using standard InfiniBand network equipment if possible. This can significantly reduce the cost for data transport compared to specialized long-haul equipment. Nevertheless in its default configuration InfiniBand EDR is only specified for reaches of 100 m. This limit is imposed by the available buffers needed to compensate the link delay and is defined by the bandwidth-delay product. Fortunately current InfiniBand switches allow to, at least partially, collapse buffers reserved for quality-of-service (QoS) features into a larger buffer at the cost of QoS. In theory this should increase the reach of the network sufficiently for CBM demands. To prove the feasibility of this concept a real world network end-to-end test was performed.

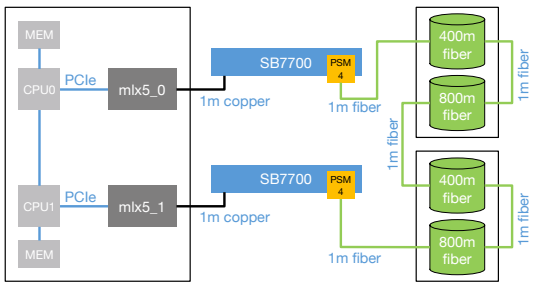

Figure 1: Overview of the long-haul test setup in its maximum configuration using 2.4 km of fiber. For shorter distances fiber elements are removed from the link by changing the patches.

A schematic overview of the setup is depicted in Figure 1. All tests were performed using Mellanox InfiniBand EDR (100 GBit/s) equipment. An Intel Skylake-SP based server with 2 Mellanox ConnectX-5 EDR HCAs served as data source and sink. Both HCAs were connected to one SB7700 switch each using short copper cables. The connection under test was realized via a single mode fiber test setup[1] allowing to test connections with distances of up to 2400 m in increments of 400 m and Mellanox PSM4 transceivers certified for up to 2 km. Measurements for up to 2.4 km were performed and show a very good agreement with theory. The maximum possible reach for one virtual lane, without loss of bandwidth has been calculated to be approximately 1020 m. This is well sufficient for CBM's needs. The available headroom suggests that also future InfiniBand generation may provide sufficient reach for CBM, even if buffer space is not increased proportionally to bandwidth.

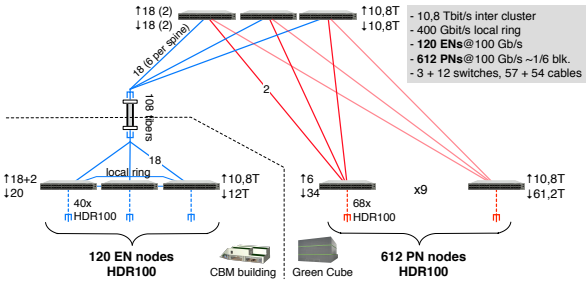

Figure 2: Possible minimal network architecture supporting a total CBM data rate of 10.8 Tbit/s and up to 612 processing nodes.

Another focus of developments has been to identify possible network architectures for the FLES. The split into two sub-clusters rules out the possibility of a simple flat network. Figure 2 shows a possible minimal architecture assuming InfiniBand EDR technology. A fat-tree like network is distributed over both sites and connected via 108 long optical links. This design allows to operate the Green Cube site independently with full network for non-data-taking periods. Additionally the experiment site can be operated separately at reduced performance for testing purposes utilizing a local ring connection. To minimize components the processing part of the network is designed with a blocking ratio of 1/6, providing sufficient bandwidth for CBM. If beneficial for non-CBM applications this can be increased easily. For even better separation of clusters an alternative solution allowing local timeslice building at the experiment site has been developed. With a total of only 8 switches needed at the experiment site this is a very viable option allowing a perfect separation of the networks.

References

[1] D. Hutter et al., "Preparations for the miniCBM FLES Setup", CBM Progress Report 2017 (2018) 185

Throttling study for the CBM DAQ chain

X. Gao[1,3], *D. Emschermann*[1], *J. Lehnert*[1], *and W. F.J. Müller*[1,2]
[1]GSI, Darmstadt, Germany; [2]FAIR, Darmstadt, Germany; [3]SIOM, Shanghai, China

Background

CBM will investigate rare probes in heavy ion collisions, and is designed for interaction rates of up to 10 MHz. To achieve these high rates, CBM has no conventional hardware trigger. The data produced by the free streaming front-end electronics (1 TB/s peak data rate) is transported by a high-bandwidth DAQ system to a compute farm, where events are reconstructed. [1]

However, significant beam intensity variations on short time scales are often seen in beams from synchrotrons. When such fluctuations occur, they can lead to a sudden increase of occupancy in the detector. Unfortunately, overload situation is incredible because of the slow extraction from detector front-end to DAQ chain. For detector systems closest to the target such as the STS, where the readout bandwidth of 320 Mbit/s may not cope with the incoming data load, incomplete event information could be transmitted. [2] Therefore, the throttling mechanism is one promising solution to achieve a high quality data stream in CBM.

Model

The data flow in DAQ system is modeled as shown in Figure 1. The model is based on STS subsystem, involving the front-end delivering data and status information via the CRI to the TFC system, where busy status is evaluated and throttling decisions are taken and distributed.

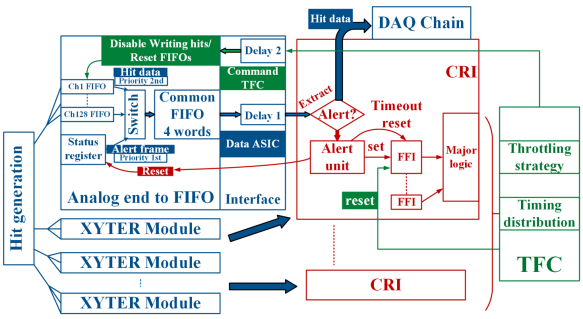

Figure 1: Data flow model of throttling system.

As the simulation core, the data flow model of throttling system can invoke hit generation and result analysis like Figure 2. The closed-loop simulation structure has been built.

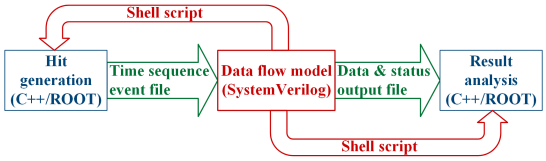

Figure 2: Simulation structure.

Model verification

The model is verified though the regular event generation. The model output can equal to input when the hit rate is up to maximum bandwidth. With the Poisson process, the model begins to lose data when the hit rate is more than about 98% of maximum bandwidth. The impact factors are throttling alert thresholds, channel disable time when throttling is on. The preliminary analysis is given as Figure 3. The first element in each plot represents no throttling mechanism. With the throttling system, controlled loss increases obviously, while total loss remains a relative stable level among the middle area. After this area, the total and controlled loss increase accordingly with longer channel disable time, while uncontrolled loss nearly stays constant. Comparing two plots in Figure 3, lower alert thresholds lead to less uncontrolled loss than higher thresholds. These conclusions approve our expectation.

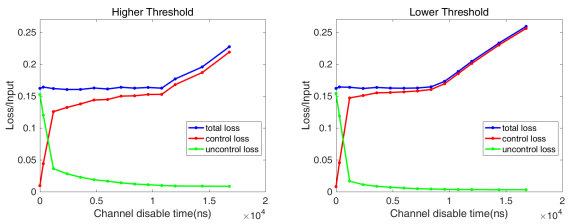

Figure 3: Loss analysis with different channel disabling time.

References

[1] D. Emschermann and C. Sturm for the CBM collaboration, "Preparation of a free-streaming DAQ system for mCBM@SIS18", GSI-FAIR Scientific Report 2017, doi:10.15120/GSI-2017-01856

[2] K. Kasinski, R. Szczygiel and W. Zabolotny, "Back-end and interface implementation of the STS-XYTER2 prototype ASIC for the CBM experiment", doi: 10.1088/1748-0221/11/11/C11018

Status and plans for the mRICH read-out chain

T. Geßler, A. Weber, E. Ovcharenko, and C. Höhne
II. Physikalisches Institut, Justus-Liebig-Universität Gießen, Gießen, Germany

The mRICH Read-Out System

The mRICH detector will be integrated into the mCBM test-setup for the first time during the March 2019 mCBM campaign. The mRICH has a detector plane consisting of 36 Hamamatsu H12700 64-channel MAPMTs, arranged as 2×3 groups of 2×3 tubes. The PMTs and the read-out electronics are identical to those used in the upgraded HADES RICH detector [1]: Each array of 2×3 PMTs attaches directly to the back plane of a front-end module. The other side of these back planes is equipped with twelve *DiRich* FPGA cards (two per PMT). Each DiRich comes with electronics for the pre-amplification and digitization of 32 PMT channels. The DiRich FPGA performs signal discrimination and time-to-digital conversion.

In addition, every front-end module has: a *power board* that distributes the necessary high- and low-voltage supplies to the DiRichs and PMTs; and a *data-concentrator board* that collects the data from all DiRichs and provides the connection to the down-stream DAQ electronics. All necessary inter-board connections on the front-end module are made on the back plane.

A single *hub board*, implemented on the TRB3sc FPGA platform, connects to all six concentrators in the mRICH read-out system. It receives external triggers and distributes the trigger information and timing to the front-end modules. The hub collects event data from all concentrators, performs sub-event building, and transmits a single UDP packet per trigger, containing all associated data, to the DAQ system.

The communication between the DiRichs, concentrator, and hub, including the distribution of trigger information and the transmission of TDC-hit data, proceeds via the TrbNet protocol at 2 Gbps. The physical medium is either a direct LVDS connection or an optical-fiber link.

Integration into the CBM DAQ-System

CBM employs a free-running, triggerless DAQ scheme, while the existing FPGA firmware for the RICH read-out boards was designed for the trigger-based HADES DAQ system. This makes significant adaptions necessary.

In order to facilitate a rapid integration of the mRICH into the current DPB-based read-out scheme for the March 2019 mCBM campaign, we decided to keep the changes to the existing and proven FPGA firmware for the DiRich, concentrator and TRB3sc to a minimum. More extensive changes will be required once the *common read-out interface* (CRI) replaces the DPB-based read-out scheme in future mCBM campaigns and the full CBM system. The changes to the firmware from HADES include:

- the integration of the *central trigger system* (CTS) for trigger generation and output—previously a separate board—into the hub FPGA, including a TDC for trigger-timing measurements;
- the reception of external MBS triggers (see below) with the hub/CTS;
- the read-out of temperature sensors on the hub; and
- the calibration of TDC channels on the concentrator.

In addition, we configure the DiRich for a different read-out mode compared to HADES: Instead of sending out hit information from a time window around the trigger, the DiRich accumulates the data from *all* hits that occurred after the previous trigger in its buffers and transmits them when a new trigger arrives.

We developed a RICH *Data Processing Board* (DPB) firmware running on the *AFCK* FPGA platform. The RICH DPB provides the interface between the trigger-based hub and the free-running CBM DAQ system. It is the last part of the chain that runs synchronously with the mCBM timing system. The FPGA logic on the hub and each front-end module run on independent clocks. A trigger signal generated by the RICH DPB is the only means of transfer of DiRich hit time stamps into the CBM time domain.

The RICH DPB performs the following functions:

- connect to the IPbus-based mCBM slow-control system and provide status and control registers;
- synchronize to the mCBM timing system, i.e., run with the distributed clock and reset the absolute time upon a slow-control register write and subsequent *pulse-per-second* (PPS) signal;
- connect to the *First-level Event Selector* (FLES) using an FPGA module provided by the FLES group;
- generate so-called MBS triggers (binary sequences with an encoded 24-bit trigger number) for every microslice interval and send them to the hub, compensating for cable delays; and
- receive UDP packets with TDC data for each trigger from the hub, unpack and parse the payload, assign the packet to a microslice index using the MBS trigger-number in the data and pass the microslice with the TDC data to the FLES.

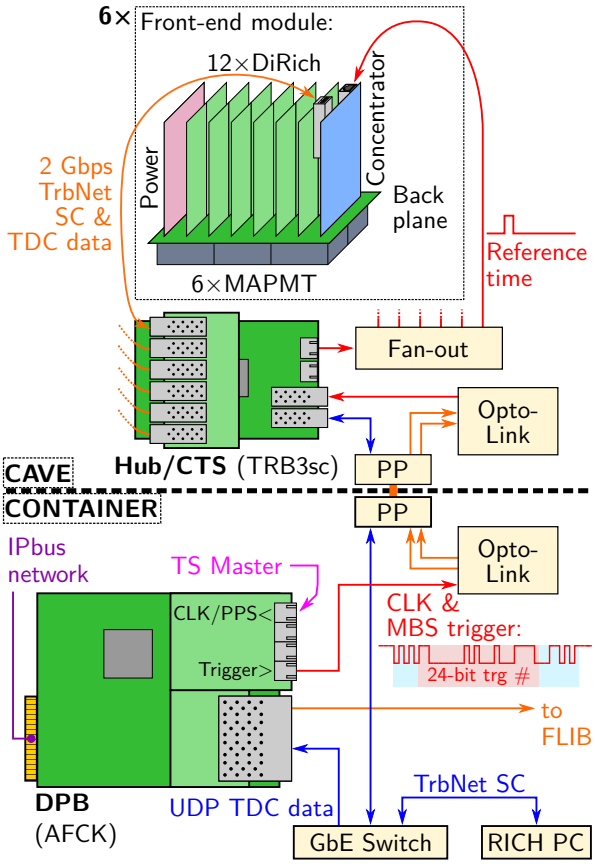

Figure 1: Read-out chain of the mRICH detector in the March 2019 mCBM campaign (power supplies not shown).

Figure 1 shows the setup of the complete mRICH read-out chain in the March 2019 mCBM campaign. The front-end modules and hub will be located in the experimental cave while the DPB will run in a MicroTCA Shelf in the DAQ container. The two sites are connected by several strands of 50 m optical fiber ending in MTP-12 patch panels. While this allows for a straightforward connection of the Ethernet/UDP links via 1000BASE-X, it poses a problem for the transmission of the trigger signal.

We use the *Optolink* FPGA-based RJ45/LVDS-to-SFP coupling board for the trigger transmission over optical fiber. This board is already used in mCBM for the distribution of the clock and PPS signals. We adapted the FPGA firmware such that the Optolink sender and receiver can encode and recover our binary trigger-sequence.

In order to find the exact hit timing of every PMT signal in the mCBM time domain, we must make sure that the first falling edge of the MBS trigger signal, when it arrives at the DiRich FPGA inputs, coincides exactly with the start of a microslice window. This causes the existing trigger logic and sub-event building mechanisms in the front-end modules and hub to create UDP data packets that include all PMT hits from the previous microslice interval. As the DiRich TDCs measure both the trigger-arrival time and the PMT-hit time, and the start time of a microslice window is defined in the mCBM time domain, we can then translate the trigger-to-hit time difference into an absolute hit time during unpacking in software.

In order to achieve such an accurate trigger timing, we must know the precise constant delay between DPB output and DiRich Input. We can then compensate this by transmitting the MBS signal from the DPB ahead of time by the same amount. Here the transfer of MBS-trigger input to reference-time output with the locally clocked 100 MHz logic on the hub is problematic, as it introduces an uncertainty of 10 ns for the trigger delay. This leads to an inevitable misassignment of some hits into the wrong microslice. It can, however, be corrected during hit-time calculation in software, as the timing of the MBS-trigger input and reference-time output on the hub are measured.

It is also possible to account for the clock drift between the mCBM clock and DiRich clock within a microslice window by measuring the interval between two triggers on the DiRich and calculating an according correction factor.

We implemented the first RICH-DPB firmware version and performed a laboratory test of the read-out chain as shown in figure 1, with one partially equipped front-end module and no PMTs. We supplied an external clock and PPS signal and fed pulses from a signal generator into the DiRich TDCs. The pulse timing was correlated to the microslice time-windows. From the recorded microslice data, we were able to extract the expected number of microslices and TDC signals with the correct timing and a resolution of about 1 ns FWHM.

For processing in software, we have created an unpacker that can parse the TDC data in each microslice and extract the PMT hits. Work on converting the hits into CbmRoot digis in ongoing.

We tested the Optolink MBS-trigger transmission with 90 m optical-fiber connections including two LC-LC couplers in lieu of the patch panels. We measured a total trigger delay from DPB to DiRich of 643 ns. The current DPB firmware can provide delay compensation in steps of 25 ns. In the next firmware version, fine delay-compensation values below 1 ns will be possible.

During an integration test at the mCBM site we were able to verify the connections to the FLIB and IPbus network as well as the synchronization of the RICH DPB with the mCBM timing system. A test of the startup-time synchronization with the mTOF and mSTS led to the discovery of firmware issues that we have since corrected.

As a next step, we plan a full setup of the available mRICH hardware for the March 2019 mCBM campaign in Gießen before installing it at GSI. Using this setup, we will perform a read-out test with a pulsed laser for PMT light injection.

References

[1] J. Michel *et al.*, "Electronics for the RICH detectors of the HADES and CBM experiments," JINST **12** (2017) C01072.

The Fault Tolerant Local Monitoring Control Board

J.A. Lucio Martínez and U. Kebschull
Infrastructure and Computer Systems for Data Processing (IRI), Frankfurt University, Frankfurt/Main, Germany

Redundant execution Micro- Controllers (MCU) are nowadays available as COTS (Commercial Off The Shelf) products, such as the CortexR5F TMS570LC4357. Among other features listed below, the device supports ECC mechanism for (multiple -bit) error detection and (1 -bit) error correction in all memories inside the MCU. Based on such MCU, a new Fault Tolerant Local Monitoring Control (FTLMC) Board was designed and built, given that electronic equipment is prone to Single Event Upsets (SEU) in ionizing radiation environments. The board was already tested providing a binary server to control up to 69 GPIO's and interface with digital signaling protocols/buses, such as SPI, 1Wire, RS232, RS485 and CanBus. The binary server was also tested as a bootloading interface for gcc compiled executable files over ethernet to a SDRAM memory present in the board.

Background

First steps for this development included porting the necessary software for physics experiments applications (EPICS) to an evaluation board provided by the manufacturer. The evaluation board had an earlier TMS570 MCU version (LS3130 -CortexR4F), which was configured with the open source RTEMS Operative System, providing APIs that support real time functionality that can be used for EPICS. Adjustments had to be made with self written patches, since officially EPICS is supported in RTEMS versions up to 4.10 and TMS570LS3130 RTEMS Board Support Package (BSP) is supported only from from 4.11 version. The safety and fault tolerance features of this MCU were afterwards tested while running the ported RTEMS 4.11/EPICS as reported in [1].

MCU capabilities

The manufacturer Texas Instruments provides in [3] the following features:

- Dual-Core Lockstep CPUs With ECC-Protected Caches,
- ECC on Flash and RAM,
- Built-In Self-Test (BIST),
- Error Signaling Module (ESM),
- Voltage and Clock Monitoring.

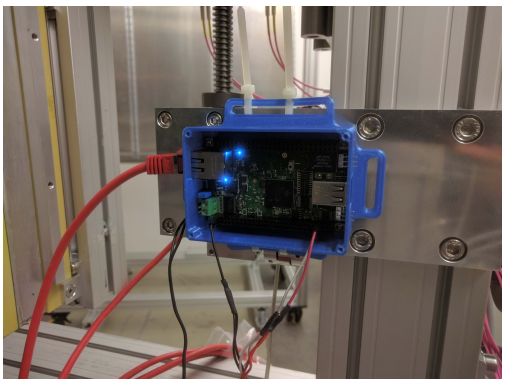

Figure 1: FTLMC second protype @mCBM.

- Embedded Trace Module (ETM) Module for full program reconstruction and real-time instruction trace. *Resources include address comparators and data value comparators, counters and sequencers.* [2]

Further steps

The MCU version mounted in the FTLMC (LC4357) differs from the RTEMS BSP supported and present in evaluation board (LS3130). Nevertheless it is convenient to use the LC4357 because it can be clocked at higher rates (300MHz vs 180MHz), has additional cache memory and significantly more GPIOs and digital interfaces. This also means additional work: The RTEMS BSP needed changes for the LC4357, mainly for the originally LS3130 written ethernet driver which changes endianess in some EMAC pre-specified Finite State Machine memory. Open source flash application OpenOCD used for Debugging needed also changes since currently only CortexR4F devices are supported. It is expected from the EPICS users community that EPICS developers release an RTEMS 5 compatible version, in which case the FTLMC would be fully supported.

References

[1] J. A. Lucio M., and Udo Kebschull, "*Adaption of Low Cost Safety COTS MCU For Low Level Radiation Applications in Accelerator Facilities*", TWEPP Poster (2016)

[2] ARM®, ARM®CoreSight™ ETM-R5 Technical Reference Manual, revision r0p0

[3] Texas Instruments, *TMS570LC4357 Hercules™ Microcontroller Based on the ARM® Cortex®-R Core*, (2016)

Computing

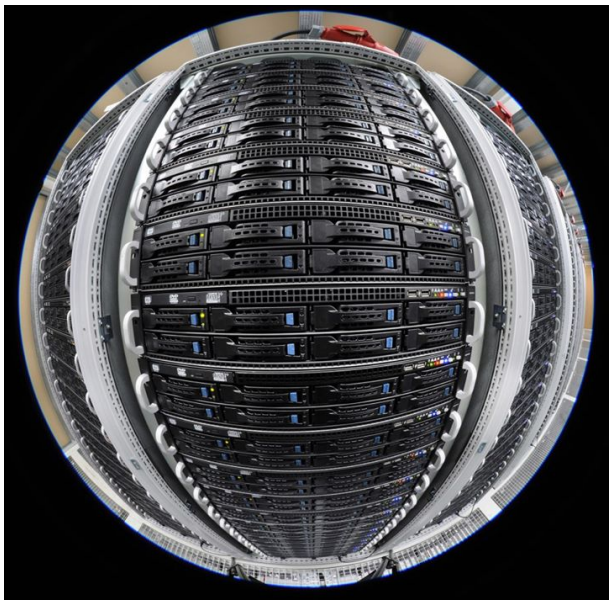

An Experiment Control System (ECS) prototype for CBM

D. Bruins, J. de Cuveland, D. Hutter, and V. Lindenstruth
FIAS Frankfurt Institute for Advanced Studies, Goethe-Universität Frankfurt am Main, Germany

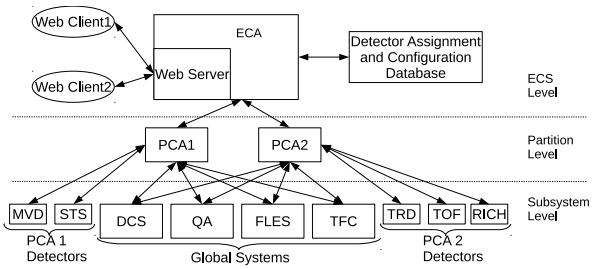

Figure 1: The ECS prototype architecture features a three-level hierarchy with support for independent partitions

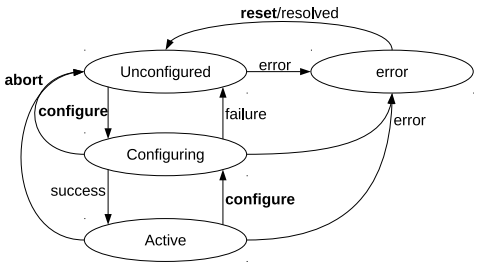

Figure 2: Example of a detector subsystem state-machine

As the integration of the different CBM subsystems progresses, the need for a common high-level control system becomes more apparent. This component, commonly named *experiment control system* (ECS) has interfaces to all subsystems. In case of CBM, this includes the detector subsystems, the central timing system (TFC), the data acquisition and online systems (DAQ/FLES), and different monitoring subsystems (DCS/QA). The design and implementation of an ECS for CBM is part of the experiment and detector control systems (EDC) computing project (cf. [1]). In order to gain a better understanding of the requirements and interfaces of such a control system, an early prototype was developed. See Fig. 1 for an overview of the system.

The basic concept foresees that each subsystem independently represents its state using a high-level state machine (see Fig. 2). These subsystem state machines communicate with a dedicated component of the ECS that maps the individual subsystem states to a set of states relevant for ECS operation. These per-subsystem components are in turn connected to a partition control agent (PCA). Each PCA controls a specific configurable set of subsystems. It provides a common state machine and ensures that the same operating parameters are used by all assigned subsystems. All partition control agents can be controlled by a central experiment controll agent (ECA) component. This ECS component includes a web-based multi-client user interface and manages the central high-level detector assignment and configuration database.

The partition control agent layer allows simultaneous parallel operation of several partitions. This partitioning will be very much needed, especially during commissioning phases of the experiment. However, it requires a certain additional complexity in the global systems. While each detector subsystem can only belong to one partition, the global subsystems like DAQ/FLES need to be part of every partition and thus support partitioning internally.

The ECS prototype is written in the Python programming language. Its web server component uses the Django framework. Each agent runs as an independent task. States and commands are communicated between the tasks by a custom-designed data point publishing protocol based on ZeroMQ. Using a high-level just-in-time compiled programming language like Python, the state machines and their transition graphs can be directly described in the programming language without the overhead of a domain-specific language.

To evaluate the performance of this ECS system prototype, a test has been performed with mockup prototypes of the individual subsystem state machines. The overhead in time introduced by the ECS system has proven negligible even for a full series of transitions from the initial startup state to full data taking conditions. Even in a test run with a number of 100 hypothetical subsystems, the overhead is in the subsecond range.

The presented ECS prototype includes all levels of state machines and contains the full functionality required to manage configuration and start of a data-taking run. For one of the subsystems, FLES, an interface was developed that allows the ECS prototype to interact with the current FLES run control software. In a test setup with FLES components and mockup detector state machines, it was shown that a data taking run can be started and stopped at the push of a button on the provided web-based user interface, successfully demonstrating the fundamental functionality of the ECS prototype.

References

[1] J. de Cuveland, V. Friese, P.-A. Loizeau, F. Uhlig, M. Zyzak, and the CBM Computing working group, “CBM Computing – Summary”, CBM Progress Report 2017 (2018) 126

Improving the throughput of a scalable FLESnet using the Data-Flow Scheduler

F. Salem, F. Schintke, T. Schütt, and A. Reinefeld
Zuse Institute Berlin

Abstract

Minimizing the latency is essential for FLESnet to achieve good aggregated bandwidth and we already improved the throughput and lowered the latency with our Data-Flow Scheduler. However, there is still a gap between the achieved and the maximally achievable bandwidth. For timeslice building, we found that FLESnet performs two RDMA writes for each contribution. This congests the network unnecessarily and increases the latency, especially in large deployments. We therefore optimized FLESnet to need only one RDMA request per contribution. We show how the aggregated bandwidth is increased when the scheduler is used. We also discuss the performance of the scheduler on an Infiniband cluster.

Introduction

The First-Level Event Selector (FLES) high performance computing cluster builds timeslices for analysis using the *FLESnet*[1] software, which is ported to Libfabric [1]. FLESnet consists of two kinds of processes, 'input nodes' and 'compute nodes'. Input nodes receive data from the sensor links and chop the stream into time intervals, called micro-timeslices. Compute nodes receive all micro-timeslices of a given time interval from the input nodes. They build a complete timeslice before analyzing them further. We implemented previously the Data-Flow Scheduler (DFS) [2] for FLESnet that synchronizes the input nodes to send their contributions within a particular time interval so that compute nodes would receive complete timeslices in a shorter time period.

Each compute node maintains one memory-buffer for each input node. Input nodes use remote direct memory access (RDMA) to write their contribution directly to the compute nodes' buffer and inform them accordingly using message passing. For each contribution, input nodes send at least two RDMA writes: (1) contribution content, and (2) timeslice descriptor. The contribution content contains the actual data coming from the sensors, which is the micro-timeslice with variable size. The timeslice descriptor contains the meta-data of the contribution such as the size and the offset.

```
struct TimesliceDescriptor {
  int index; // Global timeslice index
  int offset; // the start offset
  int num_core_microslices;
  int num_components;
}
```

[1] https://github.com/cbm-fles/flesnet

Once an input node receives the acknowledgement that the RDMA writes of a contribution left the local network card, it informs the target compute node via another message—the sync message—about this micro-timeslice. Sending multiple messages for each contribution would congest the network unnecessarily, increase the latency, and consequently increase the duration to complete timeslices. The input nodes could minimize the number of injected messages by sending the timeslice descriptor in the sync message. As a result, the network would be less congested with messages and be able to reduce the processing latency.

In this paper, we show the effect of minimizing the injected messages on the aggregated achieved bandwidth. We present our benchmark results on a CRAY supercomputer and we discuss the benchmark results of DFS on an Infiniband cluster.

Benchmarking

We tested FLESnet with Libfabric on two different supercomputers: (1) Cray XC30/XC40[2] with up to 80 nodes, and (2) an Infiniband cluster (FLES FAIR) with up to 32 nodes, each has up to 128 GB of main memory, IB QDR network card, and AMD Opteron(TM) Processor 6238. Each micro-timeslice is 1 MB and each input node has access to 1 GB of the main memory of the node that is running a compute process. Each node runs one process, either input or compute process.

RMDA Writes Enhancements

The timeslice descriptor message is 32 bytes. When FLESnet saves this message for each contribution, the aggregated bandwidth increases up to 10 %, as depicted in Fig. 1.

DFS on Infiniband

The FLES FAIR cluster suffered from unstable clocks at the time of experiment. We implemented a micro-benchmark to observe the clock difference across processing nodes. The benchmark checks the clock difference of each node every few seconds and synchronizes the nodes using MPI Barrier[3]. We found that the clock drift was up to 200 ms/min and the absolute difference between the slowest and fastest clock was up to 11 seconds at the time of

[2] https://www.hlrn.de
[3] https://www.mpich.org/static/docs/latest/www3/MPI_Barrier.html

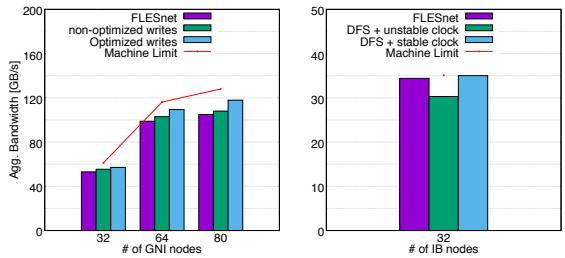

Figure 1: Aggregated bandwidth with/out RDMA writes optimization (left). Aggregated bandwidth with different clock drifts on IB cluster (right).

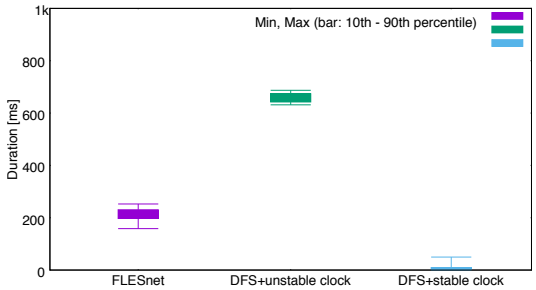

Figure 3: 10th-90th percentile of duration to receive timeslices

experiment. This affects the Data-Flow Scheduler because it will not be able to synchronize the input nodes in order to deliver the contributions almost at the same time. We were also able to check the performance of DFS when the clocks were stable. Figure 1 illustrates how the aggregated bandwidth is affected by clock drifts. It also shows a slight advantage of using DFS over normal FLESnet on 32 nodes. DFS closes the gap between FLESnet and the machine limit while scaling up.

In order to increase the throughput, FLESnet needs to complete timeslices more rapidly to free the buffer space. Figure 2 depicts the duration between the arrival of the first and the last contribution of each timeslice. It shows that DFS requires a stable clock to complete timeslices in a timely manner. Figure 3 depicts the variance of completing a timeslice after excluding the warm-up phase, which is the first few intervals. When the clocks are synchronized, DFS reduces the duration to complete timeslices by up to 90 %.

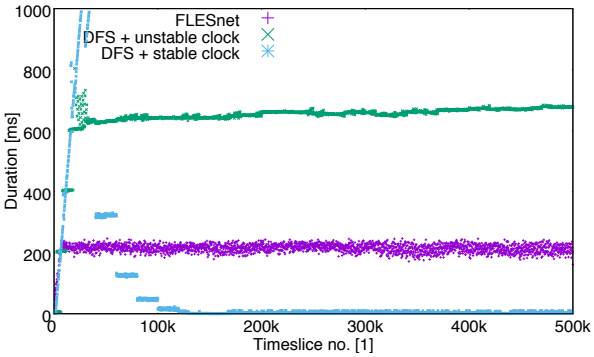

Figure 2: Duration between first and last contribution of timeslice

Challenges

The Data-Flow Scheduler checks the clock difference between nodes at the beginning and then it synchronizes the nodes accordingly to assure completing a timeslice at the same time. On clock drifts during running time, DFS does not perform as expected. Therefore, DFS should implement a clock synchronization mechanism to tolerate the clock drift, or should require better synchronized system clocks. The DFS assumes that the latency is almost equal between different pairs, therefore it attempts to start transmitting each round of contributions at the same time. DFS should deal with each pair of nodes differently to achieve the main goal, which is completing timeslices at compute nodes in timely manner, and to tolerate heterogeneous network latencies due to concurrent jobs. The scheduler also assumes that it runs on homogeneous systems. It should implement a load balancer to distribute the load over processing nodes based on the current network status.

Conclusion

FLESnet required at least two RDMA writes for each contribution, which increases communication overhead. Reducing this to one RDMA write per contribution increases the achieved aggregated bandwidth by 10 %. We also used the Data-Flow Scheduler to enhance the performance of FLESnet. We tested DFS on an Infiniband cluster, which suffered from unusually high clock drifts between different nodes at the time of experiment. The experiments show that DFS increases the throughput and minimizes the latency to complete timeslices when machine clocks are synchronized.

Acknowledgements

The project received funding from the BMBF under grants 05P15ZAFC1 and 05P19ZAFC1. We thank the HLRN and FLES FAIR for providing computing time on the Cray XC30/XC40 and InfiniBand QDR respectively.

References

[1] F. Salem, F. Schintke, T. Schütt, and A. Reinefeld, "Supporting various interconnects in FLESnet using Libfabric", CBM Progress Report 2016, p. 159.

[2] F. Salem, F. Schintke, T. Schütt, and A. Reinefeld, "Data-flow scheduling for a scalable FLESnet", CBM Progress Report 2017, p. 130.

Simple event building for mCBM

M. Prokudin, E. Dorenskaya, I. Korolko, N. Lublev, D. Mal'kevich, R. Sultanov, and Yu. Zaitsev
Institute for Theoretical and Experimental Physics, Moscow, Russia

Simple event builder developed for the CBM should operate at digi level. The event building procedure consists of two steps: finding of events in the data stream and assigning digis to the found event (i.e. event composition). In the 2018 we have adopted algorithms, developed for full SIS100 CBM setup, for the mCBM experiment.

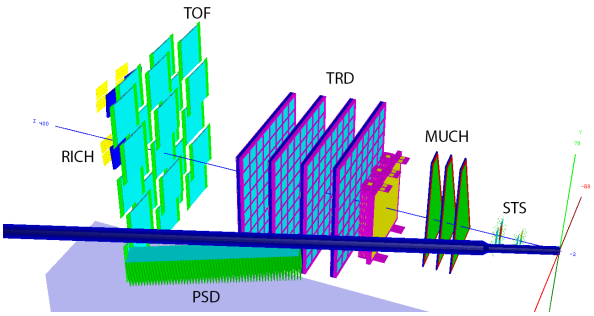

Figure 1: mCBM model used for event building. Beam comes from the right.

`sis18_mcbm_20deg_long` (see Fig. 1) geometry has been used for the studies. There are only two STS stations, which can be used for event finding, and no BFTC detector in comparison with the full CBM setup. The tracking has not been working properly at the moment of our studies so we have reconsidered the event building performance indicators. We have defined event as foundable if it has at least two MCPoints in both STS stations. Event was called good if more than 98% of its digis originates from a single MC event. Event was defined as matched with MC event if more than 50% of its digis originates from a given MC event. Finally event was defined as correctly found if it was found , good and matched with MC event.

The event finding procedure was standard [1]: the event was found if the number of incoming STS digis in the given time period exceeds the threshold. Only STS digis with charge more or equal to 2 have been used in our procedure to cut out noise of STS electronics. Event finding efficiency has been estimated as good for 93% of 1 MHz AuAu collisions at 1.24 AGeV. Optimal event finding parameters have been also determined: the time period — 13 ns and the number of digis to find an event — 3. Event finding efficiency for other collision rates and colliding systems can be found in Table 1.

Extended (-10 ns to the start and +25 ns from the end) time period has been used for event composition in the STS. The time distributions of incoming digis from a single event for STS, MUCH, TRD and TOF are shown in Fig. 2. The distribution for TRD looks odd and should be understood. The width of the distribution cores for STS, MUCH and TOF are similar. Long tails are mostly due to the delta electrons and can be discarded without negative impact to the physical performance. Same extended time period can be used for event composition in all three detectors. Time-of-flight and electronics delays shifts should be corrected. 99.2% of MUCH and 99.3% of TOF digis are correctly attached to the found events after all corrections.

Interaction rate	AuAu 1.24 AGeV	NiNi 1.94 AGeV
0.1 MHz	98%	98%
1.0 MHz	93%	95%
3.0 MHz	83%	88%
10 MHz	54%	68%

Table 1: Event finding efficiency.

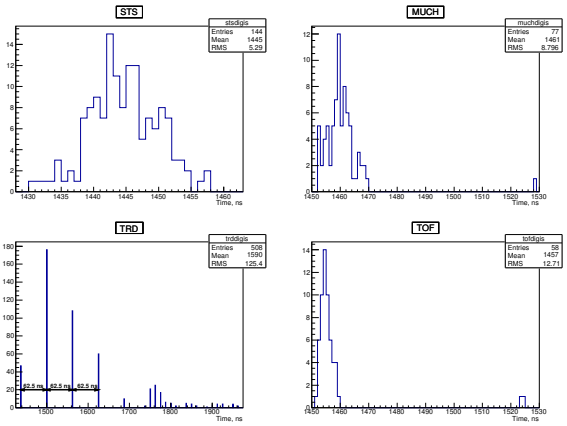

Figure 2: Digi time for a single event. STS digis are shown in top left plot, MUCH — in top right, TDR — in bottom left and TOF in bottom right.

References

[1] I. Korolko, M. Prokudin, "Event building from free streaming data at the CBM", GRID2018, September 2018, Dubna, pp. 155-159, http://ceur-ws.org/Vol-2267/155-159-paper-28.pdf

Global track reconstruction with the CA track finder

V. Akishina
Goethe-Universität, Frankfurt am Main, Germany

In this report the status of global track reconstruction with the Cellular Automaton (CA) track finder package in the CBM experiment is presented. The proposed procedure in the muon setup of the CBM detector, i.e. with MUCH (Muon Chamber) system, is based on the extended CA method, which is the standard reconstruction routine for the main tracking detector of CBM – Silicon Tracking System (STS).

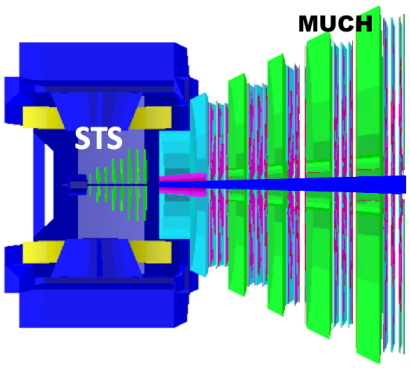

Figure 1: Schematic view of the combined system STS and MUCH SIS100-B configuration. MUCH consists of 12 detector layers and 4 absorbers including the first absorber of 60 cm carbon.

In order to benefit from the existing fast, SIMDized and parallel method developed and optimised for STS, the CA Track Finder has been extended for the global track search through the combined systems of STS and MUCH (Fig. 1). The main idea of the CA algorithm is to create short track segments (triplets) in each three neighboring stations, then link them into track candidates and select the best candidates according to the maximum length and minimum χ^2 criteria.

The existing algorithm functionality was further extended with the functions for a straight line track propagation in the region of absence of magnetic field and accounting for the energy loss and multiple scattering while passing through thick detector material of MUCH. The influence of the material on the track momentum is taken into account by calculating the expected average energy loss due to ionization according to Bethe-Bloch formula. The influence on the estimate error due to multiple scattering is included by adding process noise in the track propagation with Highland-Lynch-Dahl formula. In order to get an estimate of radiation thickness of MUCH detector layers, a special material map has been calculated based on the average energy loss of simulated straight flying particles in each layer of MUCH stations.

Long set efficiency	100
Primary set efficiency	87.5
Track length	82.0
All set efficiency	70.0
Clone rate	1.4
Ghost rate	5.7
Number of reconstructed tracks per event	211

Table 1: Track reconstruction performance for central UrQMD AuAu collisons at 10AGeV beam energy with two embedded muons per event: efficiencies (%) for different sets of tracks, clone and ghost levels (%).

Apart from extrapolation and accounting for the material effects the same procedure is used to construct triplets in the combined system, which has been used before in STS alone. After this the neighboring triplets, which share two hits in common and have the same momentum within estimated errors, are combined into a track.

It is not possible to define the momentum for the triplets in the region of no magnetic field the same manner as it is done for the triplets constructed inside STS, since the track segments in this area are straight. As the first step towards global track reconstruction in the current algorithm implementation Monte Carlo momentum information is used for the triplets in the area without magnetic field. In the future the Monte Carlo information will be replaced with momentum estimate, which can be obtained from the deflection angle of the triplet by the magnetic field assuming that the track segment comes from the target region [1].

The algorithm performance was tested with central AuAu collisons at 10AGeV beam energy from UrQMD. In addition two muons with momenta of 3 GeV/c were embedded in each event. The resulting performance is presented in Tab. 1. The mean track finding efficiency for primary tracks is 87.5% at a ghost rate of 5.7%. The reconstruction efficiency for long tracks, which have hit in every detector layer of STS and MUCH, is 100%. The mean correctly reconstructed track length for all set is 82%. The algorithm performance is to be updated after switching to the realistic estimate of triplet momentum in the area of no magnetic field.

References

[1] R. Mankel and A. Spiridonov, Nucl. Instr. and Meth. A426 (1999) p. 268

Current status of the vector finding-based track reconstruction method at the CBM muon setup

A. Zinchenko and V. Ladygin
VBLHEP JINR, Dubna, Russia

In Refs. [1–3] a track reconstruction method based on a vector finding approach was described, which was inspired by the CA track finder in the STS [4]. Originally developed for the MUCH, it was later extended to the downstream detectors (TRD and TOF) which form together the muon setup.

In a few words, the vector finding method is based on building vectors for each subdetector separately using *apriori* constraints (e.g., expected angular distribution of the particles of interest) and matching them to each other and to STS tracks. In this approach, MUCH stations are also treated independently since they are separated by thick absorbers. Presumably, such a scheme should better handle a heterogeneous tracking environment and offer higher flexibility with respect to algorithm tuning as compared with track following methods (implemented, for instance, in the *littrack* package). Moreover, this algorithm is naturally parallelizable and extendable to the triggering application.

In the "sequential" version, the tracking procedure uses vectors from more downstream detectors (with lower hit number and density) to constrain vector search in more upstream detectors in order to reduce the combinatorics and speed up the processing. In particular, if vectors in the MUCH two most-downstream stations are built, they can be matched through the absorber and propagated to the upstream stations, where the vector building is done within certain roads around extrapolated lines. The TRD vectors can also contribute to this process. Moreover, they will be necessary if the last MUCH stations are built in a "reduced" format (with the number of measurements per track being not enough to constrain a vector).

Currently, the method is implemented for the muon setup with the "baseline" MUCH design (four 3-layer GEM stations). The TOF detector does not produce its own vectors because of its quite complicated geometry but is used for track - hit matching to improve the background suppression.

To illustrate the package performance, 1k UrQMD central gold-gold events at 8A GeV containing additional ω-meson forced to decay into 2 muons from the Pluto generator were produced. The results on muon reconstruction efficiency and background contamination can be estimated from Fig. 1, where the Monte Carlo matching "trackIDs" of the reconstructed tracks are shown for both the vector finder and *littrack* packages. Both methods give very similar results while the running time of the vector finder is shorter by a factor of $\sim$20.

The results for the TRD and TOF matching can be evaluated from Fig. 2, where the reconstructed mass squared m^2 of the found tracks is plotted versus their momentum with $m^2 = (t^2c^2/l^2 - 1)p^2$, t is the time measurement from the TOF, p is the momentum from the STS, l is the distance from the target to the TOF hit and c is the speed of light. One can see, that the quality of track matching of all detectors allows one to apply a selection window in m^2 for signal muons.

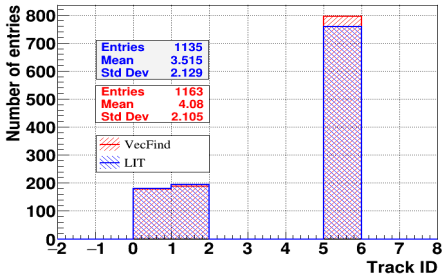

Figure 1: MC track ID of the reconstructed tracks from the vector finder and *littrack* packages: 0 and 1 correspond to the MUCH reconstructed tracks of the muons from ω-decays correctly matched to the muon tracks in the STS, 5 represents all the other tracks.

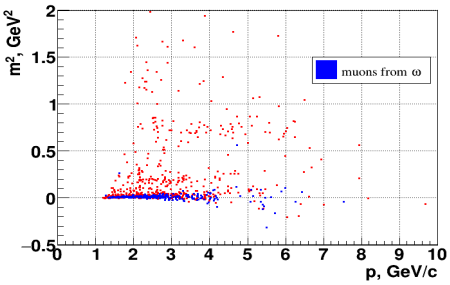

Figure 2: Reconstructed m^2 of found tracks as a function of their momentum. Blue symbols represent muons from ω-decays.

References

[1] A. Zinchenko *et al.*, CBM Progress Report 2015, GSI-2016-01450, p.121

[2] A. Zinchenko and V. Ladygin, CBM Progress Report 2016, GSI-2017-00564, p.169

[3] A. Zinchenko and V. Ladygin, CBM Progress Report 2017, GSI-2018-00485, p.146

[4] I. Kisel, Nucl. Instrum. Meth. A **566** (2006) 85

Selection of event data based on the $J/\psi \to \mu^+\mu^-$ triggering

V. Friese[1], *T.O. Ablyazimov*[2], *O. Yu. Derenovskaya*[2], *V. V. Ivanov*[2,3], *and Yu. V. Russov*[3]
[1]GSI, Darmstadt, Germany; [2]JINR, Dubna, Russia; [3]National Research Nuclear University "MEPhI", Moscow, Russia

The selection of event data from a data stream without event association is task of online data processing in the CBM experiment. Under "event" we understand a set of all detector raw data presumably corresponding to a single ion-ion interaction.

Due to complexity and ambiguity of the criteria for selecting so-called signal "events" in CBM, it was decided not to build a triggering system which is unified for all physical processes. It is proposed to include "triggering" elements into T-DAQ system of each detector, and also to record the response times of the detecting equipment. Streams of experimental information will be managed through a high-speed network that combines a high-performance computing environment. This environment will be used to filter information and identify signal "events".

The process shall be investigated and developed on the example of the simplest software trigger, namely $J/\psi \to \mu^+\mu^-$. This choice is based on the following considerations:

1. The trigger signature for the $J/\psi \to \mu^+\mu^-$ decay is a coincident pair of tracks registered in the trigger detector both pointing backwards to the target (see Fig. 1). In [1, 2] we demonstrated that using the coordinate information recorded by MUCH detector stations, it can be constructed a trigger that allows to quickly select the signal "events" (corresponding to decays $J/\psi \to \mu^+\mu^-$). In this case the background suppression factor is more than 10^3, which exceeds the maximum requirements for the CBM experiment.

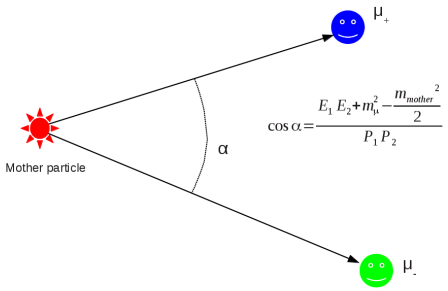

Figure 1: Matching two corresponding decay muon tracks

2. The overall simulation has been shown that the proposed procedure for selecting signal "events" allows to select in real time at least 87% of decays $J/\psi \to \mu^+\mu^-$.

These procedure, however, was based on event-by-event data, i.e. hits already associated to events. In the real case, coincidence has to be properly defined based on the time measurement of the raw data. So in future we plan to develop the existing algorithms further, taking streaming raw data (time-slices) as input instead of events.

Using this particular example, it is possible to develop a procedure of a signal "event" definition that will include:

- Procedure for generating a triggering signal for the selection of the decay $J/\psi \to \mu^+\mu^-$. The software trigger delivers a point in time when the trigger signature was detected.
- Procedure of information retrieval of "event". That is to construct the associated event by selecting for each sub-detector the corresponding raw data from the data stream. This will be done by defining appropriate time intervals with respect to the trigger time.

The next important step is the development of the above defined signal "event" for more complicated case: decays $J/\psi \to e^+e^-$ [3]. This case combines "triggering" signals from all CBM detectors. Based on the information collected from all detectors, it will be possible to formulate a decision on the expediency of including the event in the list of signal "events".

It seems to us that both cases will cover almost all the possible options necessary for the formation of a signal "event" that may arise in the study of other physical processes.

References

[1] T. Ablyazimov, V. Ivanov, PEPAN Letters, Vol.14, N3(208), 504-511 (2017)

[2] T. Ablyazimov, V. Ivanov, PEPAN Letters, Vol.12, N4, 559-565 (2015)

[3] O.Yu. Derenovskaya, T.O. Ablyazimov, V.V. Ivanov, EPJ Web of Conferences 173, 04004 (2018) https://doi.org/10.1051/epjconf/201817304004

Ladder alignment of the CBM-STS detector using cosmic muons

S. Das[1] *and H. R. Schmidt*[1,2]
[1]Eberhard Karls Universität Tübingen, Tübingen, Germany; [2]GSI, Darmstadt, Germany

Abstract

The purpose of the alignment of a detector is to determine the accurate space coordinates and the orientations of all of its components. To achieve such a spatial precision of all the components in a complex hierarchical detector, one track based alignment algorithm is developed. The next generation **unit** based STS geometry (version: **v16g**) is used for the test intent, where 8 stations are placed within 9 units and each unit is divided into two half mechanical units. The geometry is categorized by 5 hierarchies; 3 active hierarchies to be used for the alignment: half mechanical units (highest level), ladders, sensors (lowest level) and 2 inactive hierarchies to be used for the global referencing: global R.S., half side of the detector. The alignment of the ladder hierarchy is addressed in this report with a toy misalignment scenario.

Preparation of the Cosmic Muon Tracks

To be able to align the detector components (alignables) successfully using a track based alignment algorithm, the alignables should have a decent number of reconstructed tracks (at least 4 STS hits to a track) passing through them. For straight tracks, originating from the target, some ladders located at large angles have not enough overlap with other ladders for a meaningful track based alignment strategy (see Fig. 1).

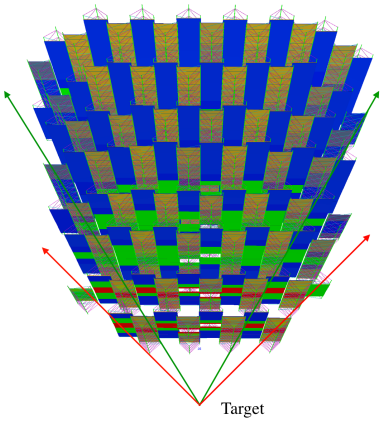

Figure 1: Green tracks are reconstructable (can be used for the alignment), where red tracks aren't.

To align these edge ladders as well, cosmic ray induced tracks having random incident angles are needed. For this purpose a simple cosmic ray generator is developed. One million cosmic straight muon tracks with a fixed momentum of 5Gev/c are simulated without the magnetic field.

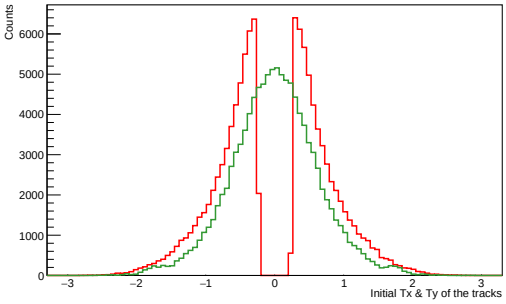

Figure 2: Track slope distribution in X direction (T_x) is in green and in Y direction (T_y) is in red with respect to the beam axis (no unit).

Then approximately, 110k tracks (see Fig. 2) can be used for the alignment with the help of the reconstruction algorithm, employing the ideal track finder.
In future, more realistic zenith angle (θ) distribution will be implemented along with the usage of board momentum range based on the cosmic ray vertical flux for the cosmic muon simulation.

Realignment Results

One toy misalignment scenario is proposed on the ladder hierarchy to test the newly built track based alignment algorithm. The first ladder in the first half unit and the last ladder in the last half unit are kept fixed (for the global referencing) and the other 104 ladders are randomly displaced using the virtual method (i.e. instead of modifying the geometry, just modifying the hit position accordingly, during the track reconstruction step) by taking $\sigma_x = 100\mu$m, $\sigma_y = 100\mu$m for the translations along the X and Y axes. The Z values are kept fixed throughout. Then, this misalignment scenario is treated by the standard alignment algorithm to produce the alignment corrections. The realignment results are discussed below:
From the Fig. 3 and 4, the residual distribution (the indicator of the track fit quality) in the both X and Y directions can clearly be seen resolved to the ideal scenario after the alignment corrections.
Although, the accuracy of the alignment corrections are of the order of 5μm in the X direction (see Fig. 5) and 20μm

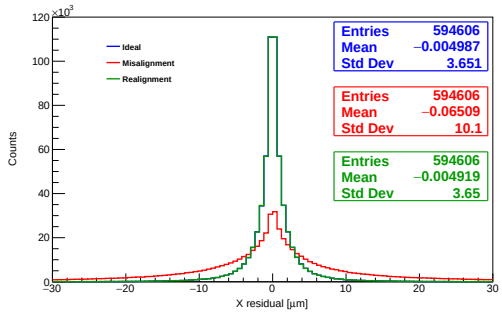

Figure 3: Residual dist. in X direction.

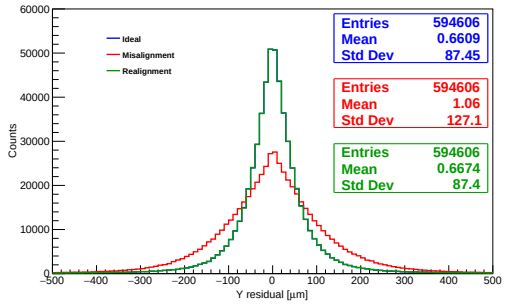

Figure 4: Residual dist. in Y direction.

in the Y direction (see Fig. 6) (which should be fine for the desired track fit quality for the physics analysis), the alignment corrections show some systematic errors, inherent to the fitting procedure (as seen on the Y corrections). This might be due to the lack of some suitable geometrical constraints. And such bias fits become predominant once the rotational degrees of freedom (DOF) are introduced which correlate translational DOF's. So, further investigations are needed to evaluate additional constraints, which should then be added to the alignment algorithm for the proper χ^2 fit, to avoid such biases of the alignment corrections.

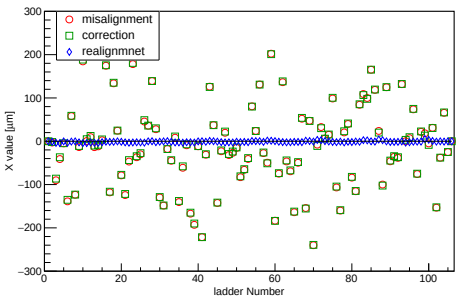

Figure 5: X directional misalignment correction.

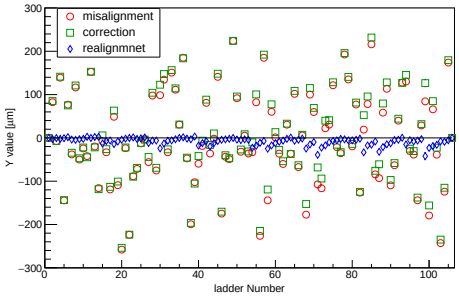

Figure 6: Y directional misalignment correction.

Conclusion

The alignment method for the ladder hierarchy is working within the spatial precision limit for the translational DOF. But at present fit biases of the alignment corrections are not resolved for the rotational DOF (work in progress). Once, this problem is solved by the proper geometrical average constraints, the sensor level alignment will be implemented.

Acknowledgement

I am really grateful to Dr. Claus Kleinwort from DESY, Hamburg for his personal advice and constant support.

References

[1] https://fair-center.eu/fileadmin/fair/publications_exp/TDR-STS.pdf

[2] V. Blobel. Millepede II. Institut für Experimentalpyhsik, Universität Hamburg. 2007. url: http://www.desy.de/ blobel/mptalks.html.

[3] C. Kleinwort, General Broken Lines as advanced track fitting method, NIM A, 673 (2012), 107-110, doi:10.1016/j.nima.2012.01.024

[4] "Introduction of General Broken Lines refit algorithm for CBM-STS", Susovan Das and H. R. Schmidt et al., CBM Progress Report, 2017

[5] "Track Based Alignment Procedure for CBM-STS Using Millepede II", Susovan Das and H. R. Schmidt et al., CBM Progress Report, 2017

KF Particle Finder as a tool for control of the systematic errors

M. Zyzak[1], *I. Kisel*[1,2,3], *P. Kisel*[1,2,4], *and I. Vassiliev*[1]

[1]GSI, Darmstadt, Germany; [2]Goethe-Universität Frankfurt, Frankfurt am Main, Germany; [3]Frankfurt Institute for Advanced Studies, Frankfurt am Main, Germany; [4]JINR, Dubna, Russian Federation

One of the key tasks of the experimental data analysis is estimation and control of systematic errors. The systematic effects should be understood and taken into account for production of precise and reliable measurements.

The KF Particle Finder package provides tools to solve this task. Currently its reconstruction scheme contains about 200 decays and long-lived particles. There are cases when spectra of the same particle specie are extracted from several independent channels, some of them are even reconstructed by completely independent methods. Obviously, the extracted spectra in this case should be the same, as we consider the same particle. Their comparison will allow to search for and correct on systematic effects in such tasks as track identification, matching between different detector subsystems, account of material budget, etc.

Ξ and Ω are reconstructed by the *conventional method* when at first proton and pion are combined into Λ candidate and then another track (pion and kaon respectively) is added; and by the *missing mass method*, when the track of the mother particle is registered directly by the tracking system and can be identified by the kink with the charged daughter particle. For instance, comparison of the extracted m_t spectra for $\Xi^- \to \Lambda\pi^-$ decay is shown in Fig. 1. Using simulated data both methods provide practically identical results, that shows correctness of the procedure. It can be further applied for the analysis of the experimental data.

The same two methods are applicable for reconstruction of hypernuclei. Moreover, for some of them several conventional and several missing mass channels are available.

Such channels as $\pi^\pm \to \mu^\pm\nu_\mu$, $K \to \mu^\pm\nu_\mu$, $K \to \pi^\pm\pi^0$ reconstructed by the missing mass method can be of great interest to control particle identification: these particle species are registered and identified directly by TOF.

CBM has great opportunity to measure low mass vector mesons in two dilepton channels: muon and electron. However, they can be registered in hadron modes as well: $\rho \to \pi^+\pi^-$ and $\phi \to K^+K^-$. These channels are considered not clean, but taking into account high branching ratios they can be extremely useful for systematic studies. Especially in case of low multiplicity events and light colliding systems.

Understanding of $\Lambda(1520)$ as a source of non-prompt K is important for extraction of primary kaon spectra. Its reconstruction is complicated due to the huge background which can not be cleaned up by the decay topology. Thus, having several independent channels will allow to rich a higher confidence level of the measurements. $\Lambda(1520)$ can be reconstructed in pK^- and $\Sigma\pi$ channels.

Open charm studies is another part of the CBM physics program where control over the systematic effects is crucial. Taking into account extremely low multiplicities, even slight variations in efficiency estimation can lead to large systematic errors.

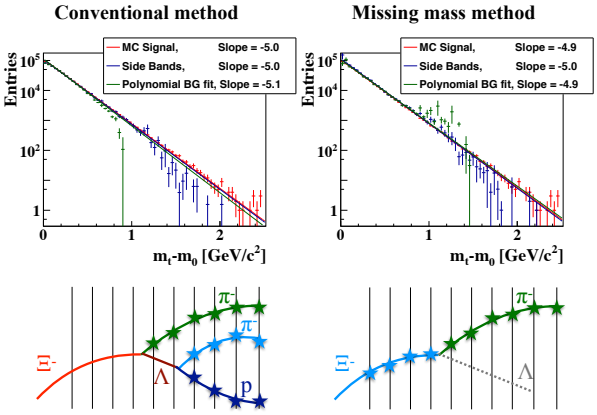

Figure 1: Efficiency corrected spectra of $\Xi \to \Lambda\pi^-$ decay as a function of m_t obtained by the conventional (left) and missing mass (right) methods from 5M central AuAu UrQMD events at 10 AGeV. For extraction of signal spectra two methods were used for each case: the side bands (blue) and polynomial background fit (green) methods, which are shown in comparison with the simulated MC signal (red). Slope is extracted from the exponential fit.

The proposed approach was successfully approbated in the STAR experiment within the FAIR Phase-0 program at example of D^0 decays: $D^0 \to K^-\pi^+$, $D^0 \to K^+K^-$, $D^0 \to K^-\pi^+\pi^+\pi^-$, and corresponding $\overline{D}^0$ decays. Comparison of spectra extracted from the $K\pi$ and KK channels allows to improve the understanding of the PID efficiency, while comparison of 2- and 4-daughter decays allows to control efficiency of the matching between the main tracking detector and the vertex detector. Thus, the method has demonstrated a great potential to control the systematic errors with real experimental data as well.

Due to its properties: similar decay topologies are reconstructed with the same methods and similar cuts, it is vectorised and fast, KF Particle Finder allows simultaneous systematic studies of several different particles in several decay channels each providing extremely powerful tools for physics analysis.

Recent development in the missing mass method

I. Kisel[1,2,3]*, P. Kisel*[1,2,4]*, P. Senger*[1]*, I. Vassiliev*[1]*, and M. Zyzak*[1]

[1]GSI, Darmstadt, Germany; [2]Goethe-Universität Frankfurt, Frankfurt am Main, Germany; [3]FIAS, Frankfurt am Main, Germany; [4]JINR, Dubna, Russian Federation

Strange particles are important probes of the properties of hot and dense nuclear matter produced in high-energy heavy-ion collisions. A large fraction of the produced strange quarks is carried by Σ^- and Σ^+ hyperons, which have decay modes with at least one neutral daughter particle.

The missing mass method is a part of the KF Particle Finder package and is designed to find channels in which the neutral particle is one of the decay products. The method is based on the conservation laws of energy and momentum and uses the mathematics of the Kalman filter.

This year, the method has been considerably reworked. First of all, the changes have affected the basic scheme and mathematics of the algorithm. The following are the main steps used in the current implementation:

- the tracks of mother and charged daughter particles are reconstructed in the tracking system;
- the track candidates are extrapolated to each other for possible intersection, then the decay point is reconstructed and later the track parameters are used in this point;
- the parameters of all particles are now calculated in one step.

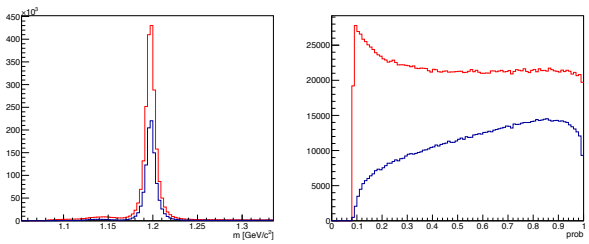

Figure 1: Σ^- mass (left) and χ^2 probability (right) distribution spectra which now has correct flat shape (red) comparing to the previous version (blue).

Such a scheme allows to reconstruct the decay vertex with accurate calculations of the covariance matrices and correct estimation of the particle correlations. This significantly reduces the number of operations, as the parameters of both the mother and all the daughter particles are calculated in a single pass, and the complex calculation of the mass constraint is not required. The advanced mathematics also opens opportunities for acceleration of the work of the algorithm.

The next change affects the extrapolation of the tracks from the nearest stations to the expected decay point. In the new realization the procedure is performed in two steps: first, the track parameters are transported to the area of the estimated secondary vertex, and then more precisely to its location. The procedure takes into account the inhomogeneity of the magnetic field and, therefore, ensures correct χ^2 distribution, which results in increased reconstruction efficiency. The corresponding probability distribution is shown in Fig. 1, right. The new distribution (in red) is almost flat, while the previous implementation of the method demonstrates incorrect prob shape (blue) because it neglects correlations between reconstructed neutron and charged pion daughter.

To recover the efficiency of particle identification, tracks without PID are considered as pions. Since pions are abundant particles, this step increases the efficiency of reconstructing particles with pion as a daughter, but does not affect the significance of the signal. As for the decay with protons and kaons in the decay channel, this compensation leads to a large increase in the background, so it is only applied to pions.

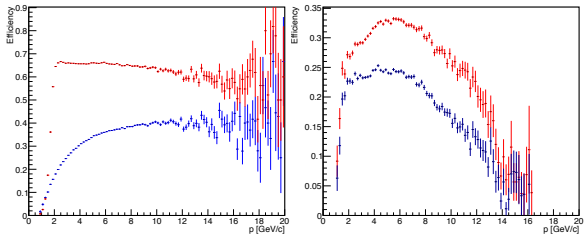

Figure 2: $\Sigma^- \to \pi^- + n$ (left) and $\Sigma^+ \to \pi^0 + p$ (right) efficiency comparison for old (blue) and new (red) versions. The increase of significance is 40% and 10% correspondingly using 5M centr Urqmd Au+Au events at 10 AGeV with TOF PID.

The Fig. 2 shows the increase in the efficiency of the method. For $\Sigma^- \to \pi^- + n$ and $\Sigma^+ \to \pi^0 + p$ decays the efficiency is improved about 2 and 1.5 times respectively. Efficiency for Σ^+ is slightly lower due to the TOF proton identification.

Summarising, the mathematics of the missing mass method is improved, which is proven by correct pulls, χ^2, and prob distributions. The new approach shows simultaneous increase in efficiency, S/B ratio and significance.

Developments in simulation software

V. Friese and the CP-SIM working group
GSI Darmstadt

The ultimate goal for the computing project Simulation Software is to provide a realistic detector response in terms of simulated raw data on the same level as real experiment raw data. This simulated response must be suitable to evaluate the appropriateness and performance of the detector sub-systems, to verify the design of the data acquisition system, to develop the reconstruction algorithms, and finally to assess the physics performance of the CBM detector setup.

The major ingredients to the simulation are the geometric description of the detector and passive systems, which are used in the transport stage using external engines like GEANT3 or GEANT4, and the detailed detector response implementations, modeling the physics processes in the active detector elements and the behaviour of the read-out electronics. It should be noted that the proper response simulation for a free-running readout system like CBM is substantially more involved than conventional, event-by-event simulation, since interference of events in the detector systems has to be taken into account. On top of that, the data acquisition system and its time-slice building have to be properly emulated.

While the respective developments in detector-specific simulation software continued in the year 2018, the need to unify and simplify the application for the non-expert users was expressed by the Physics Working Groups. This wish triggered the development of the user interface class `CbmDigitization` as a software layer between the user and the core framework. The interface shields the user from details of class names and setup parameters by introducing default settings for all detector systems, thus substantially reducing the user code whenever the default behaviour is wanted, as is the case for most physics-level simulations. Interaction of the user with the core framework on the ROOT macro level is not required any longer. The application of a particular digitizer is automatically triggered by the presence of respective input data branches from the transport simulation. At the same time, full flexibility for experts is maintained by appropriate interface methods, allowing to change the default behaviour of the digitizers or even to apply different, experimental digitizer classes. The minimal code to run the detector response simulation is shown in Fig. 1, demonstrating the significantly simplified application in comparison to the previous macro code.

Further improvements in the simulation scheme concern the simultaneous digitization (detector response simulation) for different data sources. The full data stream contains event data as well as not event-correlated background, e.g., from the non-interacting beam (delta electrons in the target) or from thermal noise in the detector

```
// -----   Digitization run   --------------
CbmDigitization run;
run.AddInput(inFile, eventRate);
run.SetOutputFile(outFile, overwrite);
run.SetParameterRootFile(parFile);
run.SetTimeSliceLength(timeSliceLength);
run.Run(nEvents);
// ----------------------------------------
```

Figure 1: Minimal code to run the digitization

read-out electronics. Such sources are usually addressed by separate transport simulations, which have to be simultaneously fed into the digitization procedure with different rates (”mixing“). In addition, the possibility to embed several transport data sources at digitization level is highly desirable, e.g., embedding a rare signal into full background events. This embedding was previously only possible at transport level by transporting signal and background together. As the transport simulation is the most compute-intensive stage, it is economically preferable to transport signal and background separately, such that the high-multiplicity background events can be re-used for a variety of signals. In contrast to mixing data inputs, where the resulting data stream is composed of events randomly chosen from one input or the other according to the respective event rates, embedding means a one-to-one correspondence of two events from different sources, i.e., both event times have to be equal.

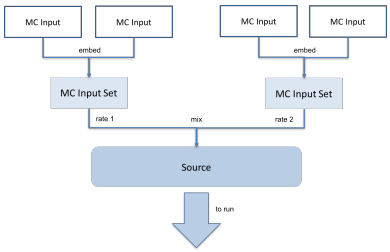

Figure 2: Schematic view of using multiple inputs for digitization

These demands were met by the introduction of the class `CbmDigitizationSource` covering the above described functionality. The working principle is demonstrated in Fig. 2: several MC (transport) inputs can be mutually embedded into one ”input set“. All inputs within an input set will be overlaid by assigning the same event time. Several input sets can be mixed with different event rates. The digitization procedure will for each input set sample the event time according to the specified rate and process the events in a time-ordered manner.

Update of STS geometry

E. Lavrik
FAIR, Darmstadt, Germany

The standard Monte Carlo STS geometry (v16g, Fig. 1) for the CBM ROOT is very detailed and includes all active and passive elements in the detector acceptance relevant for the particle track reconstruction, e.g. silicon sensors, read-out cables and carbon-fiber ladders with the proper material budget.

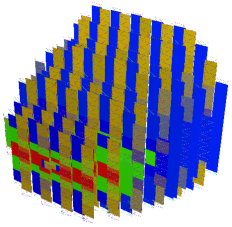

Figure 1: A render of a current standard STS geometry version v16g.

However, the standard geometry has no other major passive elements included such as thermal insulation box, aluminum frames housing the cooling elements, front-end and powering electronics, etc. There is a variety of second-order effects expected from inclusion of the passive materials, both positive (shielding of the delta electrons originating from beam-target interactions) and negative (more background in the downstream RICH detector due to gamma conversion).

Porting geometry from CAD

We use "CATIA-GDML geometry builder" [1], a set of tools for CATIA CAD program, to build the MC geometry of the passive elements. Though, no direct conversion of the model is available due to different volume hierarchy representations, this tool provides the immediate visualization of the model being built. The model can then be exported to the GDML (Geometry Definition Markup Language) file format which can be imported in ROOT.

Fig. 2 shows a render of the feature-rich Unit 4 of the STS detector without sensors. Depicted in color are: aluminum carrying C-Frame in grey, placeholders for the front-end boxes in yellow and placeholders for powering board boxes in red. The complex C-Frame shape was possible to implement by combining numerous primitive placements and binary operations.

By careful implementation of all passive elements from mechanical drawings the point of synchronization between the CAD and MC models of the passive geometry was reached.

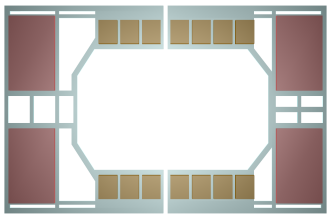

Figure 2: A render of the Unit 4 imported into ROOT.

Update of the scripted geometry

The scripted geometry was updated as well to account for updated carbon fiber ladder structuring element shape. The carbon ladders and read-out cables were extended towards the front-end plane to represent the realistic material budget with the largest impact in most peripheral ladders.

A hybrid approach was established for producing the final ROOT geometry. The ladders with sensors are produced in the well established scripted manner with many steering variables. The passive materials are imported from a GDML file and added to geometry dynamically (Fig 3).

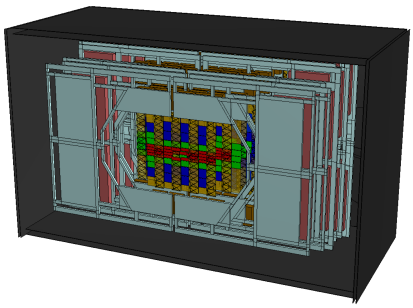

Figure 3: A render of new STS geometry version v19a with passive materials.

References

[1] S Belogurov, et.al, Development and application of CATIA-GDML geometry builder, *J. Phys. Conf. Ser.*, **513**

Realistic Muon Chamber (MuCh) geometry simulation for the CBM experiment at FAIR

O. Singh[1], P. Bhaduri[2], E. Nandy[2], S. Chattopadhyay[2], and N. Ahmad[1]
[1]Aligarh Muslim University, Aligarh, India; [2]Variable Energy Cyclotron Centre, Kolkata, India

Introduction

The Muon Chamber (MuCh) detector system [2] of the Compressed Baryonic Matter (CBM) experiment [1] at FAIR accelerator complex in Darmstadt, Germany is designed to identify muon pairs which are produced in high-energy heavy-ion collisions in the beam energy range from 4 to 40A GeV. The novel strategy of muon detection adopted in CBM is to track the particles through a hadron absorber system, and to perform a momentum-dependent muon identification. This concept is realized by an instrumented hadron absorber, consisting of staggered absorber blocks and tracking stations placed in between two consecutive absorber plates. The hadron absorbers vary in material and thickness, and the tracking stations consist of detector triplets based on different technologies.

The MuCh system will be built in stages which are adapted to the beam energies available. Within the FAIR modularized start version the SIS100 ring will provide beams with energies up to 11A GeV for heavy ions and 29 GeV for protons. Thus a modular MuCh system is presently under development which can be easily upgraded according to the beam energies under investigation. Based on the beam energy and hardness of the muon tracks two configurations are presently investigated at SIS 100 energies. The optimum design of the first version of MuCh will comprise of 12 detector chambers with 3 chambers grouped as a station between two successive absorbers and enable the measurement of Low-Mass Vector Mesons (LMVMs) (ρ, ω, ϕ) in A + A collisions at 4-11A GeV. The detector chambers are filled with 3 mm argon gas as active detection volume.

To carry out physics performance simulations, related to the Di-muon measurements, the detector geometry needs to be as realistic as possible. With this objective, recently 1 cm thick Aluminum plates have been added to each detector chamber of the simulated MuCh geometry, to provide the required cooling of the associated electronics and to act as chamber support. In the present paper, we discuss the effect of this additional material budget due to the Al cooling plates, Drift and Readout PCBs as far as the realistic MuCh geometry is concerned.

Geometry Configurations

The muon detection system at SIS100 optimized for LMVM measurements, has 4 absorbers and 4 stations. Each station consists of 3 detector layers. The first absorber is made up of high density (ρ = 2.26 gm/cm^3) Carbon and divided into two parts. The first part is 16 cm thick and trapezoidal in shape followed by a 44 cm thick parallelepiped. Rest of the absorbers are made up of Iron and parallelepiped in shape. In present simulation two variants of MuCh geometry (tag version- `v17b_lmvm` and `v19a_lmvm`) have been studied. The `v17b_lmvm` geometry contains 1.5 cm rectangular plates made of Carbon plastic as a support structure but no arrangement for cooling. In the modified version (`v19a_lmvm`) carbon plates are replaced by 1 cm thick Aluminum plates for support and cooling purpose and to make the geometry more realistic we also implemented 35 micron Copper and 3 mm G10 on both sides of active volume of the detector for all stations. The internal structure of each module as per the latest geometry concern are shown in Fig. 1.

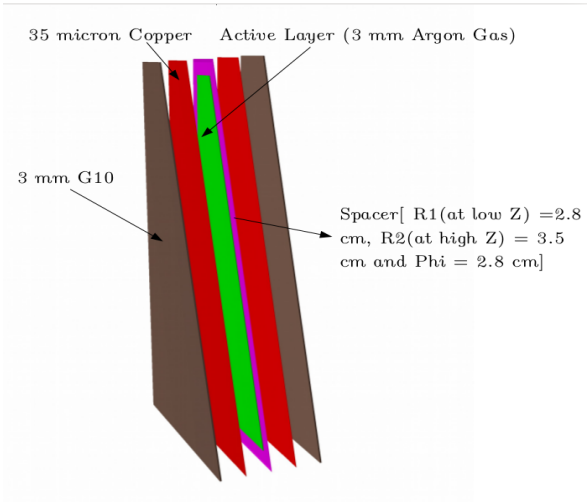

Figure 1: Internal structure of each module in realistic MuCh geometry (`v19a_lmvm`).

Results and Discussion

We simulated central Au+Au collisions at beam energy 8A GeV. As signal, we considered Di-muons from the decay of ω mesons, generated by the PLUTO generator. The signal muon pairs were embedded into background generated with UrQMD event generator and an event-by-event analysis is performed. GEANT3 has been used to transport all the particles through the CBM set up, for both geometry configurations. The point density distributions of primary and secondary particles at each station for both geometry

configurations have been plotted in Fig. 2. As evident from the figures, an absorption and an enhancement have been seen in much points for the primary and secondary particles respectively for `v19a_lmvm` geometry due to the additional material budget of cooling plates and PCBs.

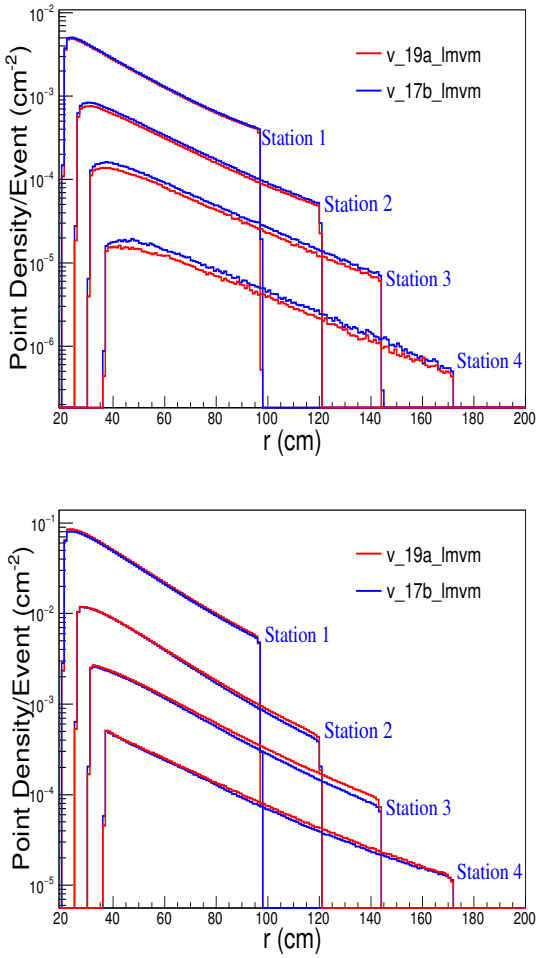

Figure 2: Point density of primary(top) and secondary(bottom) particles for each MuCh station.

To study the feasibility of Di-muon measurements with realistic MuCh geometry, we have performed full simulation and reconstruction. To select potential muon track candidates from the pool of global tracks, we have used selection cuts as associated STS hits ≥ 7, MUCH hits ≥ 11, $\chi^2_{Vertex} \leq 2.0$, $\chi^2_{STS} \leq 2.0$ and $\chi^2_{MUCH} \leq 2.0$. Moreover, the background was further reduced by using TOF information (TofM < 0.05) in the simulation.

The selected oppositely charged muon track candidates are employed to obtain the invariant mass spectra for signal as well as background. The combinatorial background has been calculated using Super Event (SE) technique to increase the statistics and plotted in Fig. 3.

The reconstruction efficiency and the signal-to-background ratio for ω were calculated in a $\pm 2\sigma$ window around the signal peak and are presented in Table 1.

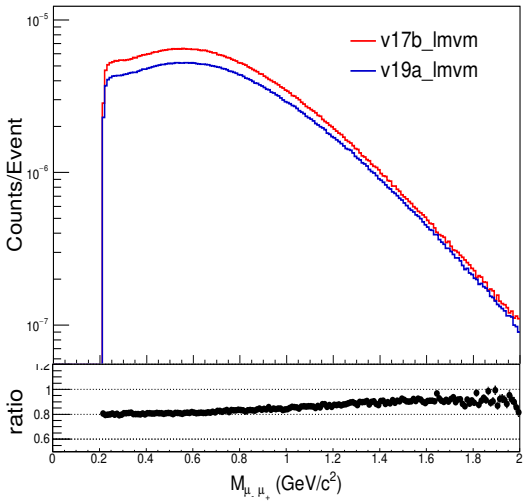

Figure 3: Invariant Mass Spectra for the Combinatorial Background.

MuCh Geometry Configuration	Efficiency ω , %	S/B
`v17b_lmvm`	0.324	0.199
`v19a_lmvm`	0.273	0.196

Table 1: Reconstruction efficiency and Signal-to-background ratio for ω in central Au+Au collision at 8A GeV for different geometry configurations.

The combinatorial background is reduced in realistic MuCh geometry, as displayed in Fig 3. However due to reduction in detection efficiency of the signal muon pairs, the overall signal-to-background ratio does not have a significant change in case of realistic geometry as evident from Table 1,

We would like to thank Ajit Kumar and Dr. Anand Dubey for many stimulating discussions.

References

[1] T. Ablyazimov *et al.* (CBM Collaboration), Eur. Phys. J. A**53** (2017) 60.

[2] Muon Chamber (MuCh) Technical Design Report (TDR), CBM Collaboration, Eds. S. Chattopadhyay *et. al.*, GSI-2015-02580.

[3] M. Bleicher *et al.* J. Phys. G**25**:1859-1896,1999

Implementation of RPC geometry and digitization in the 3^{rd} and 4^{th} MUCH station

E. Nandy[1], *O. Singh*[2], *V. Singhal*[1], *Z. Ahammed*[1], *P. P. Bhaduri*[1], *and S. Chattopadhyay*[1]
[1]Variable Energy Cyclotron Centre, Kolkata, India; [2]Aligarh Muslim University, AMU, India

Introduction

The muon chamber (MUCH) system in CBM is devoted to measure dimuons from the decay of Low Mass Vector Mesons (LMVMs) & J/ψ. A modular structure of the detector offers additional flexibility for hassle-free upgradation, as-per requirement. The CBM-MUCH consists of a segmented absorber system with three detectors layers, known as stations, placed in between the absorbers as shown in Fig 1.The Gas Electron Multiplier (GEM) is used as active detector component in the 1^{st} & 2^{nd} stations. For the 3^{rd} & the 4^{th} station use of Resistive Plate Chambers (RPCs) as active detector is under consideration. RPCs are cost-effective & can be fabricated in large area.

We have implemented the RPC sector shape geometry & realistic digitization parameters in the 3^{rd} & 4^{th} MUCH station in CbmRoot, compatible with the hardware requirements

RPC Geometry

In simulation, for the 1^{st} & 2^{nd} MUCH-stations, GEM detector with 3mm Argon based gas mixture has been used. For 3^{rd} & 4^{th} station, at the moment, we have considered sector shaped modules for RPC, similar to that used in MUCH-GEM. Each module consists of 2mm RPC gas sandwiched between 2mm RPC glass electrodes on both sides. Modules are arranged in staggerred manners on both sides of a carbon support structure as shown in Fig. 1. RPC Gas composition : TetraFluorethan ($C_2H_2F_4$) 85%, Sulfurhexafluoride (SF_6) 10% & 5% Isobutane (C_4H_{10}), presently used in simulation.

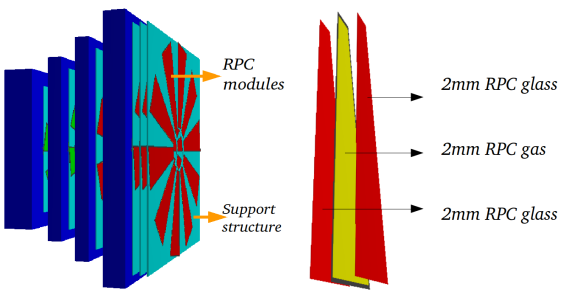

Figure 1: Arrangement of modules in staggerred manner on both sides of a carbon support structure. RPC module has been shown separately.

Each module is trapezoidal in shape. Module length is 116 cm & 138 cm for the 3^{rd} & 4^{th} station respectively.

Segmentation

MUCH covers an angular region from 5.7° to 25°. Each station has three detector layers. Detector layers are of circular shape & consists of several trapezoidal modules. In 1^{st} & 2^{nd} station azimuthal 1° segmentation on pads has been used. 1^{st} station has 16 modules, 2^{nd} station has 20 modules. For 3^{rd} & 4^{th} station 5° & 6° segmentation have been implemented as the track density is much less there and accordingly 18 & 20 modules have been used respectively as shown in Fig. 2 .

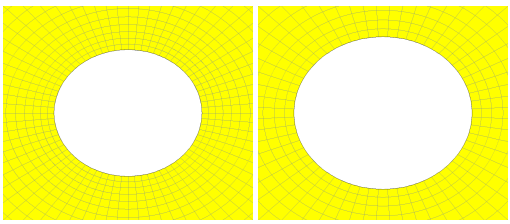

Figure 2: 5° (left fig) & 6° (right fig) azimuthal segmentation in station 3 & station 4 respectively.

There are total 1368 pads & 960 pads per layer in station 3 & station 4 with inner smallest pad dimensions 2.58 cm & 3.728 cm respectively. In earlier version of MUCH geometry, simulation has been done with GEM in all 4 stations and 1° segmentation in all GEM.

Digitization parameters

The readout planes of the modules are segmented in pads for obtaining final detectable response. The procedure of distributing the MUCH points to pads, known as digitization involves the detailed procedure of implementing the response of the gas detector to the energy deposition inside the chamber.

Table 1: Digitization parameters for GEM and RPC.

	GEM	RPC
Gain	5000	$3x10^4$
Spot Radius	500μm	2mm
Charge threshold	2fC	60fC
Maximum Charge	80fC	160fC
Drift Velocity of primary electrons (μm/ns)	100	120
Dead time	400ns	10ms
MPV for primary landau dist	from HEED	12

Digitization parameters are chosen based on the inputs from the detector hardware requirements and are listed in the table 1 for GEM and RPC.

Results and discussions

With these realistic geometry and digitization parameters we have simulated the performance of MUCH. This simulation have been done with SIS100B (4 stations + 4 absorbers) geometry at 8 AGeV central Au+Au collisions using UrQMD and PLUTO embedded events. The primary electron distribution from each MC point, within RPC detector drift volume has been shown in Fig. 3.

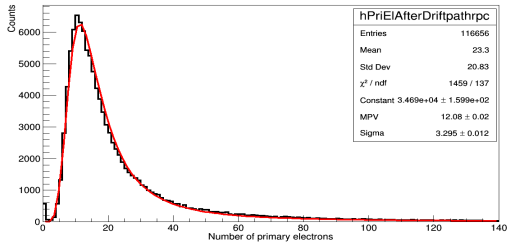

Figure 3: Number of primary electrons distribution within RPC drift volume.

The radial distribution of point density & hit density for 3^{rd} & 4^{th} station have been shown in Fig. 4 and Fig. 5 respectively. These are somewhat lower compared to previous GEM geometry and digitization [2].

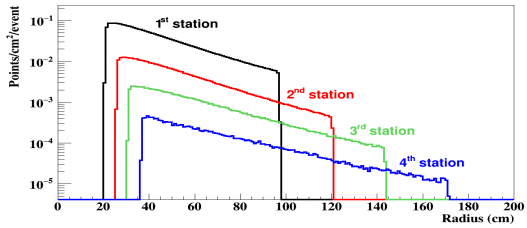

Figure 4: Radial point density distributions at different stations.

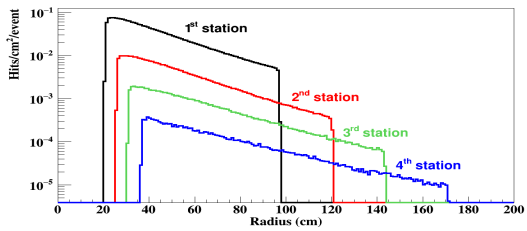

Figure 5: Radial hit density distributions at different stations.

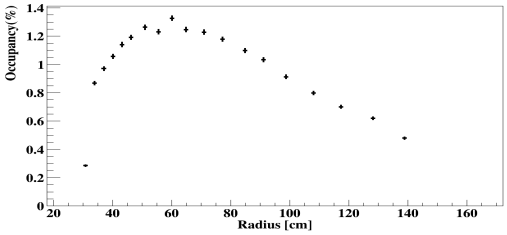

Figure 6: Radial distribution of occupancy for station 3.

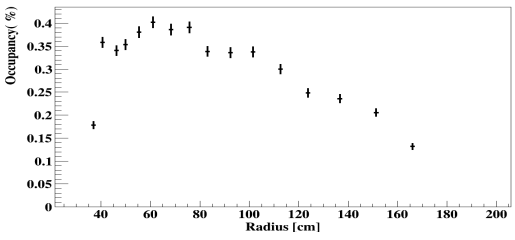

Figure 7: Radial distribution of occupancy for station 4.

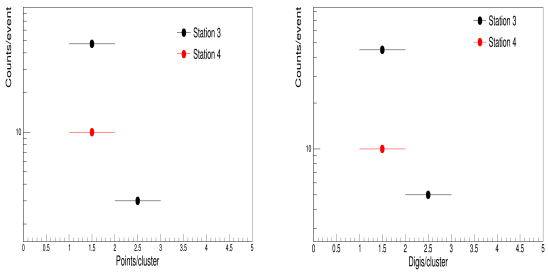

Figure 8: Points/cluster and digis/cluster distribution at station 3 and 4.

The occupancy distribution for 3^{rd} & 4^{th} station have been shown in Fig. 6 & Fig. 7 . Fig. 8 shows the distribution of number of points/cluster and digis/cluster in station 3 and 4. Finally we have calculated the pair reconstruction efficiency of ω meson decaying to dimuon from embedded events. However, the efficiency is lower compared to all GEM configurations. Investigation is on going for the effect of different Digitization parameters on efficiency.

Acknowledgement

We would like to thank all CBM-MUCH collaborators for their useful suggestions and discussions.

References

[1] Technical Design Report for the CBM : Muon Chambers (MuCh), CBM Collaboration, GSI, 190 S. (2015)

[2] Proceedings of the DAE Symp. on Nucl. Phys. 62 (2017),890-891.

Estimation of MuCh data rate: event coherent background from GEANT3 and GEANT4

S. K. Kundu[1], *P. P. Bhaduri*[2], *S. Chattopadhyay*[2], *and A. Roy*[1]

[1]Discipline of Physics, IIT Indore, Khandwa Road, Indore - 453552, Madhya Pradesh, India; [2]Variable Energy Cyclotron Centre, 1/AF Bidhan Nagar, Kolkata - 700064, India

The Muon Chamber (MuCh) detector system of the Compressed Baryonic Matter (CBM) experiment is designed to detect muon pairs coming from decay of Low Mass Vector Mesons (LMVM) and J/ψ. MuCh Detector is a combination of absorbers and detector layers as shown in Fig.1. MuCh detector will have to withstand very high interaction rate of 10^7 Hz in heavy-ion collisions, which implies that the data rate on the first few detector chambers will also be very high. Therefore, it is crucial to study the data rate handling capability of the MuCh.

In CBMROOT simulations, particles generated via event generator are made to pass through the absorbers and detector layers of MuCh using GEANT3 transport engine. But GEANT3 seems to underestimate particle rate, particularly those produced due to nuclear interaction. So we used GEANT4 instead of GEANT3 because GEANT4 includes some additional process that represents the interaction more reasonably compared to GEANT3. These phenomena inside the most recent version of GEANT4 provide good agreement of energy response, resolution of pions and protons.

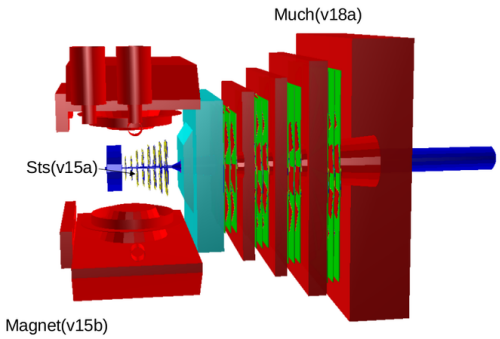

Figure 1: *CBM setup used for the present simulation.*

There are two type of sources that contribute to the data rate- coherent and incoherent sources. Main coherent source is "Target Data Rate" which is the data from ion-ion collision events. In our simulation, we generate coherent source by using UrQMD event generator. There are mainly two incoherent sources, one is data from the noise in the electronics which is called "Thermal Background", which depends on the temperature of the system. Another incoherent source is the background data from beam passing through the setup. Most of this background are delta electrons produced in the target, but they can also be produced in e.g. the beam pipe if it is not well designed. Here we are considering only event coherent sources.

For this purpose we estimate MuCh data rate by using event coherent background source from GEANT3 and GEANT4. First to see the difference in effect of GEANT3 and GEANT4 transport models, we analyse 10^5 minimum bias Au-Au events from UrQMD at beam energy 12A GeV. The produced particles are passed through the SIS-100 muon setup which includes 5 hadron absorbers and 4 tracking stations. Each station consists of three GEM layers. We compare point density/event for each station of MuCh for GEANT3 and GEANT4. It is observed that the contribution of secondary particles has been increased using GEANT4 compared to GEANT3. There is hardly any change in the contribution of primary particles as expected. It can be easily seen from Table 1.

	Average number of particles/event		
	All particles	Primary	Secondary
Station 1 (G3)	225.23	11.19	214.03
Station 1 (G4)	276.90	10.96	265.94
Station 2 (G3)	43.62	2.88	40.73
Station 2 (G4)	77.67	2.70	74.96
Station 3 (G3)	12.85	0.79	12.06
Station 3 (G4)	28.45	0.66	27.78
Station 4 (G3)	3.45	0.13	3.31
Station 4 (G4)	8.36	0.08	8.27

Table 1: *Difference in production of primary and secondary particles using GEANT3 and GEANT4.*

Next we proceed to the study of distribution of fired pads for each station. For this purpose the detector planes are segmented radially into square pads of 1^o azimuthal angle. The occupancy is defined as the fraction of fired pads per event.

Radial distribution of occupancy for each station using GEANT3 and GEANT4 are shown in Fig.2.

For the first station, there is hardly any change in occupancy. But for the second station, due to quite large increment in secondary particles with GEANT4, a significant increment in occupancy is observed.

Maximum pad hit rate is estimated by multiplying maximum occupancy for each station with peak collision rate (10^7 Hz). The estimated pad hit rate for each station using GEANT3 and GEANT4 are shown in Table 2.

There will be direct effect of beam energy on the occupancy and hence on the estimated data rate. In Fig.3, it is shown that if we take beam energy 35A GeV, the occupancy will reach upto twice as large compared to beam

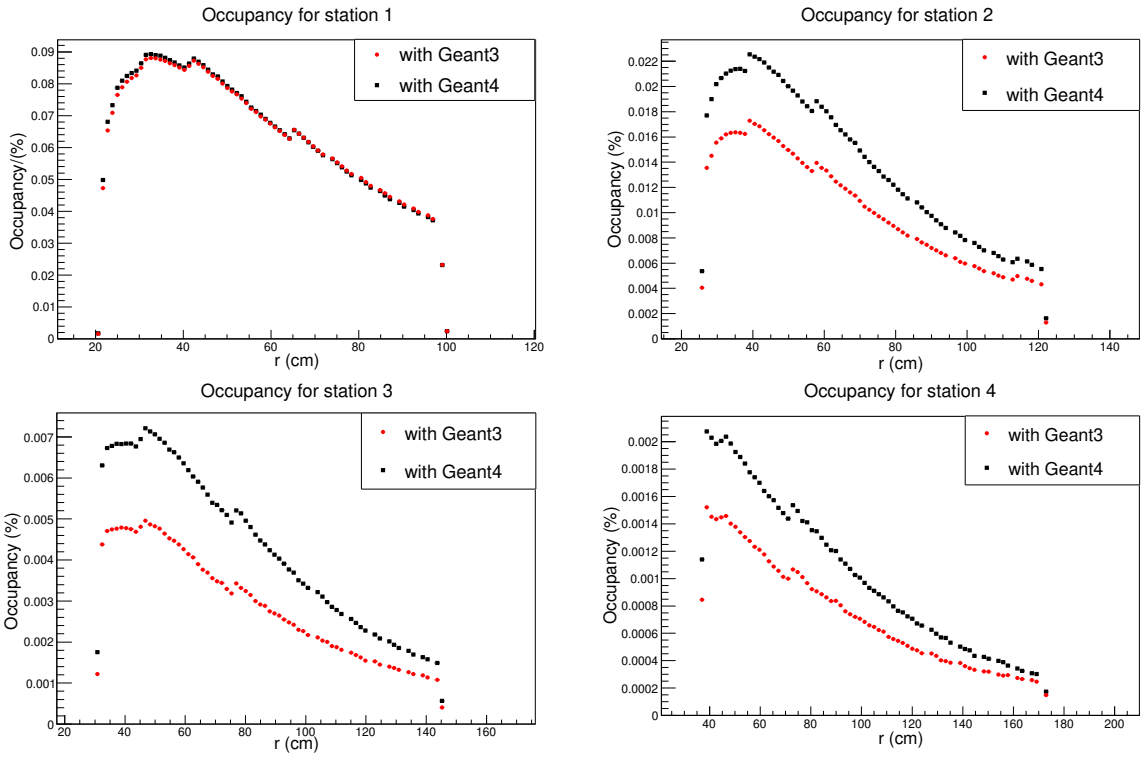

Figure 2: *Occupancy for different MuCh stations using GEANT3 and GEANT4 transport models.*

	Maximum pad hit rate
Station 1 (G3)	97 kHz
Station 1 (G4)	99 kHz
Station 2 (G3)	19.2 kHz
Station 2 (G4)	25 kHz
Station 3 (G3)	5.5 kHz
Station 3 (G4)	8 kHz
Station 4 (G3)	1.7 kHz
Station 4 (G4)	2.3 kHz

Table 2: *Maximum foreseen pad hit rate due to event coherent background source, for 12A GeV Au-Au collision for each station using GEANT3 and GEANT4.*

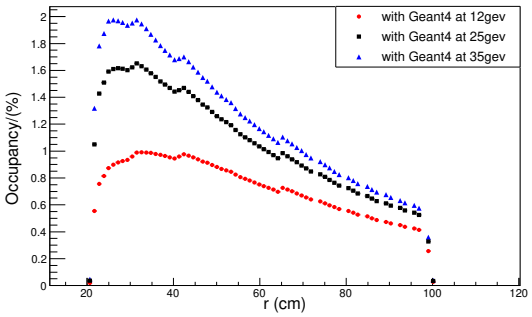

Figure 3: *Comparison of occupancy for 1st station at different beam energies.*

energy 12A GeV. So we have to use detector layers which can handle such high data rate according to our required beam energy.

We have estimated the pad hit rate for each station and found out that it is approx 100 kHz for first station and 25 kHz for second station by using GEANT4 as transport model at 12A GeV beam energy for only coherent source. There will be some effect of incoherent sources also on the data rate that we are trying to figure out.

Acknowledgement

Authors would like to acknowledge Dr. Volker Friese for many fruitful discussions and useful comments.

References

[1] CBM Progress Report 2017, [10.15120/GSI-2018-00485].

[2] The CBM Collaboration, *Technical Design Report fot the CBM: Muon Chambers*. GSI-2015-02580 .

Evolution of the geometry database

E.P. Akishina[1], E.I. Alexandrov[1], I.N. Alexandrov[1], I.A. Filozova[1], V. Friese[2], and V.V. Ivanov[1,3]
[1]LIT JINR, Dubna; [2]GSI, Darmstadt, Germany; [3]National Research Nuclear University "MEPhI", Moscow, Russia

The geometry database (Geometry DB) is an information system for storing and processing the detailed structure of the CBM experiment detectors. The description of the Geometry DB is presented in [1].

New functionality has been added to Application Programming Interface (API) and Graphical User Interface (GUI).

Two API tools are implemented as macros of the CBM ROOT framework:

- Load the Geometry DB files from central server locally;
- Load setup into CBM ROOT environment with possibility to move any module inside the setup.

And one feature is implemented to GUI which has web interface.

- Edit setup.

Load the Geometry DB files from central server locally

This tool allows user to load any setup from central CBM server to local environment. Afterwards, the user is able to work with it and test the setup locally. This feature also simplifies Lead Developer the procedure of checking new setup before its approvement.

Load setup into CBM ROOT environment with possibility to move any module inside the setup

User is able to load the setup into CBM environment and move any module inside the setup using XML file. The structure of the XML file is shown in Figure 1.

```
<setup>
<setupModule type="sts" enable="true" moveX="0" moveY="0" moveZ="0"/>
<setupModule type="magnet" enable="true" moveX="0" moveY="0" moveZ="0"/>
<setupModule type="mvd" enable="true" moveX="0" moveY="0" moveZ="0"/>
<setupModule type="rich" enable="true" moveX="0" moveY="0" moveZ="0"/>
<setupModule type="trd" enable="true" moveX="0" moveY="0" moveZ="0"/>
<setupModule type="pipe" enable="true" moveX="0" moveY="0" moveZ="0"/>
<setupModule type="much" enable="false" moveX="0" moveY="0" moveZ="0"/>
<setupModule type="tof" enable="true" moveX="0" moveY="0" moveZ="0"/>
<setupModule type="psd" enable="true" moveX="0" moveY="0" moveZ="0"/>
</setup>
```

Figure 1: Structure of the XML file

This file contains information about the shifts of setup modules chosen to be moved. The module is moved by X, Y, Z (in cm) if the value of parameter "enable" is TRUE. The module is not moved if the value of parameter "enable" is FALSE and if there is no corresponding module type specified in the XML file [2].

Edit setup

Lead Developer is able to edit any setup before its approvment. To do this Lead Developer should click Edit icon in Available Setups Edit Mode (see Figure 2). It is needed to confirm the editing of setup in the popup window. After that one can modify the setup structure.

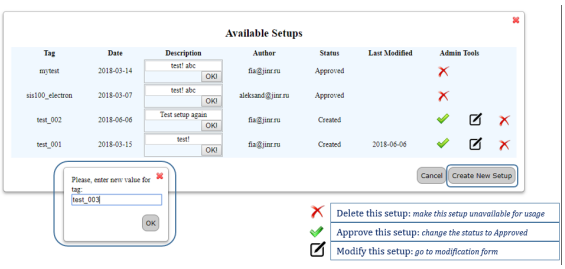

Figure 2: Web-interface: Edit Mode

The CBM Geometry DB has been developed for operating with information about the geometry of the CBM setup organized in FairRoot format. This means that it can be used by other physical experiments based on the ROOT environment.

BM@N (Baryonic Matter at Nuclotron) is the first experiment realized at the accelerator complex NICA-Nuclotron. The basic software of experiments CBM and BM@N are very similar especially in their approaches to simulation and reconstruction methods. For both experiments the details of any subdetector geometry are inside a root file. Thus CBM Geometry DB can be applied to BM@N experiment with minimal correction. The main difference for these experiments is the set of the detectors. As a result the information system Geometry DB for storing and retrieving the geometry of BM@N modules has been developed[3].

References

[1] E. Akishina a.o. Development of the Geometry Database for the CBM Experiment / Akishina E. P., Alexandrov E. I., Alexandrov I. N., Filozova I. A., Friese V., Ivanov V. V. // Particles and Nuclei, Letters, 2018, Issue 1, pp. 97-106.

[2] E. Akishina a.o. Experience of the Development of the Geometry Database for the CBM Experiment / Akishina E. P., Alexandrov E. I., Alexandrov I. N., Filozova I. A., Friese V., Ivanov V. V.//EPJ Web of Conferences (sent for publishing).

[3] E. Akishina a.o. Geometry database for the CBM experiment and its first application to the experiments of NICA project / E.P. Akishina, E.I. Alexandrov, I.N. Alexandrov, I.A. Filozova, V. Friese, K.V. Gertsenberger, V.V. Ivanov, O.V. Rogachevsky, // CEUR Workshop Proceedings, Vol. 2267, 2018, pp. 504-508.

Physics Performance

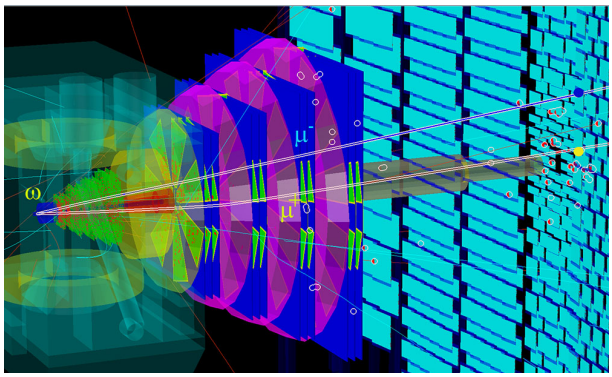

Reconstruction of η mesons using the conversion method

I. Kres, C. Pauly, and K.-H. Kampert
Department of Physics, University of Wuppertal, Germany

The CBM experiment is able to study rare dileptonic decays of J/ψ, ω, ρ, ϕ produced in heavy ion collisions at high net-baryon densities and moderate temperature. Due to the comparatively small production cross section, together with small branching ratio (BR) into e^+e^- a precise understanding of background is needed. On of the biggest background contribution in the dilepton invariant mass spectrum stems from η mesons decaying into $\eta \rightarrow \gamma+\gamma$ (BR 38.8%), or from η-Dalitz decays $\eta \rightarrow e^+ + e^- + \gamma$ (BR 0.5%). The abundance of η mesons in heavy ion collisions at CBM energies is not measured yet, and is therefore of interest to be measured precisely.

The CBM-RICH detector is able to measure photons indirectly by detecting e^+e^--pairs stemming from conversion $\gamma \rightarrow e^+e^-$ in the detector material. The detailed reconstruction procedure of γ using conversion method was already explained in details in the previous progress report [1]. In this analysis different possible cut values on the invariant mass and on the opening angle between charged particles were used (see Table 1). Two such reconstructed photons are then further combined to form a η meson. Due to the large mass of the η meson as compared to the π^0, an additional cut on opening angle between reconstructed photons $10^\circ < \theta_{\gamma\gamma} < 40^\circ$ is applied in order to filter out false combinations. The results shown here are based on 100×10^6 simulated UrQMD events of central Au+Au collisions at beam energy of 8 AGeV.

set 1	$m_{inv}(e^+e^-) < 10$ MeV; $\Theta_{e^+e^-} < 1^\circ$
set 2	$m_{inv}(e^+e^-) < 20$ MeV; $\Theta_{e^+e^-} < 2^\circ$
set 3	$m_{inv}(e^+e^-) < 30$ MeV; $\Theta_{e^+e^-} < 3^\circ$
set 4	$m_{inv}(e^+e^-) < 40$ MeV; $\Theta_{e^+e^-} < 4^\circ$
set 5	ANN value > 0.9

Table 1: Used cuts on the invariant mass and opening angle between charged particles for the γ reconstruction.

The standard reconstruction procedure of $\eta \rightarrow \gamma + \gamma \rightarrow e^+ + e^- + e^+ + e^-$ is based on full identification of daughter particles, i.e. all four leptons from double photon conversion have to be identified within the RICH detector. This requirement strongly limits the reconstruction efficiency of η, because it occurs rarely that all four leptons will be reconstructed within the RICH, due to their low momenta. In most of cases at least one out of two leptons from a converted photon is bended out of the RICH acceptance by the magnetic field. Weakening the requirements of full identification of leptons in the RICH detector will significantly increase the reconstruction efficiency. In this analysis, three different approaches are studied: full ID (4 out 4 are identified), partial ID (at least one lepton out of each pair is identified), without ID (0 or more out of 4 are identified). An example of reconstructed results can be seen in Figure 1.

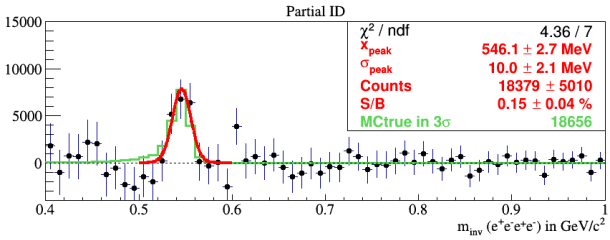

Figure 1: Reconstructed invariant mass spectrum of η after background subtraction using double conversion method.

A comparison of the reconstruction performance for each of the three identification approaches, in combination with different sets of cuts, is presented in Figure 2. The correlation between points has roughly exponential dependence (red curvature is a fit of data with an exponential function).

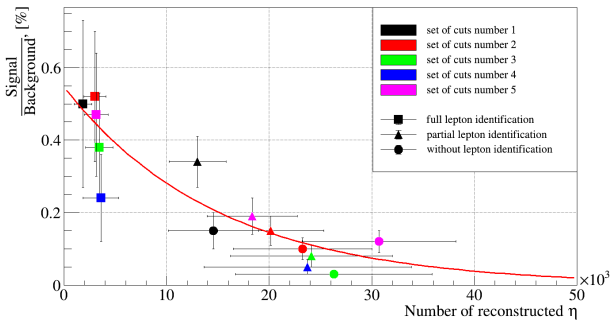

Figure 2: Correlation between reconstructed number of η and signal to background ratio.

The η conversion analysis shows, that 100 million central Au+Au events are enough to reconstruct the η meson with rather moderate precision, which is about 30%. To obtain this amount of events in CBM, one needs 28 hours of data taking at interaction rate of 100 kHz.

References

[1] I. Kres et al., CBM Progress Report 2016, p. 174

Feasibility studies of di-electron reconstruction in Au+Au collisions at 8 AGeV beam energy and Ag+Ag collisions at 4.5 AGeV beam energy

G. Pitsch[1], *S. Lebedev*[1,2], *and C. Höhne*[1,3]

[1]Justus-Liebig University Giessen, Giessen, Germany; [2]LIT JINR, Dubna, Russia; [3]GSI, Darmstadt, Germany

New feasibility studies have been performed for di-electron production in Au+Au collisions at 8 AGeV beam energy and for Ag+Ag collisions at 4.5 AGeV beam energy [1]. Au+Au collisions at 8 AGeV beam energy are a standard energy and system to be investigated with CBM at the SIS 100 accelerator. Detailed simulations have been performed before [2], however since then the RICH detector has undergone a major layout change by tilting the mirrors and re-optimizing the position of the photodetector plane [3]. The current simulation is thus performed in order to verify the new setup and for reference for the 2nd set of simulations: Ag+Ag collisions at 4.5 AGeV beam energy. This system has been chosen because being a potential candidate for a common system measured by both heavy-ion experiments at SIS 100, HADES and CBM.

All simulations have been performed in CbmRoot using the *dielectron* analysis package. For both setups a target thickness of 25 μm has been chosen. The magnetic field has been scaled to 50% for Au+Au collisions and to 60% for Ag+Ag collisions. All CBM detectors were implemented using the standard geometries as of Summer 2018 except the MVD detector. Simulations were performed using UrQMD as event generator. In each event a signal di-electron pair generated by PLUTO was embedded. As signal di-electrons either ω, ϕ and in-medium ρ [4] decays into e^+e^-, ω-Dalitz decays, or QGP radiation was implemented. Signals were scaled later according to their estimated multiplicity and branching fraction [5]. It is important to notice, that scaling factors were changed from the previously used estimates from HSD to values using a thermal model [6]. This reduced the ω multiplicity by a factor 8 but enlarged the ϕ multiplicity by a factor 3. Thus comparisons of S/B ratios from these simulations to previous simulations have to account for this factor.

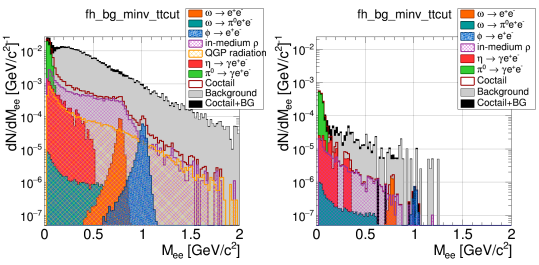

Figure 1: Invariant mass spectra for 5M central Au+Au collisions (left) at 8 AGeV and 10M minbias Ag+Ag collisions (right) at 4.5 AGeV beam energy excluding any pt-cut.

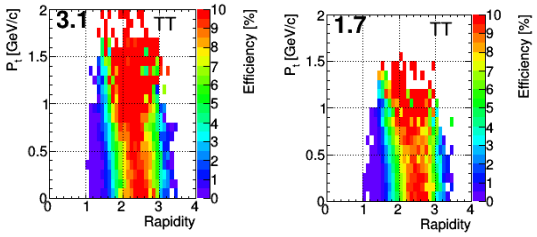

Figure 2: Efficiencies of the ω-meson reconstruction in the $y - pt$ plane compared to MC input for central Au+Au collisions (left) and minimum bias Ag+Ag collisions (right) excluding any pt-cut. Numbers in the upper left corner are total integrated efficiencies. Midrapidity is at 1.4 for 8 AGeV and 1.1 for 4.5 AGeV beam energy.

Simulations were then performed as before, final invariant mass spectra are presented in figure 1. Using the previous scaling factors for central Au+Au collisions all results agree very well to earlier results [2]. Efficiencies for the ω-meson are presented in figure 2. Clearly, the lower the beam energy, the more forward the acceptance for medium-mass di-electrons is for CBM. Thus CBM results at 4.5 AGeV will be rather complementary to HADES results as HADES has the largest acceptance around midrapidity.

Results presented here demonstrate the successful geometry optimization of the RICH detector and the feasibility of a di-electron measurement at 4.5 AGeV although in a very forward region of phase space.

References

[1] G. Pitsch, "Machbarkeitsstudien der Di-elektronen-Spektroskopie in Ag+Ag Kollisionen mit 4,5 AGeV Strahlenergie mit dem CBM Detektor", Masterthesis, University Giessen, September 2018.

[2] E. Lebedeva, "Low-mass di-electron reconstruction in the CBM experiment", CBM collaboration meeting, April 2016.

[3] I. Kres, T. Mahmoud, C. Pauly, C. Höhne, "RICH geometry optimization", CBM Progress Report, p. 64, 2016.

[4] T. Galatyuk et al., Eur. Phys. J. A52 (2016) 131.

[5] https://cbm-wiki.gsi.de/foswiki/bin/view/PWG/CbmDileptonInfoFilesAgAg, https://cbm-wiki.gsi.de/foswiki/bin/view/PWG/CbmDileptonInfoMult

[6] J. Cleymans et al., PRC 73 (2006) 034905.

CBM performance for flow measurements of charged and strange hadrons

D. Blau[1,2], O. Golosov[2], E. Kashirin[2], V. Klochkov[3,4], and I. Selyuzhenkov[2,3]

[1]National Research Center "Kurchatov Institute", Moscow, Russia; [2]National Research Nuclear University MEPhI (Moscow Engineering Physics Institute), Moscow, Russia; [3]GSI Helmholtzzentrum für Schwerionenforschung, Darmstadt, Germany; [4]Goethe University Frankfurt, Frankfurt am Main, Germany

The directed v_1 and elliptic v_2 flow of charged and strange particles and their antiparticles are important observables to study the properties of matter produced in heavy-ion collisions at FAIR energires. The scalar product (SP) method with three subevents (defined based on the PSD modules or STS+MVD tracks) was used to extract flow coefficients v_n. For strange hadron flow measurement, the v_n vs. invariant mass method was used to separate flow of the signal from that of the combinatorial background. The azimuthal non-uniformity of the CBM detector acceptance was corrected with the Q_n-vector corrections framework [1] based on method proposed in [2].

Au-Au collisions are simulated with the DCM-QGSM model extended with the Statistical Multi-fragmetation model (SMM) [3]. GEANT4 was used to simulate particle transport through the CBM detector material. The STS and MVD detectors located in the central rapidity region are used for particle's momentum reconstruction and identification, and centrality estimation. The Kalman Filter (KF) Particle Finder [4] package is used to reconstruct decays of Λ and K^0_s. The forward hadronic calorimeter PSD is used for projectile spectator plane estimation. PSD geometry used in the simulations consisted of 44 modules with tranvserse dimention of 20×20 cm^2 and a 20 cm diamond shaped hole in the detector center.

CBM perfromance for charged pion directed flow v_1 vs. transverse momentum is shown in Fig. 1(top). Results are obtained using central (PSD1) and outer (PSD3) modules for projectile spectator plane estimation. Performance for v_1 of Λ and K^0_S is shown in Fig. 1(middle) and Fig. 1(bottom).

In summary, the experimental methods for the anisotropic flow measurements are integrated into the CBMROOT software. Performance of the CBM experiment is studies for directed flow v_1 of charged hadrons, Λ and K^0_s using the DCM-QGSM-SMM model and realistic GEANT4 detector response simulations.

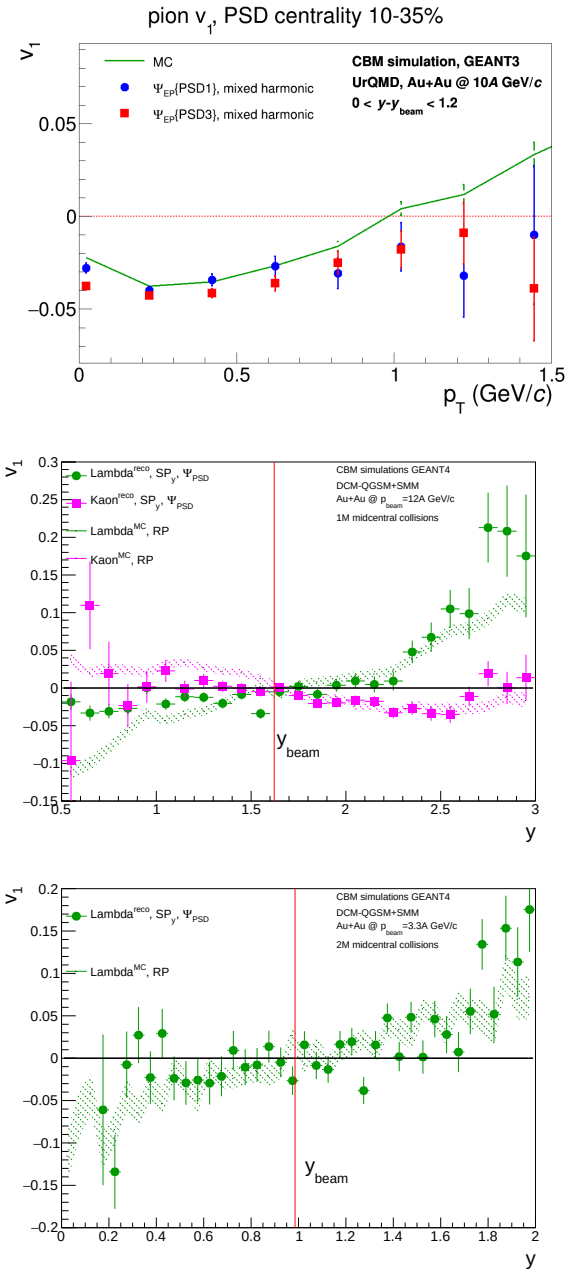

Figure 1: (top) $v_1(p_T)$ for π^+ for centrality 10-35% for $p_{beam} = 10$A GeV/c. (middle) $v_1(y)$ for Λ and K^0_s for centrality 20-30% for $p_{beam} = 12$A GeV/c. (bottom) $v_1(y)$ for Λ for $p_{beam} = 3.3$A GeV/c.

References

[1] V. Gonzalez, J. Onderwaater and I. Selyuzhenkov, GSI Annual report (p.81); https://github.com/FlowCorrections/FlowVectorCorrections

[2] I. Selyuzhenkov, S. Voloshin 2008 *Phys. Rev.* C **77** 034904

[3] A.S. Botvina, K.K. Gudima, J. Steinheimer, M. Bleicher, and I. N. Mishustin 2011 *Phys. Rev.* C **84** 064904

[4] I. Kisel 2016 *EPJ Web of Conferences* **108** 01006

Estimation of antiparticle to particle ratios at CBM energies

N. G. Ţuţuraş[1], A. Jipa[1], A. Jinaru[2], and T. Eşanu[2]

[1]University of Bucharest, Faculty of Physics, Bucharest - Romania ; [2]Horia Hulubei National Institute for R&D in Physics and Nuclear Engineering , Bucharest - Romania

The excitation function of the antiparticle to particle ratio can be used for the study of exotic states (the existence of density isomers) and phase transitions in nuclear matter formed in heavy ions nuclear collisions. The ratio of particle to antiparticle yields is of great importance to determine the freeze-out parameters, but, also, to eliminate the volume fluctuations.

In this study based on antiparticle to particle ratios, we show numerical calculations for the 6-25 A GeV energy range in Au-Au central collisions, where we have identified local tendencies of equalities in the ratio values and a peak at 18 A GeV. Two rapidity intervals were seen in our computations, ($0 < y < 0.8$ and $0.5 < y < 1.4$), for which the fluctuations in the excitation function for the antiparticle to particle ratio may suggest phase transitions, in the 10-13 A GeV and 18-20 A GeV intervals.

The analyzes in this article were performed using the UrQMD 3.3 generator, integrated in the YaPT system, with t = 200 fm/c, for which the state equation is defined by the cascade mode, and the AMPT 2.26t7 generator, which uses the string fragmentation Lund model and the popcorn mechanism (baryon stopping). AMPT shows an equal ammount of strangeness for the 10-11 and 12-13 A GeV intervals. This equality may suggest a pre-equilibrium in the highlited intervals, especially for the $0 < y < 0.8$ interval, where we can observe a liniar increase of the ratios, under and above the 10-13 A GeV interval, for both centralities (for $\frac{K^-}{K^+}$, Fig.1).

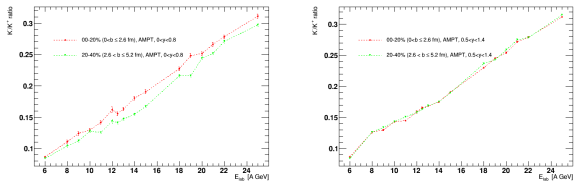

Figure 1: AMPT $\frac{K^-}{K^+}$ ratio distribution for two centralities, considering different collision energies and two rapidity intervals: left) $0 < y < 0.8$; right) $0.5 < y < 1.4$

For UrQMD results, we can notice, for the second centrality, 20-40% ($2.6 \leq b < 5.2$ fm), for both discussed rapidity intervals, equally for kaons and protons, the same behaviour: a short plateau around 18-19 A GeV (Fig. 2, 3). For the $\frac{\bar{p}}{p}$ ratio, in the 0-20% centrality interval ($0 < b \leq 2.6$ fm) a plateau well defined draws our attention. In the procedure of our calculations, we noticed a quasi-decrease (plateau) of the ratio of 11 and 13 A GeV (e.g. $\bar{p}/p$ $0 < y < 0.8$, 0-20% (Fig. 3, left), working with a step of 2 A GeV for calculating the antiparticle-particle ratio. During our workflow - as we suggested above - we were motivated to investigate 1 A GeV intervals for the excitation function and even 0.5 A GeV, such that we can see the formation or "kind" of the plateau. We can also observe a peak at 18 A GeV (Fig. 3, left). These plateaus and the peak suggest a possible mixed phase. The plateau forms that we obtained seems to be in agreement with the results from [1]. Here, the results suggest the formation of the mixed phase based on the calculations of pion/baryon, and entropy/baryon ratios in the energy range 6.9 - 11.6 A GeV, and these are compared with the AGS (Au-Au) and SPS (Pb-Pb) data for regions with anomalous thermodynamic properties.

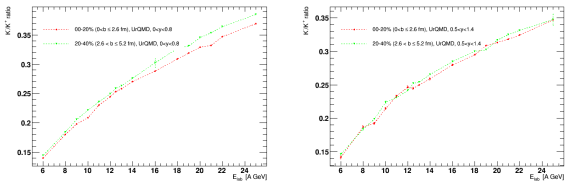

Figure 2: UrQMD $\frac{K^-}{K^+}$ ratio distribution for two centralities, considering different collision energies and two rapidity intervals: left) $0 < y < 0.8$; right) $0.5 < y < 1.4$

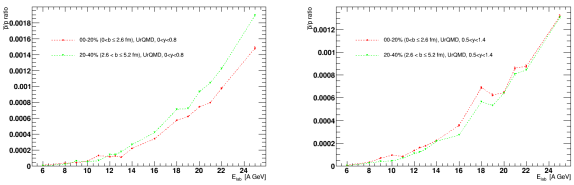

Figure 3: UrQMD $\frac{\bar{p}}{p}$ ratio distribution for two centralities, considering different collision energies and two rapidiy intervals: left) $0 < y < 0.8$; right) $0.5 < y < 1.4$

One can notice that for the second centrality, 20-40% ($2.6 < b \leq 5.2$ fm), the $\frac{K^-}{K^+}$ ratio is many times higher than that for the 0-20% (Fig. 1, right and Fig. 2), in agreement with KaoS - HADES experiment [2], which indicates a ratio of $\frac{K^-}{K^+}$ higher with increasing centrality of the collision.

As it is well known, it's hard to give an interpretation without the help of data, but nontheless, this has a predictive character of numerical computations, and we will study, in the near future, the $\frac{K}{\pi}$ and $\frac{\Lambda}{\Lambda}$ ratios (and other anti-baryon to baryion ratios), in order to verify if the behaviour which suggest mixed phase will repeat.

References

[1] K. A. Bugaev et al., Physics of Particles and Nuclei Letters 12 (2015) 2, 238–245

[2] M. Lorenz et al – for HADES Collaboration – 15'th International Confference Journal of Physics: Conference Series 668 (2016), 012022

Muon measurements at low beam energies with a CBM-MuCh start version

A. Senger and the CBM collaboration
GSI, Darmstadt, Germany

Detector configuration and muon reconstruction

This report is based on the CBM Internal Physics Note 18001. In this note we propose a start version of the Muon Chamber (MuCh) system which will be well suited for the identification of muons in heavy-ion collisions at kinetic beam energies up to about 4A GeV. The proposal is based on a MuCh comprising 2 GEM stations and 3 absorbers only. The radial segmentation of the two GEM detectors is 1°, the absorbers consist of a Carbon block of 60 cm thickness in front of the first GEM station, a 20 cm thick iron layer between the first and the second GEM station, and a 20 cm iron layer behind the second GEM station. In addition, the experimental setup includes the Silicon Tracking Stations (STS) for track reconstruction, the Time-Of-Flight wall (TOF) for particle identification, and the Transition Radiation Detector (TRD) as intermediate tracker between the second GEM station and the TOF detector, as illustrated in figure 1.

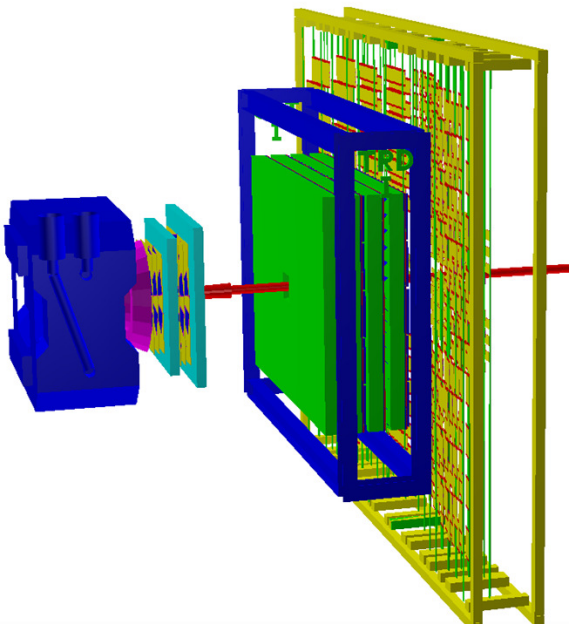

Figure 1: CBM geometry for muon measurements: STS+MuCh+TRD+ToF. Muon system (MuCh) comprising 2 GEM stations with 1° radial segmentation and 3 absorbers: 60 cm carbon and 20+20 cm iron.

The simulations discussed in the following have been performed for Au beams with momenta of 2 and 4 A GeV/c, a 1% interaction Au target, and a magnetic field of 50% of the maximum value. The low-mass vector mesons are generated using the PLUTO code, and are embedded into central Au+Au events generated with the UrQMD code. In order to identify the muons, the following cuts have been applied: primary vertex cut ($\chi \leq 2$), number of hits in STS (≥ 7), number of hits in MuCh (≥ 5), number of hits in TRD (≥ 1), and track quality in STS and MuCh ($\chi \leq 2$). Finally, a 2σ cut has been applied in the plane mass-squared versus momentum provided by TOF, as illustrated in figure 2.

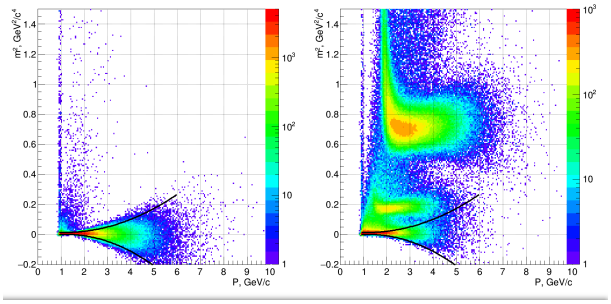

Figure 2: Reconstructed muon tracks from omega meson decays (left panel) and reconstructed background tracks (right panel) as function of mass squared and momentum based on TOF information for central Au+Au collisions with beam momentum of 4 A GeV/c. The black lines illustrate the selection criteria for muons.

Detector performance for the measurement of low-mass vector mesons

The acceptance for reconstructed omega mesons as function of transverse momentum and rapidity is presented in figure 3, calculated for central Au+Au collisions with a beam momentum of 4 A GeV/c. Due to the absorption of low-energy muons, the acceptance is shifted towards forward rapidities, as indicated by the black dots. The colored area corresponds to the 4π distribution generated by PLUTO.

The reconstructed invariant mass spectrum for muon pairs simulated for central Au+Au collisions at a beam momentum of 4 A GeV/c is shown in figure 4 as a black histogram. The figure also depicts the invariant mass spectra of the Dalitz decays of the eta and omega mesons, to-

gether with the dimuon invariant mass distributions of the eta, omega, phi, and rho decays, which have been identified by Monte Carlo information. The resulting signal-to background ratio as function of invariant mass is shown in figure 5.

The signal-to-background ratios and the reconstruction efficiencies for omega mesons via their dimuon decay in central Au+Au collisions at beam momenta of 2 A GeV/c and 4 A GeV/c are listed in table 1.

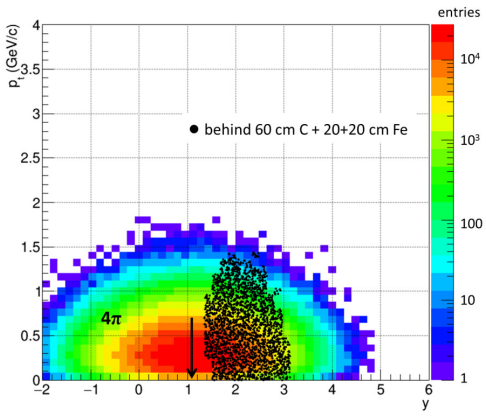

Figure 3: Acceptance for omega mesons decaying in to muon pairs as function of transverse momentum and rapidity, for central Au+Au collisions at a beam momentum of 4 GeV/c. Black dots: reconstructed omega mesons for a muon detection system with 3 absorbers (60 cm C + 20+20 cm Fe). Colored area: 4π distribution generated by the PLUTO code. The black arrow indicates mid-rapidity.

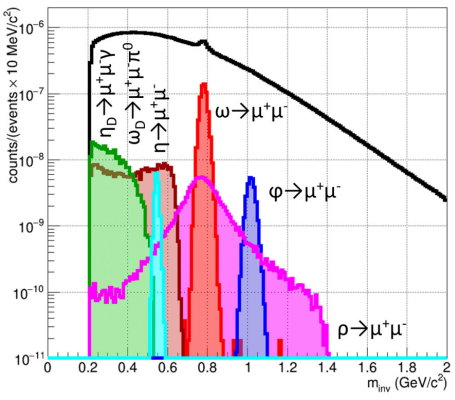

Figure 4: Reconstructed dimuon invariant mass distribution simulated for central Au+Au collisions with a beam momentum of 4 GeV/c (black histogram). The dimuon decays of low-mass vector mesons including their Dalitz decays, which have been identified using Monte Carlo particle information, are shown in different colors.

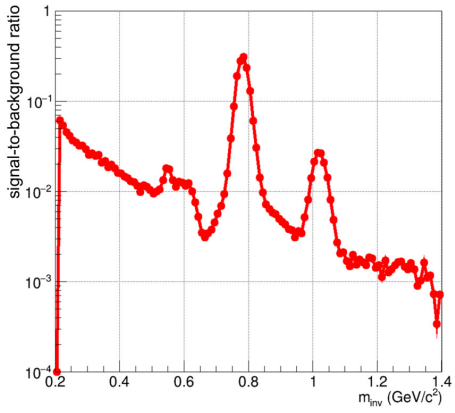

Figure 5: Signal-to-background ratio as function of invariant dimuon mass for reconstructed low-mass-vector mesons from central Au+Au collisions with 4 A GeV/c beam momentum.

Au beam momentum A GeV/c	ω S/B ratio	ω efficiency %
2	0.19	1.47
4	0.17	1.65

Summary and conclusions

A MuCh start version comprising 2 GEM stations and 3 absorber layers is proposed, which is well suited to identify muons emitted in heavy-ion collisions at beam momenta of 2 and 4 A GeV/c. In addition to the MuCh, the experimental setup includes the Silicon Tracking Stations (STS) for track reconstruction, the Time-Of-Flight wall (TOF) for particle identification, and the Transition Radiation Detector (TRD) as intermediate tracker between the second GEM station and the TOF detector. The muon identification at these relatively low beam momenta is a challenge, as the muons from hadron decays are only moderately boosted. This results in low-momentum muons, which suffer from absorption in the hadron absorbers, with the consequence that the acceptance for low-mass vector mesons is shifted towards forward rapidity. This acceptance is very similar to the one of the NA60 experiment at CERN-SPS, which also covers rapidities above midrapidity. On the other hand, the signal-to-background ratio for dimuons from vector meson decays is comparable to the one for dimuons from vector meson decays simulated for Au+Au collisions at 8 GeV/c, using a MuCh system with 4 tracking stations and 5 hadron absorbers. In view of the situation, that no final proposal yet exists for the MuCh tracking stations number 3 and 4, it is worthwhile to note, that it is possible to perform a very competitive day-1 muon experiment already with the existing 2 GEM stations and 3 hadron absorbers.

A systematic investigation of di-muon combinatorial background for CBM-MUCH

E. Nandy, P. P. Bhaduri, and S. Chattopadhyay
Variable Energy Cyclotron Centre, Kolkata, India

Introduction

The Compressed Baryonic Matter (CBM) experiment at the Facility for Antiproton and Ion Research (FAIR) in GSI, Germany is a future fixed target experiment which will perform the precision measurement of dilepton pairs in the full mass region (low mass to charmonium) in the energy range 4-40 AGeV using very high-interaction rate ($\sim$10MHz) heavy ion beams. Leptons being weakly interacting, remain unaffected by final state interactions,and act as one of the cleanest probes to explore the fireball created in heavy ion collisions. The objective of the MUon CHamber(MUCH) detector in the CBM experiment is to study the dimuon spectra at different mass regions. One of the major experimental challenges of the CBM experiment in the FAIR energy regime is the identification of low momentum muons, originating from the decay of low-mass vector mesons (LMVM), in a very high particle density environment [1]. In the multiparticle environment characteristic of relativistic nuclear reactions, the dimuon signals are superimposed on a generally large combinatorial background. Depending on the underlying physics process, the signal could either appear as a narrow peak (eg: resonance decays in muon channel) or might be a continuum (eg: Drell-Yan process, Dalitz decay of vector mesons etc.). When the signal appears as a narrow peak riding over the continuous background, it can be extracted by following standard methods of fitting the signal + background distribution with appropriate functions chosen in order to provide a good description of the overall spectrum. This technique however does not work if signal and background have a similar shape like in case of continuum signals. The same is true when resonant signal is small and burried under the background, as is the case at FAIR energies,owing to extremely small multiplicities of the resonance mesons in the di-lepton channel. The only way to overcome the problem is to estimate independently the background distribution and to subtract it from the overall S+B spectrum. In the present article, we demonstrate a method for estimating the combinatorial background and extraction of a di-muon resonance signal ($\omega \rightarrow \mu^+ \mu^-$) in 8 AGeV Central Au+Au collisions.

Analysis procedure

For this analysis we have used CBM detector setup with Silicon Tracking Stations (STS), MUon CHamber (MUCH), Transition Radiation detector (TRD) and Time of Flight (TOF) detectors [2]. Analysis has been done with the final reconstructed tracks which satisfy some optimized selection cuts specific for identification of muon like candidates viz : the track should have atleast 7 STS hits, 11 MUCH hits, χ^2_{STS} <2, χ^2_{MUCH} <1.3 & χ^2_{Vertex} <2 [2]. A track satisfying these conditions are treated as a muon candidate. Positively and negatively charged muon candidates are stored separately. Signal ω is generated from PLUTO event generator and background particles are generated from UrQMD. Particle interactions with the detector material has been taken care in GEANT3 transport code.

Results and discussion

The invariant mass distributions are obtained by pairing different charge combinations muon candidates, like, ++, - - and +-.The combinatorial background is estimated from UrQMD events only, with same event (SE) and mixed event (ME) technique. In SE, pairs are constructed from unlike charge combinations muon candidates from same event. Whereas, in ME, unlike pairs are formed from muon candidates always taken from different events . Fig. 1 and Fig. 2 shows the background distribution calculated from these two methods.

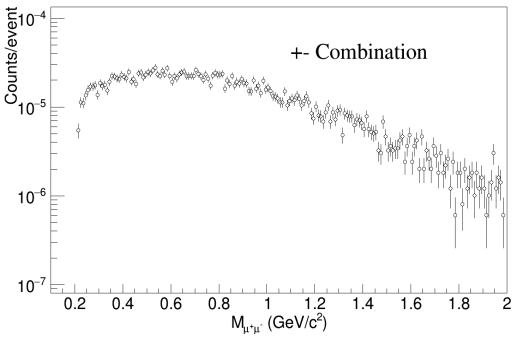

Figure 1: Combinatorial unlike sign background from same event

Combinatorial background in general,refers to uncorrelated pairs of muon candidates not originating from the decay of same mother particle. So one may expect background shape obtained from different methods, to be identical. This has been shown in Fig. 3 the ratio of SE and ME background distibution. The ratio was found flat over the entire range. Now to estimate signal (S) strength, we reconstruct the invariant mass of ω decaying to $\mu^+\mu^-$ from embedded events (PLUTO + UrQMD). The signal

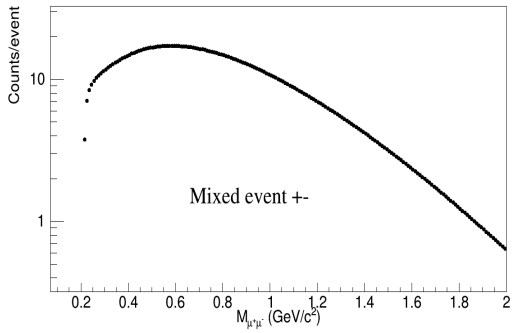

Figure 2: Combinatorial unlike sign background from mixed event

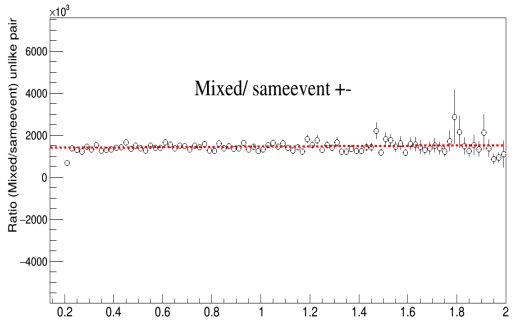

Figure 3: background ratio of mixed event to same event

pairs are weighted by ω multiplicity in the dimuon channel (19×9×1e-5). To get a realistic dimuon invariant mass spectra, the signal invariant mass distribution was added to background distribution obtained from ME.

As the signal peak over background is very small, so to get a significant yield of signal we need very high statistics for a stable background & ME background has been well suitable for its smooth shape due to large statistics. Here ME background has been scaled to the same lavel as same

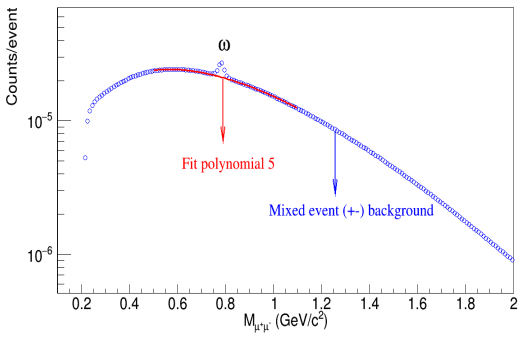

Figure 4: Mixed event background superimposed with signal ω.

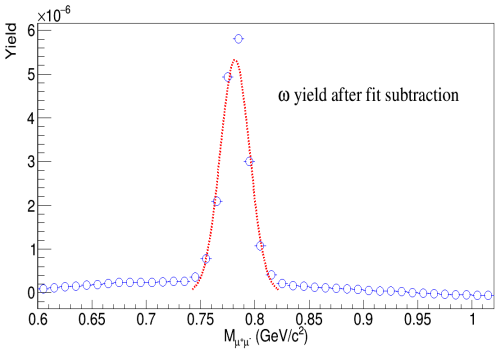

Figure 5: Signal ω yield.

event background. The ME background has been properly fitted with 5^{th} order polynomial. The total signal + ME background along with the background fit have been shown in Fig. 4. Finally fit is subtracted from the total S+B spectra to get the signal ω yield as shown in Fig. 5. We get pair reconstruction efficiency of ω ∼0.97 % which is comparable with the signal efficiency obtained from true dimuons using PDG information.

References

[1] Technical Design Report for the CBM : Muon Chambers (MuCh), CBM Collaboration, GSI, 190 S. (2015)

[2] DAE Symp. on Nucl. Phys. **61**, 808-809 (2016).

[3] I. Froehlichet, et al.,Journal of Physics:Conference Series 219 (2010) 032039.

[4] S.A. Bass, et al., Progress in Particle and Nuclear Physics 41 (1998) 225.

[5] Proceedings of the DAE Symp. on Nucl. Phys. 63 (2018), 1016-1017.

Multi-strange hyperon reconstruction with the CBM experiment

I. Vassiliev[1], *I. Kisel*[1,2,3], *M. Zyzak*[1], *and the CBM Collaboration*
[1]GSI, Darmstadt; [2]FIAS, Frankfurt am Main; [3]Goethe-Universität, Frankfurt am Main

The main goal of the CBM experiment at FAIR is to study the behavior of nuclear matter at very high baryonic density. This includes the exploration of the high density equation of state, search for the transition to a deconfined and chirally restored phase, critical endpoint. The promising diagnostic probes for this new states are the enhanced production of multi-strange (anti-)particles. The CBM detector is designed to measure such rare diagnostic probes multi-differentially with unprecedented precision and statistics. The CBM detector will provide a unique opportunity to measure yields, direct and elliptic flow, excitation functions of multi-strange hyperons at different energies and sizes of the colliding nuclei.

Multi-strange hyperons will be identified in CBM by their decay into charged hadrons, which are detected in the Micro Vertex detector (MVD), Silicon Tracking System (STS) and in the Time-of-Flight detector (TOF). Four layers of the Transition radiation detector (TRD) are used by the global tracking to propagate tracks found in STS to TOF. In addition energy deposition dE/dx measured by the TRD detector will be used to identify fragments like ^{3}He and ^{4}He.

To study the performance of multi-strange hyperon reconstruction with the CBM experiment, a set of $5 \cdot 10^6$ central Au+Au UrQMD events at 10 AGeV for the SIS-100 electron/hadron setup have been simulated with the GEANT 3 transport engine. The STS hits were produced assuming 100 kHz interaction rate with 10^4 ns length of the time-slice. Event-by-event mode was used.

The KF Particle Finder package [1] was used in order to reconstruct multi-strange hyperons. Currently its reconstruction scheme contains about 200 decays including $K^0_s \rightarrow \pi^+\pi^-$, $\Lambda \rightarrow p\pi^-$, $\bar{\Lambda} \rightarrow \bar{p}\pi^+$, $\Xi^- \rightarrow \pi^-\Lambda$, $\bar{\Xi}^+ \rightarrow \pi^+\bar{\Lambda}$, $\Omega^- \rightarrow K^-\Lambda$ and $\Omega^+ \rightarrow K^+\bar{\Lambda}$. Corresponding invariant mass spectra are shown in Fig. 1. All signals are clearly visible with high signal to background ratios.

Doubly-differential p_t versus rapidity efficiency distribution, integrated efficiency as a function of p_t and rapidity are shown in Fig. 2 for the reconstructed (filled red histogram at the lower right plot) Ξ^-s. These functions will be used for the comparison of theoretical models with measured data. Average Ξ^- reconstruction efficiency is about 12.7%, an invariant mass resolution of 2.0 MeV/c^2 with signal to background ratio of about 6 was obtained. The Ω^- reconstruction efficiency results to about 6.0% for central UrQMD events. An excellent signal to background ratio of about 18 is observed. The reconstructed mass value 1.672 ± 0.003 GeV/c^2 is in a good agreement with the PDG's data. An invariant mass resolution of 2.1 MeV/c^2 is obtained.

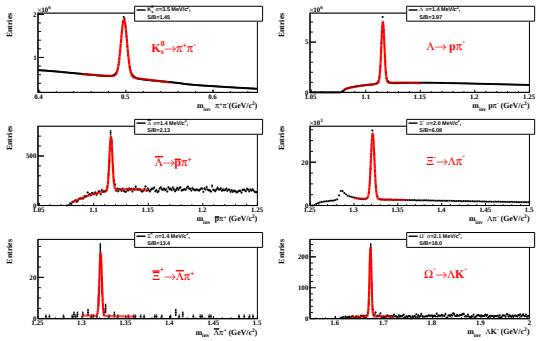

Figure 1: Reconstructed invariant mass distribution of K^0_s, Λ, $\bar{\Lambda}$, Ξ^-, $\bar{\Xi}^+$ and Ω^- in central Au+Au collisions at 10 AGeV, the red line indicates the signal plus background fit by a polynomial plus Gaussian functions.

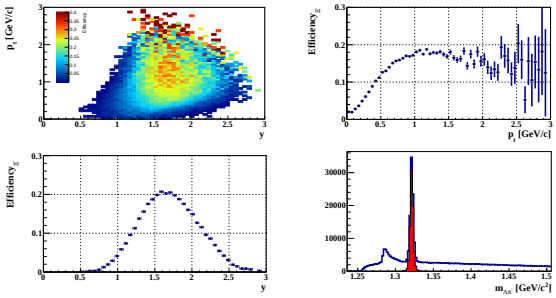

Figure 2: 2D Ξ^- reconstruction efficiency as a function of p_t and rapidity (upper left), integrated Ξ^- reconstruction efficiency as a function of p_t (lower left) and rapidity (upper right). Selected Ξ^- invariant mass signal and total mass plots (lower right).

High statistics allows to calculate even rare probes like $\Omega^{\pm}$ reconstruction efficiency directly, avoiding signal embedding into model events. It allows to investigate systematic behavior of different physics observables, e.g. direct and elliptic flow, excitation function and antihyperon-to-hyperon ratios.

References

[1] I. Kisel, I. Kulakov and M. Zyzak, *Standalone First Level Event Selection Package for the CBM Experiment*, IEEE Transactions on Nuclear Science, vol. 60, No. 5, October 2013, p. 3703.

Mixed cumulants in Au-Au collisions with CBM detector at SIS100

D. Roy, R. Singh, and B. Mohanty
School of Physical Sciences, National Institute of Science Education and Research, HBNI, Jatni - 752050, India

Introduction

Recent model calculations have predicted a QCD critical point (CP) and a first order phase boundary between quark-gluon and hadronic phases at finite μ_B [1]. A good signature of a phase transition and a CP is the non-monotonic variation of observables related to the cumulants of the distributions of conserved quantities such as net-baryon (B), net-charge (Q), and net-strangeness (S) number with $\sqrt{s_{NN}}$. These cumulants (κ^n_α; $\alpha = B, S, Q$) are related to the higher order (n) thermodynamic susceptibilities (χ^n_α) of the system, and takes large values near the phase transition. One of the main physics goal of CBM experiment in FAIR and BES-II in RHIC is to look for such signatures associated with the existence of a critical point with high statistical precision.

In addition to the diagonal cumulants mentioned above, it is also possible to construct off-diagonal cumulants for the conserved quantities (Q,B,S). These off-diagonal cumulants of orders m and n ($\kappa^{m,n}_{\alpha,\beta}$) relate to the off-diagonal thermodynamic susceptibilities ($\chi^{m,n}_{\alpha,\beta}$) [2] and allow the study of baryon-strangeness correlations, through the measurement of the energy dependence of the ratio of off-diagonal over diagonal cumulants ($\kappa^{1,1}_{B,S}/\kappa^2_S$) [3]. This can be related to the susceptibility ratio $C_{B,S} = -3\chi^{1,1}_{B,S}/\chi^2_S$, and is expected to show a rapid change during the transition of the system from de-confined to confined state [4]. The off-diagonal cumulants are also expected to elucidate the character of chromodynamic matter. The mixed susceptibilities (baryon-strange, baryon-charge) have been reported to differ significantly in the Hadron Resonance Gas (HRG) model and lattice QCD calculations [2, 3]. The off-diagonal cumulants at second-order is also shown to be sensitive to the difference between calculations from the ideal HRG and lattice QCD [5]. Therefore, measurement of these cumulants of net-multiplicity distributions can put constraints on various models which describe QCD matter [3]. In most heavy-ion collision experiments, the total number of baryons can not be determined, as neutrons are not detected. It is also difficult to perform high purity net-multiplicity measurements on strange baryons like Λ, Σ, Ξ and strange meson like K^0_S, as they are reconstructed using invariant mass technique, and have reduced efficiency and purity. As such, net-proton ($\Delta N_p = N_p - N_{\bar{p}}$), and net-kaon ($\Delta N_K = N_{K^+} - N_{K^-}$) are used as proxies for net-baryon and net-strangeness [7], and $\kappa^{1,1}_{p,k}$ is expected to illustrate the qualitative features of a rapid change near the QCD phase transition, as predicted [4]. The second-order thermodynamic susceptibilities of the conserved quantities are related to the corresponding second-order cumulants of event-by-event net multiplicity distributions [6] as

$$\chi^2_\alpha = \frac{1}{VT^3}\kappa^2_\alpha;\ \chi^{1,1}_{\alpha,\beta} = \frac{1}{VT^3}\kappa^{1,1}_{\alpha,\beta} \quad (1)$$

The moments of these distributions are defined by $\delta N_\alpha = N_\alpha - \langle N_\alpha \rangle$. Then, the cumulants are:

$$\kappa^2_\alpha = \sigma^2_\alpha = \langle (\delta N_\alpha - \langle \delta N_\alpha \rangle)^2 \rangle \quad (2)$$

$$\kappa^{1,1}_{\alpha,\beta} = \sigma^{1,1}_{\alpha,\beta} = \langle (\delta N_\alpha - \langle \delta N_\alpha \rangle)(\delta N_\beta - \langle \beta N_\beta \rangle) \rangle \quad (3)$$

In this report, we will present $\kappa^{1,1}_{p,k}$ as a function of collision centrality.

Analysis Details

We have performed this analysis over 3 million Au-Au minimum bias collision events, generated using the UrQMD model [8], at E_{lab} = 10 AGeV. The detector configuration used for the simulation is "sis100_electron" which can be used for both electron and hadron physics. The charged particle are selected with transverse momentum $0.2 < p_T < 2.0$ GeV/c in the pseudorapidity range of $1.5 < \eta < 3.8$.

Particle Identification and Centrality Selection

The particle identification is done using the information from the Time-of-Flight (TOF) detector, which measures the flight-time of the particle (t), for a path length (L) from the primary vertex of a collision. To calculate the mass square (m^2), one uses the following formula.

$$\beta = \frac{L}{ct}\ ; m^2 = p^2\left(\frac{1}{\beta^2} - 1\right) \quad (4)$$

The proton(anti-proton) and $K^+(K^-)$ are identified using m^2 cut of $0.6 < m^2\ (\mathrm{GeV}^2/\mathrm{c}^4) < 1.2$ and $0.18 < m^2\ (\mathrm{GeV}^2/\mathrm{c}^4) < 0.32$, respectively.

The centrality selection is done using charged particle multiplicity distributions measured in STS detector. the charged particles are selected with $m^2 < 0.15\ \mathrm{GeV}^2/\mathrm{c}^4$. The m^2 cut is used to remove the autocorrelation effects. The analysis is performed in nine centrality bins ($0-5\%$, $5-10\%$, $10-20\%$, $20-30\%$, $30-40\%$, $40-50\%$, $50-60\%$, $60-70\%$ and $70-80\%$).

Efficiency Correction

The measured cumulants are affected by the finite detector efficiencies and we need to correct for those in order

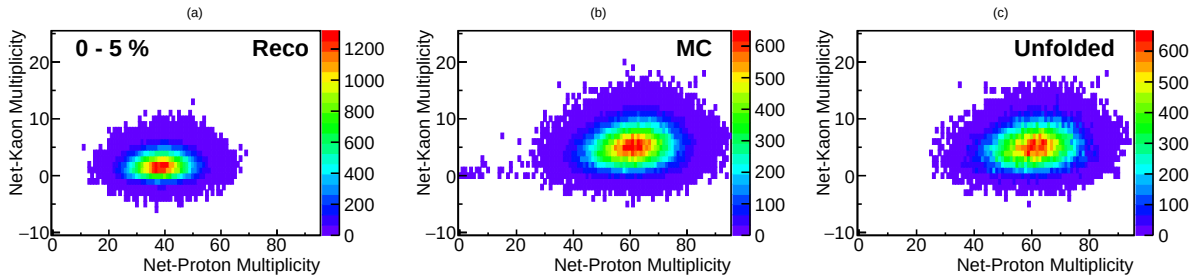

Figure 1: The 2D plots for net-proton and net-kaon multiplicity distributions from reconstructed tracks (a), incident particles (b) and after unfolding (c) in Au-Au collisions at E_{lab} = 10 AGeV.

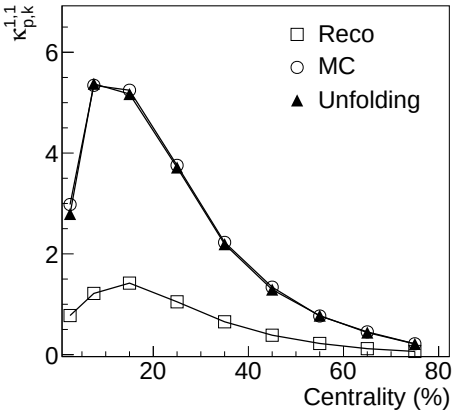

Figure 2: The centrality dependence of $\kappa_{p,k}^{1,1}$ in Au-Au collisions at E_{lab} = 10 AGeV.

to get the actual cumulants. The efficiency correction is done for $\kappa_{p,k}^{1,1}$ using the Bayesian unfolding approach [10]. The unfolding algorithm has been implemented using the *RooUnfold* package [11], available in ROOT. The formulation of the algorithm for the correction of event-by-event distributions can be found in [12]. Here, we briefly outline the process. For a given true distribution S, we measure a distribution M that is affected by the detector effects described by response matrix R. Then for a binned distribution

$$M_i = \sum_{j=1}^{m} R_{ij} S_j \qquad i = 1, 2, ..., n \tag{5}$$

We use the response matrix R_{ij} to 'deconvolute' the measured distribution for which we have calculated the cumulants. The result of unfolding procedure in centrality bin 0-5% for Au-Au collisions at E_{lab} = 10 AGeV is shown in Fig. 1. Here, we have shown the 2D plots for net-proton and net-kaon multiplicity distributions from reconstructed tracks (a), incident particles (b) and after unfolding (c). The cumulants are also affected by the volume fluctuations which arises due to the finite centrality width. We apply centrality bin width correction to address such effects on net-proton and net-kaon cumulants within a centrality bin of finite width.

Results and Outlook

Fig. 2 shows the off-diagonal cumulant $\kappa_{p,k}^{1,1}$ as a function of centrality in Au-Au collisions at E_{lab} = 10 AGeV. The open squares show the $\kappa_{p,k}^{1,1}$ for reconstructed tracks (Reco), open circles for incident particles (MC) and solid triangles for the unfolded ΔN_p-ΔN_K multiplicity distributions. The statistical uncertainties on the data points have been calculated using Delta theorem [9]. There is decreasing trend of $\kappa_{p,k}^{1,1}$ as one goes from central to peripheral collision centralities except for top central bins $0-5\%$ and $5-10\%$. The $\kappa_{p,k}^{1,1}$ values for MC and unfolding are in good agreement for all centrality bins which implies that unfolding procedure is able to get back the original ΔN_p-ΔN_K multiplicity distributions. In future, we will extend this study to the other off-diagonal cumulants $\kappa_{p,Q}^{1,1}$ and $\kappa_{k,Q}^{1,1}$ and at other SIS100 energies.

References

[1] Y. Aoki *et al.*, Nature **443**, 675 (2006).

[2] R. V. Gavai and S. Gupta, Phys. Rev. D **73**, 014004 (2006).

[3] V. Koch *et al.*, Phys. Rev. Lett. **95**, 182301 (2005).

[4] A. Bazavov *et al.*, Phys. Rev. Lett. **111**, 082301 (2013).

[5] F. Karsch, Nucl. Phys. A **967**, 461 (2017).

[6] M. Cheng *et al.*, Phys. Rev. D **79**, 074505 (2009).

[7] A. Chatterjee *et al.*, J. Phys. G **43**, 125103 (2016).

[8] S. A. Bass *et al.*, Prog. Part. Nucl. Phys. **41**, 225 (1998).

[9] A. DasGupta, Asymptotic Theory of Statistics and Probability, Published by Springer-Verlag New York, doi:10.1007/978-0-387-75971-5.

[10] G. D'Agostini, Nucl. Instrum. Meth. A **362**, 487 (1995).

[11] T. Adye, Proceedings of the PHYSTAT 2011, CERN–2011–006, pp. 313–318.

[12] P Garg *et al.*, J. Phys. G: Nucl. Part. Phys. **40**, 055103 (2013).

Study of net-proton fluctuations in Au-Au collisions with CBM

S. Samanta, R. Singh, and B. Mohanty
School of Physical Sciences, National Institute of Science Education and Research, HBNI, Jatni - 752050, Odisha, India

Introduction

The Lattice Quantum Chromodynamics (LQCD) calculation suggests a smooth crossover transition from hadronic to a quark-gluon plasma (QGP) phase at high temperature T and small baryon chemical potential μ_B region of the QCD phase diagram [1]. Whereas at high μ_B and low T a first-order phase transition is predicted by various QCD based models [2, 3]. So there must be a critical point (CP) where the first-order phase transition line ends. Several heavy-ion collision experimental program world-wide have been devoted to the investigation of strongly interacting nuclear matter over a wide range of T and/or μ_B. The main goal of these experiments is to map the QCD phase diagram in terms of T and μ_B. The heavy ion collision experiments at the Large Hadron Collider (LHC), CERN and Relativistic Heavy Ion Collider (RHIC), BNL are presently investigating QCD matter at high T and small μ_B region of the phase diagram. To search for the QCD critical point a Beam Energy Scan (BES) program [4] is ongoing at RHIC. The Compressed Baryonic Matter (CBM) experiment [5] at the Facility for Antiproton and Ion Research (FAIR), GSI and the Nuclotron-based Ion Collider Facility (NICA) at JINR, Dubna will study nuclear matter at large μ_B region of the phase diagram. The HADES experiment [6] at the same experimental facility as for CBM will compliment its physics program [7]. The heavy-ion beam will be provided by the SIS100/300 accelerator, where SIS100 is capable of delivering Au beam upto E_{lab} = 11 AGeV ($\sqrt{s_{NN}}$ = 4.7 GeV).

In the search of the QCD phase transition and the speculated critical point, the most reliable way is to study the fluctuations and correlations of conserved charges. Experimentally net-charges N_q ($= N_q^+ - N_q^-$) (q = baryon number B, strangeness number S or electric charge Q) are measured within a finite acceptance in an event-by-event basis. The n^{th} order central moment is defined as

$$\langle(\delta N_q)^n\rangle = \langle(N_q - \langle N_q\rangle)^n\rangle, \quad (1)$$

where $\langle N_q\rangle$ is the mean value of the distribution. The higher order moments $\langle(\delta N_q)^3\rangle$ and $\langle(\delta N_q)^4\rangle$ are very sensitive observable for the search of critical point [8]. In presence of critical point the net-particle distributions are expected to be non-Gaussian.

To characterise a distribution, cumulants are used which have advantage over moments being additive in nature for independent random variables. The cumulants are related to the central moments by the following relations:

$$C_1 = \langle N_q\rangle, \quad (2)$$

$$C_2 = \langle(\delta N_q)^2\rangle, \quad (3)$$

$$C_3 = \langle(\delta N_q)^3, \quad (4)$$

$$C_4 = \langle(\delta N_q)^4\rangle - 3\langle(\delta N_q)^2\rangle^2. \quad (5)$$

Here we have written the definition of cumulants up to order four only. The experimentally measured cumulants are related to the susceptibilities of the conserved charges by the relation [9]

$$C_n = VT^3\chi_q^n, \quad (6)$$

where χ_q^n, V and T are the n^{th} order susceptibility corresponding to conserved charge q, volume and temperature of the system, respectively. Eq. 6 directly connects theoretical calculation with the experimental measurement.

The mean (M_q), variance (σ_q^2), skewness (S_q) and kurtosis (κ_q) of net-charge distribution are related to the different order of cumulants by the following relations,

$$M_q = C_1, \quad \sigma_q^2 = C_2, \quad S_q = \frac{C_3}{\sigma_q^3}, \quad \kappa_q = \frac{C_4}{\sigma_q^4}. \quad (7)$$

The mean, variance, skewness and kurtosis are estimations of the most probable value, width, asymmetry and the peakness of the distribution, respectively.

Analysis details

In this simulation work, we have studied net-proton (which can be used as a proxy for net-baryon) fluctuation in $Au-Au$ collision at the energy $E_{lab} = 10$ AGeV. The simulations have been performed within the CbmRoot framework. Three million minimum bias events generated using Monte Carlo event generator UrQMD [10] are transported through the CBM detector set up `sis100_electron` using GEANT3. The detector configuration `sis100_electron` can be used for both electron and hadron physics simulations and consists of several sub detectors like Micro Vertex Detector (MVD), Silicon Tracking System (STS), Ring Imaging Cherenkov Detector (RICH), Transition Radiation Detector (TRD) and Time-of-Flight Detector (TOF). The MVD is used for the reconstruction of primary vertex of the event. The STS is used for charged particle tracking and momentum information. The charged particles are selected in the pseudorapidity range $1.5 < \eta < 3.8$. The particle identification is performed using TOF detector.

Particle identification

TOF detector provides time of flight (t) information of the charged tracks falling within its acceptance. By using the momentum (p) and length of the track (L) one can calculate squared mass m^2 property of the track using the following formula

$$\frac{1}{\beta} = \sqrt{1 + (\frac{m}{p})^2} = \frac{tc}{L}, \quad (8)$$

where c is the velocity of light. Figure 1 shows m^2 distribution of charged particles in the transverse momentum range $0.2 < p_{\rm T} < 2.0$ GeV/c. Three well separated peaks are clearly visible which corresponds to π, K and proton respectively. The protons and anti-protons are selected using m^2 cut of $0.6 < m^2 < 1.2$ GeV^2/c^4 with purity of more than 96%. We have observed that number of anti-proton is very less compared to that of proton.

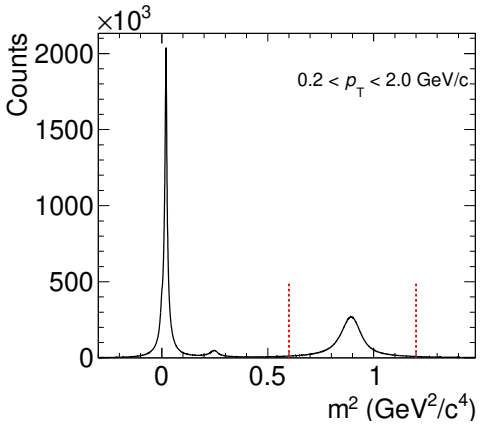

Figure 1: Distribution of squared the mass (m^2) of charged particles in transverse momentum range $0.2 < p_{\rm T} < 2.0$ GeV/c. Vertical dotted lines indicate m^2 region for proton and antiproton selection.

Centrality estimation

The centrality of the collision is determined using the efficiency uncorrected charged particle multiplicity distribution measured using STS. The charged particles are selected using m^2 less than 0.4 GeV^2/c^4 which exclude the protons for multiplicity measurements and avoids auto correlation effects in the measurement. The analysis is done in nine centrality bins (0-5)%, (5-10)%, (10-20)%, (20-30)%, (30-40)%, (40-50)%, (50-60)%, (60-70)% and (70-80)%. The centrality bin (0-5)% corresponds to most central whereas (70-80)% corresponds to the most peripheral collision events.

Results and discussion

We have calculated the cumulants upto 4^{th} order for net proton ΔN_p $(N_p - N_{\bar{p}})$ multiplicity distributions. The protons and anti-protons are counted within the transverse momentum range $0.2 < p_{\rm T} < 2.0$ GeV/c and the rapidity range $1.2 < y < 2.2$. The $y - p_{\rm T}$ acceptance for proton selection in Au-Au collisions at 10 AGeV is shown in Fig. 2. The reconstruction efficiency of protons and anti-protons in different centrality varries between 64 - 69 %. Figure 3 shows the event-by-event reconstructed (without efficiency correction) net-proton multiplicity distributions for different centrality bins.

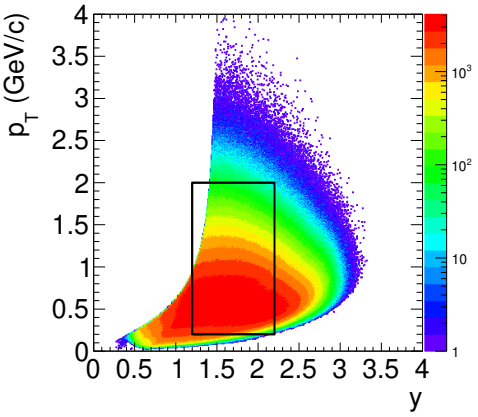

Figure 2: $y-p_{\rm T}$ acceptance for protons in Au-Au collisions at 10 AGeV. The box shows the $y - p_{\rm T}$ region used for the present analysis.

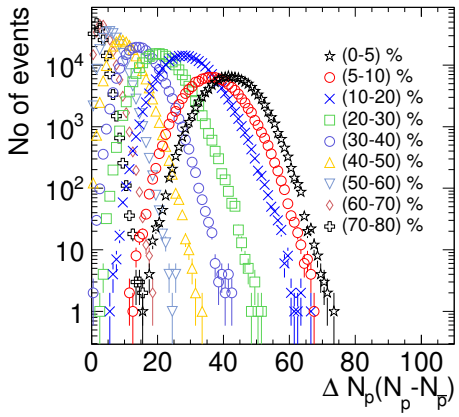

Figure 3: The net-proton multiplicity distributions in different centrality bins in Au-Au collisions at 10 AGeV.

In each centrality bin we then calculate cumulants of net-proton. The finite width of a centrality bin may cause volume fluctuations within a centrality bin. The cumulants need to be corrected for such effects. The centrality bin width corrected cumulants are calculated as

$$C_n = w_r C_{n,r}, \quad (9)$$

where w_r is the weight factor which is the fraction of event

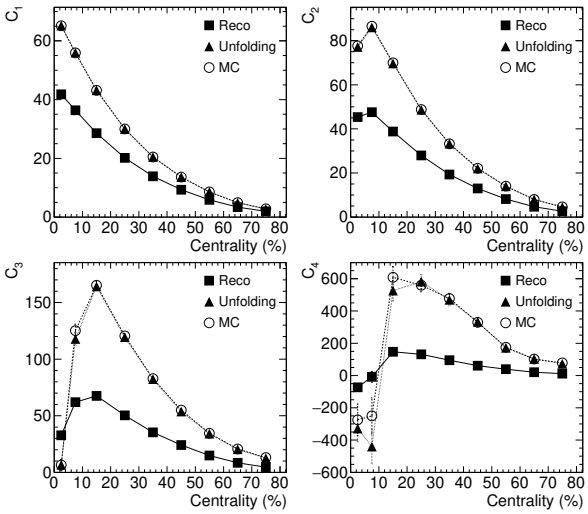

Figure 4: The centrality dependence of cumulants in Au-Au collisions at 10 AGeV. The solid square markers show the centrality bin width corrected cumulants of reconstructed net-proton, open square markers show the cumulants of incident net-proton and solid traingle markers show the cumulants of unfolded net-proton distributions. The cumulants are shown upto 4^{th} order.

in r^{th} multiplicity bin i.e.,

$$w_r = \frac{n_r}{\sum_r n_r}. \tag{10}$$

In Eq. 10, n_r is the number of events in r^{th} multiplicity bin.

The measured cumulants are also affected by the reconstruction efficiencies of the charged particles. We have done this correction using the method of unfolding. For this purpose we use the RooUnfoldBayes algorithm which is based on the Bayes theorem [11]. In this method [12], measured and true number of particles are related by the relation

$$y = Rx, \tag{11}$$

where y and x are the measured and true distributions and R is a response matrix. We have divided the simulated data set in two halves where first half is used to reconstruct the response matrix. The second half of the data set is used for the analysis where this response matrix is used to get the true number of protons and anti-protons from the information of measured (reconstructed) protons and anti-protons. Fig. 4 shows the centrality dependence of cumulants of net-proton upto 4^{th} order. The solid square markers correspond to the centrality bin width corrected cumulants from reconstructed net-proton distributions whereas open circle markers shows the cumulants from incident net-proton. The solid traingle markers show the cumulants obtained after the application of unfolding procedure. Within statistical uncertainties unfolding method is able to reproduce the cumulants of true distributions. As we go from central to peripheral collisions, volume of the collision system (or the number of participants) decreases. Hence, we expect decrease of cumulants from central to peripheral collisions which is indeed observed except for few centrality bins (C_2, C_3, C_4 in 0-5% and C_3, C_4 in 0-5% and 5-10 %). The error bars shown on the data point are statistical only which are estimated using delta theorem approach [13].

We have performed the first physics simulation of net-proton fluctuations in CBM detector setup and the results look promising. In future we want to analyse cumulants upto order six with large statistics and other energies of SIS100. Similar analysis will also be done for net-kaon, net-charge and mixed cumulants.

References

[1] Y. Aoki *et al.*, Nature **443**, 675 (2006).

[2] M. Asakawa and K. Yazaki, Nucl. Phys. A **504**, 668 (1989).

[3] E. S. Bowman and J. I. Kapusta, Phys. Rev. C **79**, 015202 (2009).

[4] L. Adamczyk *et al.* [STAR Collaboration], Phys. Rev. Lett. **112**, 032302 (2014); M. M. Aggarwal *et al.* [STAR Collaboration], Phys. Rev. Lett. **105**, 022302 (2010).

[5] T. Ablyazimov *et al.* [CBM Collaboration], Eur. Phys. J. A **53**, no. 3, 60 (2017).

[6] G. Agakishiev *et al.* [HADES Collaboration], Eur. Phys. J. A **52**, no. 6, 178 (2016).

[7] B. Friman *et al.* (Eds.), *The CBM PhysicsBook*, Lect. Notes Phys. **814**, Springer-Verlag Berlin Heidelberg 2011.

[8] M. A. Stephanov, Phys. Rev. Lett. **102**, 032301 (2009).

[9] F. Karsch and K. Redlich, Phys. Lett. B **695**, 136 (2011).

[10] M. Bleicher *et al.*, J. Phys. G **25**, 1859 (1999).

[11] G. D'Agostini, Nucl. Instrum. Meth. A **362**, 487 (1995).

[12] P Garg *et al.*, J. Phys. G: Nucl. Part. Phys. **40**, 055103 (2013).

[13] A. DasGupta, Asymptotic Theory of Statistics and Probability, Published by Springer-Verlag New York. doi:10.1007/978-0-387-75971-5.

Initial state longitudinal asymmetry in the AMPT model under FAIR – CBM condition

S. Sarkar[1,2], *P. Mali*[1], *and A. Mukhopadhyay*[1]

[1]Department of Physics, University of North Bengal, Siliguri-734013, West Bengal, India; [2]Department of Physics, Siliguri College, Siliguri-734001, West Bengal, India

The geometrical overlapping parts of two colliding nuclei is called the participant region. Even in symmetric (AA) systems the number of nucleons participating in the collision and contributed by either of the colliding nuclei may be unequal, which is attributed to the event to event fluctuation in the positions of these nucleons. This initial state asymmetry in the number of participating nucleons is called the longitudinal asymmetry as it produces a rapidity shift in the participant region on an event by event basis, leading thereby to a forward-backward asymmetry in the rapidity distribution of the hadrons in the final staate. The rapidity is shifted with respect to the center of momentum (CM) frame by an amount

$$y_0 = \frac{1}{2}\ln\frac{A}{B} \tag{1}$$

where A and B are the number of participating nucleons of the two colliding nuclei [1]. Recent studies have shown that the measurement of this shift have facilitated our understanding about the effects of longitudinal asymmetry on various final state observables [2]. Fluid dynamical simulations have established the effects of this asymmetry on the azimuthal anisotropy coefficients, particularly on the directed flow parameter $v_1(y)$ [3]. Let us define the asymmetry in participant nucleon number as

$$\alpha_{\rm part} = \frac{A-B}{A+B},$$

which leads to

$$y_0 = \frac{1}{2}\ln\frac{1+\alpha_{\rm part}}{1-\alpha_{\rm part}} \tag{2}$$

Similarly the spectator asymmetry defined by,

$$\alpha_{\rm spec} = \frac{(N-A)-(N-B)}{(N-A)+(N-B)}$$

is related to the rapidity shift (y_0) as

$$y_0 = \frac{1}{2}\ln\frac{(A+B)(1+\alpha_{\rm spec})-2N\alpha_{\rm spec}}{(A+B)(1-\alpha_{\rm spec})+2N\alpha_{\rm spec}} \tag{3}$$

In this analysis we have generated 10^6 minimum bias Au + Au events at $E_{\rm lab} = 30$A GeV using the AMPT [4] model in its string melting configuration. The Monte Carlo Glauber (MCG) mechanism is employed to compute the different initial state quantities. Fig. 1 shows the centrality dependence of the participant-zone rapidity shift (y_0), the magnitude of which is maximum for the peripheral events

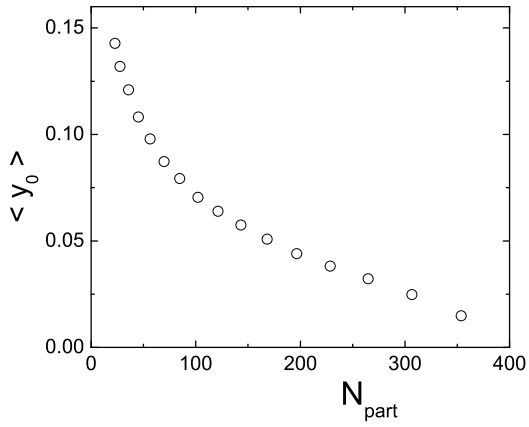

Figure 1: Mean participant-zone rapidity shift $(\langle y_0 \rangle)$ as a function of $N_{\rm part}$.

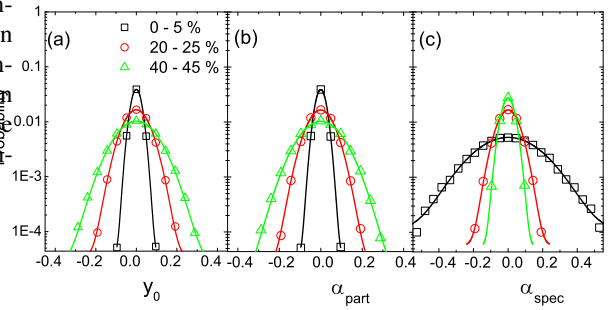

Figure 2: (Color on line) Distribution of (a) participant-zone rapidity shift (y_0), (b) participant asymmetry $(\alpha_{\rm part})$, and (c) spectator asymmetry $(\alpha_{\rm spect})$ for different centrality classes.

and gradually decreases non-lineraly with increasing centrality. This is consistent with the fact that the relative fluctuations in $N_{\rm part}$ are considerably high in peripheral collisions. The variation in y_0 with centrality is found to be stiffer in the peripheral than in the central collisions. The probability distributions of y_0, $\alpha_{\rm part}$, and $\alpha_{\rm spec}$ for different centrality classes are presented in Fig. 2. The width of y_0 distribution is found to be increasing with decreasing centrality which is in agrement with Fig. 1. It is also interesting to note that the nature of $\alpha_{\rm part}$ distribution is almost identical to the y_0 distribution, but not to that of the $\alpha_{\rm spec}$. The $\alpha_{\rm spec}$ distribtion is complimentary to the $\alpha_{\rm part}$ distribtion. The event by event distribution of y_0 against $\alpha_{\rm spec}$ and

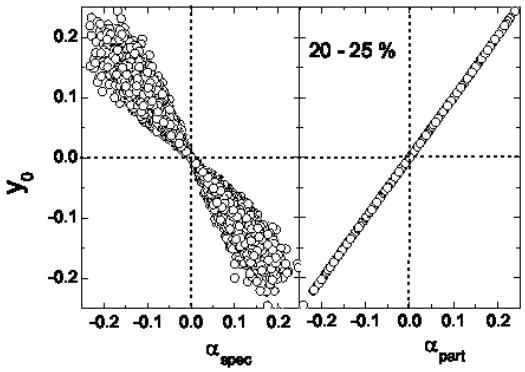

Figure 3: Event by event participant-zone rapidity shift (y_0) as a function of (a) spectator asymmetry $(\alpha_{\rm spect})$ and (b) participant asymmetry $(\alpha_{\rm part})$ for the $20-25\%$ centrality class.

$\alpha_{\rm part}$ for the $20-25\%$ centrality class is presented in Fig. 3. This unveils the exclusive correlation between y_0 and $\alpha_{\rm part}$. The dispersion in eventwise y_0 values at a particular $\alpha_{\rm spec}$ is also established which can be understood in terms of the term $(A+B)$ present in Eq.(3). Fig. 4 shows the

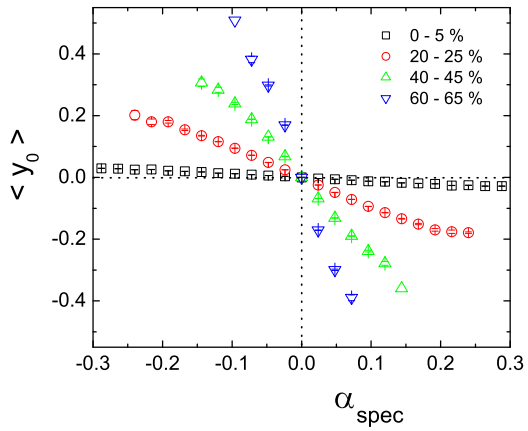

Figure 4: (Color on line) Spectator asymmetry $(\alpha_{\rm spect})$ dependence of the mean participant-zone rapidity shift (y_0) at different centrality classes.

$<\|y_0\|>$	c_1	c_2	c_3
0.0442	0.0504	0.0001	-0.00033
0.0706	0.0868	0.0065	-0.00078
0.0872	0.1052	0.0104	-0.00136
0.1081	0.1307	0.0130	-0.00189
0.1323	0.1505	0.0268	-0.00225

Table 1: Fit parameter values corresponding to different $<|\ y_0\ |>$.

mean rapidity shift (y_0) as a function $\alpha_{\rm spect}$ for different centrality classes. We also intend to scrutinize the effects,

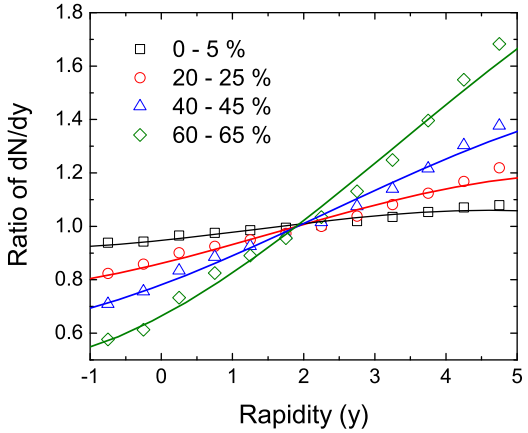

Figure 5: (Color on line) Ratio of dN/dy for events with positive asymmetry $(y_0 > 0)$ and those with negative asymmetry $(y_0 < 0)$ as function of rapidity (y) for different centrality classes. The solid lines are fits to third order polynomial.

if there is any, of the participant-zone rapidity shift on the final state observables. For a preliminary investigation we separate out the events with positive asymmetry $(y_0 > 0)$ and negative asymmetry $(y_0 < 0)$. Respective rapidity distributions (dN/dy) are obtained and their ratios are plotted against the rapidity. The corresponding results at different centrality classes along with a third order polynomial fit is presented in Fig. 5. The linear term in the fitted equation is consistently dominant over the quadratic and cubic terms. The fit parameters at different $(<|\ y_0\ |>)$ corresponding to different centrality class are provided in Table. 1. Our simulation results are very much in qualitative agreement with a HIJING – MCG based similar analysis of Pb+Pb interaction at $\sqrt{s} = 2.76$ TeV [5]. We believe that this kind of investigation on the effects of longitudinal asymmetry will be useful to study the evolution of fireball and to explore the particle production mechanism.

References

[1] S. Acharya *et al.*, Phys. Lett. B **781**, 20 - 32 (2018).

[2] L. P. Csernai *et al.*, Phys. Rev. C **86**, 024912 (2012)

[3] L. P. Csernai *et al.*, Phys. Rev. C **84**, 024914 (2011).

[4] B. Zhang, C. M. Ko, B.-A. Li, and Z.-W. Lin, Phys. Rev. C **61**, 067901 (2000).

[5] R. Raniwala, S. Raniwala and C. Loizides, Phys. Rev. C **97**, 024912 (2018).

Cumulant ratios in the UrQMD model under FAIR - CBM condition

S. Ghosh, P. Mali, and A. Mukhopadhyay
Department of Physics, University of North Bengal, Siliguri-734013, West Bengal, India

The study of cumulants of conserved quantities at FAIR – CBM conditions provide us with a unique opportunity to explore the properties of deconfined QGP state created in the nucleus-nucleus (AB) collision. The intermediate fireballs produced during such collisions are expected to be rich in baryons. Theoretical study predicts that cumulants of different orders and the volume independent cumulant ratios of conserved quantities are proportional to both correlation length and thermodynamic susceptibilities of the fireball medium [1]. It is also found that the particle multiplicity distribution can be described more suitably by the negative binomial distribution (NBD) than the Poisson distribution (PD) [2]. While the PD implies a coherent emission of particles, the NBD pertains to a clan structure. Many sources of correlation like the conservation principles, resonance decays, dynamics of particle production etc. can result in significant deviations from either a pure Poisson type or a negative binomial type of statistics. So it is a worthwhile exerciase to study and compare the results with the predictions of the above mentioned statistical distributions in AB collisions at FAIR energies. Here we present a simulation study of cumulant ratios of the net multiplicity distributions of some conserved quantities as a function of acceptance size in $Au+Au$ interactions at tw different incident beam energies $E_{\rm lab} = 20A$ and $40A$ GeV. The event samples are generated by the Ultra-relativistic Quantum Molecular Dynamics (UrQMD) model [3]. Out of 10^6 minimum bias events we have taken only the $0-10\%$ most central events for our analysis. Mathematically the cumulants $C_{n,N}$ of order n and mulplicity N are defined as

$$\begin{aligned} C_{1,N} &= \langle N \rangle \\ C_{2,N} &= \left\langle (\delta N)^2 \right\rangle \\ C_{3,N} &= \left\langle (\delta N)^3 \right\rangle \\ C_{4,N} &= \left\langle (\delta N)^4 \right\rangle - 3\left(\left\langle (\delta N)^2 \right\rangle\right)^2 \end{aligned} \quad (1)$$

Once we have the definitions of cumulants, the moments of the distributions like the mean M, the variance σ^2, the skewness S, and the kurtosis κ are denoted respectively by,

$$M = C_{1,N}, \;\; \sigma^2 = C_{2,N}, \\ S = \frac{C_{3,N}}{(C_{2,N})^3/2}, \;\; \kappa = \frac{C_{4,N}}{(C_{2,N})^2} \quad (2)$$

$\delta N = N - \langle N \rangle$ denotes the deviation from mean multiplicity. The cumulant ratios are constructed to elliminate the trivial volume dependence of the cumulants and are expressed as,

$$S\,\sigma = \frac{C_{3,N}}{C_{2,N}}, \;\; \kappa\,\sigma^2 = \frac{C_{4,N}}{C_{2,N}} \quad (3)$$

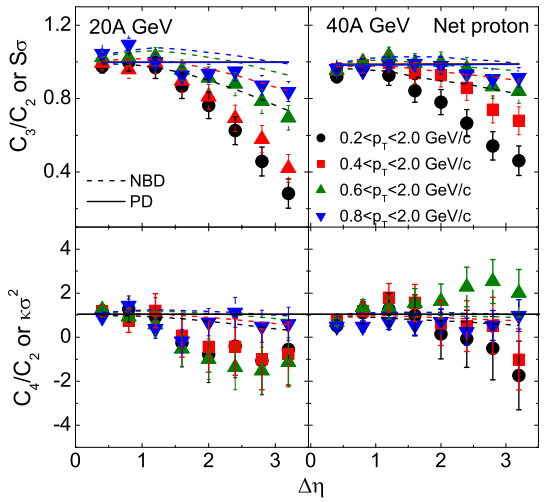

Figure 1: (Color on line) Cumulant ratios of net-proton distribution as a function of $\Delta\eta$ in various p_T windows.

To analyze the simulated data in a large centrality bin, one should modify the cumulant values according to the centrality-bin-width correction method as proposed in [4]. One should also eliminate the effect of auto-correlation among the particles. The statistical uncertainties are calculated by using the Delta theorem [5]. In Fig.1 we have shown the $\Delta\eta$ dependence of the cumulant ratios C_3/C_2 and C_4/C_2 of the net-proton distribution in different p_T windows. The pseudorapidity intervals $(\Delta\eta = |\eta - \eta_0|)$ are chosen symmetrically about the centroid of the respective overall η-distribution. At FAIR energies the antiproton yeild is largely influenced by the effect of baryon stopping. Now at higher p_T and in large $\Delta\eta$ a decreasing trend in the cumulant ratios is observed at both energies. In most of the cases the ratio remains below unity, while the Poisson expectations of these cumulant ratios is unity. Neither PD nor NBD can satisfactorily reproduce the simulated results. The deviations from both PD and NBD are more prominent at lower energy and at higher acceptance size. At $E_{\rm lab} = 20A$ GeV the dominance of baryons over antibaryons is perhaps stronger than that at $E_{\rm lab} = 40A$ GeV. The results are almost similar to that of [6]. For the net-

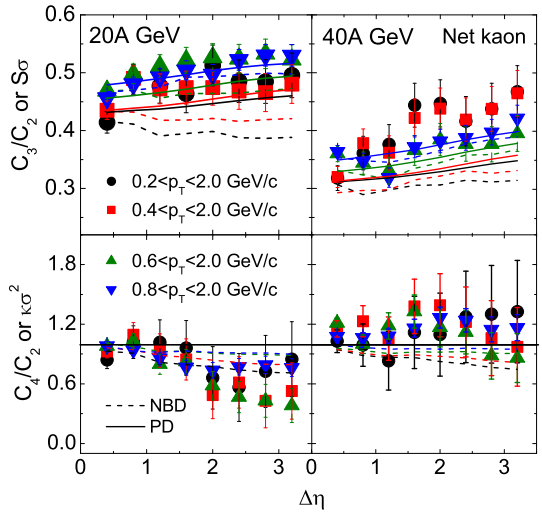

Figure 2: (Color on line) Cumulant ratios of net kaon distribution as a function of $\Delta\eta$ for various p_T windows.

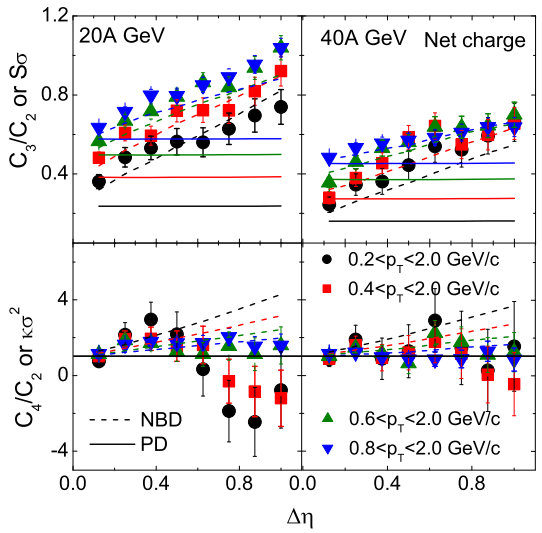

Figure 3: (Color on line) Cumulant ratios of net charge distribution as a function of $\Delta\eta$ for various p_T windows.

kaon distribution however we observe a completely different behaviour. It is implicitly assumed that the total strangeness production at FAIR energies would be in the form of kaons. In this case one can not just ignore the contribution of anti-kaons. The Poisson expectation of C_3/C_2 ratio is not equal to unity like it was in the case of protons. In Fig.2 we have plotted the variation of C_n ratios of the net kaon distribution as a function of accepatnce window size. $S\,\sigma$ values increases almost linearly with $\Delta\eta$. Corresponding PD predictions, though insufficient, but are closer to the simulated results than the NBD predictions. The nature of $\kappa\,\sigma^2$ plot on the other hand is a little bit erratic. We observe a decreasing trend at $20A$ GeV energy, and an increasing one at $40A$ GeV. In this regard both NBD and PD expectations significantly deviate from the simulated data, which however are associated with large statistical errors. Finally in Fig.3 we have plotted the $\Delta\eta$ dependence of the C_n ratios for the net charge distribution. We have chosen a smaller η coverage here for better description of the shape of the netcharge distribution. The $S\,\sigma$ values show an increasing trend similar to that of the net kaon distribution, which is also in accordance with the NBD prediction. However PD miserably fails to describe that nature. For almost all cases Poisson prediction remains flat with increasing $\Delta\eta$. At lower energy the deviations from both NBD and PD are more prominent. In this case the C_4/C_2 ratio behaves differently, the values are associated with large errors, they fluctuate erraticaly around the Poisson prediction, and NBD too cannot replicated the simulated results. The deviations are larger in higher acceptance windows. The effect of both global conservation principle and resonance decays become more important as the phase space coverage increases. In most of the occassions the NBD prediction better matches the simulated results than the PD prediction. This preliminary simulation study of cumulants and their ratios of distributions of conserved numbers reveals an expected behaviour of the observables concerned. However to compare the model results to the real experimental data one has take into account different correlation factors, the limited detector acceptance and finite detector efficiency.

References

[1] C.Zhou et al, arxiv :1703.09114v2[nucl.ex] (2017)

[2] T.J. Tarnosky and G.D. Westfall, Phys. Lett. B **724** 51 (2013)

[3] S. A. Bass et al, Prog. Part. Nucl. Phys. **41**, 255 (1998)

[4] X. Luo, J. Xu, B. Mohanty and N. Xu, J. Phys. G **40**, 105104 (2013)

[5] X. Luo, J. Phys. G **39**, 025008 (2012)

[6] S. He and X. Luo, Phys.Lett. B **774** 623 (2017)

FAIR Phase-0 Activities

Start of mCBM Commissioning

C. Sturm[1], D. Emschermann[1], N. Herrmann[2] for the CBM collaboration
[1]GSI, Darmstadt, Germany; [2]Ruprecht-Karls-Universität Heidelberg, Germany

The Compressed Baryonic Matter experiment (CBM) at FAIR is consequently designed to measure nucleus-nucleus collisions at unprecedented interaction rates up to 10 MHz which will allow to study extremely rare probes with high precision. To achieve this high rate capability CBM will be equipped with fast and radiation hard detectors, readout by a free-streaming data acquisition system transporting data with up to 2 TB/s to a large scale computer farm which provides event reconstruction and first level event selection.

In 2017 and 2018 we have constructed the experimental site as well as the first stage of a CBM full-system test-setup at the SIS18 facility of GSI/FAIR called *mCBM@SIS18* ("mini-CBM" or short mCBM), depicted in the upper panel of Fig. 1. The installation site of mCBM is the detector test area named cave-D (see Fig. 1) situated at the beam entrance of the experimental area cave-C (HTC) hosting the nuclear structure experiment R^{3}B. Although the space is very limited in the HTD area, the compact mCBM setup measuring a full length of about 5 m will fit into the HTD cave.

The primary aim of mCBM is to develop, commission and optimize (i) the free-streaming data acquisition system including the data transport to a high performance computer farm inside the GreenITCube, (ii) the online track and event reconstruction and event selection algorithms and (iii) the offline data analysis as well as the controls software package. mCBM will comprise final prototypes and pre-series components of all CBM detector subsystems and their read-out systems. Hence, the setup offers additional high-rate detector tests in nucleus-nucleus collisions under realistic experiment conditions. Commissioning and running mCBM will complete our knowledge on proper functioning as well as on the performance of the CBM detector systems and their associated Front-End Electronics (FEE) before the final series production starts. The experiences gained during the complete mCBM campaign will significantly shorten the commissioning period for the full CBM experiment at SIS100.

As depicted in Fig. 1 the mCBM test-setup is positioned downstream a solid target under a polar angle of about 25° with respect to the primary beam. mCBM does not feature a magnetic field, and, therefore, will measure charged particles produced in nucleus-nucleus collisions traversing the detector stations following straight trajectories. In the final configuration, the mCBM tracking system comprises 2x STS (mSTS, see [7]), 3x MUCH (mMUCH) [8] and 4x TRD (mTRD) stations in total 9x tracking layers which provide redundant position information and allow to perform tracklet searches.

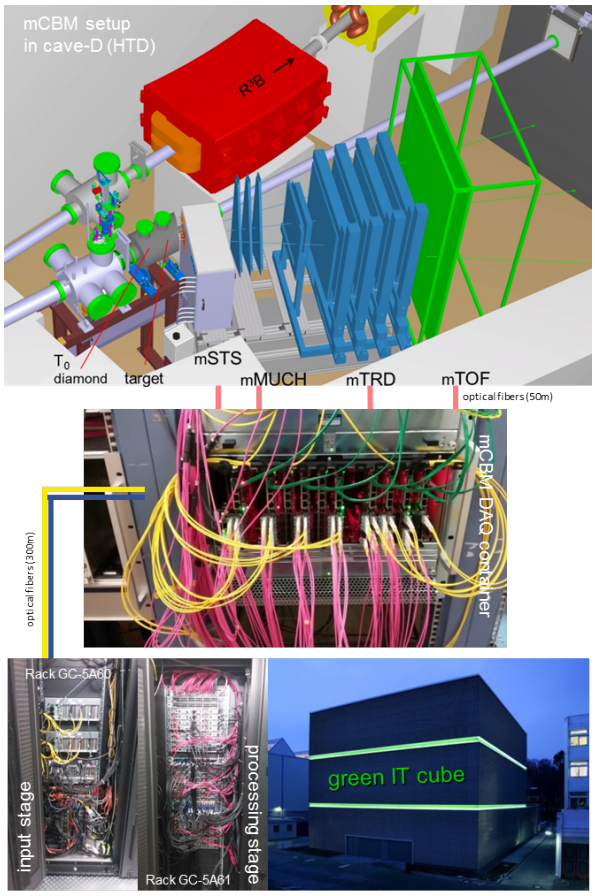

Figure 1: The upper picture shows the engineering design of the mCBM setup inside cave-D (HTD). The middle and lower pictures sketch the data transport path, via the first FPGA layer (middle picture: AFCKs, MicroTCA crate) located inside the DAQ container, connected by optical fibers with the input as well as processing stage mounted inside the Green-IT-Cube (lower panels).

mCBM includes a high-resolution time-of-flight system consisting of a fast and 8-fold segmented diamond counter (vertical strips, 2 mm width) for time-zero (T0) determination in front of the target as well as a TOF stop wall (mTOF) [9]. An aerogel type RICH detector will be placed as the mRICH subsystem behind the mTOF detector and deliver a second measurement of the particle velocity in a selected acceptance window [11]. A small calorimeter (mECAL) will also be mounted behind the mTOF cover-

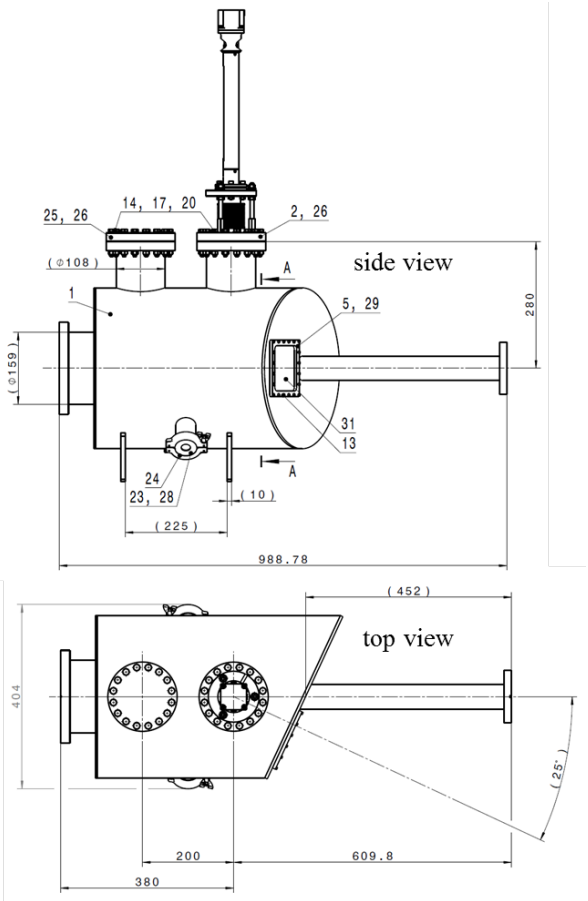

Figure 2: Design of the new mCBM target chamber, manufactured at GSI.

ing a reduced acceptance. Additionally, a PSD prototype-module (mPSD, see [12]) will be positioned directly under the beam pipe, 5° tilted relative to the beam axis while pointing to the target.

The two mSTS stations and the 4^{th} layer of mTRD are centered in x and y. For tracks passing the active area of the mSTS, mMUCH, mTRD and mTOF subsystems the covered Θ_{lab} range results to $8° - 32°$. The overall acceptance is limited by the mSTS, which is located very close to the beam pipe [7] and cannot be moved further upstream.

In a later stage MVD stations (mMVD) will be added into the test-setup enabling a high-precision vertex reconstruction. However, the initial configuration of the mCBM test-setup is rather versatile and can be variably adapted according to the needs. Therefore, the detector stations are mounted on sliders of a rail system on top of the mounting table.

Experimental site

As illustrated in Fig. 1, the incoming beam will be either transported to the R^3B experiment or deflected to the mCBM setup by a switching magnet (dipole magnet)

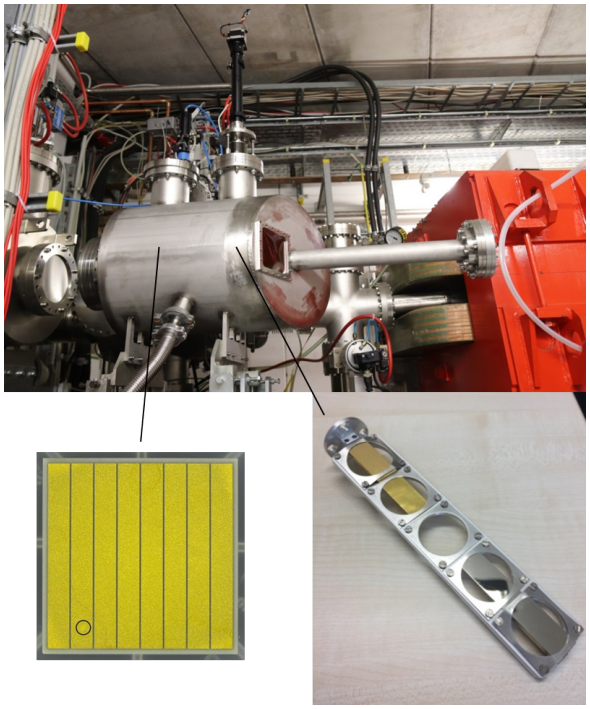

Figure 3: Photograph of the new mCBM target chamber, equipped with a five-fold target ladder (right) and a 8x strip diamond T0 counter (left). The width of the 8x vertical strips of the T0 detector measures to 2 mm each.

mounted directly in front of cave-C/cave-D carrying the name HTD-MU1 in GSI's nomenclature. In order to exploit the full beam energy range of SIS18 the HTD-MU1 vacuum chamber had been exchanged. Hence, beams are now bent on trajectories with a radius of $\rho = 11.25$ m corresponding to an effective deflection angle of 8.0°. Setting the magnetic induction of HTD-MU1 to the maximum value of 1.6 T the modified HTD beamline can now be operated with the maximum magnetic SIS18 rigidity of about 18 Tm. The modified HTD beamline had been successfully commissioned during the machine engineering runs in November and December 2018.

Fig. 2 shows the design of the new mCBM target chamber manufactured at GSI, see photograph Fig. 3. The target chamber hosts the five-fold target ladder (Fig. 4 and Fig. 3) as well as the diamond T0 counter mounted 20 cm upstream the target. The five slots of the vertically aligned target ladder are filled with:

2.5 mm	Au
0.25 mm	Au
	empty
0.4 mm	Ni
4.0 mm	Ni

targets (top to bottom), corresponding to either approx. 10% or 1% interaction probability in a symmetric collision. With a step motor the target position can be controlled re-

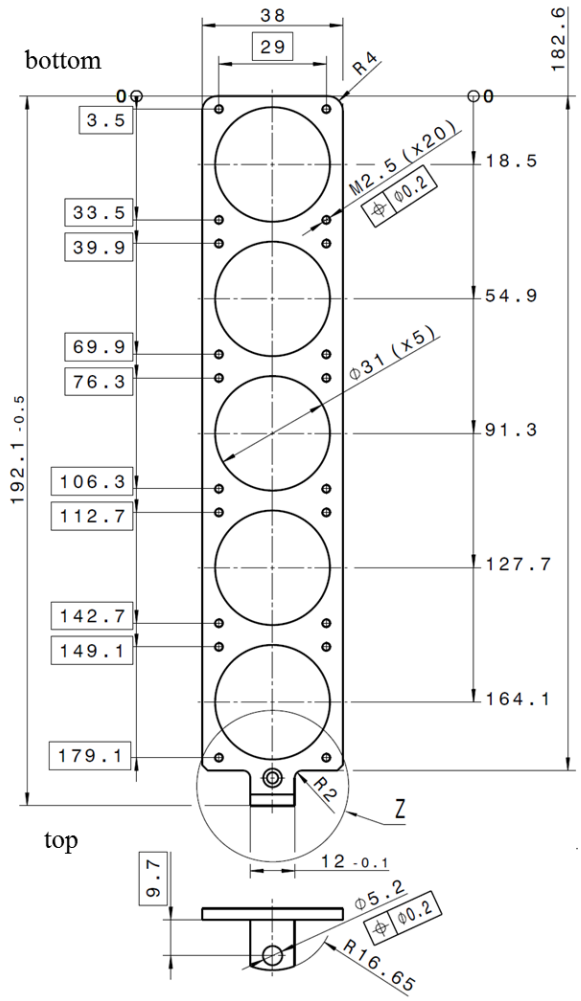

Figure 4: Design of the 5-fold target ladder.

motely.

The ultra-fast, 8-fold segmented diamond T0 detector (2 mm strip width) (see Fig. 3) provides the time-zero (T0) of the collision as well as delivers valuable information for beam monitoring. The latter turned out to be important as well since the HTD beamline could not be sufficiently equipped with beam diagnostics for the first mCBM commissioning campaign. The T0 detector is readout by the TOF read-out electronics and therefore included into the TOF data transport chain.

First commissioning with beam

The first commissioning test has been performed in December 2018 during the machine engineering runs while the main commissioning run had been scheduled for March 2019. Hence, the very first beam tests in December 2018 aimed to commission the common DAQ system and identify open issues therein. The corresponding mCBM setup is depicted in Fig. 5 and shown in Fig. 6:

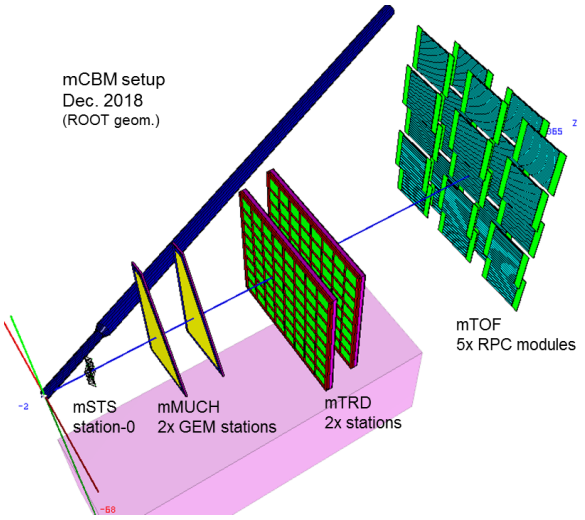

Figure 5: ROOT geometry of the mCBM test setup (ROOT geometry) at the HTD cave as of December 2018 (beam: left to right).

Figure 6: Photography of the mCBM setup as of December 14, 2018 (beam: right to left).

- The first station (station-0) of the mSTS subsystem had been equipped with 2x modules [7] comprising front-end ASICs STS-XYTER v2.0. The next generation STS ASIC STS-XYTER v2.1 has been delivered in January 2019 and will come into operation during the upcoming beam tests in 2019 and subsequent campaigns.

- Two GEM counters of the mMUCH system had been mounted and partially readout with front-end boards FEB-B equipped with front-end chips of type MUCH-XYTER v2.0 [8]. A dedicated MUCH front-end board equipped with the front-end ASIC MUCH-XYTER v2.1 is under development.

- Two mTRD stations had been mounted providing each

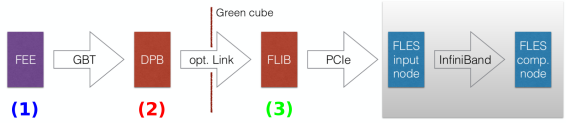

Figure 7: Realized mCBM readout chain for the first commissioning campaign, based on DPB and FLIB. The mCBM subsystems are equipped with individual front-end electronics FEE (1). These front-ends are interfaced by the GBTx ASIC, which forwards the detector data via optical GBT link. All GBT links are received by the DBP layer located at 50 m distance in the DAQ container (2). The DPB is a FPGA based board which allows for subsystem specific pre-processing of the arriving data stream. A long distance optical link connects the DPB output to the FLIB board installed in the FLES input node in the Green IT Cube (3).

horizontal or vertical position information. Although the MWPCs of both mTRD stations had been fully operational the data transport through the GBTx ASICs failed due to open issues of the TRD DPB firmware which is why the mTRD data could not be included into the common data stream. The preparation for future beam tests is ongoing [10].

- All five supermodules of the mTOF subsystem had been fully operational containing 5x RPC counters each, in total 1600x RPC electronic channels had been readout [9]. The mTOF subsystem has been later reconfigured into a supermodule double and a triple stack enabling internal tracklet search as well as detailed efficiency studies.

Fig. 7 sketches the DAQ system and data transport which has been realized for the first commissioning campaign. The detector stations are equipped with readout electronics containing ultra-fast and radiation-tolerant ASICs as front-end chips (1). During the commissioning runs the mCBM detector front-ends have been time-synchronized to the nanosecond level by a mTOF timing module (CLOSY) as an interim solution. A final, central Timing and Fast Control (TFC) system is under development. The detector front-end digitizes signals above threshold and assigns a time stamp to the hit. This data is then forwarded via an electrical (copper) connection to the GBTx readout boards, CERN GBTx-based radiation-tolerant data aggregation units. The electrical signals acquired through a large number of e-links are converted and merged into an optical GBT link operating at 4.48 Gbit/s.

Further down-stream, the data streams are handled by Data Processing Boards (DPB) (2) containing powerful FPGAs and are forwarded via FLES Input Boards (FLIB) (3), a PCIe based FPGA board, to a large-scale computer farm which will in a later stage serve as a First-Level Event Selector (FLES) performing on-line track and event reconstruction and selection.

Thanks to the colleagues from the R^{3}B experiment, the mCBM teams could start the preparation of the first commissioning campaign as well as data taking during the machine engineering runs in December 2018 using a part of the R^{3}B counting house. The photography of Fig. 8 shows the shift crew during the last night shift in December 2018. Shortly after, the construction of the mCBM control room has been completed.

Figure 8: Shift crew during data taking on December 14, 2018.

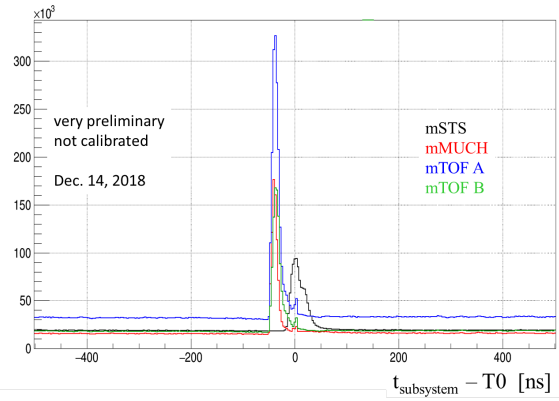

Figure 9: Time correlations obtained as preliminary results from the first common, synchronized data transport of the subsystems mSTS, mMUCH and mTOF (2x mTOF systems) during commissioning with beam. Data has been taken on December 14, 2018, run-id 48.

During the engineering runs in December 2018 a common, synchronized data transport of the installed detector subsystems mSTS, mMUCH and mTOF could be successfully established for the first time. As a first, (very) preliminary result, time correlations between the synchronized data streams of the detector subsystems are shown in Fig. 9 plotting time differences to the T0 measurement. The general time-offset of the detector subsystems has been subtracted within the corresponding unpacker, no further calibration has been applied. Fig. 9 includes data taken within two beam spills, in total about 10 s. Event building has

not been performed. Incident beam had been ^{107}Ag(45+) with 1.2 AGeV kinetic projectile energy bombarded on a 0.25 mm Au-Target.

Next steps and perspectives

The main commissioning beam time in 2018/2019 has been scheduled for March 2019. Major goal is to identify both time and spatial correlations between the mCBM subsystems mSTS, mMUCH, mTOF and mRICH. Hence, substantial software developments regarding the mCBM data analysis such as event building, calibration as well as detector specific tasks have to be made.

Equally important is the completion of the detector subsystems. The next steps in 2019 towards the data campaign in 2020 are:

- production of new mSTS modules for station-0 and station-1 incl. upgrade to the latest (final) version of the read out electronics,
- upgrade of the mMUCH read out electronics to the final version, fully read-out of at least 2x GEM modules,
- solving the DPB firmware issues of the mTRD subsystem and upgrading to the final read-out electronics,
- completion of the mRICH subsystem and integration of the FPGA TDCs chain into the (m)CBM data transport, first tests with beam are scheduled for March 2019, and
- integration and completion of the mPSD subsystem (FPGA TDCs chains).

Furthermore, the noise level of the mSTS and mMUCH subsystems has to be improved as well as the time-synchronization of the mMUCH stabilized. A major DPB firmware revision for all subsystems may become necessary, especially in view of the migration to a Common Readout Interface (CRI) which merges the two FPGA layers DPB and FLIB (see 7 and next paragraph). To test and verify the modifications as well as new hard- and firmware dry runs are going to be scheduled, starting from fall 2019 up to the 2020 data campaign. Additional beam tests are foreseen during the machine engineering runs in November and December 2019.

On the road towards the full CBM DAQ system the mCBM DAQ system will be deployed in two phases. During phase I in the years 2019 – 2020, mainly the commissioning phase of mCBM, the GBTx-based subsystems (mSTS, mMUCH, mTRD and mTOF) are read out using already available readout chains based on existing prototype implementations of DPB and FLIB, see Fig. 7. As current prototype hardware, an AMC FMC Carrier Kintex (AFCK) board [14] is used for the DPB, a HiTech Global HTG-K700 PCIe board for the FLIB. Both boards are based on a Xilinx Kintex-7 FPGA.

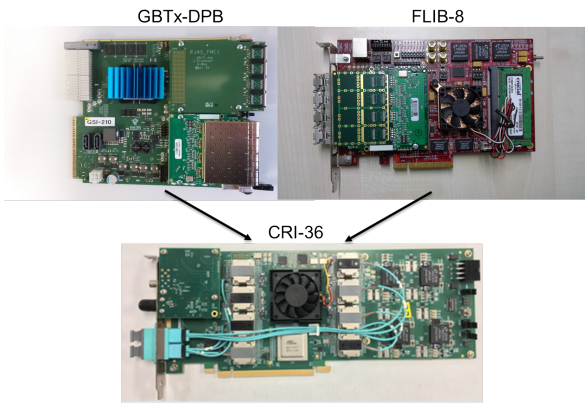

Figure 10: Upgrade of the mCBM DAQ scheduled for 2019 and 2020 : DPB and FLIB will be replaced by a prototype of the Common Readout Interface (CRI).

In phase II, DPB and FLIB will be replaced by a prototype of the Common Readout Interface (CRI) (see Fig. 10) in the FLES input stage, as it is foreseen for the CBM experiment. A small number of CRIs will be delivered in 2019, tests incl. necessary firmware adaptations start in fall 2019 and the main migration steps will be initiated after the 2020 data taking.

The data transport into the GreenITCube as depicted in Fig. 1 and Fig. 7 has been successfully established and tested in 2018. While the input nodes act as data server and storage during the first commissioning in 2018 and 2019 first simplified reconstruction and selection tasks are foreseen for the data campaign in 2020.

All the background rejection strategies necessary to reconstruct rare probes with CBM at SIS100 can be prepared and exercised with mCBM. In addition, if the technical goals of mCBM are achieved, a measurement of the Λ production excitation function should become feasible. This was not yet measured in the SIS18 beam energy range thus offering a unique opportunity to contribute to world data, although the covered phase space is limited and therefore systematic errors become large when extrapolating to unmeasured regions.

The successful implementation and demonstration of the technical capabilities would also open the road to more relevant physics observables like the measurement of light hypernuclei. The beam time request for more physics oriented observables will be placed in the next beamtime period 2021 – 2022, once the preliminary results are supporting the high expectations.

References

[1] J. Heuser, W. F.J. Müller, V. Pugatch, P. Senger, C. J. Schmidt, C. Sturm and U. Frankenfeld, Technical Design Report for the CBM Silicon Tracking System (STS), GSI-2013-05499, http://repository.gsi.de/record/54798

[2] S. Chattopadhyay, Y. P. Viyogi, P. Senger, W. F.J. Müller and C. J. Schmidt, Technical Design Report for the

CBM : Muon Chambers (MuCh), GSI-2015-02580, https://repository.gsi.de/record/161297

[3] C. Höhne et al., Technical Design Report for the CBM Ring Imaging Cherenkov Detector (RICH), GSI-2014-00528, http://repository.gsi.de/record/65526

[4] C. Blume et al., Technical Design Report for the CBM Transition Radiation Detector (TRD), to be published

[5] N. Herrmann et al., Technical Design Report for the CBM Time-of-Flight System (TOF), GSI-2015-01999, https://repository.gsi.de/record/109024

[6] F. Guber and I. Selyuzhenkov, Technical Design Report for the CBM Projectile Spectator Detector (PSD), GSI-2015-02020, https://repository.gsi.de/record/109059

[7] H. R. Schmidt, J. M. Heuser and the CBM STS working group, Silicon Tracking System – Summary,
C. Simons et al., Assembly of modules for mSTS applying complete quality assurance,
J. Heuser et al., Assembly and commissioning of the mSTS detector for mCBM startup,
(this) CBM Progress Report 2018

[8] A. Kumar et al., Installation, commissioning and testing of mMUCH modules in the mCBM experiment,
A. Kumar et al., Fabrication of Mv2 module for mCBM experiment and first test with optocoupler based HV biasing,
V.S. Negi et al., Low Voltage and sensor control system for m-CBM Experiment,
(this) CBM Progress Report 2018

[9] I. Deppner , N. Herrmann , and the CBM TOF working group, TOF - Summary,
Q. Zhang, I. Deppner, and N. Herrmann, The first beam test of mTOF at GSI,
Ph. Weidenkaff et al., Hitbuilding and Calibration of CBM-ToF detectors in the StRoot-Framework for Phase-0 activities,
(this) CBM Progress Report 2018

[10] C. Blume and the CBM-TRD working group, Summary on the TRD project,
A. Bercuci et al., FEE readiness of Bucharest TRD chamber for mCBM,
A. Bercuci et al., Data format and long term tests for FASP/GETS FEE in view of mCBM integration,
A. Bercuci et al., Realistic response of the Bucharest TRD for mCBM simulations at top rates,
(this) CBM Progress Report 2018

[11] T. Geßler et al., Status and plans for the mRICH read-out chain, (this) CBM Progress Report 2018

[12] F. Guber, Projectile Spectator Detector - Summary,
F. Guber et al., Status of mPSD front-end and read-out electronics development,
A. Senger, Radiation damage and activation of CBM-PSD modules after use in FAIR-Phase0 experiments,
(this) CBM Progress Report 2018

[13] M. Prokudin et al., Simple event building for mCBM, (this) CBM Progress Report 2018

[14] W.M. Zabołotny and G. Kasprowicz, ”Data processing boards design for CBM experiment”, Proc. SPIE 9290 (2014) 929023, doi:10.1117/12.2073377

The HADES RICH detector - getting ready for first beam

C. Pauly[1], M. Dürr[2], M. Faul[4], J. Förtsch[1], J. Friese[5], C. Höhne[2,4], K.-H. Kampert[1], S. Lebedev[2], J. Michel[3], J.-H. Otto[2], V. Patel[1], D. Pfeifer[1], E. Schwab[4], M. Traxler[4], C. Ugur[4], A. Weber[2], and P. Zumbruch[4]

[1]Bergische Universität Wuppertal; [2]Justus-Liebig Universität Giessen; [3]Göthe-Universität Frankfurt; [4]GSI Darmstadt; [5]Technische Universität München

In 2018, the HADES RICH group could finally assemble the upgraded HADES RICH photon detector after several years of preparations, prototype tests [1] and electronic development. The key concept of this upgrade is the exchange of the old MWPC based photon detector with a modern photomultiplier readout using a part (40 %) of the Hamamatsu H12700 Multianode PMTs recently obtained for the CBM RICH detector. Motivation and goals of this update have been discussed previously [2, 3]. In order to make optimum use of the MAPMTs with respect to efficiency and timing, the new, fully FPGA based DIRICH readout chain has been developed [4] and built as a joint effort of GSI electronic department and Wuppertal university.

Completion of the detector upgrade was originally anticipated for Autumn 2018, just in time for a scheduled 4 week HADES production run Ag+Ag@1.58A GeV. Delays in the accelerator beam commissioning provided a few months of extra time which turned out vital for the successful completion of the upgrade. The upgraded HADES RICH detector is taking data right now since end of February 2019, with very promising first results.

Mounting the new photon detector

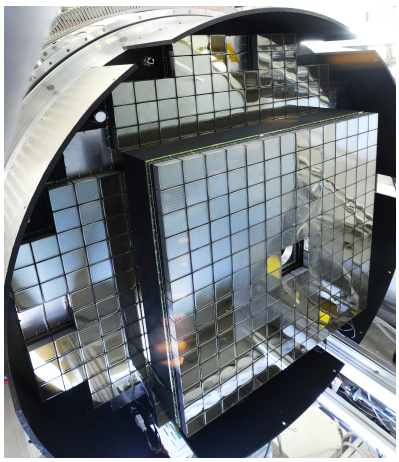

Figure 1: Photograph of the HADES RICH photon detector with most of the 428 Hamamatsu H12700 MAPMTs already mounted (Photo: G. Otto, GSI).

Figure 1 shows a photograph of the new HADES RICH photon detector, shortly before closing the detector. Most of the 428 Hamamatsu H12700 MAPMTs are already mounted, with only few outer PMTs missing. The sensors are arranged in 3x2 MAPMT readout modules (plus few 2x2 modules), with the readout electronic front-end cards sitting outside of the photon detector, directly backwards of the MAPMTs. A multilayer backplane PCB is providing all analog and digital interconnections between PMTs and front-end cards, and at the same time serves for high-voltage and power distribution.

The individual backplanes are mounted on an aluminum carrier frame, providing a gas tight seal of the radiator and PMT volume towards the outside. The inner region with 14x14 MAPMTs is slightly elevated in order to better match the focal plane of the spherical HADES RICH focusing mirror (curvature radius 0.87 m only).

The most inner MAPMTs were coated with a p-Terphenyl based wavelength shifter (WLS), in order to further enhance the photon yield under small scattering angles where the Cherenkov photon yield is small due to short path length in the radiator gas. The use of WLS has been studied extensively before [5] for usage in the CBM RICH detector, its application in the HADES RICH also serves as a final test under realistic conditions.

The photon detector is operated in the fringe field region close to the HADES superconducting magnet. Cylindrical soft iron shields surrounding the PMT plane help to reduce the magnetic field in the region of the MAPMTs to acceptable values (2 mT at maximum magnet current). The magnetic field, as well as temperature of the radiator gas and backplanes, is measured using custom sensor boards mounted below- and close to the MAPMTs.

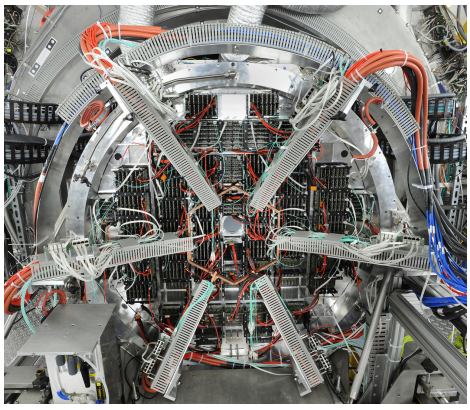

Figure 2: Photograph of the electronic readout modules mounted backwards of the PMTs (Photo: G. Otto, GSI).

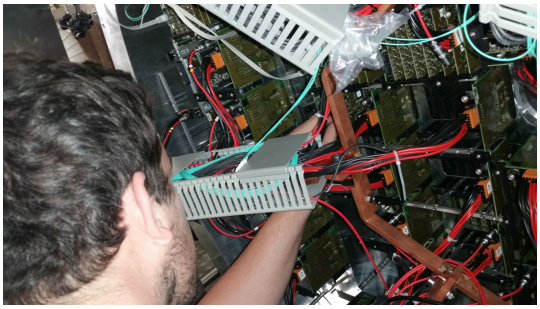

Figure 3: Close view of the LV supply arms and copper grounding ring, and of the mounting structures for individual readout modules.

Figure 2 shows the outside of the new photon detector with all readout front-end boards mounted. Signals of each MAPMT are digitized by two DIRICH front-end cards with 32 channels each, providing precise leading- and trailing edge time measurement. The Time-over-Threshold information is useful to suppress background and capacitive cross talk from neighboring PMT pixels [6], and serves as an amplitude measurement.
Data from 12 DIRICH modules on each backplane are merged by the data combiner module, and then transferred via a single optical link to the data hubs. A dedicated power module on each backplane serves for both low-voltage supply of all modules, as well as for high-voltage distribution to the PMTs. Each 6 MAPMTs on a backplane share a common HV supply channel, requiring a careful gain matching of all installed MAPMTs.
The original design intended to use DC-DC converters on each power module in order to provide all required voltages (1.1V, 1.2V, 2.5V and 3.3V) from a single 48V supply line. Prototype tests however revealed a significantly increased noise level despite very careful circuit- and PCB design. An external LV powering scheme was therefore used in the final design. A well defined grounding scheme is essential in view of the large supply currents at low voltage (up to 200A per sector). A central copper grounding ring, visible in Figure 3, provides a common GND potential for all floating LV power supplies. Total power dissipation of the readout electronics is around 2.5 kW, cooling is achieved using forced air flow (fans).

First beam Nov' 2018

After final assembly of the detector during summer 2018, a first commissioning beam (argon on silver target) was provided by SIS 18 in November 2018, which turned out to be vital for the success of the detector upgrade.
Initial data after first start up of the photon detector and readout looked very promising. Figure 4 (left) shows the single photon dark rate (in Hz, without beam) as detected by each of the 27k readout pixels. Dark rates in the order of 20-50 Hz were slightly higher than expected, but still tolerable. However, after first beam was focused on the

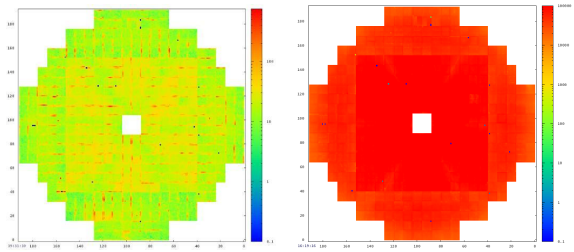

Figure 4: Hit rates (in Hz) on each of the 27k readout Pixels without beam (left) and with beam on target (right). Green: $\sim$20 Hz, red: $>$100 kHz

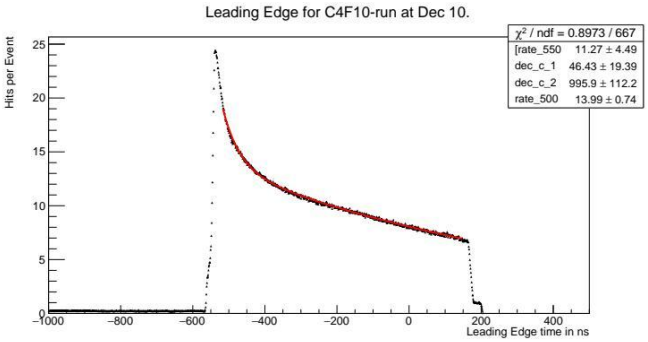

Figure 5: Leading edge time distribution with respect to the trigger for data taken with the CaF_2 window still in place.

target, the second impression was alarming: The observed pixel rates on the PMTs were enormous, up to MHz per pixel at moderate intended target interaction rates of 10-50 kHz. This is already more than expected for the CBM RICH operation at maximum interaction rates of 10 MHz, and would lead to premature aging of the MAPMTs and large non-coincident background.
The reason for this large amount of light was quickly understood when looking at the leading edge timing distribution, shown in Figure 5. In the triggered PMT readout, the prompt signal contribution at t=-550 ns is followed by a slow exponential decay with a measured decay constant of τ=995 ns, which fits well the optical scintillation properties of undoped, pure CaF_2 [7].
In the original HADES RICH detector design, a monocrystalline CaF_2 window was separating the radiator volume (C_4F_{10} gas) from the MWPC photon detector volume (operated with CH_4 gas). Scintillation of this CaF_2 window caused no problems with the old photon detector (sensitive in the deep-UV range below 160 nm), but turned out to be crucial in view of the blue-sensitivity of the new MAPMTs. Scintillation of both C_4F_{10} [8], and in particular of the CaF_2 window was expected before, but the magnitude of scintillation light from the window was underestimated and not evident from simulations.

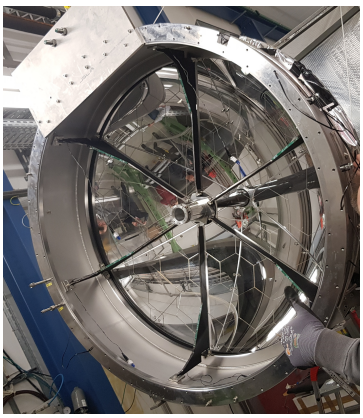

Figure 6: View of the open HADES RICH radiator vessel with the multi-hexagon-segmented CaF_2 window still mounted in front of the focusing mirror.

Removing the CaF2 window

Removing the CaF_2 window in front of the PMTs was the only option in order to salvage the scheduled 4 week HADES production run, and this risky operation could be successfully completed in January 2019. The complete HADES RICH detector had to be dismounted before the window could be finally removed. Figure 6 shows a photograph of the opened RICH radiator with the multi-hexagon-segmented CaF_2 window still in place. Removing the CaF_2 window increased the RICH radiator volume significantly, such that it could no longer be handled by the original gas system which was designed for closed circuit operation and cleaning of the C_4F_{10} radiator gas. This could be solved by changing the Cherenkov radiator gas to iso-Butane, C_4H_{10}, now operating the gas system in simple free flow configuration. C_4H_{10} has very similar Cherenkov properties (in terms of refractive index and Cherenkov threshold) as compared to C_4F_{10}, but has lower density. In addition, the scintillation light yield of C_4H_{10} is significantly lower compared to C_4F_{10}, where the Cherenkov photon yield is even slightly higher (and further increased by missing reflection losses on the window). In summary, removing the CaF2 window was a very critical and difficult operation (in particular in view of the short preparation time available), but in the end it even provides a further performance improvement due to higher photon yield and less scintillation background. With these modifications, the HADES RICH detector was finally ready for beam in February 2019, just in time for the 4 week HADES production run.

Summary and outlook

The upgrade of the HADES RICH photon detector has been successfully completed, and allows now for the reliable and efficient operation of the HADES RICH detector during the recently started FAIR Phase 0 program and even beyond. First data look very promising as demonstrated in Figure 7, showing a typical single event image with a pair of dilepton Cherenkov rings (as it might stem from an omega decay...). The development of a common electronic readout chain, using same MAPMTs for both the HADES- and CBM RICH photon detectors, as well as its full-scale operation under most realistic conditions within HADES already now, as part of the FAIR phase 0 scientific program, allows for valuable synergies and optimum resource utilization, and provides the necessary experience for a smooth startup of the CBM RICH detector once first beam at SIS100 will become available. Analysis of the first data has just started.

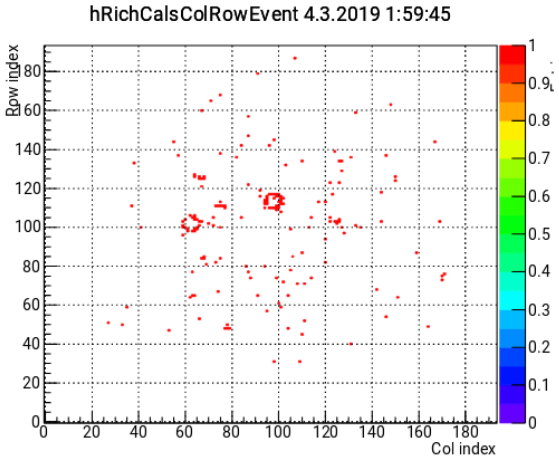

Figure 7: One of the first single event images of the upgraded HADES RICH detector, showing a close pair of electron Cherenkov rings.

References

[1] C. Pauly et al., "COSY testbeam for DIRICH qualification", CBM progress report (2017) pg. 60, http://repositry.gsi.de/record/209729.

[2] C. Pauly et al., "Upgrade of the HADES RICH photon detector with H12700 MAPMTs", NIM A 876, 164-167.

[3] V. Patel, M. Traxler, "The HADES-RICH upgrade using Hamamatsu H12700 MAPMTs with DIRICH FEE + Readout", JINST 13, C03038.

[4] J. Michel et al., "Electronics for the RICH Detectors of the HADES and CBM Experiments", JINST 12 (2017) C01072.

[5] J. Adamczewski-Musch et al., "Influence of wavelength-shifting films on multianode PMTs with UV-extended windows", NIMA 783 (2015) 43-50.

[6] V. Patel et al., "Time over Threshold (ToT) cuts for optimising the signal information of MAPMT signals", this report.

[7] V. B. Mikhailic et al., "Scintillation properties of pure CaF2", NIM A 566, Vol 2, 522-525.

[8] K. Schmidt-Sommerfeld, MSc Thesis TUM 2014, and J. Friese, private communication.

CBM Publications 2018

- T. Ablyazimov, V. Friese and V. Ivanov
Time Based Global Track Reconstruction in CBM
EPJ Web Conf. 173 (2018) 04001 (Proceedings of MMCP 2017)

- E. Akishina *et al.*
Development of the geometry database for the CBM experiment
Phys. Part. Nucl. Lett. 15 (2018) 97

- V. Akishina and I. Kisel
Online Event Reconstruction in the CBM Experiment at FAIR
EPJ Web Conf. 173 (2018) 01002 (Proceedings of MMCP 2017)

- V. Akishina *et al.*
Time-based Reconstruction of Free-streaming Data in CBM
EPJ Web Conf. 173 (2018) 04002 (Proceedings of MMCP 2017)

- P. Bhaduri, M. Deveaux and A. Toia
Charmonium interaction in nuclear matter at FAIR
J. Phys. G 45 (2018) 05510)

- P. Bhaduri and A. Bhattacharyya
Ψ(2S) production in p+A collisions
EPL 124 (2018) 22001

- D. Blau *et al.*
Performance Studies for Strange Hadron Flow Measurements in CBM at FAIR
KnE Energ. Phys. 3 (2018) 195 (Proceedings of ICPPA 2017)

- O. Derenovskaya, VT. Ablyazimov and V. Ivanov
Towards J/$\psi \rightarrow e^+e^-$ Decays Triggering with TRD in CBM Experiment
EPJ Web Conf. 173 (2018) 04004 (Proceedings of MMCP 2017)

- D. Finogeev *et al.*
The PSD CBM Supermodule Response Study for Hadrons in Momentum Range 2 - 6 GeV/c at CERN Test Beams
KnE Energ. Phys. 3 (2018) 333 (Proceedings of ICPPA 2017)

- M. Guminski *et al.*
Systemy elektroniczne dla toru odczytu danych w eksperymencie CBM
Elektronika : konstrukcje, technologie, zastosowania, 59 Nr 5 (2018) 8 (Proceedings of Photonics Applications in Astronomy, Communications, Industry, and High-Energy Physics Experiments 2018)

- K. Kasinski *et al.*
Characterization of the STS/MUCH-XYTER2, a 128-channel time and amplitude measurement IC for gas and silicon microstrip sensors
Nucl. Instrum. Methods A 908 (2018) 225

- I. Kisel *et al.*
Event Topology Reconstruction in the CBM Experiment
J. Phys. Conf. Ser. 1070 (2018) 012015 (Proceedings of WWND 2018)

- P. Kisel *et al.*
Strange Particle Reconstruction by the Missing Mass Method
EPJ Web Conf. 173 (2018) 04009 (Proceedings of MMCP 2017)

- V. Klochkov and I. Selyuzhenkov
CBM Performance for Anisotropic Flow Measurements
KnE Energ. Phys. 3 (2018) 416 (Proceedings of ICPPA 2017)

- C. Li *et al.*
Quality Evaluation System for CBM-TOF Super Module
Springer Proc. Phys. 212 (2018) 210 (Proceedings of TIPP2017)

- C. Li *et al.*
Clock and trigger distribution for CBM-TOF quality evaluation of RPC super module detector assemblies
JINST 13 (2018) P03013

- P. Lyu and Y. Wang
High Rate Time of Flight System for FAIR-CBM
Springer Proc. Phys. 212 (2018) 263 (Proceedings of TIPP2017)

- I. Momot *et al.*
Investigation into the charge collection efficiency of prototype microstrip sensors for the CBM Silicon Tracking System
J. Phys. Conf. Ser. 1024 (2018) 012004 (Proceedings of FAIRNESS 2017)

- D. Nag *et al.*
Design and Fabrication of a Controlled Water Based Cooling System for CBM Muon Chamber
Springer Proc. Phys. 203 (2018) 893 (Proceedings of 22nd DAE-BRNS High Energy Physics Symposium)

- E. Nandy and S. Chattopadhyay
Performance Study of Muon Detector with CBM Experiment at FAIR
Springer Proc. Phys. 201 (2018) 157 (Proceedings of ADNHEAP 2017)

- E. Nandy and S. Chattopadhyay
Detection of Low Mass Vector Mesons in the Muon Detector of CBM Experiment
Springer Proc. Phys. 203 (2018) 383 (Proceedings of 22nd DAE-BRNS High Energy Physics Symposium)

- E. Nandy, P. Bhaduri and S. Chattopadhyay
A systematic investigation of di-muon combinatorial background for ω in the CBM experiment at FAIR
Proceedings of the DAE Symposium on Nuclear Physics 63 (2018) 1016

- E. Nandy, P. Bhaduri and S. Chattopadhyay
Strangeness Enhancement at FAIR
Proceedings of the DAE Symposium on Nuclear Physics 63 (2018) 1018

- M. Petris *et al.*
In-beam test of the RPC architecture foreseen to be used for the CBM-TOF inner wall
J. Phys. Conf. Ser. 1023 (2018) 012007 (Proceedings of 22nd International School on Nuclear Physics, Neutron Physics and Applications)

- F. Roether *et al.*
  Construction of Multi Wire Proportional Chambers for the CBM Transition Radiation Detector
  J. Phys. Conf. Ser. 1024 (2018) 012040 (Proceedings of FAIRNESS 2017)

- P. Senger and N. Herrmann
  Cosmic Matter in the Laboratory: The CBM Experiment at FAIR
  Nucl. Phys. News 28 (2018) 23

- W. Zubrzycka and I. K. Kasinski
  Leakage current-induced effects in the silicon microstrip and gas electron multiplier readout chain and their compensation method
  JINST 13 (2018) T04003

Doctoral, diploma, master and bachelor theses 2018

http://cbm-wiki.gsi.de/cgi-bin/view/Public/Thesis2018

CBM presentations 2018

http://cbm-wiki.gsi.de/cgi-bin/view/Public/PublicPresentations2018

CBM PhD Award 2017

The CBM PhD Award decorates the best doctoral work related to the CBM experiment. With this award, the CBM collaboration especially wants to honour the contributions of students to the CBM project. The award was granted for the first time at the CBM Collaboration Meeting in April 2016 for PhD theses defended in the year 2015. It is given annually and is endowed with a prize money of 500 Euro.

For the year 2017, three candidates were nominated by their doctoral advisers. The selection was carried out by a committee appointed by the CBM collaboration, consisting of A. Kugler, M. Petrovici and S. Chattopadhyay. The criteria for the evaluation were:

- Impact on the CBM present and future activities, taking into account active participation in CBM (40%);
- Added scientific value in the field of the PhD thesis (30%);
- Publications in refereed journals to which the candidate had a significant contribution (30%).

The prize winner for 2017 is

Dr Valentina Akishina

from Goethe-Universität Frankfurt for her work on

Four-dimensional event reconstruction in the CBM experiment

Dr Valentina Akishina, winner of the CBM PhD Award 2017

The CBM Collaboration

- **Aligarh, India, Department of Physics, Aligarh Muslim University**
  N. Ahmad, M.D. Azmi, M. Irfan, H. Jahan, M.M. Khan, O. Singh
- **Beijing, China, Department of Engineering Physics, Tsinghua University**
  Zhi Deng, Dong Han, Xinjie Huang, Yuanjing Li, Pengfei Lyu, Yi Wang, Xianglei Zhu
- **Berlin, Germany, Konrad-Zuse-Zentrum für Informationstechnik Berlin (ZIB)**
  A. Reinefeld, F. Salem, F. Schintke, T. Schütt
- **Bhubaneswar, India, Institute of Physics**
  P.K. Sahu, S.K. Sahu
- **Bhubaneswar, India, National Institute of Science Education and Research (NISER)**
  A. Jash, V.K.S. Kashyap, B. Mohanty, S. Samanta, R. Singh
- **Bucharest, Romania, Horia Hulubei National Institute of Physics and Nuclear Engineering (IFIN-HH)**
  A. Bercuci, M. Petriş, M. Petrovici, L. Radulescu, C. Schiaua
- **Bucharest, Romania, Atomic and Nuclear Physics Department, University of Bucharest**
  D. Argintaru, V. Baban, M. Călin, T. Eşanu, A. Jipa, I. Lazanu, C. Ristea, O. Ristea, N.G. Tuturas
- **Budapest, Hungary, Eötvös Loránd University (ELTE)**
  M. Csanád, A. Olar
- **Budapest, Hungary, Institute for Particle and Nuclear Physics, Wigner Research Centre for Physics, Hungarian Academy of Sciences**
  T. Kiss, T. Tölyhi, D. Varga, Gy. Wolf
- **Chandigarh, India, Department of Physics, Panjab University**
  L. Kumar
- **Chongqing, China, Chongqing University**
  Liang-ming Pan, Qiqi Wu, Wenxiong Zhou
- **Darmstadt, Germany, Facility for Antiproton and Ion Research in Europe GmbH (FAIR)**
  J. Eschke[1], E. Lavrik, W.F.J. Müller[1], M. Teklishyn[2]
- **Darmstadt, Germany, GSI Helmholtzzentrum für Schwerionenforschung GmbH (GSI)**
  M. Al-Turany, M. Bajdel, D. Bertini, O. Bertini, H. Deppe, D. Emschermann, H. Flemming, P. Foka, U. Frankenfeld, V. Friese, J. Frühauf, Xin Gao, J. Hehner, J.M. Heuser, R. Holzmann, R. Kapell, R. Karabowicz, M. Kiš, V. Klochkov[3], K. Koch, P. Koczoń, D. Kresan, P. Kuhl, A. Lebedev[4], J. Lehnert, Y. Leifels, S. Löchner, P.-A. Loizeau, A. Lymanets, O. Maragoto Rodriguez[3], A.M. Marin Garcia, J. Markert, D. Miskowiec, T. Morhardt, W. Niebur, J. Pietraszko, A. Rodriguez Rodriguez, C.J. Schmidt, I. Selyuzhenkov[5], A. Senger, P. Senger[3], C. Simons, D. Soyk, C. Sturm, A. Toia[3], M. Träger, F. Uhlig, I. Vassiliev, O. Vasylyev, R. Visinka, C. Wendisch, A. Wilms, P. Zumbruch, M. Zyzak
- **Darmstadt, Germany, Institut für Kernphysik, Technische Universität Darmstadt**
  T. Galatyuk[1], A. Rost, F. Seck
- **Dresden, Germany, Institut für Strahlenphysik, Helmholtz-Zentrum Dresden-Rossendorf (HZDR)**
  Xingming Fan[12], B. Kämpfer[12], R. Kotte, L. Naumann, D. Stach
- **Dubna, Russia, Laboratory of Information Technologies, Joint Institute for Nuclear Research (JINR-LIT)**
  T. Ablyazimov, P. Akishin, E. Alexandrov, I. Alexandrov, S. Belogurov[5], O. Derenovskaya, Victor Ivanov[5], A.V. Kryanev[5]

- **Dubna, Russia, Veksler and Baldin Laboratory of High Energy Physics, Joint Institute for Nuclear Research (JINR-VBLHEP)**

  A. Bychkov, D. Dementiev, V.V. Elsha, O. Fateev, K. Gudima, Yu. Gusakov, G. Kekelidze, A. Kolozhvari, P. Kurilkin, S. Kuznetsov, V. Ladygin, A. Malakhov, Yu. Murin, S. Parzhitskiy, A. Shabunov, A.D. Sheremetiev, M. Shitenkow, N.I. Zamiatin, A. Zinchenko

- **Frankfurt, Germany, Frankfurt Institute for Advanced Studies, Goethe-Universität Frankfurt (FIAS)**

  A. Belousov, J. de Cuveland, S. Gorbunov, H. Hartmann, D. Hutter, I. Kisel, P. Kisel[1,4], G. Kozlov[4], V. Lindenstruth[1], M. Pugach[1,2], A. Redelbach

- **Frankfurt, Germany, Institut für Kernphysik, Goethe-Universität Frankfurt**

  V. Akishina[4,1], H. Appelshäuser, E. Bechtel, C. Blume[1], T. Bus, H. Cherif[1], M. Deveaux, P. Dillenseger, I. Fröhlich, S. Gläßel, P. Klaus, M. Koziel, Qiyan Li[6], B. Linnik, H. Malygina[1,2], J. Michel, I. Momot[1,2], C. Müntz, M. Petri, F. Roether, P. Sitzmann, D. Spicker, J. Stroth[1]

- **Frankfurt, Germany, Institute for Computer Science, Goethe-Universität Frankfurt**

  A. Adler, H. Engel, T. Janson, U. Kebschull, C. Lara, J.A. Lucio Martínez, C. Stüllein

- **Gatchina, Russia, Petersburg Nuclear Physics Institute named by B.P.Konstantinov of National Research Centre "Kurchatov Institute" (PNPI)**

  D. Ivanishchev, Vladimir Ivanov[5], A. Khanzadeev[5], L. Kochenda[5], B. Komkov, V. Kozlov, P. Kravtsov[5], E. Kryshen, L. Kudin, V. Nikulin, E. Rostchin[5], Yu. Ryabov, V. Samsonov[5,13], O. Tarassenkova, M. Zhalov

- **Gießen, Germany, Justus-Liebig-Universität Gießen**

  J. Bendarouach[1], C.A. Deveaux, M. Dürr, T. Geßler, C. Höhne, S. Lebedev[4], E. Lebedeva, J.H. Otto, E. Ovcharenko[4], G. Pitsch, C. Riesen, A.A. Weber

- **Guwahati, India, Nuclear and Radiation Physics Research Laboratory, Department of Physics, Gauhati University**

  B. Bhattacharjee, S. Gope

- **Hefei, China, Department of Modern Physics, University of Science & Technology of China (USTC)**

  Zhiguo Ding, Dongdong Hu[7], Chao Li, Yongjie Sun, Junfeng Yang, Rongxing Yang, Jianhui Yuan, Jian Zhou

- **Heidelberg, Germany, Physikalisches Institut, Universität Heidelberg**

  I. Deppner, D. Gottschalk, N. Herrmann, C. Simon, P. Weidenkaff, Qiunan Zhang[8]

- **Heidelberg, Germany, Institut für Technische Informatik, Universität Heidelberg**

  P. Fischer, M. Krieger

- **Indore, India, Indian Institute of Technology Indore**

  S.K. Kundu, A. Roy, R. Sahoo

- **Jammu, India, Department of Physics, University of Jammu**

  A. Bhasin, A. Gupta, S. Mahajan, S.S. Sambyal

- **Karlsruhe, Germany, Karlsruhe Institute of Technology (KIT)**

  S. Bähr, M. Balzer, J. Becker, T. Blank, S.P.D. Figuli, P. Pfistner, O. Sander, V. Sidorenko, M. Weber

- **Kharagpur, India, Indian Institute of Technology Kharagpur**

  T.K. Bhattacharyya, S. Sarangi, A.K. Singh, I. Som

- **Kolkata, India, Department of Physics, Bose Institute**

  R.P. Adak, S. Biswas, Supriya Das, S.K. Ghosh, S. Mukherjee, S.K. Prasad, S. Raha, R. Ray, S. Roy

- **Kolkata, India, Department of Physics and Department of Electronic Science, University of Calcutta**

  A. Bhattacharyya, A. Chakrabarti, G. Gangopadhyay, S. Sau

- **Kolkata, India, Variable Energy Cyclotron Centre (VECC)**

  Z. Ahammed, P.P. Bhaduri, S. Chattopadhyay[9], A.K. Dubey, C. Ghosh, Ajit Kumar, M. Mandal, E. Nandy, T. Nayak, J. Saini, V. Singhal

- **Kraków, Poland, AGH University of Science and Technology (AGH)**

  M. Baszczyk, P. Dorosz, P. Gryboś, K. Kasiński, R. Kłeczek, P. Kmon, A. Krzyżanowska, W. Kucewicz, P. Maj, L. Mik, P. Otfinowski, R. Szczygieł, M. Żołądź, W. Zubrzycka

- **Kraków, Poland, Marian Smoluchowski Institute of Physics, Jagiellonian University**

  J. Brzychczyk, K. Łojek, Z. Majka, R. Płaneta, P. Staszel, A. Wieloch

- **Kyiv, Ukraine, High Energy Physics Department, Kiev Institute for Nuclear Research (KINR)**

  A. Chaus, O. Kot, A. Kovalchuk, V. Kyva, V. Militsija, V. Pugatch, D. Ramazanov, D. Storozhyk

- **Kyiv, Ukraine, Department of Nuclear Physics, Taras Shevchenko National University of Kyiv**

  O. Bezshyyko, L. Golinka-Bezshyyko, I. Kadenko, O. Lubynets, V. Plujko

- **Moscow, Russia, Institute for Nuclear Research (INR)**

  M. Golubeva, F. Guber, A. Ivashkin, N. Karpushkin, A. Kurepin, N. Kurepin, A. Maevskaya, S. Morozov, O. Petukhov, A. Reshetin, A. Shabanov, N. Topil'skaya, E. Usenko

- **Moscow, Russia, Institute for Theoretical and Experimental Physics named by A.I. Alikhanov of National Research Centre "Kurchatov Institute" (ITEP)**

  A. Akindinov, I. Alekseev, D. Golubkov, F. Khasanov, S. Kiselev, I. Korolko, D. Malkevich, K. Mikhailov, V. Plotnikov, M. Prokudin, A. Semennikov, R. Sultanov, D. Svirida, Yu. Zaitsev, I. Zivko

- **Moscow, Russia, National Research Nuclear University MEPhI**

  E. Atkin, O. Golosov, P. Ivanov, N. Kargin, E. Kashirin, E. Malankin, O. Malyatina, D. Normanov, V. Shumikhin, M. Strikhanov, A. Taranenko

- **Moscow, Russia, National Research Centre "Kurchatov Institute"**

  D. Blau[5], A. Kazantsev, V. Manko, I. Sibiryak, I. Yushmanov

- **Moscow, Russia, Skobeltsyn Institute of Nuclear Phyiscs, Lomonosov Moscow State University (SINP-MSU)**

  N. Baranova, D. Karmanov, M. Korolev, M. Merkin, A. Voronin

- **Münster, Germany, Institut für Kernphysik, Westfälische Wilhelms-Universität Münster**

  A. Andronic, J. Beckhoff, R. Berendes, F. Fidorra, N. Heine, P. Kähler, Ch. Klein-Bösing, M. Kohn, A. Meyer-Ahrens, P. Munkes, P.M. Schneider, J.P. Wessels

- **Prague, Czech Republic, Czech Technical University (CTU)**

  V. Petráček, L. Škoda

- **Protvino, Russia, Institute for High Energy Physics (IHEP)**

  S. Golovnya, S. Gorokhov, A. Kiryakov, I. Lobanov, E. Lobanova, Yu. Tsyupa, A. Vorobiev

- **Pusan, Korea, Pusan National University (PNU)**

  In-Kwon Yoo

- **Řež, Czech Republic, Nuclear Physics Institute of the Czech Academy of Sciences**

  A. Kugler, V. Kushpil, V. Mikhaylov

- **Srinagar, India, Department of Physics, University of Kashmir**

  A. Ahmad, F. Ahmad, S. Bashir, S.A. Bhat, M.F. Mir, W. Raja

- **Tübingen, Germany, Physikalisches Institut, Eberhard Karls Universität Tübingen**

  K. Agarwal, Susovan Das, E. Friske, S. Mehta, I. Panasenko[2], H.R. Schmidt, M. Völkl, E. Volkova

- **Varanasi, India, Department of Physics, Banaras Hindu University (BHU)**

  B.K. Singh, C.P. Singh

- **Warsaw, Poland, Institute of Electronic Systems, Warsaw University of Technology**

  A. Byszuk, M. Gumiński, G. Kasprowicz, M. Kruszewski, J. Pluta, K. Poźniak[10], R. Romaniuk, D. Wielanek, W. Zabołotny[10]

- **Warsaw, Poland, Faculty of Physics, University of Warsaw**

  T. Matulewicz, K. Piasecki, D. Wójcik

- **Wuhan, China, College of Physical Science and Technology, Central China Normal University (CCNU)**

  Wendi Deng, Sheng Dong[7], Shu He, Guangming Huang, Feng Liu, Xiaofeng Luo, Shusu Shi, Dong Wang, Nu Xu[11], Zhongbao Yin, Yu Zhang, Daicui Zhou

- **Wuppertal, Germany, Fakultät für Mathematik und Naturwissenschaften, Bergische Universität Wuppertal**

  K.-H. Becker, J. Förtsch, K.-H. Kampert, I. Kres, V. Patel, C. Pauly, D. Pfeifer, S. Querchfeld, J. Rautenberg

- **Yichang, China, College of Science, China Three Gorges University (CTGU)**

  Sheng-Qin Feng, Ke-Jun Wu, Yan-Qing Zhao, Sheng Zheng

Additional affiliations:
[1] GSI Helmholtzzentrum für Schwerionenforschung GmbH (GSI), Darmstadt, Germany
[2] High Energy Physics Department, Kiev Institute for Nuclear Research (KINR), Kyiv, Ukraine
[3] Institut für Kernphysik, Goethe-Universität Frankfurt, Frankfurt, Germany
[4] Laboratory of Information Technologies, Joint Institute for Nuclear Research (JINR-LIT), Dubna, Russia
[5] National Research Nuclear University MEPhI, Moscow, Russia
[6] College of Physical Science and Technology, Central China Normal University (CCNU), Wuhan, China
[7] Physikalisches Institut, Universität Heidelberg, Heidelberg, Germany
[8] Department of Engineering Physics, Tsinghua University, Beijing, China
[9] Department of Physics, Bose Institute, Kolkata, India
[10] Faculty of Physics, University of Warsaw, Warsaw, Poland
[11] National Institute of Science Education and Research (NISER), Bhubaneswar, India
[12] also: Technische Universität Dresden, Dresden, Germany
[13] also: St. Petersburg Polytechnic University (SPbPU), St. Petersburg, Russia

Contacts

Chairman of the Collaboration Board
Nu Xu
nxy@lbl.gov

Spokesman
Norbert Herrmann
n.herrmann@physi.uni-heidelberg.de

Deputy Spokesman
Subhasis Chattopadhyay
sub@vecc.gov.in

Deputy Spokesman
Vladimir Ladygin
vladygin@jinr.ru

Technical Coordinator
Walter Müller
w.f.j.mueller@gsi.de

Physics Coordinator
Ilya Selyuzhenkov
i.selyuzhenkov@gsi.de

Computing Coordinator
Volker Friese
v.friese@gsi.de

Resource Coordinator
Jürgen Eschke
j.eschke@gsi.de

Chairman of the Conference Board
Hans-Rudolf Schmidt
h.r.schmidt@gsi.de

Management Board
Peter Senger, Joachim Stroth, Wojciech Zabołotny

http://www.fair-center.eu/for-users/experiments/cbm.html

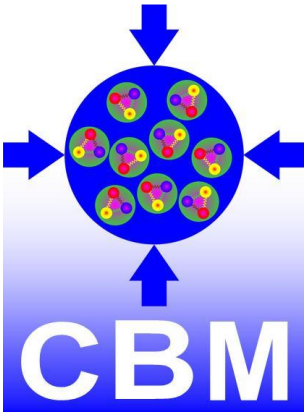
CBM


FAIR


HELMHOLTZ
GEMEINSCHAFT


GSI


Bundesministerium
für Bildung
und Forschung


HIC
for
FAIR
Helmholtz International Center

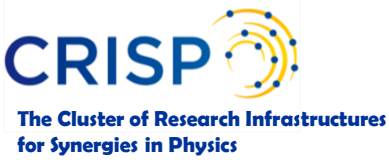
CRISP
The Cluster of Research Infrastructures
for Synergies in Physics


Study of Strongly Interacting Matter
HadronPhysics